Structural Characterization of Sarcolipin by Solid State NMR and Investigation of its Role in the Regulation of Sarco(endo)plasmic Reticulum Calcium Adenosine-Triphosphatase

A DISSERTATION

SUBMITTED TO THE FACULTY OF

UNIVERSITY OF MINNESOTA

BY

Kaustubh Rajeev Mote

IN PARTIAL FULFILLMENT OF THE REQUIREMENTS

FOR THE DEGREE OF

DOCTOR OF PHILOSOPHY

Dr. Gianluigi Veglia

February 2014

Acknowledgements

I am indebted to my advisor Dr. Gianluigi Veglia for all his guidance, support and his seemingly unending enthusiasm for all things, science and otherwise. The goals that I set out with as my Ph.D. project seemed too difficult to me, but his determination to push the envelope on seemingly intractable problems have guided me through all the failures, blind-alleys and wrong-turns.

Gianluigi's talent as an advisor has also meant that I have always had the support of a number of great graduate students and post-docs to work with. Dr. Tata Gopinath has led the methodological development in our lab, without which it would be difficult to envisage any of the work reported here. He has been a tremendous source for all things NMR throughout my Ph.D. I learned all my wet-lab techniques from Dr. Nathaniel Traaseth, Dr. Kim Ha, Dr. Raffaello Verardi and Dr. Larry Masterson – I could not have asked for a more systematic and talented set of co-workers to teach me all these techniques. I have benefitted tremendously from discussions with Dr. Martin Gustavsson and more recently Dr. Vitaly Vostrikov with whom I continue to collaborate with and come up with new ideas to test. It would be difficult to imagine what these five years would be like without the support and help of Fa-an Chao, in and out of lab. Jonggul Kim, Geoffrey Li, Alysha Dicke, Kailey Soller and Sarah Nelson have all been great in their enthusiasm for the project – and have made me see my project with newcomers' eyes – something that has helped me tremendously in designing new experiments that they will hopefully continue forward. Our collaboration with Dr. David Thomas's lab has a been a great source of knowledge on muscle physiology, especially Dr. Autry and Dr. Li, who have provided wonderful insights through their discussions.

I have had great support from my family and friends and I find it hard to imagine myself here today had it not been for them, and certainly not without Girija - my friend and my family.

Dedication

To my mother, for without her none of this would have been possible.

Abstract

Structural characterization of membrane proteins and their complexes is an important and ever growing challenge to the classical techniques of biomolecular structural characterization. Rapid developments in the field of solid state NMR (ssNMR) have opened up an exciting new alternative to X-ray crystallography, as these studies can now be performed in fully hydrated lipid bilayers that faithfully mimic the physiologically relevant conditions. Nonetheless, routine application of ssNMR on biomolecular systems is hampered by their low sensitivity and spectral resolution. In this work, we have addressed these challenges by developing new strategies to study membrane proteins by ssNMR. With a set of improved pulse sequences for oriented and magic angle spinning techniques in ssNMR, we determined the topology (i.e. the structure and transmembrane orientation) of sarcolipin, a regulator of the Sarco(endo)plasmic Reticulum Ca^{2+}-ATPase (SERCA), in lipid bilayers. These techniques are further used to study the complex between these two proteins and understand the molecular basis for this regulatory interaction. The methodological developments reported here are transferable to studies on other membrane proteins and they clear several roadblocks in the successful application of ssNMR for these challenging bio-molecular systems. Finally, we present how these studies have furthered our understanding of the regulation of muscle relaxation process by SERCA. These findings represent the first steps in designing new therapeutic approaches for cardiac and skeletal muscle disorders.

TABLE OF CONTENTS

List of Figures

1. Introduction

2. Sensitivity and Resolution Enhancement of Oriented Solid-State NMR: Application to Membrane Proteins

3. Multidimensional Oriented Solid-State NMR Experiments Enable the Sequential Assignment of Uniformly 15N Labeled Integral Membrane Proteins in Magnetically Aligned Lipid Bilayers

4. Determination of Structural Topology of a Membrane Protein in Lipid Bilayers using Polarization Optimized Experiments (POE) for Static and MAS Solid State NMR Spectroscopy

5. Topological allostery architects sarcolipin's regulation of the SR-Ca2+-ATPase

6. Structural dynamics and topology of phosphorylated phospholamban homopentamer reveal its role in the regulation of calcium transport.

7. Allosteric regulation of SERCA by phosphorylation-mediated conformational shift of phospholamban

Appendix

LIST OF TABLES

3. Multidimensional Oriented Solid-State NMR Experiments Enable the Sequential Assignment of Uniformly 15N Labeled Integral Membrane Proteins in Magnetically Aligned Lipid Bilayers

4. Determination of Structural Topology of a Membrane Protein in Lipid Bilayers using Polarization Optimized Experiments (POE) for Static and MAS Solid State NMR Spectroscopy

6. Structural dynamics and topology of phosphorylated phospholamban homopentamer reveal its role in the regulation of calcium transport.

7. Allosteric regulation of SERCA by phosphorylation-mediated conformational shift of phospholamban

Preface

Chapters II - VII are taken directly from manuscripts that are published, submitted or in preparation.

Chapter II consists of sections 1, 3 and 4 from the following review article

'T. Gopinath, K. R. Mote, and G. Veglia, "Sensitivity and resolution enhancement of oriented solid-state NMR: application to membrane proteins", *Progress in Nuclear Magnetic Resonance Spectroscopy*, vol. 75, pp. 50–68, Nov. 2013.'

This review includes data from the following original research articles:

T. Gopinath, K. R. Mote, and G. Veglia, "Proton evolved local field solid-state nuclear magnetic resonance using Hadamard encoding: theory and application to membrane proteins.," *Journal of Chemical Physics.*, vol. 135, no. 7, p. 074503, Aug. 2011.

T. Gopinath, N. J. Traaseth, K.R. Mote, and G. Veglia, "Sensitivity enhanced heteronuclear correlation spectroscopy in multidimensional solid-state NMR of oriented systems via chemical shift coherences.," *Journal of the American Chemical Society*, vol. 132, no. 15, pp. 5357–63, Apr. 2010.

Chapter III consists of the following article:

K. R. Mote, T. Gopinath, N. J. Traaseth, J. Kitchen, P. L. Gor'kov, W. W. Brey and G. Veglia, "Multidimensional oriented solid-state NMR experiments enable the sequential assignment of uniformly 15N labeled integral membrane proteins in magnetically aligned lipid bilayers.," *Journal of Bimolecular NMR*, vol. 51, no. 3, pp. 339–46, Nov. 2011.

Chapter IV consists of the following article:

K. R. Mote, T. Gopinath, and G. Veglia, "Determination of structural topology of a membrane protein in lipid bilayers using polarization optimized experiments (POE) for static and MAS solid state NMR spectroscopy.," *Journal of Bimolecular NMR*, vol. 57, no. 2, pp. 91–102, Oct. 2013.

Chapter V consists of the following article:

K. R. Mote, V. V. Vostrikov, S. K. Sahoo, A. Dicke, A. Cembran, M. Gustavsson, T. Gopinath, M. Periasamy and G. Veglia, "Topological allostery architects sarcolipin's regulation of the calcium pump" , in preparation

Chapter VI consists of the following article:

V. V Vostrikov, K. R. Mote, R. Verardi, and G. Veglia, "Structural dynamics and topology of phosphorylated phospholamban homopentamer reveal its role in the regulation of calcium transport.," *Structure*, vol. 21, no. 12, pp. 2119–30, Dec. 2013.

Chapter VII consists of the following article:

M. Gustavsson, R. Verardi, D. G. Mullen, K. R. Mote, N. J. Traaseth, T. Gopinath, and G. Veglia, "Allosteric regulation of SERCA by phosphorylation-mediated conformational shift of phospholamban.," *Proceedings of the National Academy of Sciences. U. S. A.*, vol. 110, no. 43, pp. 17338–43, Oct. 2013.

1. Introduction

Structural Studies of Membrane Proteins

Membrane proteins are a major challenge to the classical techniques of protein structure determination – X-ray crystallography and NMR. This is in part due to the necessity of maintaining a lipid bilayer environment for maintaining their structural integrity (*1*, *2*). The lipid bilayer is not just a passive matrix, but often plays a crucial role in enabling protein function – may it be ion transport (*3*–*5*), metabolite transport (*6*, *7*), signal propagation (*8*, *9*) or maintaining structural integrity in an organelle (*10*). The discovery of lipid rafts as well as the organelle-dependent variability in lipid composition has shed light on the critical role played by the membrane in dictating membrane protein function (*11*, *12*). Changes in lipid composition, concentration and phase can have significant effect on the activity of membrane proteins (*13*–*15*). Structural characterization in context of the native lipid environment is thus imperative for a complete understanding these proteins at the molecular level. This field of study has assumed an even greater importance, as membrane proteins are estimated to be 40% of the current drug targets (*16*).

Although a number of advances have been made in the past decade in improving and adapting X-ray crystallographic techniques to better handle membrane proteins (*17*), only ~380 unique membrane protein folds have been identified so far (http://blanco.biomol.uci.edu/mpstruc/). Even with large polytopic membrane proteins, where X-ray crystallography has been most successful (*18*, *19*), the lack of a bilayer environment remains a significant obstacle for identifying key structural features in their biological context. Solid state NMR spectroscopy (ssNMR) offers an alternative to X-ray crystallography as well as solution NMR spectroscopy, as membrane protein samples can be prepared in fully hydrated lipid bilayers that faithfully mimic the physiologically relevant conditions (*20*). In addition, NMR techniques offer a *dynamic* picture of the

protein, as opposed to a *static* picture obtained from X-ray crystallography where the protein is confined to a minimum (local or global) on the energy landscape, accessing fewer conformational states than in its native environment. This offers a significant advantage in studies on membrane protein complexes by solid state NMR, as their interactions are often driven and modulated by the bilayer environment (*13*, *14*, *21*). Depending on the choice of the membrane mimic (Fig. 1.1), one can then undertake either magic angle spinning (MAS) ssNMR (in lipid vesicles or bicelles) or oriented solid state NMR (O-ssNMR; in aligned bilayers or aligned bicelles). Of these, O-ssNMR can provide a description of the structural topology of a membrane protein, i.e. its secondary and tertiary structure along with the transmembrane orientation – information that is difficult to obtain by any other technique (Fig. 1.2). MAS-ssNMR, on the other hand, can provide information on the secondary and tertiary structure for the backbone as well as the side chain atoms.

Challenges to the methodology

The rapid technical development in O-ssNMR (*20*, *22*) and MAS-ssNMR (*23*) has allowed number of strategies to be developed to study membrane proteins (*24–32*). Nonetheless, their application to membrane proteins remains a challenging task (*23*). Low sensitivity and resolution, the two major problems in NMR spectroscopy, are often exacerbated in ssNMR. These problems are even more pronounced in the study of membrane proteins, where the necessity of maintaining a lipid bilayer environment reduces the effective protein concentration. Repeating secondary structure elements (e.g. transmembrane α-helices) are often subject to similar chemical environment, reducing the inherent resolution of resonances of a protein. Finally, unlike solution state NMR, only a few standardized pulse sequences have been developed to assign ssNMR spectra. Thus, the application of ssNMR to membrane proteins will involve designing new strategies in terms of both, NMR spectroscopy as well as sample preparation techniques (*25*, *29*, *33–40*).

In this thesis, these problems are addressed in Chapters 2, 3 and 4. Chapter 2 discusses the development of sensitivity enhanced pulse sequence for oriented ssNMR. The newly developed pulse sequences show a sensitivity enhancement from 40% to 180%, speeding up data acquisition 2-fold to 7-fold (*41–44*). This work forms the basis of Chapter 3, where the improved pulse sequences along with improved sample preparation techniques are utilized to assign oriented ssNMR spectra of a uniformly labeled sample (*39*). The use of improved pulse sequences in O-ssNMR and MAS-ssNMR is shown in Chapter 4, which describes the *de novo* determination of the complete topology of a transmembrane protein (*29*). These improved techniques are applied in order to understand the regulation of SERCA is described in Chapters 5-7 (*45*, *46*). Appendix-I details the basic theory behind these experiments. The introduction to chapters 2, 3 and 4 have a more detailed description of the new pulse sequences and the new methodology. The following sections in this introduction describe the physiological role membrane proteins SERCA, sarcolipin and phospholamban which are studied using these ssNMR techniques.

Muscle cell physiology

The Sarco(endo)plasmic Reticulum Calcium ATPase belongs to the P-II type ATPase family (*19*, *47*) and is present primarily in the sarco(endo)plasmic reticulum (SR) of cardiac and skeletal muscle cells. It is primarily responsible for the active transport of Ca^{2+} from the cytosol of the muscle cell into the sarcoplasmic lumen (Fig. 1.3) (*4*). It utilizes ATP hydrolysis in order to transport Ca^{2+} against a steep concentration gradient. ATP hydrolysis and Ca^{2+} transport by SERCA increase cooperatively with increasing Ca^{2+} concentrations, with the K_M for Ca^{2+}-dependent Ca^{2+}-transport and ATP hydrolysis approximately 0.3μM, and the k_{cat} saturates at approximately 10μM (*48–50*). Cytosolic Ca^{2+} concentration increases to ~10μM during the contraction phase of the muscle cycle. SERCA can thus, effectively induce relaxation in the muscle (See Figure 1.4 for a mechanistic description of the cycle) by actively transporting this Ca^{2+} back into the lumen. SERCA is thus involved in a *beat-to-beat* regulation of cardiac and skeletal

muscle contraction and relaxation cycle, giving it a unique importance in the study of a number of associated disorders (*51*). Understanding the regulation of SERCA thus has far reaching biological consequences in the context of designing therapeutics for these disorders.

Regulation of SERCA by sarcolipin and phospholamban

Several SERCA isoforms are regulated by peptides encoded by small open reading frames (smORFs) (*52*). This regulatory pathway is evolutionarily conserved for more than 1 million years, and is active among species varying from arthropods to humans. In humans, two homologous peptides – phospholamban (PLN) and sarcolipin (SLN) – are responsible for the regulation of SERCA in different tissues. PLN is the regulator of SERCA2a isoform in cardiac ventricles (*53*), while SLN is the regulator of SERCA2a in cardiac atria and SERCA1a in skeletal muscle (*54*). Both PLN and SLN increase the K_M for Ca^{2+}-dependent ATP hydrolysis and decrease the maximal Ca^{2+} transport (Figure 1.5) (*49*, *55*). The resulting shift in SERCA activation to higher Ca^{2+} concentrations slows down the relaxation phase of the muscle cycle.

Sarcolipin (SLN) is a 3.8 kDa peptide (31 residues) consisting of a single transmembrane helix and short N- and C-terminal loops. Its transmembrane domain is similar to phospholamban (PLN), a 6 kDa peptide (52 residues), which contains in addition an N-terminal amphipathic helix. Mutational and cross-liking studies have demonstrated that SLN and PLN bind SERCA in a regulatory groove formed by its transmembrane helices M2, M4, M6 and M9. This was recently confirmed by crystal structures of SLN bound to SERCA under saturating Mg^{2+} concentrations and a super-inhibitory mutant of PLN bound to SERCA (*56–58*). SLN and PLN remain bound to SERCA throughout its catalytic cycle (*59*, *60*). Hence, it is proposed that the relief of inhibition at high Ca^{2+} concentrations (Figure 5) is due to a conformational change and not due to its detachment from SERCA (*46*, *59*, *61*). For PLN, the conformational dynamics of the cytoplasmic domain has been shown to play an important role in its interaction with SERCA (*46*, *49*,

62, *63*). Another aspect of SLN/PLN regulation is their phosphorylation by Protein Kinase A (*46*, *64*, *65*) or Calmodulin-dependent Protein Kinase II (CamK-II) that relieves inhibition (*66*), allowing for efficient cardiac muscle relaxation. However, the transmembrane domain for PLN and SLN alone are capable of inhibiting SERCA (*46*, *55*). How this inhibition is achieved by the transmembrane domain and what conformational changes mediate the relief of inhibition is at present not understood. *In vitro* studies that show a decrease in the apparent Ca^{2+} affinity for SERCA (*55*, *59*, *67*) in presence of SLN and PLN are consistent with SLN/PLN ablation (*68*, *69*) and overexpression (*70*, *71*) in mice, leading to increased and decreased cardiac contractility respectively. Several lethal mutations in PLN have been identified in humans (*53*, *72*). Although no lethal mutation in SLN have been discovered, its regulation seems to be governed at the expression level (*73*), as disorders of cardiac muscle such as Takotsubo cardiomyopathy (*74*) are associated with abnormal SLN expression (*75*).

Although a number of studies have shed light on the regulation of SERCA by SLN and PLN in heart muscle, the role of SLN in skeletal muscle was not well understood. A recent study has shown that SLN knockout mice are unable to maintain core body temperatures when subject to cold conditions (*76*). It was shown that SERCA, through its interaction with SLN, contributes more to heat generation via non-shivering thermogenesis than the mitochondrial uncoupling protein (*77*) in brown adipose tissue (*76*, *78*). SLN-knockout mice on a high-fat diet have a phenotype that is prone to obesity and increased glucose-intolerance (*76*). WT-mice on a high fat diet show a 4-fold increase in SLN expression that prevents them from the same fate as SLN-knockout mice (*76*). Based on these results, it is proposed that SLN, in addition to decreasing apparent Ca^{2+} affinity, also causes an uncoupling of ATP hydrolysis from Ca^{2+} transport, thereby increasing the heat production (*76*, *79*).

Objective

Several questions about SLN/PLN and their interaction with SERCA remain unanswered. How do SLN and PLN reduce Ca^{2+} affinity of SERCA? Why does SLN's interaction

with SERCA result in increased heat production? How does phosphorylation of PLN and SLN result in the relief of inhibition? In order to answer these questions, a detailed atomistic description of the complex is required. Solid state NMR under physiologically relevant conditions has allowed us to not only determine the topology of SLN in complex with SERCA, but also to monitor the changes in this topology at different stages of its catalytic cycle. A combination of MAS-ssNMR, solution NMR and oriented ssNMR have allowed us to understand the effect of phosphorylation on PLN and how it changes its interaction with SERCA.

Chapters 2-4 in this thesis describe the development of suitable solid state NMR techniques that in effect allow us to study SLN by itself and in complex with SERCA in lipid bilayers. The knowledge and technical gains from these studies have been utilized in Chapter 5, where a detailed characterization of the complex at several steps of the catalytic cycle has enabled us to deduce the molecular basis for inhibition of SERCA by SLN and also shed light on the mechanics of its role in heat generation via non-shivering thermogenesis. Chapters 6-7 deal with the application of these techniques to understand how phosphorylation of phospholamban affects its structure and interaction with SERCA.

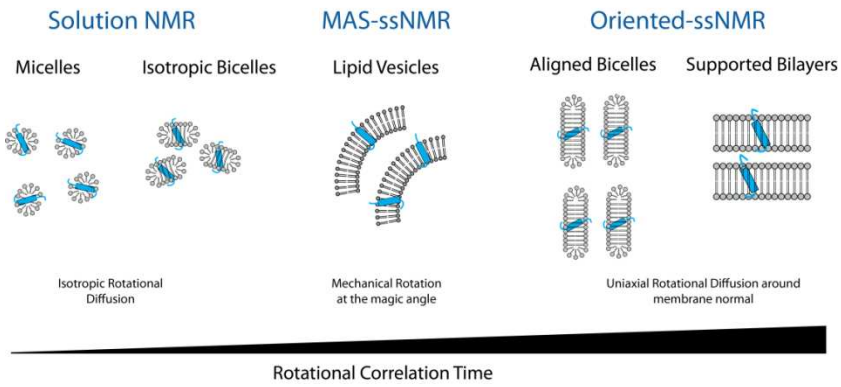

Figure 1.1: Membrane mimics for NMR studies of membrane proteins

For solution NMR, micelles and isotropic bicelles allow recording of high resolution data due to their short rotational correlation times (τ_c). Lipid vesicles and aligned bicelles/bilayer have very large rotational correlation times and can only be studied by solid state NMR. Note that although vesicles have a very large inherent τ_c, the entire sample undergoes fast mechanical rotation during MAS-ssNMR studies. See Appendix-I for the theory behind magic angle spinning NMR).

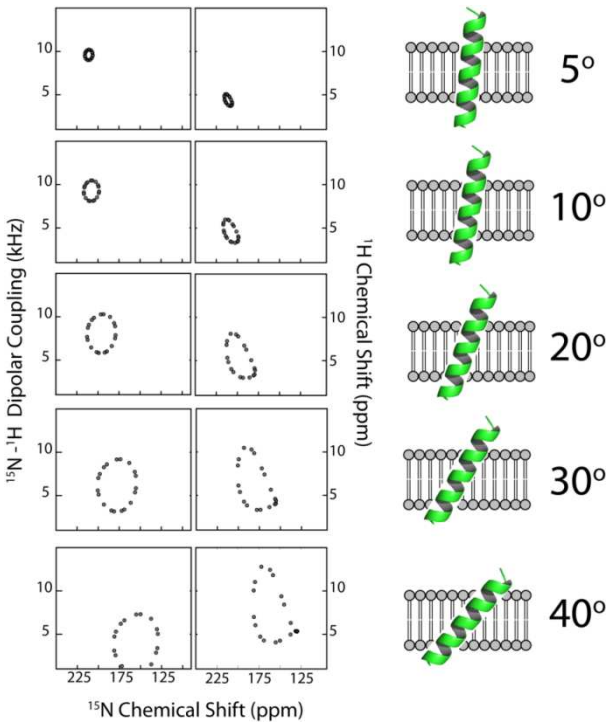

Figure 1.2: Transmembrane Topology and Oriented state NMR

Simulated PISEMA (^{15}N chemical shift – ^{1}H-^{15}N dipolar coupling correlation; left panels) and HETCOR (^{15}N chemical shift – ^{1}H chemical shift correlation; right panels) spectra for an ideal α-helix tilted at different tilt angles with respect to the lipid bilayer. The size and the position of circular pattern of resonances, called the Polar Index Slant Angle (PISA) wheel pattern is a direct indicator of transmembrane topology. See Appendix I for details on these experiments. Each point on the PISA wheel corresponds to a single residue on the protein backbone.

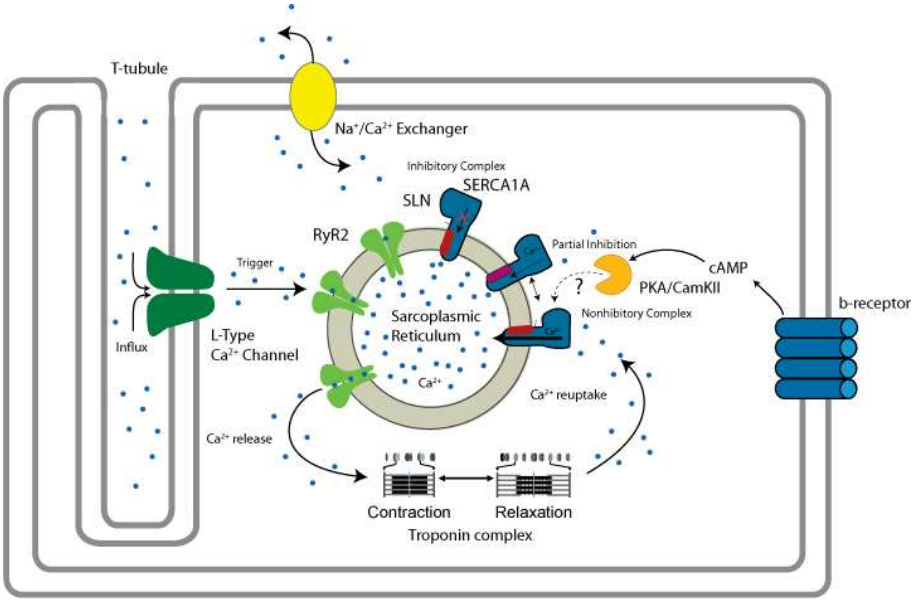

Figure 1.3: A schematic of a muscle cell

The contraction-relaxation cycle begins with a small influx of Ca^{2+} through the L-type Ca^{2+}-channels. This allows Ca^{2+}-mediated opening of Ryanodine Receptor (RyR), resulting in a massive release of Ca^{2+} into the cytosol from the lumen (calcium-induced calcium release) (*80*, *81*). The cytosolic Ca^{2+} concentrations increase from approximately 10 nM (low Ca^{2+}) to 10 μM (high Ca^{2+}) during this stage (*48*). Ca^{2+} binds to the troponin-myosin complex inducing conformational changes that finally result in contraction of the muscle cell (*82*). Contraction is sustained until Ca^{2+} concentrations are maintained at high levels in the cytosol. In order to relax the muscle cell to its resting state, Ca^{2+} must be removed. Approximately 70% of Ca^{2+} re-uptake into the lumen by is achieved by the sarco(endo)plasmic reticulum Ca^{2+} ATPase (SERCA) (*48*).

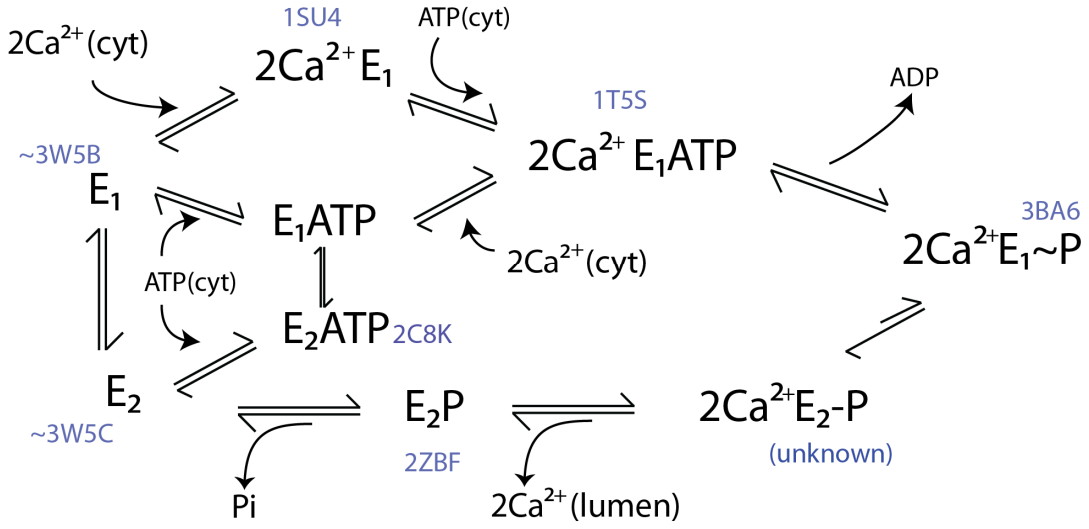

Figure 1.4: A mechanistic description of the catalytic cycle of SERCA.

The coupling of ATP hydrolysis to Ca^{2+} transport is explained by ligand induced conformational changes between a high Ca^{2+} affinity E1 and low Ca^{2+} affinity E2 states. The E1 state is responsible for binding Ca^{2+} from the cytosol. Phosphoryl transfer from ATP to SERCA is coupled to the transition to the E2 state and release of Ca^{2+} into the lumen. Dephosphorylation brings SERCA back to the E2 state. PDB codes for X-ray crystal structures of SERCA trapped at each of the conformations are indicated in a blue legend.

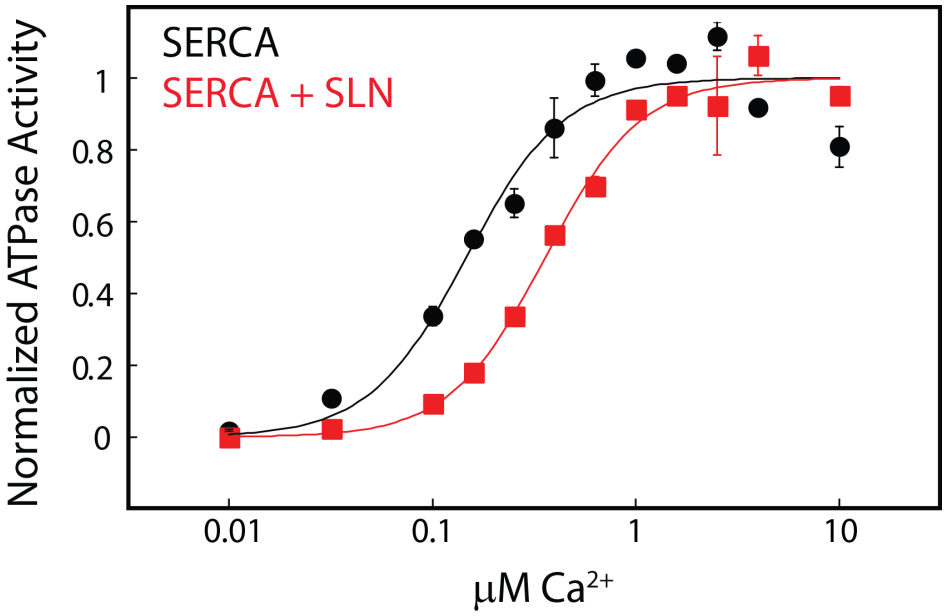

Figure 1.5: Ca^{2+}-dependent ATP hydrolysis for SERCA and the effect of SLN.

ATP hydrolysis is monitored by a coupling ADP release to a NADH-dependent ATP regeneration system and monitoring the decrease in NADH absorbance. The Ca^{2+} dependent curves fit to a Hill equation, with the Hill coefficient of 1.4 and K_M of 0.8 μM. The presence of SLN does not cause an appreciable change in the Hill coefficient, but K_M changes to 1.5μM. This is clearly visualized by the right shift of the curve in presence of SLN.

2. Sensitivity and Resolution Enhancement of Oriented Solid-State NMR: Application to Membrane Proteins

T. Gopinath, Kaustubh R. Mote and Gianluigi Veglia

Adapted with permission from

Progress in NMR Spectroscopy (2013), 75, 50

With data from the following original research articles:

1. T. Gopinath, N. J. Traaseth, K.R. Mote, and G. Veglia, "Sensitivity enhanced heteronuclear correlation spectroscopy in multidimensional solid-state NMR of oriented systems via chemical shift coherences.," *J. Am. Chem. Soc.*, vol. 132, no. 15, pp. 5357–63, Apr. 2010.
2. T. Gopinath, K. R. Mote, and G. Veglia, "Proton evolved local field solid-state nuclear magnetic resonance using Hadamard encoding: theory and application to membrane proteins.," *J. Chem. Phys.*, vol. 135, no. 7, p. 074503, Aug. 2011.

Oriented solid-state NMR (O-ssNMR) spectroscopy is a major technique for the high-resolution analysis of the structure and topology of transmembrane proteins in native-like environments. Unlike magic angle spinning (MAS) techniques, O-ssNMR spectroscopy requires membrane protein preparations that are uniformly oriented (mechanically or magnetically) so that anisotropic NMR parameters, such as dipolar and chemical shift interactions, can be measured to determine structure and orientation of membrane proteins in lipid bilayers. Traditional sample preparations involving mechanically aligned lipids often result in short relaxation times which broaden the ^{15}N resonances and encumber the manipulation of nuclear spin coherences. The introduction of lipid bicelles as membrane mimicking systems has changed this scenery, and the more favorable relaxation properties of membrane protein ^{15}N and ^{13}C resonances of make it possible to develop new, more elaborate pulse sequences for higher spectral resolution and sensitivity. Here, we describe our recent progress in the optimization of O-ssNMR pulse sequences. We explain the theory behind these experiments, demonstrate their application to small and medium size proteins, and describe the technical details for setting up these new experiments on the new generation of NMR spectrometers.

Introduction

High-resolution structures of membrane proteins are being solved with an exponential progression similar to that of soluble membrane proteins. To date, however, the total number of membrane proteins determined is dramatically lower, with only 300 unique folds identified compared to ~70,000 for the soluble counterpart. Without any doubt, X-ray spectroscopy plays a major role in the structure determination of membrane proteins. Nonetheless, crystallized membrane proteins do not contain physiologically relevant concentrations of the lipids that enable biological function. In contrast, solid-state NMR is the only spectroscopic technique that provides atomic-resolution structural information of membrane proteins in lipid preparations and under functional conditions (*1*, *83*, *84*). Unfortunately, the throughput of solid-state NMR structures has been very low. In fact,

solving membrane protein structure at high resolution by solid-state NMR methods requires not only great skill in protein expression and sample preparation (*1*, *35*) but also a great deal of knowledge of spectroscopic methods that need to be adapted to the sample behavior.

Currently, there are two major methodologies that enable the structure determination of membrane proteins: magic angle spinning (MAS), and oriented-solid-state (O-ssNMR). In MAS-NMR, membrane protein samples reconstituted in lipid membranes are spun at the magic angle (54.7^{o}) to attenuate dipolar and chemical shift anisotropic interactions with resonances that are dispersed according to their local chemical environment. However, dipolar couplings (DC) and chemical shift anisotropy (CSA) can be recovered using recoupling techniques and used for structure determination (*3*, *85–87*). In contrast, O-ssNMR experiments that directly measure DCs and CSAs require oriented samples, whose preparation is more laborious. Traditionally, uniaxially oriented membrane protein preparations involved the reconstitution of membrane proteins in aligned membrane bilayers immobilized onto glass plates (*3*, *85–95*). Excellent references regarding these preparations can be found in many reviews (*96–101*). These preparations suffer from lack of control over sample hydration and pH, and are also not optimal with regards to coil-filling and compatibility with all proteins. More recently, oriented samples of membrane proteins have been prepared in lipid bicelles (*102*, *103*), which are preparations of mixtures of short-chain detergent-like lipids (e.g., DHPC. CHAPSO, TritonX-100, DPC) and long-chain lipids (typically DMPC or DMPC doped with 20% unsaturated lipids such as POPC) (*103*, *104*). Bicelles with a sufficiently large ‘q-ratio’, i.e., the molar ratio of long to short chain lipids, are capable of spontaneously aligning in the high field of the NMR spectrometers and are thus an alternative to mechanically aligned bilayers for oriented solid state NMR experiments (*103*). Fully hydrated bicelles undergo fast rotational diffusion, averaging out part of the anisotropy and increasing the $T_{1\rho}$. The latter renders line-shapes for amide resonances of membrane proteins that are similar to those of globular proteins (*105*, *106*). In addition, bicelles offer complete control over sample hydration and pH, and the preparations, although limited to a small subset of lipids, are

generally compatible with single TM and polytopic membrane proteins (*107*). The preparations tend to minimize the conformational heterogeneity of membrane proteins as compared to the mechanically aligned bilayers, giving spectra with higher resolution (*108*).

A significant advantage of O-ssNMR over MAS is that the resonances are more dispersed because there is an anisotropic contribution to nuclear shielding, which produces a larger breadth of chemical shifts. More importantly, the anisotropic interactions with the external magnetic field obtained from these experiments allow the calculation of the entire membrane protein topology as parameters such as tilt and rotation angle of transmembrane segments are encoded directly in these spectra (*109*, *110*). In order to take advantage of these spectral features, we recently developed new methods to obtain higher resolution and sensitivity. We re-crafted the classical separated local field (SLF) experiments into sensitivity enhanced (SE) versions (*41–43*, *111*) as well as constant time (CT) variants (*112*) that enabled us to carry out 2D and 3D NMR experiments on membrane proteins. In this review, we describe the theory, the technical details as well as our recent applications of these new techniques for the structure resolution of membrane proteins.

Hadamard encoding proton evolved local field experiments

Theory for HE-PELF

Proton detected/evolved local field (PDLF or PELF) experiments were initially utilized to separate the heteronuclear DC and ^{13}C chemical shifts for CH, CH_2 and CH_3 spin systems in liquid crystalline samples (*113–115*). Unlike the R-SLF experiments, PELF can resolve multiple DCs (short- and long-range) in the presence of a strong homonuclear DC sequence applied on protons (*116*). For liquid crystalline molecules, PELF experiments combined with PDSD leads to the complete assignment of ^{13}C resonances, especially the CH_3, CH_2 and NH_2 spin systems of small molecules or lipids (*116–118*). For membrane proteins embedded in lipid bicelles, PELF experiments are more sensitive than R-SLF for

the detection of mobile ^{15}N-^{1}H spin systems of protein backbone and side chains (*119*, *120*).

Fig. 2.1A shows the PELF pulse sequence that correlates the chemical shifts of spin *S* and *I-S* DC. The experiment consists of a 90^{o} pulse on the *I*-spin that creates transverse magnetization, which evolves under *I-S* DC during t_1 in the presence of ^{1}H homonuclear decoupling (FSLG). A π pulse on *I* and *S* spins refocuses the *I*-spin chemical shift and recouples the *I-S* DC. Dipolar evolution is followed by WIM24 heteronuclear polarization transfer from spin I to S. The S spin magnetization is then detected during t_2 acquisition under ^{1}H decoupling. Several variants of PELF experiments have been implemented using different homonuclear decoupling - WAHUHA (*121*, *122*), MREV-8 (*123*, *124*), BR-24 (*125*), FSLG (*126*), PMLG (*127*), BLEW (*128*), MSHOT (*129*), and heteronuclear polarization transfer (CP, LG, FSLG, WIM24) schemes. The sensitivity of the PELF experiments depends on the duration (τ_1) of heteronuclear polarization transfer and the dipolar-coupling values. In other words, the τ_1 period needs to be optimized according to the range of DCs of the resonances. Note that for membrane proteins, it has been shown that heteronuclear polarization transfer is more efficient with WIM than ramp-CP sequence (*41*) that is why WIM-CP is routinely used for O-ssNMR (*130*, *131*), .

The t_1 evolution of PELF experiments results in both in-phase and anti-phase spin operators for the cosine and sine dipolar coherences, respectively. However, the conventional PELF experiment detects only the in-phase cosine dipolar coherence. Indeed, all four coherences can be detected simultaneously, and our newly designed HE-PELF, i.e., Hadamard-encoded PELF enables the encoding and decoding of the different coherences into two separated 2D spectra with an optimized sensitivity for a wide range of DCs (*42*). The evolution of the magnetization according to the HE-PELF is the following:

$$
\begin{aligned}
\text{HE-PELF: } I_z &\xrightarrow{(90^o_{-x})} I_y \xrightarrow{H_{FSLG}(t_1/2)-(180^o_y)^{I,S}-H_{FSLG}(t_1/2)} I_y\cos(s_{FSLG}\omega_{IS}t_1) - 2I'_xS_z\sin(s_{FSLG}\omega_{IS}t_1) \\
&\xrightarrow{(35^o)^I_{-y}-(90^o)^I_{\varphi 1=y}} I_y\cos(s_{FSLG}\omega_{IS}t_1) - 2I_xS_z\sin(s_{FSLG}\omega_{IS}t_1) \\
&\xrightarrow{H_{WIM24}(\tau\tau)} \left[I_y\cos^2(\theta_1/2) + S_y\sin^2(\theta_1/2) + \frac{1}{2}(2I_zS_x - 2I_xS_z)\sin(\theta_1)\right]\cos(s_{FSLG}\omega_{IS}t_1) \\
&- \left[2I_xS_z\cos^2(\theta_1/2) + 2I_zS_x\sin^2(\theta_1/2) + \frac{1}{2}(I_y - S_y)\sin(\theta_1)\right]\sin(s_{FSLG}\omega_{IS}t_1) \\
&\xrightarrow{(90^o)^I_{-y}(90^o)^S_x(35^o)^I_y} \left[I_y\cos^2(\theta_1/2) + S_z\sin^2(\theta_1/2) + \frac{1}{2}(2I'_zS_x - 2I'_xS_y)\sin(\theta_1)\right]\cos(s_{FSLG}\omega_{IS}t_1) \\
&- \left[2I'_xS_y\cos^2(\theta_1/2) + 2I'_zS_x\sin^2(\theta_1/2) + \frac{1}{2}(I_y - S_z)\sin(\theta_1)\right]\sin(s_{FSLG}\omega_{IS}t_1) \\
&\xrightarrow{H_{FSLG}(1.16\tau 1)} \left[S_z\sin^2(\theta_1/2) + \frac{1}{2}(S_y)\sin(\theta_1)\sin(\theta_2)\right]\cos(s_{FSLG}\omega_{IS}t_1) \\
&- \left[S_y\sin^2(\theta_1/2)\sin(\theta_2) + \frac{1}{2}(-S_z)\sin(\theta_1)\right]\sin(s_{FSLG}\omega_{IS}t_1) \\
&\xrightarrow{(90^o)^S_{\varphi 2=y}-t_2} \left[S_x\sin^2(\theta_1/2) + \frac{1}{2}(S_y)\sin^2(\theta_1)\right]\cos(s_{FSLG}\omega_{IS}t_1)\cdot e^{i\omega_s t_2} \\
&+ \left[-S_y\sin^3(\theta_1/2) + \frac{1}{2}(S_x)\sin(\theta_1)\right]\sin(s_{FSLG}\omega_{IS}t_1)\cdot e^{i\omega_s t_2}
\end{aligned}
\qquad (1)
$$

Where $H_{FSLG} = s_{FSLG}\omega_{IS}2I'_zS_z$, $H_{WIM24} = s_{WIM24}\omega_{IS}(I_xS_x + I_yS_y)$, $\omega_{IS} = 2\pi D_{IS}$, $s_{FSLG} = 0.57$, $s_{WIM24} = 0.66$, $\theta_1 = s_{WIM24}\omega_{IS}\tau$, $I'_x = e^{-i\theta_m I_y}I_x e^{i\theta_m I_y}$, $I'_y = I_y$, $I'_z = e^{i\theta_m I_y}I_x e^{-i\theta_m I_y}$.

For each t_1 increment, four interleaved scans are acquired with phases (φ_1, φ_2) defined as (y, y), (y, -y), (-y, y) and (-y, -y), respectively. The resultant four density matrices are:

$$
\begin{aligned}
\rho_1 &= \left[c_1S_x + c_2S_y\right]\cos(s_{FSLG}\omega_{IS}t_1).e^{i\omega_s t_2} + \left[-c_3S_y + c_4S_x\right]\sin(s_{FSLG}\omega_{IS}t_1).e^{i\omega_s t_2} \\
\rho_2 &= \left[-c_1S_x + c_2S_y\right]\cos(s_{FSLG}\omega_{IS}t_1).e^{i\omega_s t_2} + \left[-c_3S_y - c_4S_x\right]\sin(s_{FSLG}\omega_{IS}t_1).e^{i\omega_s t_2} \\
\rho_3 &= \left[c_1S_x + c_2S_y\right]\cos(s_{FSLG}\omega_{IS}t_1).e^{i\omega_s t_2} + \left[c_3S_y - c_4S_x\right]\sin(s_{FSLG}\omega_{IS}t_1).e^{i\omega_s t_2} \\
\rho_4 &= \left[-c_1S_x + c_2S_y\right]\cos(s_{FSLG}\omega_{IS}t_1).e^{i\omega_s t_2} + \left[c_3S_y + c_4S_x\right]\sin(s_{FSLG}\omega_{IS}t_1).e^{i\omega_s t_2}
\end{aligned}
\qquad (2)
$$

where $c_1 = \sin^2(\theta_1/2)$, $c_2 = \frac{1}{2}\sin^2(\theta_1)$, $c_3 = \sin^2(\theta_1/2).\sin(\theta_1)$, and $c_4 = \frac{1}{2}\sin(\theta_1)$.

In Eq. (2), each density matrix consists of four terms whose signs correspond to the four rows of a four-dimensional Hadamard matrix (**H**). The coefficients c_1, c_2, c_3, and c_4 depend on the DC values that modulate the coherences in the time domains to give mixed line shapes. In the density matrices, the absorptive and dispersive signals associated with

cosine and sine DC coherences are separated by Hadamard decoding of the time domain data resulting from four scans:

$$\begin{aligned}
\rho_{H1-PELF} &= \rho_1 - \rho_2 + \rho_3 - \rho_4 = 4c_1 \cdot S_x \cos(s_{FSLG}\omega_{IS}t_1).e^{i\omega_s t_2} \\
\rho_{H2-PELF} &= \rho_1 + \rho_2 + \rho_3 + \rho_4 = 4c_2 \cdot S_y \cos(s_{FSLG}\omega_{IS}t_1).e^{i\omega_s t_2} \\
\rho_{H3-PELF} &= -\rho_1 - \rho_2 + \rho_3 + \rho_4 = 4c_3 \cdot S_y \sin(s_{FSLG}\omega_{IS}t_1).e^{i\omega_s t_2} \\
\rho_{H4-PELF} &= \rho_1 - \rho_2 - \rho_3 + \rho_4 = 4c_4 \cdot S_x \sin(s_{FSLG}\omega_{IS}t_1).e^{i\omega_s t_2} \ .
\end{aligned} \tag{3}$$

The conventional PELF pulse sequence with four scans for each t_1 increment detects only the S_x spin operator associated with cosine dipolar coherence, *i.e.*:

$$\rho_{PELF} = 4c_1 \cdot S_x \cos(s_{FSLG}\omega_{IS}t_1).e^{i\omega_s t_2}. \tag{4}$$

In contrast, each density matrix of the HE-PELF experiment results in a 2D spectrum that correlates DC values with the chemical shift of the *S*-spin. The intensities of the 2D peaks depend on the values of the coefficients (c_1, c_2, c_3 and c_4), while the phase modulation is a function of the corresponding trigonometric terms of Eq. 2. To obtain the maximum intensity upon summation of the four data sets, it is necessary to phase correct the data in Eq. (2) by 90°. This operation results in pure absorptive line shapes in both dimensions. Fig. 2.2 shows the plot of the coefficients c_1, c_2, c_3, and c_4 versus DC for a mixing time of 144 μs. For certain values of DC, c_3 and c_4 become negative. In this case, positive lines are obtained processing each data set using magnitude mode. The resultant frequency domain data sets are added together to obtain an H-PELF spectrum:

$$\begin{aligned}
\rho_{H-PELF}(\omega_1,\omega_2) &= \left|\rho_{H1-PELF}(\omega_1,\omega_2)\right| + \left|\rho_{H2-PELF}(\omega_1,\omega_2)\right| + \left|\rho_{H3-PELF}(\omega_1,\omega_2)\right| + \left|\rho_{H4-PELF}(\omega_1,\omega_2)\right| \\
&= 4\left[|c_1| + |c_2| + |c_3| + |c_4|\right]\rho(\omega_1,\omega_2) \ .
\end{aligned}$$

(12)

Adding the four 2D spectra $\left|\rho_{H1-PELF}(\omega_1,\omega_2)\right|$, $\left|\rho_{H2-PELF}(\omega_1,\omega_2)\right|$, $\left|\rho_{H3-PELF}(\omega_1,\omega_2)\right|$, and $\left|\rho_{H4-PELF}(\omega_1,\omega_2)\right|$ after relative zeroth-order phase corrections will increase the RMS noise of the resulting spectrum by $\sqrt{4}$. The RMS noise of the four spectra is identical to the

$\rho_{PELF}(\omega_1, \omega_2)$ spectrum in Eq. (4). The signal to noise ratio (SNR) for the H-PELF and PELF spectra can be written as:

$$\left(\frac{S}{N}\right)_{H-PELF} = \frac{4\left[|c_1| + |c_2| + |c_3| + |c_4|\right]}{2}$$

and (5)

$$\left(\frac{S}{N}\right)_{PELF} = 4c_1 .$$

The Hadamard decoded dataset $\rho_{H1-PELF}$ (Eq. (3)) is identical to ρ_{PELF} (Eq. (4)), i.e., they both have the same SNR.

$$\left(\frac{S}{N}\right)_{H1-PELF} = \left(\frac{S}{N}\right)_{PELF} . \quad (6)$$

The sensitivity of the conventional PELF (Eq. (4)) experiment as a function of DC value, is given by the blue curve of Fig. 2.1. On the other hand, the HE-PELF pulse sequence results in two 2D spectra (H1-PELF and H-PELF) covering the dipolar couplings in the ranges defined by the blue and red curves of Fig. 2.1. Note that the HE-PELF experiment requires a number of scans that is a multiple of four. Typically a two-step phase cycle is applied to initial 90^o pulse on the proton. In that case the number of scans is set to a multiple of eight.

Application of HE-PELF to single crystal and membrane proteins.

To demonstrate the SE obtained using the HE-PELF as compared to the PELF experiment, we performed the experiments on a single crystal of N-Acetyl-Leucine (Fig. 2.3) and $U^{15}N$-SLN in aligned bicelles (Fig. 2.4 and 2.5). From the 1D slices, the two spectra, H1-PELF and H-PELF, obtained from HE-PELF experiment cover the entire

range of the dipolar couplings in the crystal. H-PELF gives a substantial increase in sensitivity for resonances with low DC values, while the H1-PELF retains the high sensitivity for residues with high DCs. The integrated intensity of the peaks between 60 to 120 ppm and 0 to 5 kHz of H-PELF is 2.2 times (120% enhancement) that of the PELF spectrum. This feature is of important consequence for studying membrane bound and embedded proteins which have transmembrane domains (which would have high DCs), as well as flexible loops and an extra-membrane segment (which would have either scaled or lower DCs). As expected, a significant sensitivity enhancement of 50-100% is seen for SLN reconstituted in unflipped bicelles, where DCs are scaled down by a factor of ~2 due to the orientation of the bilayer normal which is perpendicular to the magnetic field and the resonances are narrower due to the fast uniaxial rotation (*132*) about the bilayer normal (Fig. 2.5). Essentially, the HE-PELF experiment allows the mapping of all of these domains in a single experiment rather than multiple experiments optimized for each domain individually.

SE heteronuclear chemical shift correlation experiments

Theory of SE-HETCOR

The heteronuclear correlation (HETCOR) experiment is used to correlate the chemical shifts of the two nuclei, typically ^{13}C-^{1}H or ^{15}N-^{1}H (*133*). This experiment shares a close similarity with the PELF experiment. In the PELF experiment ^{1}H CS is refocused and ^{15}N-^{1}H DC is evolved during t_1, whereas in the HETCOR experiment ^{15}N-^{1}H DC is decoupled and ^{1}H CS is evolved during t_1. The pulse sequence of HETCOR consists of three parts (Fig. 2.6): a) ^{1}H CS evolution under ^{1}H-^{1}H homonuclear decoupling and ^{15}N heteronuclear decoupling; b) polarization transfer from ^{1}H to directly bonded ^{15}N; and c)

detection under ^{15}N CS evolution and ^{1}H decoupling. This experiment, however, is rarely used for membrane proteins due to its poor sensitivity and resolution. The typical ^{1}H linewidths obtained in the HETCOR experiments range from 0.6 to 1.2 kHz (*134*). Several variants have been proposed, differing mainly in the design of the ^{1}H chemical shift evolution period. For liquid crystalline and aligned lipid bicelles, it has been shown that the application of the BLEW-12 homonuclear decoupling sequence results in ^{1}H linewidths narrower than those of the FSLG sequence. A recent implementation of HETCOR for membrane proteins undergoing fast uniaxial rotation demonstrated that the use of the MSHOT sequence for ^{1}H homonuclear decoupling reduces the ^{1}H line width up to 300 Hz (*130*), which is very promising and opens up further improvements with respect to conventional experiments.

In a HETCOR experiment (Fig. 2.6A), ^{1}H CS coherences are encoded into cosine and sine components during t_1 evolution that are transferred to ^{15}N via Hartmann-Hahn CP schemes, such as continuous wave CP or FSLG-CP. A key feature of this experiment is the optimization of the τ_1 period, which depends on the values of the DCs for the specific protein sample. The quadrature detection in the F_1 acquisition dimension is obtained using the States mode (*135*), where cosine and sine components are detected in separate scans followed by FT.

As for the SE scheme for the PISEMA experiment, it is possible to recover both components of the CS coherences (sine and cosine) and enhance sensitivity by designing an appropriate pulse scheme. A fundamental difference between the two experiments is that for the SE-PISEMA we recovered both sine and cosine components of the dipolar coherences, whereas for the HETCOR experiment we recover the CS coherences. In fact, both cosine and sine components of ^{1}H CS in the SE-HETCOR experiment can be simultaneous transferred to ^{15}N using a WIM-CP sequence. Unlike the CP and FSLG-CP schemes, the heteronuclear DC Hamiltonian of the WIM-CP sequence contains an isotropic mixing term ($\vec{I} \cdot \vec{S}$) that enables the simultaneous transfer of both cosine and sine components from ^{1}H to ^{15}N, which are detected during t_2 after a 90^{o} pulse on ^{15}N

with phase +y. The evolution of the density matrix for the SE-HETCOR pulse sequence **(**Fig. 2.6B**)** is given by:

$$
\begin{aligned}
\text{SE}-\text{HETCOR}: I_z &\xrightarrow{(90)^o_x} -I_y \xrightarrow{t_1} -I_y\cos(s_{fslg}\omega_I t_1) + I_x^{'}\sin(s_{fslg}\omega_I t_1) \\
&\xrightarrow{(35)^o_y} -I_y\cos(s_{fslg}\omega_I t_1) - I_z\sin(s_{fslg}\omega_I t_1) \\
&\xrightarrow{\tau_2} -\left[S_y\cos(s_{fslg}\omega_I t_1) + S_z\sin(s_{fslg}\omega_I t_1)\right]\frac{1}{2}\left[1-\cos(s_{wim24}\omega_{IS}\tau_2)\right] \\
&\xrightarrow{(90)^o_{\pm y}-t_2} -\left[S_y\cos(s_{fslg}\omega_I t_1) \pm S_x\sin(s_{fslg}\omega_I t_1)\right]\frac{1}{2}\left[1-\cos(s_{wim24}\omega_{IS}\tau_2)\right]e^{i\omega_s t_2}
\end{aligned}
\qquad (7)
$$

where $\omega_{IS} = 2\pi\pi_{IS}, I_x^{'} = e^{-i(\theta_M^O+90^O)I_y}\cdot I_x \cdot e^{i(\theta_M^O+90^O)I_y}, I_z^{'} = e^{i(90^O)I_y}\cdot I_x \cdot e^{-i(90^O)I_y}$,
$S_z^{'} = S_x, s_{FSLG} = 0.82, s_{WIM24} = 0.66.$

In Eq. 7, D_{IS} is the DC between *I* and *S* spins, and s_{fslg} and s_{wim24} are the scaling factors during the t_1 and τ_2 periods, respectively. The inversion of the phase for the 90^o pulse on ^{15}N inverts the sign for the sine component only, whereas the sign of the cosine component remains unaltered. Addition and subtraction of these two interleaved scans separates the cosine and sine components that are subsequently Fourier transformed to obtain the quadrature detection in the F_1 dimension. The density matrix becomes:

$$\rho_{SE-HETCOR} = \frac{2}{\sqrt{2}} S_x . e^{is_{fslg}\omega_I t_1} . [1-\cos(s_{wim24}\omega_{IS}\tau_2)] . e^{i\omega_s t_2} . \qquad (8)$$

Although the signal is enhanced by a factor of 2 (eq. 8), the processing increases the RMS noise by $\sqrt{2}$. Hence, the theoretical sensitivity gain is $(2/\sqrt{2})$ or 40%.

Application of SE-HETCOR to single crystals and membrane proteins

Two-dimensional HETCOR experiments, performed on a single crystal of NAL and U^{15}N-SLN in aligned bicelles, are shown in Fig. 2.7 and Fig. 2.8 respectively (*41*). Although the theoretical SE of SE-HETCOR is 40%, the net SE also depends on the efficiency of WIM24 polarization transfer with respect to FSLG-CP. For single crystal SE, factors of 1.3 (30%) to 1.6 (60%) are observed, whereas for SLN an average SE of

60% was observed. Although SE-HETCOR improves the sensitivity compared to the classical HETCOR, the resolution in 2D spectra remains a serious concern. One of the main reasons for the poor resolution is that the inherent spread of anisotropic chemical shifts for amide protons in the transmembrane segments is low. Nonetheless, the SE-HETCOR experiment makes it possible to develop 3D experiments that enable one to resolve the chemical shifts in three dimensions, while simultaneously taking advantage of not only the higher resolution in the R-SLF spectra, but also improvements in sensitivity in both R-SLF and HETCOR spectra.

SE three-dimensional experiments

Theory

The 3D versions of the HETCOR experiments (i.e., HETCOR-SLF and SE-HETCOR-SLF) (Fig. 2.6) are obtained by incrementing (t2) τ_1 τ_2, followed by the ^{15}N CS acquisition period (t_3) from the experiments reported in Fig. 2.9. In the case of the 3D experiments, the density matrices for an *I-S* spin system are:

$$\rho_{HETCOR-SLF} = \frac{S_x}{2} S_x . e^{is_{fslg}\omega_I t_1} . e^{i\omega_s t_3} - \frac{S_x}{2} \cdot e^{is_{fslg}\omega_I t_1} . \cos(s_{fslg\,cp}\omega_{IS} t_2) \cdot e^{i\omega_s t_3}$$
$$\rho_{SE-HETCOR-SLF} = \sqrt{2}\frac{S_x}{2} . e^{is_{fslg}\omega_I t_1} . e^{i\omega_s t_3} - \sqrt{2}\frac{S_x}{2} \cdot e^{is_{fslg}\omega_I t_1} . \cos(s_{fslg\,cp}\omega_{IS} t_2) \cdot e^{i\omega_s t_3} . \quad (9)$$

The t_1 dimension for the HETCOR-SLF and SE-HETCOR-SLF experiments are processed using States (*135*) and Rance-Kay (*136*, *137*) modes, respectively. During dipolar evolution (t_2), the HETCOR-SLF experiment requires a SEMA (spin exchange at magic angle) spin-lock sequence, while the SE-HETCOR-SLF experiments make use of a WIM24 spin-lock on ^{1}H and ^{15}N. Since the SEMA spin-lock sequence is less efficient for large ^{1}H offsets, it is likely to cause scaled DC values. The WIM24, on the other hand, is more efficient for large ^{1}H offsets and gives more accurate DC values. The dipolar linewidths and the scaling factors for SEMA and WIM24 play a role in the sensitivity

gain; in the absence of these effects Eq. (10) shows that the theoretical SE for SE-HETCOR-SLF is 40 %.

Both HETCOR-SLF and SE-HETCOR-SLF experiments give a zero frequency peak in the dipolar dimension, which results from the first term of eq. 10. In the 2D PISEMA and SE-PISEMA experiments, the zero frequency term in the dipolar dimension is eliminated by applying a polarization inversion (PI) scheme on the ^{1}H channel, which creates only a ZQ term evolving under heteronuclear DC. The PI not only removes the zero frequency term, but also doubles the sensitivity of DC peaks.

For the 3D HETCOR-SLF and SE-HETCOR-SLF, the PI sequence cannot be applied prior to the t_2 dipolar evolution period, since the polarization at this point is only on the *I* spin (^{1}H). In this case, only the ZQ term would oscillate with the DC, while DQ would only contribute to the zero-frequency peak in the dipolar dimension (t_2). To avoid this, we designed a new 3D experiment (SE-PISEMAI-HETCOR, Fig. 2.9C) switching the dipolar (t_2) and chemical shift (t_1) dimensions in the original HETCOR-SLF experiment (Fig. 2.9A). In this new scheme, we apply the PI prior to the DC evolution (t_1) and the SE scheme right after the chemical shift evolution, t_2 (Fig. 2.9C). The PI increases the sensitivity by a factor of 2 and SE up to $\sqrt{2}$, resulting in a theoretical enhancement of up to $2\sqrt{2}$ or 180%. Importantly, in the HETCOR-SLF and SE-HETCOR-SLF experiments, the *S*-spin dipolar evolution is detected. In contrast, during the t_1 evolution of SE-PISEMAI-HETCOR, the I-spin dipolar coherence is detected and transferred to the *S* spin for CS evolution and detection. After the CP period, PI is obtained by a 35^{o} pulse on ^{1}H that creates a ZQ state (I_z'-S_z'), which evolves under ^{1}H-^{15}N DC, ^{1}H CS, and ^{15}N CS in the t_1, t_2, and t_3 dimensions, respectively:

SE – PISEMAI – HETCOR :

$$
\begin{aligned}
&(I_z^{'} - S_z^{'}) \xrightarrow{H_{FSLG-CP}(t_1)} (I_z^{'} - S_z^{'})\cos(s_{FSLG-CP}\omega_{IS}t_1) - (2I_y^{'}S_x^{'} - 2I_x^{'}S_y^{'})\sin(s_{FSLG-CP}\omega_{IS}t_1) \\
&\xrightarrow{(90)_y^1} I_x^{'} + \ldots\ldots \xrightarrow{H_{FSLG}(t_2)} \cos(s_{FSLG-cP}\omega_{IS}t_1)\left[I_x^{'}\cos(s_{FSLG}\omega_I t_2) + I_y\sin(s_{FSLG}\omega_I t_2)\right] \\
&\xrightarrow{(90\text{-}\theta_m)_y^o} \cos(s_{FSLG-CP}\omega_{IS}t_1)\left[I_z\cos(s_{FSLG}\omega_I t_2) + I_y\sin(s_{FSLG}\omega_I t_2)\right] \\
&\xrightarrow{H_{WIM24}(\tau\tau} \cos(s_{FSLG-CP}\omega_{IS}t_1)\left[S_z\cos(s_{FSLG}\omega_I t_2) + S_y\sin(s_{FSLG}\omega_I t_2)\right] \\
&\xrightarrow{(90)_{\pm y}^o - t_3} \cos(s_{FSLG-CP}\omega_{IS}t_1)\left[S_x\cos(s_{FSLG}\omega_I t_2) \pm S_y\sin(s_{FSLG}\omega_I t_2)\right]e^{i\omega_s t_3} \quad .
\end{aligned}
\tag{10}
$$

Using the Rance-Kay (*136*, *137*) mode of processing in the t_2 dimension, the resulting density matrix is given by:

$$\rho_{SE-PISEMAI-HETCOR} = \frac{2}{\sqrt{2}} S_x \cdot \cos(\omega_{IS} t_1) \cdot e^{i\omega_I t_2} \cdot e^{i\omega_S t_2}. \tag{11}$$

where the factor 2 indicates the simultaneous acquisition of two components, S_x and S_y, and the factor $\sqrt{2}$ in the denominator indicates the RMS noise increase resulting from data processing. Compared to the density matrix of HETCOR-SLF (Eq. 17), the sensitivity gain in SE-PISEMAI-HETCOR is $2\sqrt{2}$ or 180%.

Application to 3D spectroscopy to membrane proteins

Due to the poor sensitivity of the oriented membrane protein samples, the application of 3D experiments is rather sparse. Currently, only four papers report on the utilization of 3D spectroscopy for structural studies of oriented membrane proteins. Nevertheless, the congestion of the amide resonances in 2D experiments necessitates the use of 3D experiments to separate and assign the amide resonances in multispan membrane proteins. The SE methods optimized in our laboratory make it possible to carry out 3D experiments on membrane protein samples. For instance, in our 3D SE version of SLF-HETCOR experiment (^{15}N, ^{1}H and ^{15}N-^{1}H DC correlation) we were able to achieve 80-180% fold increase in sensitivity, corresponding to a factor of 3-7 in time saving. We applied the SE-PISEMAI-HETCOR experiment to SLN in oriented bicelles and obtained a completely resolved spectrum, detecting all of the transmembrane resonances (*29*). The total experimental time was ~ 3.3 days, which is comparable to the routine experiments

carried out for proteins using solution and MAS-ssNMR experiments. A strip plot displaying individual resonances is reported in Fig. 2.10. In addition to giving accurate assignments for ^{15}N-chemical shift and NH DCs, we were able to extract ^{1}H-anisotropic chemical shifts that were implemented in the structure calculations of SLN in lipid bilayers.

Summary and conclusions

O-ssNMR is a powerful technique for the determination of the secondary structure and orientation of membrane proteins. How- ever, low resolution and sensitivity have plagued this technique, hampering the structure determination of large membrane proteins in lipid membranes. With the advent of bicelles and the concomitant technological advancements in probe design and performance, it is now possible to obtain more sensitive and better resolved spectra. The increase in sensitivity has spearheaded new developments in pulse sequences that offer enough sensitivity and resolution for the sequential assignments of membrane proteins in oriented samples via three-dimensional NMR spectroscopy.

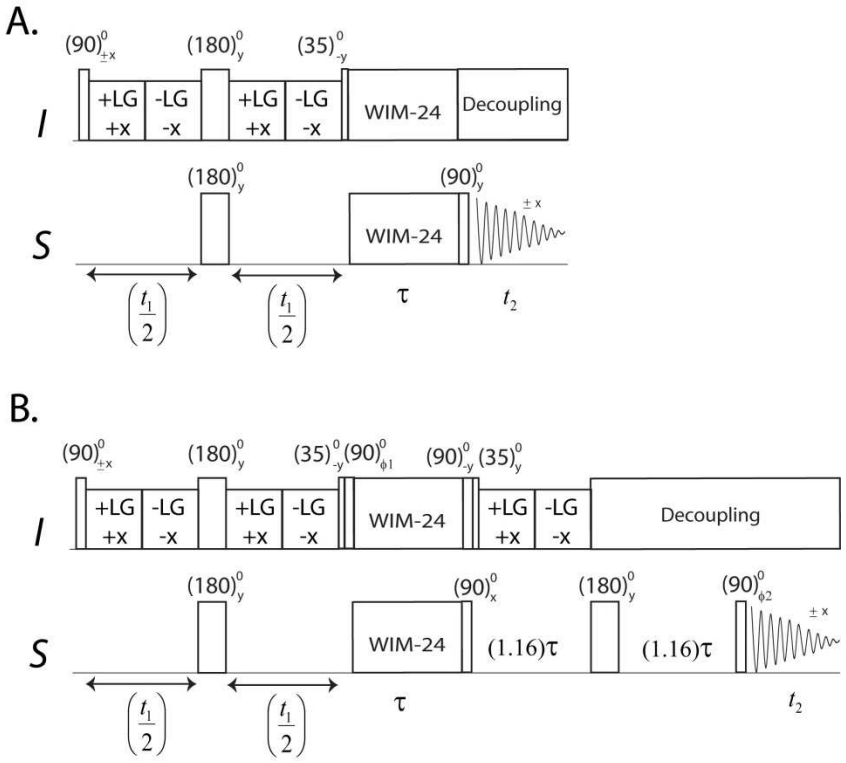

Figure 2.1: Pulse sequence for HE-PELF

(A) PELF, and (B) HE-PELF (Hadamard-encoded PELF) experiments. In the HE-PELF experiments, the phases (φ_1, φ_2) are set to (y, y), (y, −y), (−y, y), and (−y, −y) in four interleaved acquisitions, where the number of scans for each (φ_1, φ_2) data set is one fourth of total number of scans used in PELF.

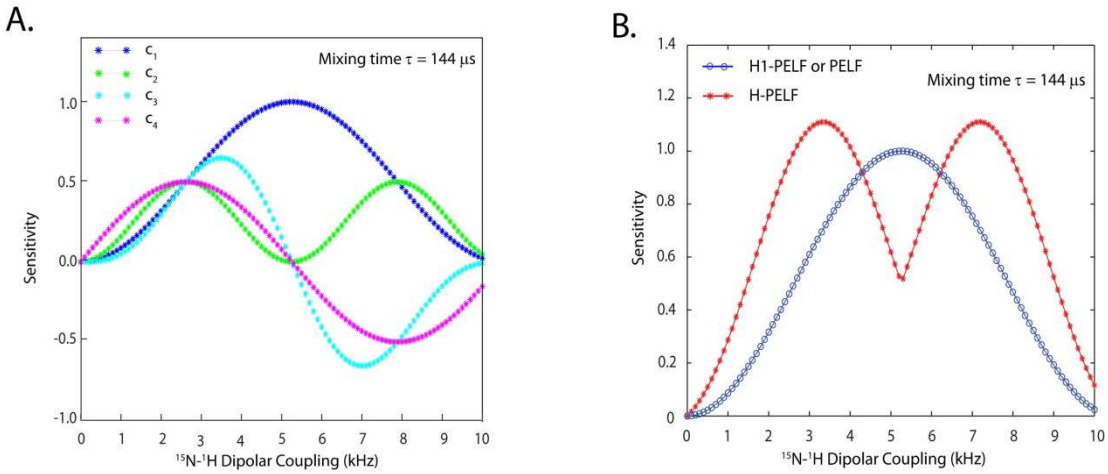

Figure 2.2: Simulated gains in sensitivity using HE-PELF

(A) Simulated relative sensitivities of Hadamard decoded data sets obtained by plotting the coefficients c_1, c_2, c_3 and c_4 of Eq. (1) for a mixing time of 144 μs. (B) Comparison of the relative sensitivities of H-PELF and PELF (or H1-PELF) spectra obtained by plotting 2 ($|c_1| + |c_2| + |c_3| + |c_4|$) and $4c_1$, respectively (Eq. 1) for a mixing time of 144 μs.

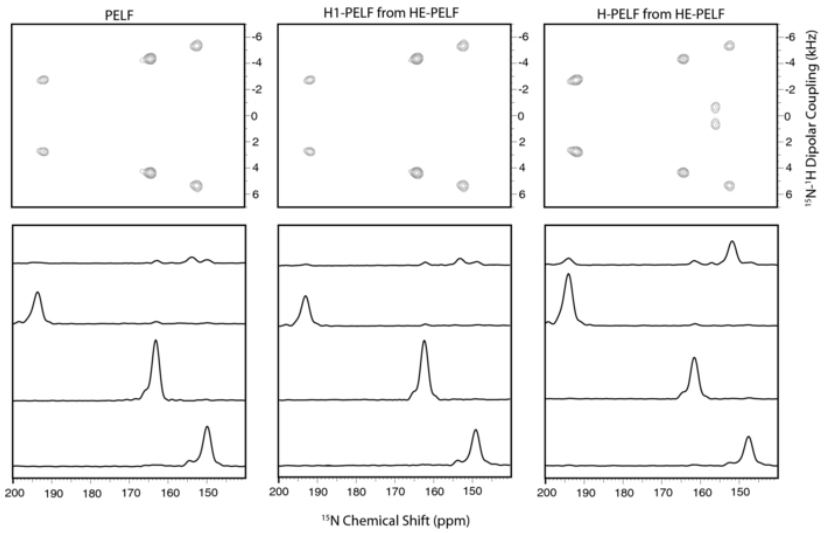

Figure 2.3: Comparison of PELF and H-PELF on single crystal

Comparison of PELF and H-PELF spectra of an ^{15}N-labeled NAL single crystal and the 1D slices for the 4 peaks at 16.5T. Reproduced from Ref. (*42*) with permission from American Chemical Society.

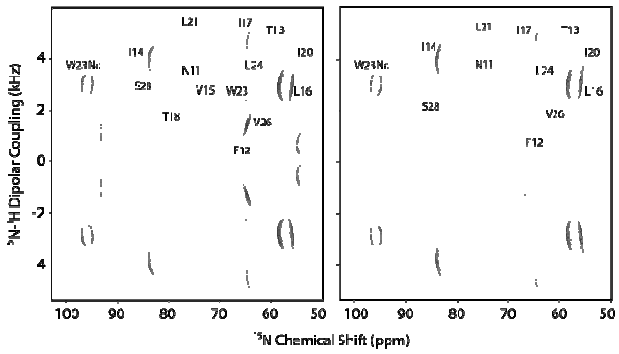

Figure 2.4: Comparison of PELF and H-PELF on sarcolipin in unflipped bicelles

Comparison of (left) H1-PELF and (right) HE-PELF spectra for U^{15}N-SLN in unflipped bicelles at 16.5T. Spectra were acquired with 56 transients for each of 32 t1 points (t_1 evolution = 0.90 ms)

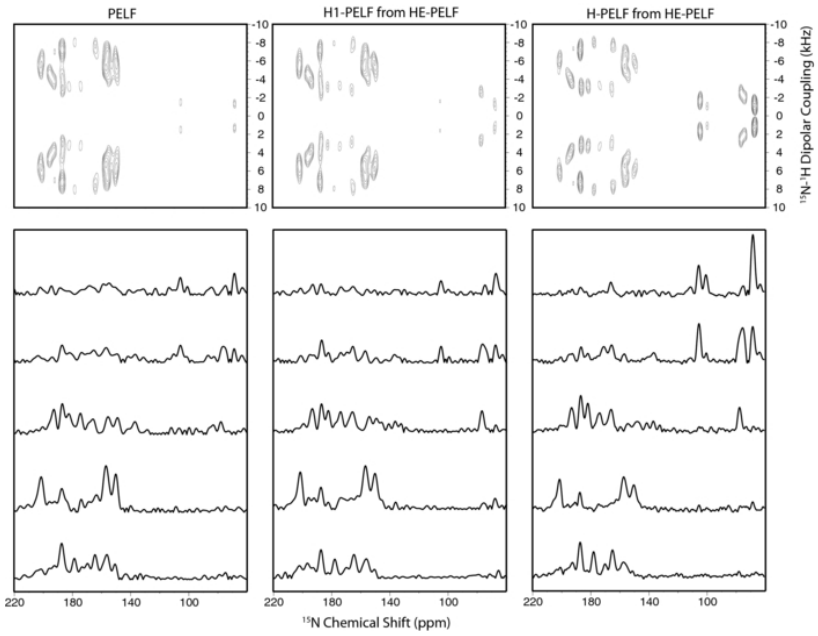

Figure 2.5: Comparison of PELF and H-PELF on sarcolipin in flipped bicelles

Comparison of PELF and HE-PELF spectra (H1-PELF and H-PELF) for U^{15}N-SLN in flipped bicelles and dipolar couplings at 16.5T. Reproduced from Ref. (*42*) with permission from American Chemical Society.

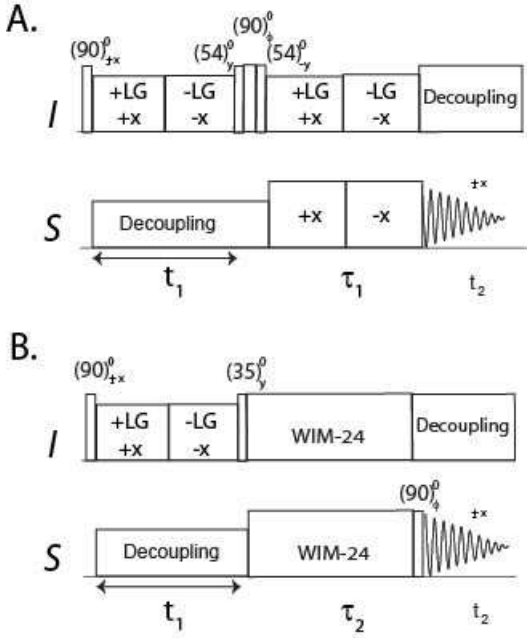

Figure 2.6: Pulse sequence for the SE-HETCOR experiment

(A) The HETCOR pulse sequence and (B) the corresponding sensitivity enhanced HETCOR experiment, SE-HETCOR.

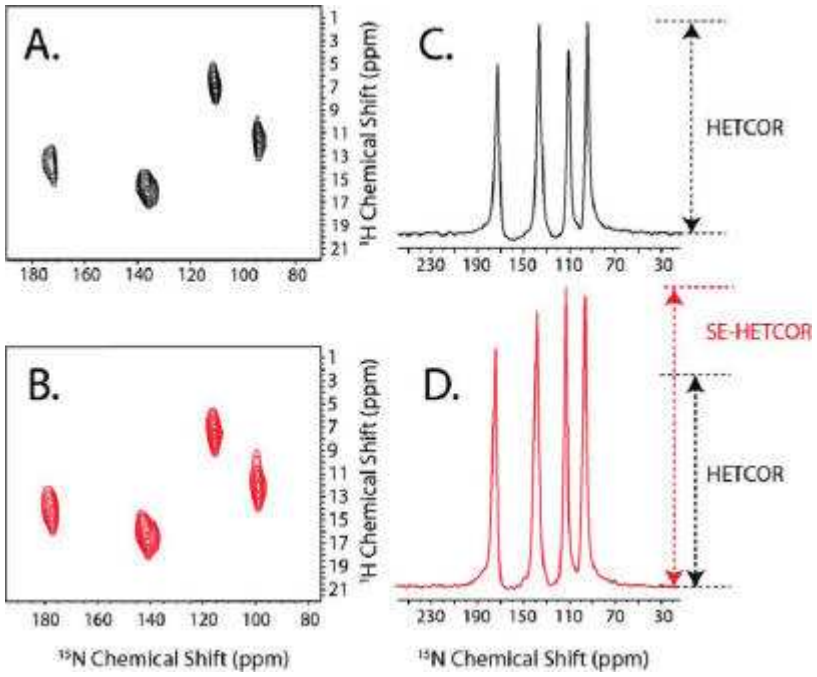

Figure 2.7: Improvements by SE-HETCOR on single crystal

Comparison between (A) conventional ^{1}H-^{15}N-HETCOR and (B) ^{1}H-^{15}N-SE-HETCOR spectra for a single crystal of ^{15}N-NAL with corresponding 1D slices in (C) and (D) showing the improvement in sensitivity. Reproduced from Ref. (*41*) with permission from American Chemical Society.

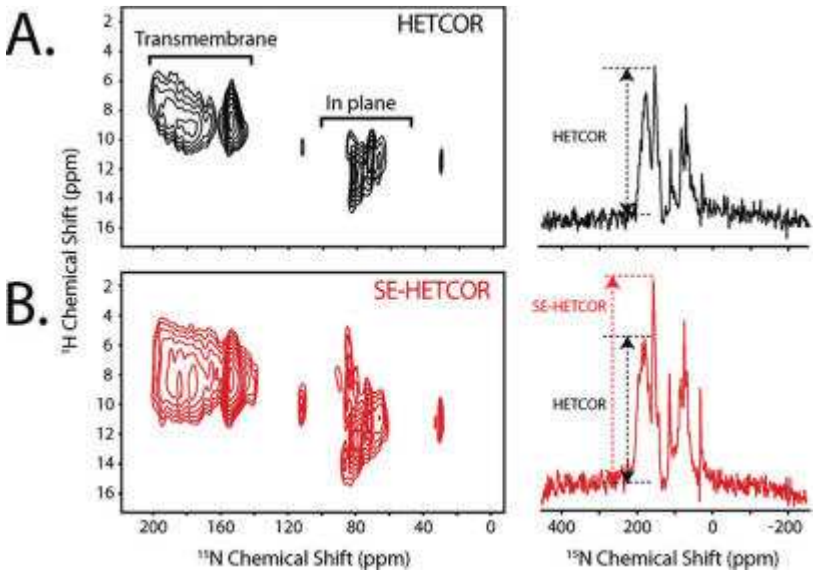

Figure 2.8: Improvements by SE-HETCOR on sarcolipin in biphenyl bicelles

(A) The ^{1}H-^{15}N-HETCOR and (B) the ^{1}H-^{15}N-SE-HETCOR spectra of U-^{15}N-SLN in aligned TBBPC bicelles at 16.5T with the corresponding 1D-slices showing the improvement in sensitivity for the SE-HETCOR experiment. Reproduced from Ref. (*41*) with permission from American Chemical Society.

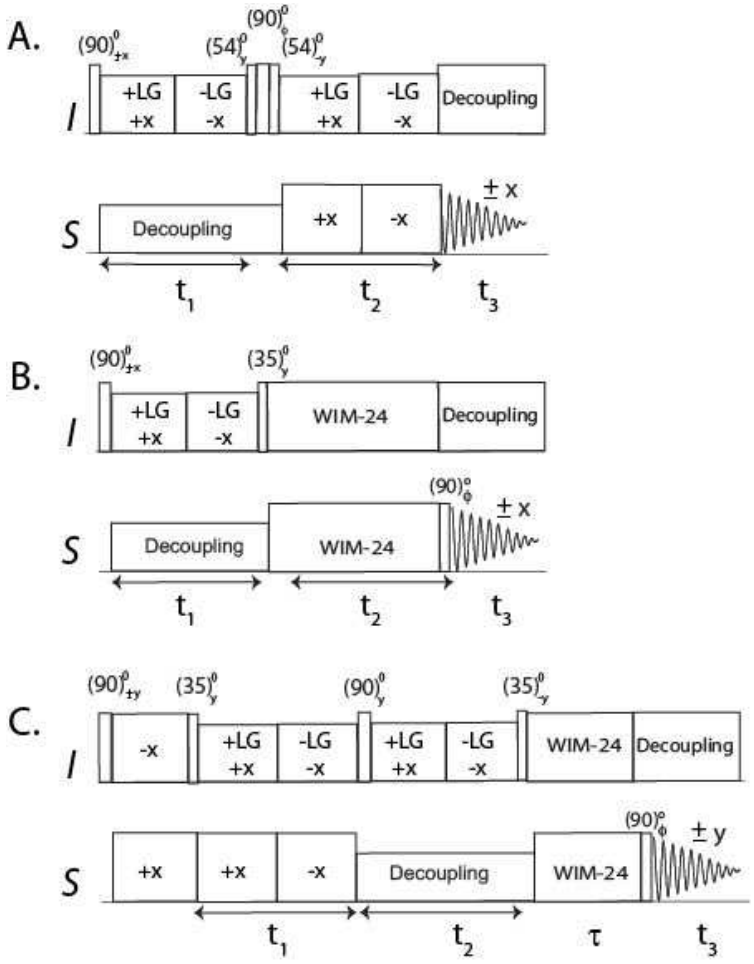

Figure 2.9: Pulse sequence for sensitivity enhanced 3D experiments

3D experiments to correlate ^{1}H chemical shifts, ^{15}N-^{1}H dipolar couplings, and ^{15}N chemical shifts. (A) HETCOR-SLF, (B) SE-HETCOR-SLF, and (C) SE-PISEMAI-HETCOR pulse sequences.

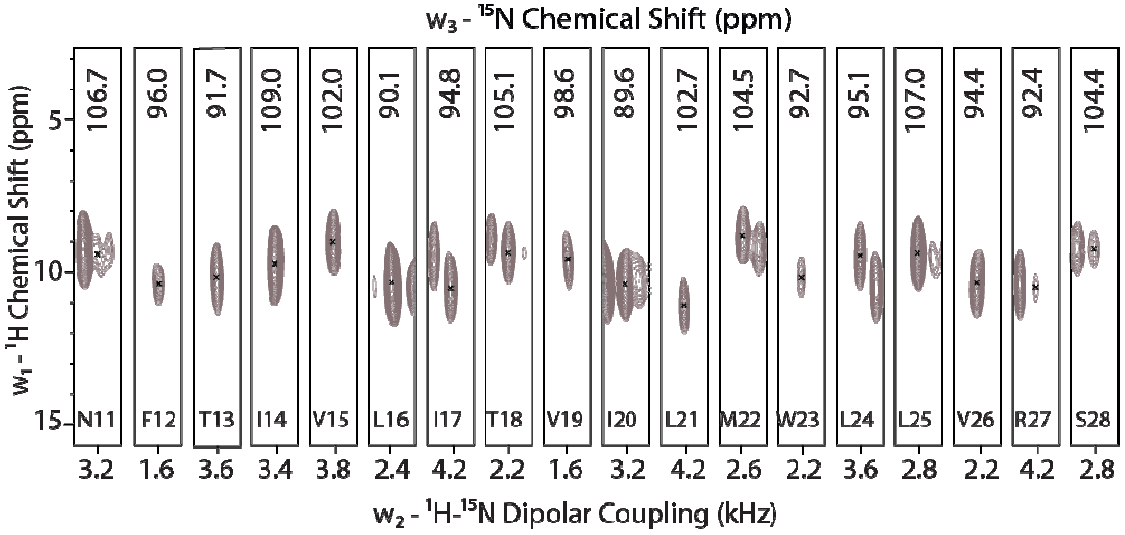

Figure 2.10: Strip plot from a 3D-SE-PISEMAI-HETCOR experiment on sarcolipin

Strip plots from a single 3D-SE-PISEMAI-HETCOR experiment on $U^{15}N$-SLN in unflipped bicelles at 16.5T. We utilized 80 transients for each of the 20 t_1 and 15 t_2 dimensions with a total experimental time of ~80h. (*29*)

3. Multidimensional Oriented Solid-State NMR Experiments Enable the Sequential Assignment of Uniformly ^{15}N Labeled Integral Membrane Proteins in Magnetically Aligned Lipid Bilayers

Kaustubh R. Mote, T. Gopinath, Nathaniel J. Traaseth, Jason Kitchen, Peter L. Gor'kov, William W. Brey, and Gianluigi Veglia

Reprinted with permission from **Journal of Bimolecular NMR (2011), 51, 339**

Oriented solid-state NMR is the most direct methodology to obtain the orientation of membrane proteins with respect to the lipid bilayer. The method consists of measuring dipolar couplings (DC) and anisotropic chemical shifts (CSA) for amide backbone for proteins that are uniformly aligned with respect to the membrane bilayer. A significant advantage of this approach is that tilt and azimuthal (rotational) angles of the protein domains can be directly derived from analytical expression of DC and CSA values, or, alternatively, obtained by refining protein structures using these values as harmonic restraints in simulated annealing calculations. The Achilles' heel of this approach is the lack of suitable experiments for sequential assignment of the amide resonances. In this Article, we present a new pulse sequence that integrates proton driven spin diffusion (PDSD) with sensitivity-enhanced PISEMA in a 3D experiment ([^{1}H,^{15}N]-SE-PISEMA-PDSD). The combination of 2D ^{15}N/^{15}N spin diffusion experiments with this new 3D experiment leads to the complete, unambiguous assignment of ^{15}N resonances. The feasibility of this approach is demonstrated for the membrane protein sarcolipin (SLN) reconstituted in magnetically aligned lipid bicelles. Taken with low electric field probe technology, this approach will propel the determination of sequential assignment as well as structure and topology of larger integral membrane proteins in aligned lipid bilayers.

Introduction

The complete determination of membrane protein structures requires the characterization of their architecture within the membrane (topology), which dictates their biological activity (*138*). Oriented solid-state NMR (OSS-NMR) spectroscopy is uniquely suited to elucidate membrane protein topology (e.g., tilt and azimuthal or rotation angles) in both mechanically and magnetically aligned lipid bilayers (*3*, *85–89*, *139–141*). To date, the majority of the solid-state NMR structures of isolated domains and intact membrane proteins deposited in the protein data bank originated from OSS-NMR or a combination of this approach with solution NMR restraints from micelle studies (i.e. hybrid approach) (http://www.drorlist.com/nmr/SPNMR.html).

In OSS-NMR, the membrane protein fingerprint is imaged by 2D separated local field (SLF) experiments (*142*). Pulse sequences such as, PISEMA (*43*, *112*, *143–146*), SAMPI-4 (*105*), HIMSELF (*111*, *147*), and PELF (*120*) are now routinely used to correlate backbone dipolar couplings (DC) with anisotropic chemical shifts (CSA) of uniformly ^{15}N labeled proteins. These anisotropic parameters are used as orientation restraints for structure calculations, assuming prior knowledge of the CSA and DC tensors (*85*, *86*, *148*, *149*).

However, the bottleneck of the OSS-NMR remains the sequential assignment of the amide resonances. Currently, multiple selectively labeled samples in combination with periodic patterns of anisotropic NMR observables originating from regular secondary structures (*110*, *150*) are used to assign OSS-NMR spectra. Also, several algorithms have been developed to obtain the resonance assignment through "shotgun" approaches (*151*), geometric search algorithms (*152*), or exhaustive search algorithms (*90*, *150*). Recently, Opella and co-workers have suggested a new procedure for resonance assignment based on DC values measured in bicelles with orthogonal orientations (*flipped* and *unflipped*, where the orientation of the bilayer normal is parallel and perpendicular to the direction of $\mathbf{B}_o$, respectively) in combination with isotropic chemical shifts obtained from experiments in micelles or isotropic bicelles (*134*). These approaches, however, are labor intensive and time consuming, and if the protein structural domains deviate significantly from ideality, they become prone to errors.

A classical experiment used to correlate ^{15}N resonances is the proton driven spin diffusion (PDSD) (*153*, *154*) . The 2D and 3D versions of this experiment have been used to assign ^{15}N backbone atoms in small proteins aligned in mechanically oriented lipid bilayers (*155*, *156*). However, the low sensitivity of these experiments limited their application to only a few selected cases.

In the past few years, there has been a significant effort to develop robust bicelle systems to increase the sensitivity and resolution for membrane protein SLF spectra (*104*, *108*, *157*). Bicelles allow for higher and more consistent levels of hydration over mechanically aligned lipid bilayers, have a higher tolerance to protein concentrations, and increase the

filling factor in the NMR coil. These factors in combination with low electric field (low-*E*) static probes (*22*) dramatically boost both sensitivity and resolution of OSS-NMR techniques. These technological developments have led to the development and use of several diffusion schemes, including mis-matched Hartman-Hahn (MMHH) (*158*, *159*), radio-frequency driven spin diffusion (RFDSD) (*160*), and proton spin diffusion (PSD) (*161*) to assign SLF spectra. Nonetheless, most of these applications have been done with 2D spectra, with inadequate resolution for obtaining a complete sequential assignment.

Here, we show that the combination of PDSD with sensitivity enhanced methods is able to resolve most of the inter-residue correlations in a small (3.7kDa) single-pass membrane protein sarcolipin (*54*, *67*, *71*, *162–164*). Unlike the other methods, PDSD has the advantage of higher signal-to-noise per unit time, and more importantly, it transfers the majority of magnetization between *i* and *i*+1 spin systems (*165*), allowing the classical main-chain *walk* to connect all of the amide resonances in proteins. These results establish the feasibility of sequential assignment of backbone resonances for membrane proteins reconstituted in magnetically oriented systems.

Methods and materials

Uniformly ^{15}N-sarcolipin (SLN) was expressed in *E. coli* and purified as previously described (*166*, *167*). Briefly, SLN was expressed as a fusion protein with maltose binding protein (MBP), and was purified by affinity chromatography on an amylose column followed by cleavage with tobacco etch virus protease. SLN was collected as a precipitate after dialysis and further purified to homogeneity by reversed-phase HPLC. Lyophilized SLN was dissolved in NMR sample buffer containing 6.7 mg D6PC, 20 mM HEPES, 30 mM $CaCl_2$ or 100 mM NaCl, and 0.02% NaN_3. This was then added to 31 mg of long chain lipid (DMPC or DMPC/POPC 4/1 w/w) suspended in H_2O to give a final lipid concentration of 25% (w/v). Bicelles with a q-ratio (long-chain lipid/short-chain lipid) of ~3.2 and an approximate order parameter of 0.8 (as measured by the comparison of the long-chain ^{31}P chemical shift in these aligned bicelles with the ^{31}P resonance in

mechanically aligned lipid bilayers) were formed after several freeze-thaw-vortex cycles. For making *flipped* bicelles (*i.e.*, with the membrane normal parallel with the direction of the static field), $YbCl_3$ was added to give a final concentration of 5 mM. All NMR experiments were performed on a 700MHz VNMRS spectrometer at a temperature of 38˚C for DMPC-D6PC bicelles and 25˚C for DMPC-POPC-D6PC bicelles, with a low-*E* bicelle probe built by the RF Program at the National High Magnetic Field Laboratory (NHMFL) in Florida (*22*). Cross polarization times of 500 μs or 1000 μs with ^{1}H RF field amplitudes of 62.5 kHz or 50.0 kHz were used for flipped or unflipped bicelles, respectively. FSLG decoupling was obtained by ramping the phase of ^{1}H RF with effective field strength amplitudes of 62.5 and 50.0 kHz for flipped and unflipped bicelles, respectively. A recycle delay of 4 sec was used in all experiments. A mixing time of 3 sec was used during the PDSD element. An acquisition time of 5ms was used in the direct dimension with 62.5 and 50.0 kHz SPINAL decoupling (*168*) on the proton channel for flipped and unflipped bicelles, respectively. Parameters for evolution in the indirect evolution are reported in figure legends. Spectra were processed in NMRPipe (*169*) and analyzed with Sparky (T. D. Goddard and D. G. Kneller, SPARKY 3, University of California, San Francisco). All 2D FIDs were zero-filled to a final matrix size of 8192 × 4096 (direct × indirect dimensions). For the SE-PISEMA and PDSD experiments, indirect dimensions were processed using the Rance-Kay and States mode (*136*), respectively. For the 3D SE-PISEMA-PDSD, the t_1 and t_2 dimensions were processed in Rance-Kay and States mode, respectively. A Lorentz-to-Gaussian window function (50-150 Hz) was used before Fourier transformation of the FID.

Results and discussion

The most basic 2D PDSD experiment used to establish dipolar correlations among the backbone ^{15}N chemical shifts is shown in Fig. 3.1A (*153–155*). This element has been combined with the PISEMA pulse sequence as shown in Fig. 3.1B (*156*). The spectra resulting from this experiment display 2D correlations between ^{15}N anisotropic chemical shifts and ^{1}H-^{15}N dipolar couplings overlaid to spin diffusion cross-peaks among the ^{15}N resonances.

The initial resonance assignments were carried out with the 2D experiments with SLN reconstituted in flipped bicelle samples. These samples do not require fast uniaxial rotational diffusion of the protein and give narrow linewidths with good sensitivity and resolution. Fig. 3.2 shows spectra obtained from 2D PDSD ($^{15}N/^{15}N$; pulse sequence in Fig. 3.1A and spectrum in Fig. 3.2A) and 2D PISEMA-PDSD (^{1}H-$^{15}N/^{15}N$; pulse sequence in Fig. 3.1B and spectrum in Fig. 3.2B) correlation experiments in flipped DMPC-D6PC bicelles. Spectra were assigned by comparing with the SECT-PISEMA spectrum (*112*), which gave a significant increase in resolution due to 5-15% narrower linewidths, as compared to SE-PISEMA, in the dipolar dimension. The overlap of the resonances in the 2D-PISEMA-PDSD makes it challenging to assign the cross-peaks. Although we were able to assign a total of 26 residues, there were many overlapped resonances and ambiguous assignments.

To resolve these ambiguities, we designed a new 3D experiment that combines the PISEMA-PDSD scheme with the sensitivity-enhancement (SE) element (*43*). The SE scheme detects both sine and cosine modulated dipolar coherences to boost the sensitivity of OSS-NMR spectra and can be used for both SLF and HETCOR experiments (*41*). In the 3D [^{1}H,^{15}N]-SE-PISEMA-PDSD experiment (pulse sequence in Fig. 3.1C and spectrum in Fig 3.3), the magnetization is created via cross polarization and tilted at the magic angle. The ^{1}H-^{15}N DC coupling is evolved in the first indirectly detected dimension (t_1) in the same way as PISEMA using phase-modulated Lee-Goldburg homonuclear decoupling (*170*). Subsequently, the *in-phase* single-quantum ^{15}N magnetization is stored along the Z-direction, while the multiple-quantum magnetization

is converted to single-quantum during the echo period (2τ). Note that the optimal transfer during the echo period must be optimized for the average DC values within the sample. In the case of unflipped bicelle samples, the optimal delay is set for 3.0 kHz, while for flipped bicelle samples a value of 5.5 kHz was chosen. A 90˚ pulse is then applied which places magnetization in the XY plane to evolve in t_2 under ^{15}N chemical shift. Following t_2 evolution, the coherences are positioned along the z-axis for the PDSD to take place, and finally tilted in the XY plane for detection during t_3. As a result this experiment correlates ^{1}H-^{15}N dipolar coupling (t_1), ^{15}N chemical shift (t_2), and ^{15}N chemical shift (t_3), with dipolar cross-peaks that can be easily observed in the $^{15}N/^{15}N$ dimensions. Fig 3.3 shows the strip plots from the 3D [^{1}H,^{15}N]-SE-PISEMA-PDSD spectrum in unflipped DMPC-POPC-D6PC bicelles. In this experiment we set the PDSD mixing time to 3 sec, which gives most intense cross-peaks per unit time in model compounds (*165*).

The intensities of the dipolar cross peaks with a 3 sec PDSD mixing period were 20% to 30% of the diagonal peak intensities. Each diagonal peak displayed one or two intense correlations, corresponding to the adjacent residues in the primary sequence. Interestingly, a closer inspection revealed weaker {*i*, *i*+2} and {*i*, *i*+3} cross-peaks for some of the residues, showing that a residual long-range transfer can be observed in the PDSD experiment. Nonetheless, the more intense {*i*, *i*+1} correlations led to a straightforward determination of the backbone connectivity. In addition, we also observed that the cross-peak pattern obtained in flipped and unflipped bicelles is asymmetric with respect to the diagonal peaks as previously reported in the literature (*154*, *159*, *171*). This was not problematic, since the stronger of the equivalent cross peaks was used for obtaining the assignments.

In total, correlations were obtained for 21 resonances from the datasets in flipped and unflipped bicelles. Fig. 3.4 shows a comparison of SE-PISEMA spectra in flipped and unflipped bicelles. The assignments obtained for these spectra were confirmed by comparing the ^{15}N-^{1}H dipolar coupling for each residue and the order parameter for flipped bicelles relative to the unflipped bicelles was found to be ~0.94. The first

assignment was made from the flipped spectrum by a cross-peak between residues 30 and 31 at the C-terminal end (Fig 3.2A-inset). Another correlation between residue 29 at the C-terminus to residue 28 within the PISA wheel (Fig 3.2A-inset) was observed in the spectra. Starting from these connectivities and using the spectra shown in Fig 3.2 and 3.3, we unambiguously assigned 21 residues (N11-Y31) in a way consistent with the known α-helical structure of sarcolipin (Fig 3.5 and Table S1). The unflipped PDSD spectrum, however, did not show cross-peaks for C-terminal residues or for residues 16-17, possibly due to scaling of ^{15}N-^{15}N DCs that reduces the probability for spin diffusion between ^{15}N nuclei. In addition, cross peaks were indistinguishable for two residue pairs (21-22 and 23-24) that had nearly identical ^{15}N CSA in the unflipped spectrum. Residues 6-10 were assigned based on the α-helical model in the flipped spectrum due to significant overlap in the unflipped PISEMA spectrum. Thus, we report assignments for 26 out of the 31 residues (R6 to Y31) that were also consistent with selectively labeled PISEMA spectra obtained in mechanically aligned bilayers (*90*). Residues 1-5 form the dynamic N-terminus of the protein (*162, 163, 172*), and could not be detected by cross-polarization used in our experiments.

The PISA wheel patterns in binary and ternary lipid bicelles are very similar. The resonances of the transmembrane domain were only slightly perturbed by these lipids, showing that the tilt and rotation angles are independent of these small changes in lipid composition and bilayer thickness. This allows for the possibility of screening different lipids to obtain optimal resolution without substantially affecting the topology and structure. Bicelles containing POPC improve sample stability by aligning at a lower temperature (25˚C) compared to DMPC-only bicelles (38˚C) and increasing bilayer thickness to better mimic the lipids present in the sarcoplasmic reticulum (primarily DOPC/DOPE). The DC and CSA oscillation pattern for transmembrane domain of SLN is shown in Fig. 3.5. The regularity of the pattern and the uniformity of the PISA wheel suggest that the SLN transmembrane domain adopts a conformation close to an ideal α-helix in lipid bilayers (*173*).

The PDSD experiment depends on the ^{15}N-^{15}N dipolar couplings (Fermi's golden rule) (*154*). Since the dipolar couplings have a periodic oscillation for helical proteins (*110*, *150*), this can lead to unequal cross peak intensities. In the most extreme cases, no cross peak will be observed when the DC value between ^{15}N spins is equal to zero (Fig 3.6). This effect is exacerbated by the unequal peak intensities obtained for SLF experiments, which has been shown to be a reflection of the mosaic spread of tilt angles (*90*, *174*). As a result, the cross-peak intensity cannot reliably be correlated to distance and should be used for assignment purposes only. The dependence of the cross-peak intensity on dipolar coupling (and hence distance) results in few cross peaks, most of which connect neighboring residues. The comparatively high intensity of the cross-peak is a direct result of using PDSD, which relies on T_1 rather than $T_{1\rho}$ spin exchange (*165*). Although there is evidence of {*i*, *i*+2} and {*i*, *i*+3} cross-peaks, these are without exception less intense than {*i*, *i*+1} cross peaks and in practice, serve as an additional confirmation for the assignment.

Conclusions

We have obtained a *de novo* sequential assignment of the integral membrane protein SLN in magnetically aligned bicelles using only uniformly ^{15}N labeled protein. This strategy is universally applicable to assigning membrane proteins with ideal and non-ideal α-helical domains as well as β-barrels, since it does not assume ideal secondary structures. The use of proton driven spin diffusion facilitates semi-selective transfer of magnetization over short distances, which avoids ambiguity in resonance assignment. A robust assignment was made possible by a new 3D experiment that combined the sensitivity enhancement scheme with PISEMA and PDSD (^{15}N-SE-PISEMA-PDSD). Further developments in sample preparation, pulse sequences, and innovative probe designs will continue to advance this growing and exciting field. Although selective labeling and computational approaches will continue to be important, sequential assignment is the only approach that will be possible to fully assign large membrane proteins.

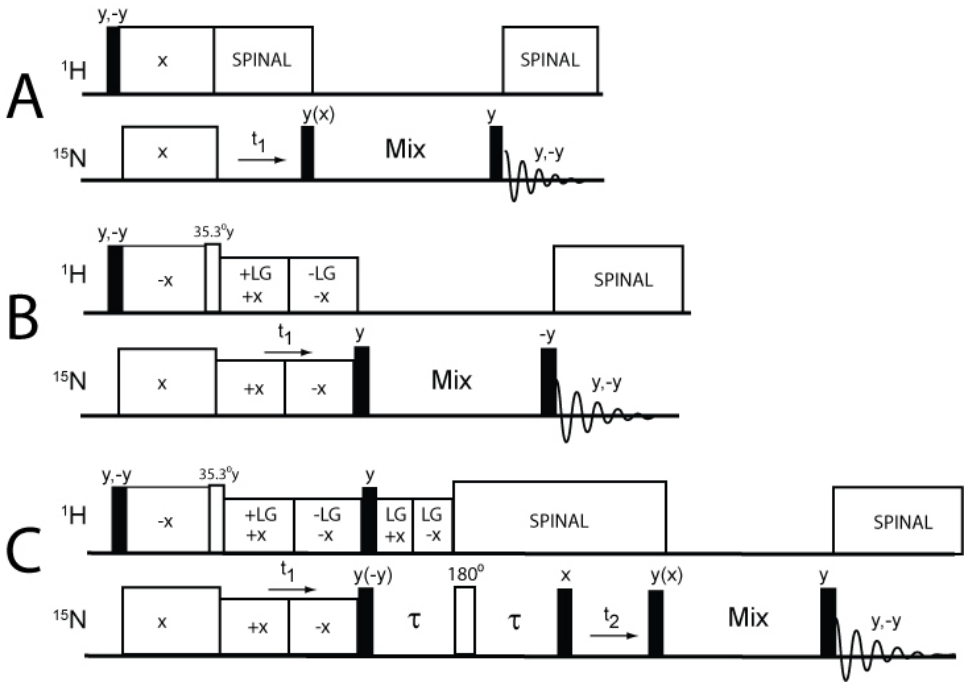

Figure 3.1: Pulse sequences used to assign SLN spectra

The PDSD was used for each mixing element in combination with **(A)** ^{15}N/^{15}N correlation, **(B)** ^{1}H-^{15}N/^{15}N correlation (2D-PISEMA-PDSD), and **(C)** ^{1}H-^{15}N/^{15}N/^{15}N (^{15}N-SE-PISEMA-PDSD). A mixing time of 3 sec was used for all experiments. The τ-value was set to 125μsec for the 3D experiment in unflipped bicelles.

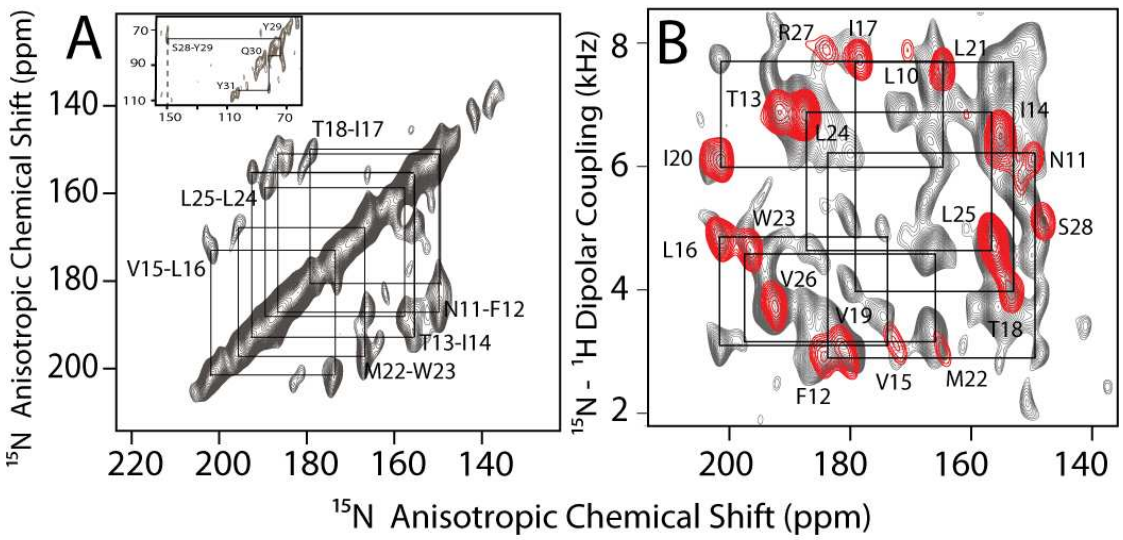

Figure 3.2: Two-dimensional PDSD Spectra

[U-^{15}N]-SLN spectra in flipped DMPC-D6PC bicelles at a protein to lipid ratio of 1:150 (~1.5mg SLN) and temperature of 38˚C. (A) ^{15}N-^{15}N 2D correlation spectrum with a 3 sec PDSD mixing time. 512 transients were co-added for 32 t_1 increments with a final t_1 evolution time of 1.5 msec. A few of the correlations obtained are shown in the figure. Inset: Correlations between the transmembrane domain and the C-terminus. Cross peak intensities are ~20-30% of the diagonal peak intensity. (B) In red, [^{1}H,^{15}N]-SECT-PISEMA spectrum with 1024 transients for each of the 21 t_1 increments and a constant time evolution period of 1.28 msec. In grey is the [^{1}H,^{15}N]-PISEMA-PDSD spectrum with 1696 transients for each of the 20 t_1 increments. Only the transmembrane section of the spectrum is shown.

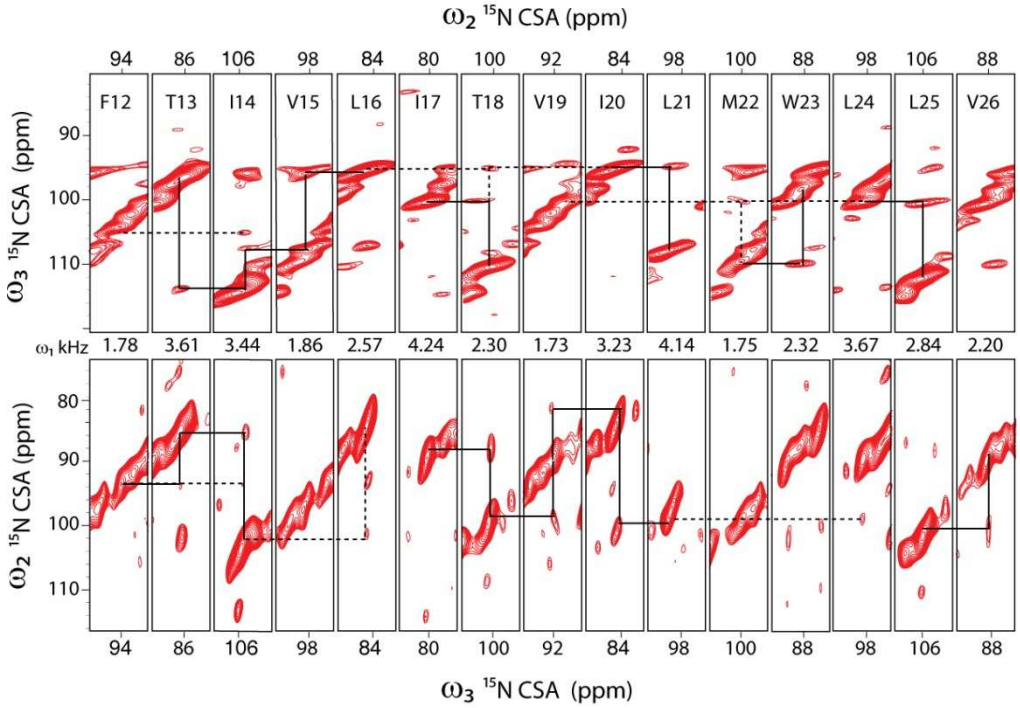

Figure 3.3: Strip plots from 3D-SE-PISEMA-PDSD experiment

3D strip plots at specific dipolar coupling values from a [^{1}H,^{15}N] SE-PISEMA-PDSD spectrum of [U-^{15}N]-SLN in unflipped DMPC-POPC-D6PC bicelles at 25˚C and with a protein to lipid ratio of 1:75 (~3.0 mg SLN). A total of 40 transients were co-added for 20 t_1 and 32 t_2 increments corresponding to final t_1 and t_2 acquisition times of 2.4msec and 1.5msec, respectively. Bold lines indicate {*i*, *i*+1} cross peaks and dotted lines indicate {*i*, *i*+2} cross peaks. The same data set is plotted twice after interchanging the X- and Y-axes in order to account for the unequal intensities of the equivalent cross peaks in the spectrum. See Fig S1 for representative 2D planes from this spectrum.

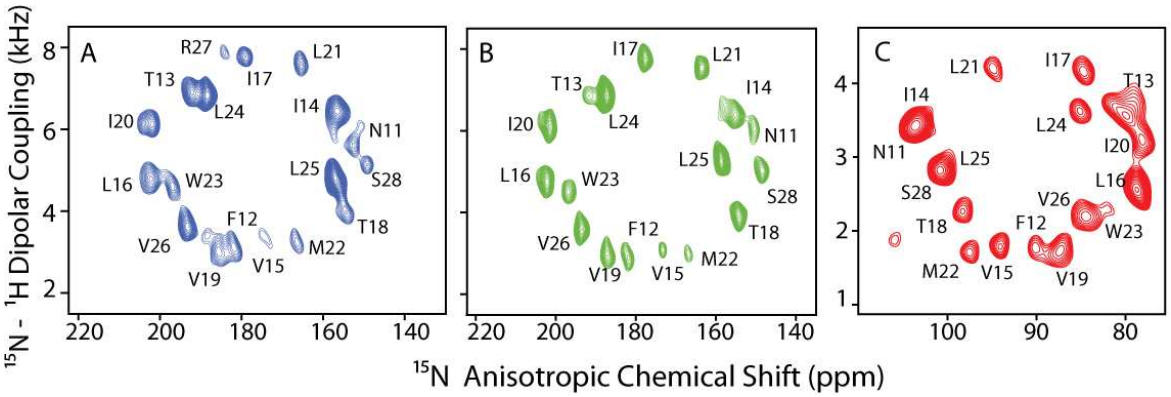

Figure 3.4: Comparison of assignments of SLN in flipped and unflipped bicelles

(A) [^{1}H,^{15}N] SE-PISEMA in flipped DMPC-D6PC bicelles with 256 transients and 25 t_1 increments at 38˚C. (B) [^{1}H,^{15}N] SE-PISEMA in flipped DMPC-POPC-D6PC bicelles with 256 transients and 25 t_1 increments at 25˚C. (C) [^{1}H,^{15}N] SE-PISEMA in unflipped DMPC-POPC-D6PC bicelles with 288 transients and 25 t_1 increments with a final t_1 evolution time of 3.0 ms at 25˚C. The τ-value in sensitivity enhanced pulse sequence was set to 75μs and 125μs for flipped and unflipped bicelles, respectively.

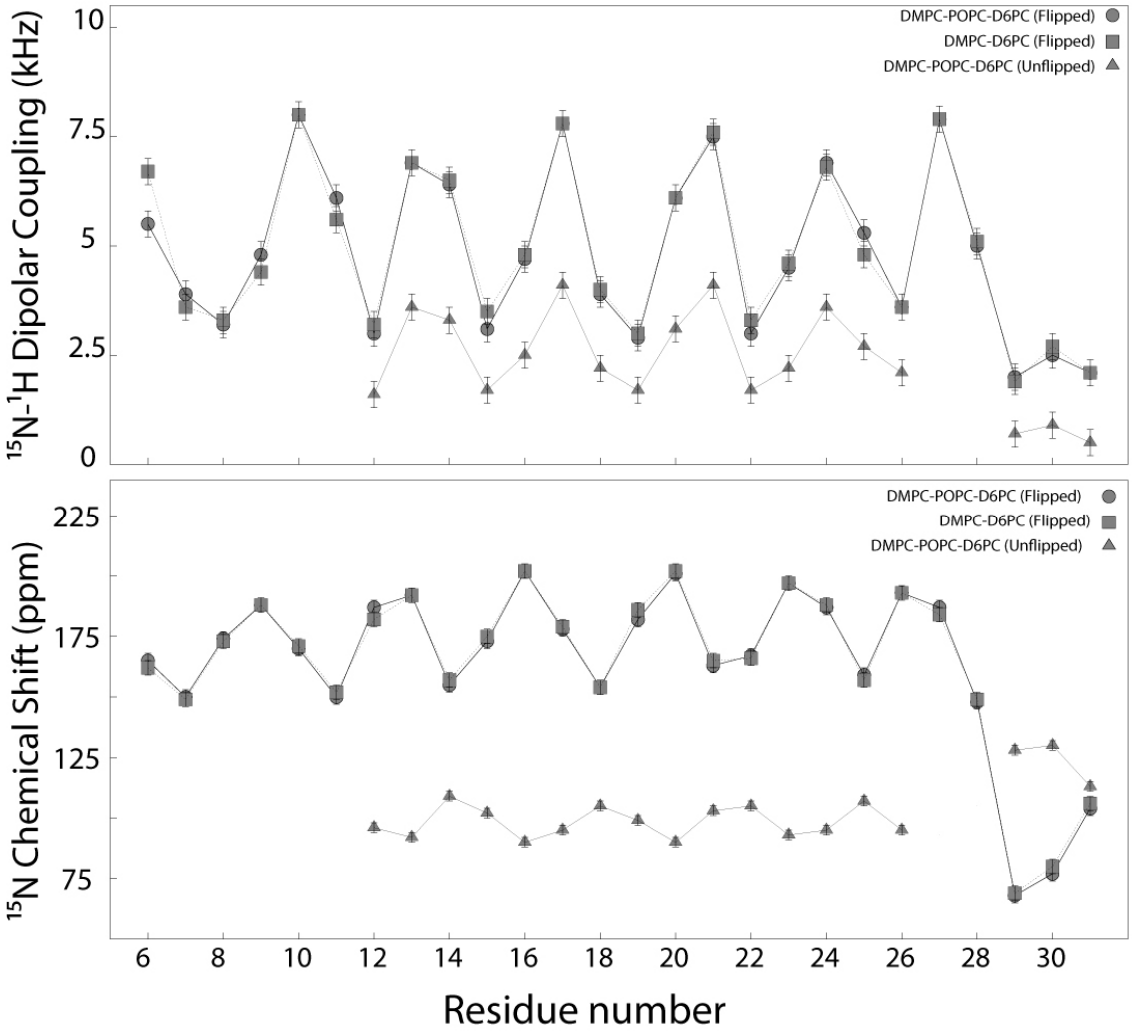

Figure 3.5: ^{15}N CSA and ^{1}H-^{15}N DC oscillation patterns

^{15}N CSA and ^{1}H-^{15}N DC oscillation patterns for the assigned resonances of SLN in flipped and unflipped bicelles. The error bars reflect the average experimental line-widths.

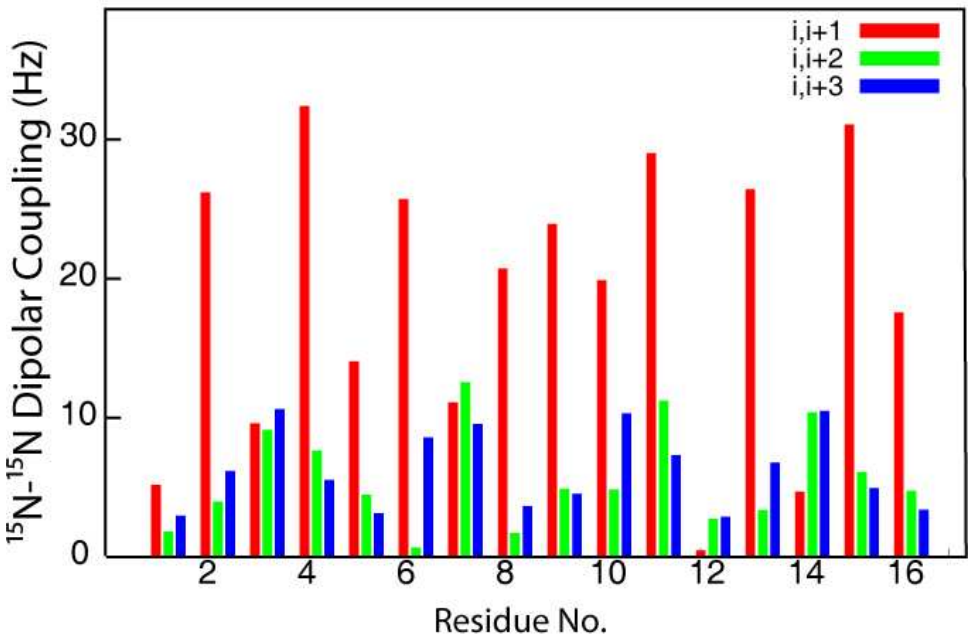

Figure 3.6: Calculated ^{15}N-^{15}N dipolar couplings for an ideal α-helix

Calculated ^{15}N-^{15}N dipolar couplings (absolute value) for an ideal α-helix (with torsion angle □=-60˚ and ψ=-45˚) tilted at an angle of 25˚ with respect to the membrane normal in flipped bicelles. DCs would be scaled by 0.5 in unflipped bicelles. Since the rate of PDSD is proportional to ω^2 (Suter et al. 1985), it is expected that ^{15}N nuclei with the largest DCs will be observed (i.e., primarily {*i*, *i*+1} correlations). However, some of the {*i*, *i*+1} DCs are close to zero and weaker correlations would be expected in the spectra.

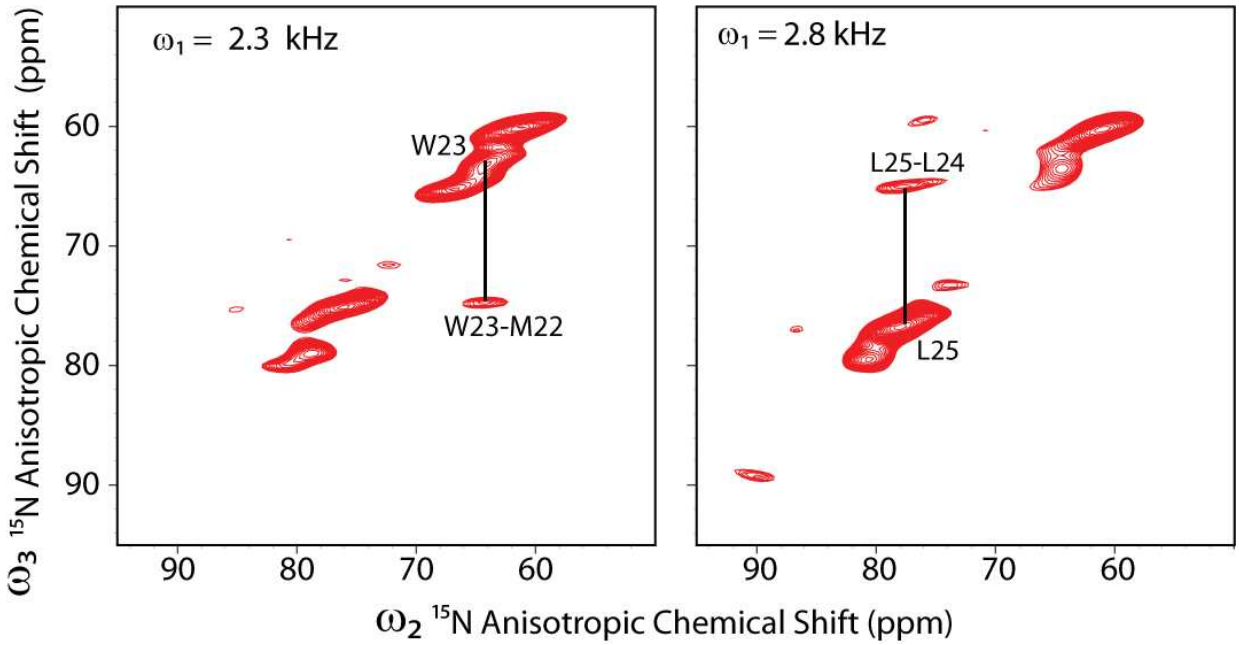

Figure S3.1: 2D Planes from the SE-PISEMA-PDSD experiment

Representative 2D planes (^{15}N-^{15}N dimension) at specific ^{15}N-^{1}H DC values for the 3D – ^{15}N-SEPISEMA-PDSD spectrum of SLN in DMPC-POPC-D6PC bicelles. These plots are the same as in Fig 3.3 shown here from 95ppm to 50ppm to illustrate the single site resolution obtained.

Table S3.1: Assignment for sarcolipin in different bicelles.

The experimental errors are based on the linewidths (~0.3 kHz for DC and ~2.5 ppm for ^{15}N-CSA). In bold are residues assigned sequentially using spin-diffusion cross peaks. Marked with asterisks are residues assigned using the periodicity of the PISA wheels. Marked with a pound are residues expected to give scaled DC and CSA values due to dynamic disorder. OL indicates overlapped resonances that were not assigned.

Residue No.	**DMPC-POPC-D6PC (Flipped)**		**DMPC-D6PC (Flipped)**		**DMPC-POPC-D6PC (Unflipped)**	
	DC (kHz)	CSA (ppm)	DC (kHz)	CSA (ppm)	DC (kHz)	CSA (ppm)
6*	6.9	161	6.7	162	OL	OL
7*	5.8	152	3.6	149	OL	OL
8*	3.2	173	3.3	173	OL	OL
9*	4.8	188	4.4	188	OL	OL
10*	8.0	170	8.0	171	OL	OL
11	**6.1**	**150**	**5.6**	**152**	OL	OL
12	**3.0**	**187**	**3.2**	**182**	**1.6**	**96**
13	**6.9**	**192**	**6.9**	**192**	**3.6**	**92**
14	**6.4**	**155**	**6.5**	**157**	**3.3**	**109**
15	**3.1**	**173**	**3.5**	**175**	**1.7**	**102**
16	**4.7**	**202**	**4.8**	**202**	**2.5**	**90**
17	**7.8**	**178**	**7.9**	**179**	**4.1**	**95**
18	**3.9**	**154**	**3.0**	**154**	**2.2**	**105**
19	**2.9**	**182**	**6.1**	**186**	**1.7**	**99**
20	**6.1**	**201**	**7.6**	**202**	**3.1**	**90**
21	**7.5**	**163**	**7.8**	**165**	**4.1**	**103**
22	**3.0**	**167**	**3.3**	**166**	**1.7**	**105**
23	**4.5**	**197**	**4.6**	**197**	**2.2**	**93**
24	**6.9**	**187**	**6.8**	**188**	**3.6**	**95**
25	**5.3**	**159**	**4.8**	**157**	**2.7**	**107**
26	**3.6**	**193**	**3.6**	**193**	**2.1**	**95**
27	**7.9**	**187**	**7.9**	**184**	OL	OL
28	**5.0**	**148**	**5.1**	**149**	OL	OL
29#	**2.6**	**76**	**1.9**	**69**	0.7	128
30#	**2.6**	**80**	**2.7**	**80**	0.9	130
31#	**2.0**	**106**	**2.1**	**106**	0.5	113

4. Determination of Structural Topology of a Membrane Protein in Lipid Bilayers using Polarization Optimized Experiments (POE) for Static and MAS Solid State NMR Spectroscopy

Kaustubh R. Mote, T. Gopinath, and Gianluigi Veglia

Reprinted with permission from **Journal of Bimolecular NMR (2013), 57, 902**

The low sensitivity inherent to both the static and magic angle spinning techniques of solid-state NMR (ssNMR) spectroscopy has thus far limited the routine application of multidimensional experiments to determine the structure of membrane proteins in lipid bilayers. Here, we demonstrate the advantage of using a recently developed class of experiments, polarization optimized experiments (POE), for both static and MAS spectroscopy to achieve higher sensitivity and substantial time-savings for 2D and 3D experiments. We used sarcolipin, a single pass membrane protein, reconstituted in oriented bicelles (for oriented ssNMR) and multilamellar vesicles (for MAS ssNMR) as a benchmark. The restraints derived by these experiments are then combined into a hybrid energy function to allow simultaneous determination of structure and topology. The resulting structural ensemble converged to a helical conformation with a backbone RMSD ~ 0.44 Å, a tilt angle of 24˚ ± 1˚, and an azimuthal angle of 55˚ ± 6˚. This work represents a crucial first step toward obtaining high-resolution structures of large membrane proteins using combined multidimensional O-ssNMR and MAS-ssNMR.

Introduction

Membrane protein function is modulated by lipid membranes (*10*, *138*). Therefore, understanding the structure-function relationship of these proteins requires their characterization in fully hydrated lipid bilayers. Multidimensional solid-state NMR, *i.e.* oriented solid-state NMR (O-ssNMR) and magic angle spinning solid-state NMR (MAS-ssNMR), allows for such structural characterization in the presence of fluid lipid bilayers – the most faithful mimetic of natural membranes. O-ssNMR provides information on dipolar couplings and anisotropic chemical shifts that enable the determination of topological parameters, such as the tilt and rotation angles of transmembrane and membrane anchored domains (*175*). On the other hand, MAS-ssNMR provides chemical shift information on both main chain and side chains that can be converted into torsion angles for assessing secondary structure elements. MAS-ssNMR can also be utilized to

measure residual dipolar couplings in aligned bicelles (*176*). In the case of fast uniaxial rotation around membrane normal, MAS-ssNMR can provide orientational restraints that can further refine the structure of small peptides (*177*) as well as large membrane proteins (*27, 37*).

As we demonstrated for phospholamban (*86, 87*), the *ab initio* determination of the structural topology of a membrane protein in the absence of homology models entails the combination of all of the above information. Lack of information or even relying on only one approach to determine the structural topology of membrane proteins leads to misinterpretation of the experimental results (*178*, *179*).

A major advantage of combining MAS-ssNMR and O-ssNMR data is to obtain structural and topological data using similar lipid compositions in the sample preparations, circumventing the necessity for cross-validation of the structural information obtained from different membrane mimetic systems. Nonetheless, the ssNMR experiments applied to membrane proteins are inherently insensitive. This is due in part to the need for high lipid-to-protein ratios that, while maintaining protein's functional integrity, reduce the effective protein concentrations in the sample. In addition, recurring secondary structure elements (multiple transmembrane α helices) as well as sample heterogeneity tend to give poorly resolved spectra for these proteins. As a result only a few structures of membrane proteins have been determined by ssNMR techniques (*3, 85–87, 180, 181*). Our work is motivated by the necessity of improving these techniques for membrane protein samples. Toward this goal, we recently designed several new pulse sequences to improve the sensitivity of both O-ssNMR and MAS-ssNMR experiments. An underlining concept for these new experiments is the *optimization of nuclear spin polarization* (polarization optimized experiments, POE) to augment the NMR signals or deconvolute multiple excitation pathways to obtain several 2D or 3D experiments simultaneously. The latter translates into a substantial decrease in experimental time.

For O-ssNMR, the polarization is optimized by recovering the previously discarded dipolar (*43*) and chemical shift coherences (*41*). We demonstrated that these experiments

improve the sensitivity of traditional rotating frame SLF experiments such as PISEMA (*143*), HIMSELF (*147*), SAMPI-4 (*182*) and HETCOR (*133*) by ~40%, thereby cutting experimental time in half (*41*, *111*). Such a strategy has also been demonstrated for the original PELF experiment (*115*), and enhances sensitivity by > 100% for highly mobile segments in proteins (*42*). The gain in sensitivity has allowed us to record comparatively insensitive constant-time experiments, such as the SECT-PISEMA (*112*) for increasing resolution in 2-dimensional experiments (*39*). In the 3D SE-PISEMAI-HETCOR experiment (*41*), we designed a pulse scheme to recover chemical shift coherences in addition to retaining the sensitivity gain obtained by the polarization inversion. The resulting boost in sensitivity is 80-180%, which enables the implementation of 3D spectroscopy to correlate ^{15}N chemical shifts, ^{15}N-^{1}H dipolar couplings, and ^{1}H chemical shifts. The three- to seven-fold savings in time alone bring a number of membrane protein systems within reach of this technique. This experiment is used here to obtain the complete set of backbone orientation restraints for sarcolipin in oriented bicelles (*103*).

In contrast to O-ssNMR, MAS-ssNMR experiments have reached a much higher level of sophistication. In the past decade, many groups have used MAS to for high-resolution structural studies of macromolecular systems, including microcrystalline proteins (*31*, *38*, *183*), fibrillar systems (*30*), membrane proteins (*184*, *185*), protein complexes (*186*), cell extracts (*187*) and whole cell (*188*). Nonetheless, membrane protein structural biology still offers the biggest challenge for MAS techniques, due to dynamic and static disorder that broaden the resonances of ^{13}C and ^{15}N spectra. Various approaches have been devised to overcome these hurdles: faster spinning rates (*189*), extensive (*190*) and partial deuteration (*191*) coupled with ^{1}H detection (*23*, *192*, *193*), sparse ^{13}C labeling to reduce spectral complexity (*194*) and minimize ^{13}C-^{13}C couplings as a source of line-broadening (*36*) as well as the use of techniques such as RELOAD (*195*) to gain sensitivity . One can boost sensitivity to an even higher degree by Dynamic Nuclear Polarization (DNP) (*196*), opening up this technique to even bigger systems (*197*).

All of the above experiments, however, do not take full advantage of the sparse nuclear spin polarization. To address this issue, we introduced the Dual-Acquisition MAS

strategy (DUMAS) (*33*). This novel strategy allows the concatenation of 2D or 3D pulse sequences into a single experiment and thus potentially combines all the aforementioned advances, boosting the capacity of any NMR spectrometer at least two-fold without the need for sample manipulation or additional hardware. At the heart of this approach is simultaneous cross-polarization from ^{1}H to ^{13}C and ^{15}N, which has also been used in time-shared experiments (*198*, *199*), and long lived ^{15}N longitudinal magnetization (*200*) which can be stored and recalled to perform additional experiments. The DUMAS scheme enables one to acquire two experiments: the first with 100% of the sensitivity with respect to classical pulse sequences, and a second experiment generated from the ^{15}N polarization with typically 80% of the sensitivity(*33*). A well-designed combination of these experiments allows sequential assignment as well as side chain assignment in a single 3D experiment (*24*). Using the initial scheme of the DUMAS experiments, it is possible to decode the coherences in multidimensional NMR experiments to recover the orphan spin operators that are discarded from the classical experiments. This approach that we called MEIOSIS (Multiple Experiments via Orphan SpIn operatorS) enables one to collect up to four multidimensional NMR experiments with a time saving greater than 50% (*201*). See Supplementary Tables 1-3 and Fig 4S.5 and 4S.6 for a detailed comparison of time savings using different sequences on SLN.

In this article, we use POE both in O-ssNMR and MAS spectroscopy to determine the structural topology of sarcolipin, a 3.8 kDa single transmembrane regulator of the sarco(endo)plasmic reticulum Ca^{2+}-ATPase (SERCA) (*67*, *164*). The traditional approach to solve membrane protein structure by ssNMR would involve the following experimental steps before structure calculation: a) Obtaining preliminary 2D spectra to optimize elements in the pulse sequence such as DARR mixing times, indirect evolution times as well as the determining the relative sensitivity and resolution attainable in each dimension, b) Obtaining 3D experiments based on the knowledge gained from the 2D experiments to sequentially assign the protein and c) complementing these secondary structure restraints obtained from MAS-ssNMR with orientation restraints on the backbone amide residues from O-ssNMR. We show the utility of DUMAS and MEIOSIS

in combining multiple experiments to reduce experimental time, so one can simultaneously optimize mixing times, indirect evolution times as well as make decisions about which 3D experiments have the best chance of giving a complete sequential assignment. We also show the use of complementary 3D experiments simultaneously acquired to sequentially assign the protein. Finally we show the tremendous time savings that can be obtained by using the sensitivity enhanced versions of 3D O-ssNMR pulse sequences which give the complete set of orientation restraints on the protein backbone, viz. ^{15}N and ^{1}H anisotropic chemical shifts and ^{15}N-^{1}H dipolar couplings. The individual restraints (anisotropic and isotropic) obtained exclusively by these solid state NMR approaches are then combined in a manner analogous to the previously described hybrid approach (*149*, *175*) using an improved algorithm to converge to a structure ensemble with sub-angstrom precision.

Experimental methods

Protein expression, purification and sample preparation: SLN was over-expressed in *E. coli* bacteria fused to a maltose binding protein (MBP), cleaved, and purified as described earlier (*166*, *167*). Recombinant SLN was purified using reverse-phase HPLC. The fractions containing the protein were lyophilized and used for all solid state NMR experiments. The protein concentration was assessed using UV spectrophotometry using absorption at 280 nm (ε=10,300 M^{-1} cm^{-1}) as well as SDS-PAGE gels using densitometry. For the bicelle preparations, approximately 3.5mg SLN was dissolved in 6.7mg D6PC in 20mM HEPES/100mM NaCl buffer at pH 7.0 and then added to 31mg 4:1 DMPC/POPC vesicles suspension. After several freeze thaw cycles, the bicellar phases were formed and transferred to a cylindrical sample holder. For MAS preparations, 2.2mg of uniformly-[^{13}C,^{15}N]-SLN was reconstituted in DPC micelles and added to 15mg deuterated DMPC lipids dissolved in DPC micelles. The detergent was removed by incubating the solution with Biobeads SM2 (30:1 ratio with the detergent) for 3h at room temperature. The protein-lipid vesicles were collected as a pellet by

centrifugation at 200,000xg at 4˚C for 1 hour and packed in a 3.2mm MAS rotor for NMR experiments without further treatment.

NMR spectroscopy

O-ssNMR Experiments: Experiments on bicelle preparations were carried out on a 16.85T VNMRS Spectrometer with a low-E bicelle probe built by the RF Program at NHMFL, Tallahassee, FL (*22*). Temperature was maintained constant at 298.15 K and bicelle alignment was confirmed by a ^{31}P spectrum. After initial optimization, the 3D-SE-PISEMAI-HETCOR experiment **(**Fig 4.1A**)** was performed with 80 transients for each of the 20 t_1 (^{1}H-^{15}N-DC dimension, evolution time of 2.4ms) and 15 t_2 (^{1}H-CS dimension, evolution time of 1.13ms). A cross polarization time of 1000 μs, direct dimension acquisition time of 5ms, and a recycle delay of 3s were used in all experiments. A 50-70Hz Lorentz-to-Gauss apodization was used in the direct dimension and a 100Hz Gaussian apodization was used in the indirect dimensions. The matrix size before Fourier transformation was 8192 x 256 x 256.

MAS-ssNMR Experiments: MAS experiments on SLN in lipid vesicles were carried out on either a 14.09T or a 16.85T VNMRS Spectrometer with a 3.2mm BioMAS™ probe (Agilent Technologies) at a spinning speed of 10.0kHz and a temperature of 277.15 K. Two-dimensional MAS-ssNMR experiments were carried out by combining ^{13}C-^{13}C DARR, CA(N)CO, NCO and N(CA)CX experiments into a single 2D experiment using the MEIOSIS (Multiple Experiments via Orphan Spin Operators) strategy **(**Fig 4.1B**)** (*201*). Simultaneous cross-polarization from ^{1}H to ^{13}C and ^{15}N was obtained using a contact time of 300μs, with the RF power of ^{15}N and ^{13}C channels set to 35kHz and ^{1}H RF power optimized to achieve the n=2 side-band matching condition (59kHz). The phase of ^{15}N spinlock during NCA transfer is altered between +x and –x and the resultant data is stored in separate files. Sum and difference of the two data sets with phases x and –x respectively gives DARR and N(CA)CX for the first acquisition, and NCO and CA(N)CO for the second acquisition. Fig S4.3 and Fig S4.4 show the dependence of the contact time for the first SPECIFIC-CP step on the distribution of polarization amongst

different pathways. It was found that 3000μs was the optimal contact time, as it gave the maximum NCα transfer for both N(CA)CX and CA(N)CO experiments. As with a microcrystalline preparation of ubiquitin (*201*), we found that at this contact time, 54% residual polarization is left on ^{13}C (to be used for a ^{13}C-^{13}C DARR experiment) and 34% residual polarization is left on ^{15}N (to be used for a NCO experiment).

The ^{13}C-edited experiments (DARR and CA(N)CO) were acquired with a dwell time of 32μs for 128 indirect points (t1 evolution of 4.096ms) while the ^{15}N-edited experiments were acquired with a dwell time of 320μs for 16 indirect points (t1 evolution of 4.8ms). Acquisition time of 15ms and recycle delay of 2s was used. 64 transients were used for each t1 increment. Due to the reduced spectral width in the ^{15}N dimension, the ^{15}N-edited experiments can be acquired eight times along with a single acquisition of ^{13}C-edited experiments. The number of transients for the NCO and N(CA)CX experiments thus becomes 512 (64 x 8). We acquired two independent experiments at the mixing times of 10ms and 50ms during the DARR transfer. As this transfer does not affect the NCO and CA(N)CO experiments, a further boost in sensitivity is obtained by adding these experiments, giving the total number of transients for NCO and CA(N)CO as 1024 and 128, respectively. As these are the least sensitive amongst the four concatenated experiments (Fig S4.3), this design allowed us to boost its sensitivity by repetition, even while optimizing the other experiments. Thus, in the end, we had a total of 6 spectra from 2 separate experiments – ^{13}C-^{13}C DARR with 2 different mixing times (with 64 transients each), N(CA)CX with 2 different mixing times (with 512 transients each), CA(N)CO (128 transients) and NCO (1024 transients). Note that the traditional approach would have allowed the recording of only 2 of these 6 experiments in the same time.

3D-DUMAS-ssNMR: To assign the backbone and side chain atoms, we performed the 3D-DUMAS-NCACX-CANCO experiment (Fig 4.1C) at 277.15 K and 10.0 kHz MAS spinning. The t1 dimensions for both experiments were co-evolved with a dwell time of 150μs for the ^{13}C-dimension (CANCO) and 300μs for the ^{15}N-dimension (NCACX). 16 t1 points were obtained, giving a total of 2.4ms evolution for ^{13}C and 4.8ms evolution for ^{15}N respectively. Bidirectional cross polarization (*24*) from $^{13}C\alpha$ to ^{15}N (CANCO) and

^{15}N to ^{13}Cα (NCACX) was achieved with a contact time of 3ms at RF field strength of 25 kHz (5.ω_r/2) on ^{15}N, and a ^{13}C RF amplitude of 15 (3.ω_r/2) and 35 (7.ω_r/2) kHz for Cα and CO transfer respectively.^{15}N magnetization was stored along the z-direction with a 90˚ pulse after the t1 evolution periods. ^{13}C-dimension (NCACX) was then evolved, followed by a 10ms DARR mixing period and finally detected (NCACX) with a 20ms acquisition time. After this acquisition, the ^{15}N magnetization was brought to the transverse plane with another 90˚ pulse and evolved (CANCO). Magnetization was then transferred to ^{13}CO with a 3ms contact time. The second detection of the ^{13}C dimension (CANCO) was again carried out with an acquisition time of 20ms. The t2 dimensions were thus evolved independently for both experiments with 16 points each, giving a ^{15}N (CANCO) evolution time of 4.8ms and ^{13}C (NCACX) evolution time of 2.4ms. 512 transients were co-added for each t1 and t2 points. A recycle delay of 2 sec was used.

The ^{13}C-dimension was referenced externally with adamantane at 40.48ppm and the ^{15}N dimension was referenced indirectly from the ^{13}C-dimension. All spectra were processed with NMRPipe (*169*) and analyzed with Sparky (*202*). A Lorentz-to-Gauss apodization of 60-80Hz was used in the direct and indirect dimensions. The matrix size before Fourier transformation was 16384 X 512 X 512.

Structure calculations

As the experiments were performed in lipid bicelles with the bicelle-director perpendicular to the external magnetic field, the ^{15}N average isotropic chemical shift of 120ppm and ^{1}H isotropic chemical shift of 8.1ppm were subtracted from each observed anisotropic chemical shift and scaled by 2.5 to obtain the input restraints to obtain the input for structure calculations. Observed dipolar couplings were also scaled by 2.5 to obtain the necessary restraints. This factor of 2.5 is a combination of the scaling of anisotropic parameters by 2 in the parallel orientation and a scaling factor of 1.25 to account for bicelle motions (*132*). Restraints were incorporated with an associated error of ±5ppm for ^{15}N chemical shifts, ±1.5ppm for ^{1}H chemical shifts and ±0.5kHz for dipolar couplings. Dihedral angle restraints from MAS-ssNMR were calculated using the

isotropic chemical shifts of Cα, Cβ, C' and N (amide) atoms as an input for TALOS+ (*203*) and implemented with an error of ±30˚.

All oriented ssNMR restraints (anisotropic chemical shifts for amide ^{15}N and amide ^{1}H and ^{15}N-^{1}H dipolar couplings) and MAS-ssNMR restraints (dihedral restraints from TALOS) were combined in a single energy function along with potentials corresponding to standard peptide geometry ($E_{chem} = E_{bond} + E_{angle} + E_{improper} + E_{vdW}$) (*204*). In addition, hydrogen bonds between the carbonyl oxygen and amide proton of {i} and {i+4} residues were implemented for the transmembrane segment. Orientation restraints were implemented with flat-well harmonic potentials using csaPot and rdcPot modules from XPLOR-NIH (version 2.29). These inbuilt C++ based modules allow for a faster calculation of structure than the PYTHON based modules (*148*) we previously used (*149*) for the structure determination. The ^{15}N tensor was defined with the requisite parameters in XPLOR-NIH with the following traceless CSA tensor components: σ11=55.3ppm, σ22=-97.6ppm, σ33=43.3ppm, β= -17˚ and γ=0˚. Similarly, ^{1}H traceless tensor components were defined with σ11 = 6.3 ppm, σ22 = 1.3ppm, σ33 = -7.6ppm, β = 97˚ and γ = 0˚(*205*).

The hybrid energy function ($E_{O\text{-}ssNMR,}$ $E_{MAS\text{-}ssNMR}$ and E_{chem}) was minimized using a simulated annealing protocol in the torsion angle space. Starting from an extended conformation of SLN, we carried out simulated annealing after an initial equilibration step at 6000K for 10ps. The temperature was decreased in steps of 5 K with a 0.5 ps time step to reach a final temperature of 10 K. A knowledge based E_z-potential (*206*) was implemented as this stage to insert SLN into a virtual membrane bilayer. The structure was then equilibrated at 10 K for 20 ps and subjected to Powell Minimization in Cartesian space. Of 200 structures generated, 10 lowest energy structures were selected for simulated annealing in the Cartesian space to relax local geometries. ^{1}H-CSA restraints were included at this stage. After a 10ps equilibration at 300K, the temperature was reduced to 5K in steps of 2.5K, with 0.5ps simulation at each step. E_z-potential was again implemented and a final equilibration at 5K for 20ps followed by Powell minimization was carried out to give the final structure. One hundred structures were

generated and the ten lowest energy conformers were selected for further analysis. The convergence of the lowest energy structures was determined by aligning the projections of each of the structures on the XY plane (*149*). The RMSD of each conformer from the average structure was calculated without further manipulation of the coordinates in order to maintain the topology calculated from anisotropic NMR parameters. The tilt angle (with respect to the bilayer normal) and rotation angle (with respect to the Cα atom of residue R6) were calculated by aligning a model 20-residue alpha helix with the residues 14-28. Quality of the final structure ensemble was validated by ProCheck (*207*) and MolProbity (*208*), as well as the convergence of R-values for individual orientation restraints.

Results

Magnetically aligned bicelle samples give resolved spectra with a sensitivity and resolution higher than mechanically aligned samples. The latter combined with the ease of sample preparation, better hydration, pH control and sample stability makes bicelles an excellent membrane mimetic for O-ssNMR experiments (*103*, *175*). This allows highly sensitive samples to be prepared for 3-dimensional spectroscopy. Fig S4.1 shows a typical 1D spectrum after initial optimization of CP conditions. For SLN, these preparations give 2D SLF spectra with remarkable resolution and a distinct PISA-wheel pattern (*39*, *173*). All these improvements make it possible to acquire 3D experiments with the sensitivity enhancement pulse sequences. Fig 4.2A shows strip plots from the 3D-SE-PISEMAI-HETCOR experiment. All of the resonances belonging to the transmembrane domain of SLN are present and well resolved, with characteristic oscillatory patterns (*110, 150*) evident for the chemical shifts and the dipolar couplings. We have previously assigned the 2D SE-PISEMA spectrum for SLN in these lipids using a 3D-SE-PISEMA-PDSD experiment that allowed for a sequential assignment using ^{15}N-^{15}N correlations established by proton driven spin diffusion (*39*). This allowed a straightforward transfer of the assignment to the resonances observed in the 3D SE-

PISEMAI-HETCOR experiment. The high quality of the spectrum, with linewidths for ^{15}N-CS of ~150Hz, ^{1}H-CS of ~800-1000 Hz and the ^{15}N-^{1}H DC of ~100Hz allowed us to obtain the set of orientation restraints that completely describe the backbone topology.

For a rapid screen to determine the relative dispersion attainable in each dimension, as well as optimizing mixing times for the DARR element (*209*) in the pulse sequence, we used the 2D-MEIOSIS experiment. Fig 4.3 shows a variant of this experiment, i.e. MEIOSIS-(DARR-CA(N)CO-NCO-N(CA)CX), in which the four 2D spectra are obtained simultaneously within a single experiment. Although several peaks are resolved and residue type assignments are easily obtained from these experiments, they give only an ambiguous assignment. The comparatively low resolution in the 2D spectra is a direct result of fast T2 relaxation, which is also observed for other small membrane embedded proteins (*210*), and underscores the importance of 3D experiments to assign these proteins. In the N(CA)CX obtained at 10ms mixing time, it is possible to identify several intense correlations, indicating that the mixing period is sufficient to transfer the polarization from the backbone to the side chains. At a 10ms mixing time, the N(CA)CX spectrum shows several Cβ and C' resonances. At a 50ms mixing time, the Cβ and possibly the other side chain peaks increase in intensity at the expense of both C' and Cα. Our assignment strategy relies on obtaining information on residue type using statistically predicted chemical shifts and connecting these residues via a 'backbone-walk'. Based on this screening, we concluded that the DUMAS-CANCO/NCACX pulse sequence with a 10ms mixing time during the DARR transfer in NCACX is optimal for assigning SLN, as it would give information on the residue type in the NCACX spectrum and also allow a simultaneous main-chain walk via the common carbonyl resonance of the {i} and {i+1} spin systems. A mixing time of 10ms was deemed optimal as longer mixing times decreased the intensity of the C' resonances. Therefore, we acquired two 3D experiments simultaneously using the 3D-DUMAS-CANCO/NCACX pulse sequence, with a 10ms mixing time for the NCACX spectrum during ^{13}C-^{13}C DARR transfer. After assignment of a majority of residue types in the transmembrane segment based on the statistical Cα and Cβ chemical shifts obtained from the 2D and the 3D spectra, we sequentially

assigned the transmembrane segment from residue E7 to V26 by the classical 'main chain walk', aligning the carbonyl chemical shifts for {i} and {i+1} residues. This assignment was aided by relatively high sequence variability in the SLN transmembrane domain, which has threonine, methionine and tryptophan residues in addition to the hydrophobic leucine, isoleucine and valine residues frequently found in TM domains. The leucine region of the spectrum (~56ppm) suffers from severe overlap of resonance. However, with resolution in the carbonyl region of the spectrum, we were also able to assign these residues. Residues N4-R6 which are known to undergo conformational dynamics, were not assigned, possibly due to inefficient cross-polarization for these residues. The terminal residues M1-I3 and Y31 were assigned in a refocused-INEPT experiment at 298.15K (Fig S4.2).

Fig. 4.5A shows the ensembles of the SLN conformers obtained. The high precision of the ensemble (backbone, incl. H^N + Cβ RMSD ~0.44 Å) is also reflected in low energies for all structural restraints. The global as well as the individual R-values for all orientation restraints are converged below 1 (Fig. 4.5 E-G), indicating a good agreement between the calculated structures and the experimental O-ssNMR data. Table 4.1 summarizes the structural statistics for these calculations. The hybrid NMR ensemble shows disordered N- and C- termini in agreement with the solution NMR ensemble obtained in DPC micelles (*162, 163*). In fact, experiments utilizing cross polarization both in bicelles and lipid bilayers are unable to detect the resonances corresponding to residues 1-3 and 31. These were assigned using the refocused-INEPT experiment at 298K (Fig S4.3). The resonances corresponding to residues 29-31 detected by SE-PISEMA experiments in aligned bicelles show dipolar couplings that are averaged by the substantial motions in these segments and hence were not included in the final structure calculations. For the most structured residues (Residues 6-28), hybrid NMR ensemble shows a higher precision than the corresponding solution NMR ensemble (PDB Code: 1JDM). The topology is converged to a well-defined minimum in the conformational space. The tilt angle for SLN with respect to the bilayer normal was found to be 24±1˚ and the rotation angle was 57±5˚. The indole ring of W23 is oriented with its plane

parallel to the bilayer normal, with the N-H bond vector oriented in the direction of the C-terminal bilayer interface, possibly making contact with the phosphate head groups. Along with W23, the conserved residues R6, located near the cytosolic N-terminus, and R27, near the lumenal C-terminus, anchor SLN to the lipid membrane, modulating the tilt and rotation angles which seem to be only minimally affected in the different membrane mimetic systems (*39*). The NMR structural ensembles determined by the hybrid method are in good agreement with molecular dynamics simulations (*172*) which show a similar orientation of the indole side chain of W23, and a previous oriented solid state NMR study (*90*) carried out mechanically aligned DOPC/DOPE bilayers, which shows a similar the tilt angle of ~23˚ with respect to the bilayer.

Discussion

While multidimensional MAS-ssNMR techniques are mature for structure determination of large systems, their application to membrane proteins is limited by the sensitivity and resolution that can be attained in these systems. Obtaining complete resolution is often not possible without 3D experiments, which take a long time due to the poor sensitivity of these systems. The DUMAS strategy allowed us to substantially reduce experimental time as compared with traditional MAS-ssNMR pulse sequences. The initial experiments with MEIOSIS allowed the determination of parameters, such as the appropriate mixing time, that were important to set up the 3-dimensional experiments for assignments. These initial experiments also allowed us to determine the best possible experimental approach to assign the protein based on relative resolution attainable in each dimension. The DUMAS-CANCO/NCACX experiment allowed us to assign a majority of the protein sequentially as the experiment combines the complementary pulse sequence into a single experiment. Moreover, the simultaneous acquisition of both the experiments allowed the data to be fairly compared without the need for concern regarding sample stability or correction factors.

Compared to MAS-ssNMR, multidimensional O-ssNMR spectroscopy is still in its infancy, in spite of the fact that the number of membrane protein structures being solved by this technique is greater. Sensitivity gains obtained from the 3D-SE-PISEMAI-HETCOR are a substantial leap forward in obtaining complete resolution for these studies. It must be noted here that the resolution of the structure depends primarily on the O-ssNMR data, as the secondary structure obtained from MAS-ssNMR experiments contains no information on the topological parameters of tilt and rotation angle. As such, the O-ssNMR experiments described herein are indispensable in order to characterize the structure of membrane proteins precisely. TALOS based dihedral angle restraints obtained from MAS-ssNMR are a perfect complement to these orientation restraints from O-ssNMR and help convergence of the structure ensemble in spite of inherent degeneracy in the observed values of dipolar couplings and anisotropic chemical shifts.

In the past these MAS-ssNMR and O-ssNMR techniques were thought to be mutually exclusive and most of the researchers used either MAS or O-ssNMR to obtain de novo structure determination. Recent developments of structural biology emphasize the use of multiple techniques to substantiate biological and structural data (*178, 179*). In this spirit, we combined MAS-ssNMR and O-ssNMR restraints into a unique refinement protocol. The idea to combine these techniques is similar to solution NMR, where distance and torsion angle restraints are energy minimized together with residual dipolar couplings to obtain high-resolution structures and reciprocal orientations of protein domains. While some concerns can be raised regarding the compatibility of solution NMR restraints in micelles, which can also serve as complements to O-ssNMR restraints, the agreement between MAS and O-ssNMR data stems from the similarity between the two membrane mimicking environments.

Conclusions

We show here that the complete set of high resolution restraints for both MAS-ssNMR and O-ssNMR can be conveniently obtained for membrane proteins using POE for both

oriented and MAS-ssNMR spectroscopy. The combination of structural and topological restraints from these techniques into a hybrid NMR calculation approach makes it possible to determine the high resolution structure and topology of membrane proteins. Although we anticipate that POE experiments will have the biggest impact on data acquisition of membrane proteins, they are universally applicable to other biomacromolecular systems.

Table 4.1: Summary of Structure Ensemble Statistics

RMSD from MAS NMR Restraints	
NH-C(O) hydrogen bond, Å	0.052 ± 0.004
Dihedral Angles (TALOS)	0.000 ± 0.000
PISEMA R-factors	
^{15}N CSA	0.5 ± 0.4
^{15}N-^{1}H DC	0.7 ± 0.3
^{1}H CSA	0.3 ± 0.3
RMSD from Idealized Covalent Geometry	
Bond, Å	0.004 ± 0.000
Angle, °	0.60 ± 0.01
Improper angle, °	0.13 ± 0.01
Measure of Structure Quality, %	
Most Favored Region	99 ± 1
Additionally Allowed Region	1 ± 1
Generously Allowed Region	0
Disallowed Region	0
MolProbity® Score	98 ± 2 percentile
Precision of Structures (RMSD for atoms N^{H}+H^{N}+C'+O+Cα+Cβ), Å	
Domain Ib+II (Res 6-28)	0.43
Domain Ib (Res 6-13)	0.44
Domain II (Res 14-28)	0.40
Protein Topology	
Tilt Angle (Res 6-28), °	24 ± 1
Rotation Angle (from R6-Cα), °	55 ± 5
Depth of Insertion (R6-Cα), Å	16.1 ± 0.2

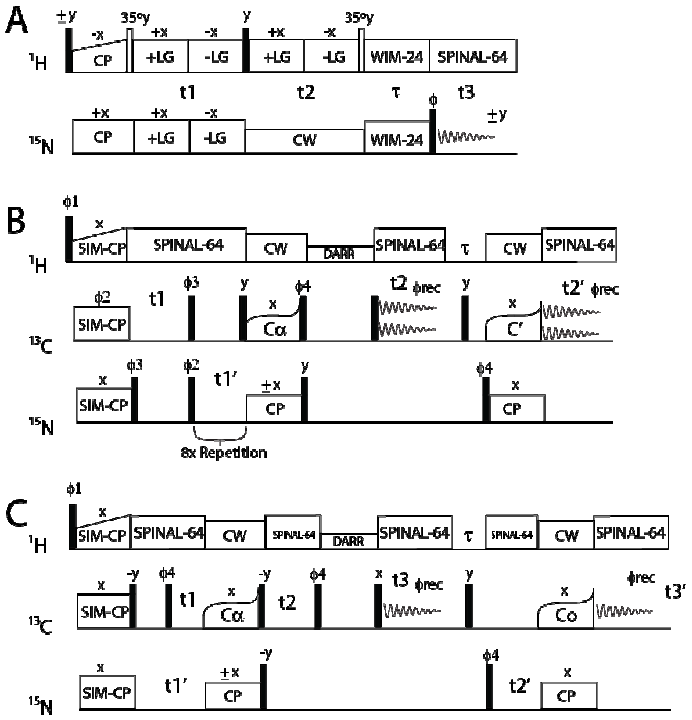

Figure 4.1: Pulse sequences O-ssNMR and MAS-ssNMR experiments

(A) SE-PISEMAI-HETCOR, (B) 2D-MEIOSIS-(DARR/N(CA)CX/CA(N)CO/NCO) with the following phases: □1={y y y y –y –y –y –y}, □2={x x –x –x}$_2$, □3={y –y y –y}$_2$, □4={y y –y –y}, □rec={x –x –x x –x x x –x} and (C) 3D-DUMAS(CANCO/NCACX) with the following phases: □1 = (***y***, −***y***)$_4$, □2 = (***y***, ***y***, ***y***, ***y***, −***y***, −***y***, −***y***, −***y***), □3 = (***x***, ***x***, −***x***, −***x***)$_2$, □rec = (***x***, −***x***, −***x***, ***x***, −***x***, ***x***, ***x***, −***x***). For the pulse sequence in (B), the ^{13}C carrier frequency is placed in the center of the spectral window for DARR (100ppm). SPECIFIC-CP is achieved by a phase modulated pulse on ^{13}C that effectively changes the offset to ^{13}C□ (65ppm) for the first transfer and to C' (178ppm) for the second transfer.

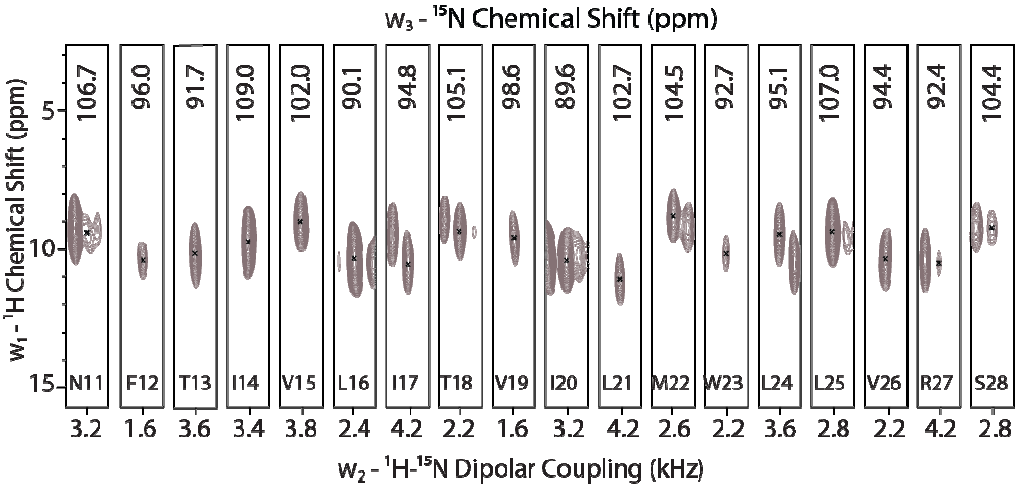

Figure 4.2: Strip plot of the 3D-SE-PISEMAI-HETCOR spectrum

All resonances from N11 to S28 are completely resolved and assigned based on our previous assignment for the 2D spectrum. Average signal is 55σ (range of 24σ-124σ). Spectrum is plotted starting at 18σ with contours progressing by factor of 1.2.

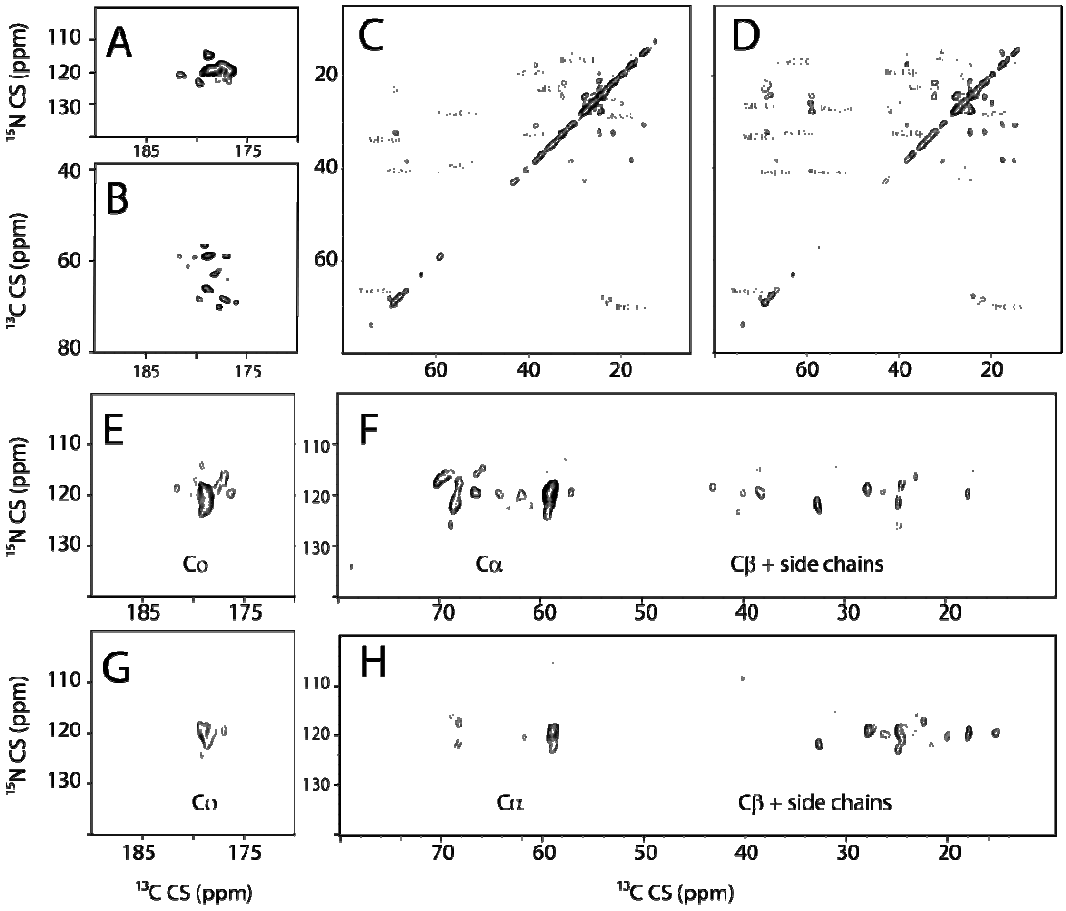

Figure 4.3: Spectra obtained with 2D-MEIOSIS pulse sequence

(A) NCO Correlation, (B) CA(N)CO Correlation. (C) ^{13}C-^{13}C DARR Correlation with 10ms mixing time, (D) ^{13}C-^{13}C DARR Correlation with 10ms mixing time, (E,F) N(CA)CX correlations with 10ms mixing time and (G,H) N(CA)CX correlation with 50ms mixing time. (C) and (D) are plotted starting at 7σ and contours progressing by a factor of 1.1. All other spectra are plotted starting at 6σ with contours progressing by a factor of 1.1.

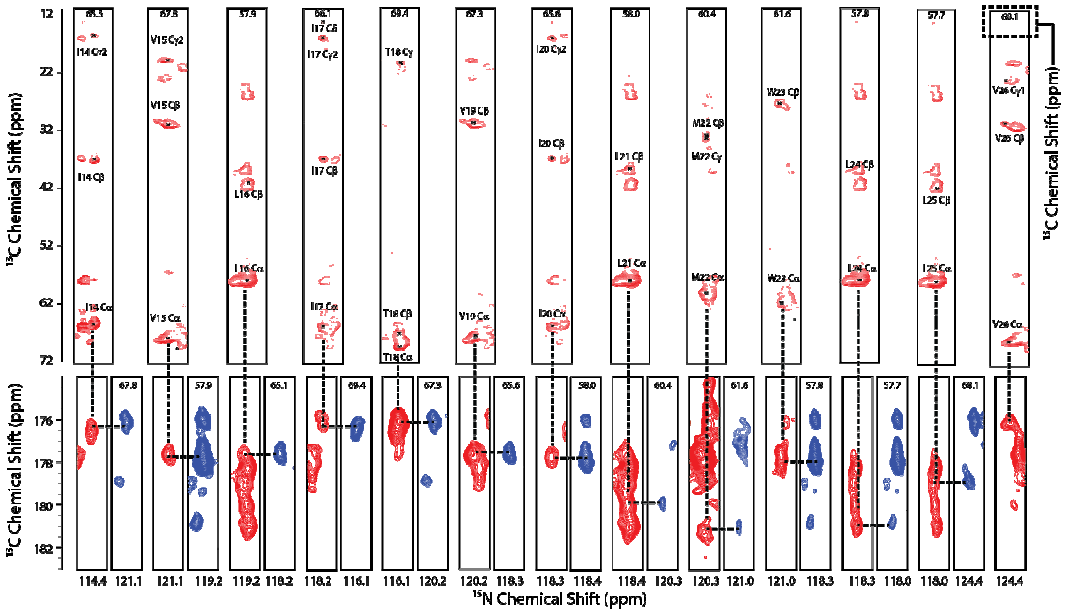

Figure 4.4: Strip plots from the 3D-DUMAS-NCACX/CANCO experiment

NCACX spectrum (red) is plotted starting at 12σ (Cα-Cβ region) and 8.5σ (C' region) and contours progressing by a factor of 1.1. Average signal per residue for NCACX is 28σ (Cα-Cβ region, range 12σ-63σ) and 15σ (carbonyl region, range 9σ to 25σ). CANCO spectrum (blue) is plotted starting at 6σ and contours progressing by a factor 1.1. The average signal for per residue is 10σ (range 7σ to 20σ). The average linewidth in each spectrum is ~1.1 ppm for ^{13}Cα (indirect dimension), 1.0ppm ^{13}C' (direct dimension) and 2.5ppm for ^{15}N (indirect dimension)

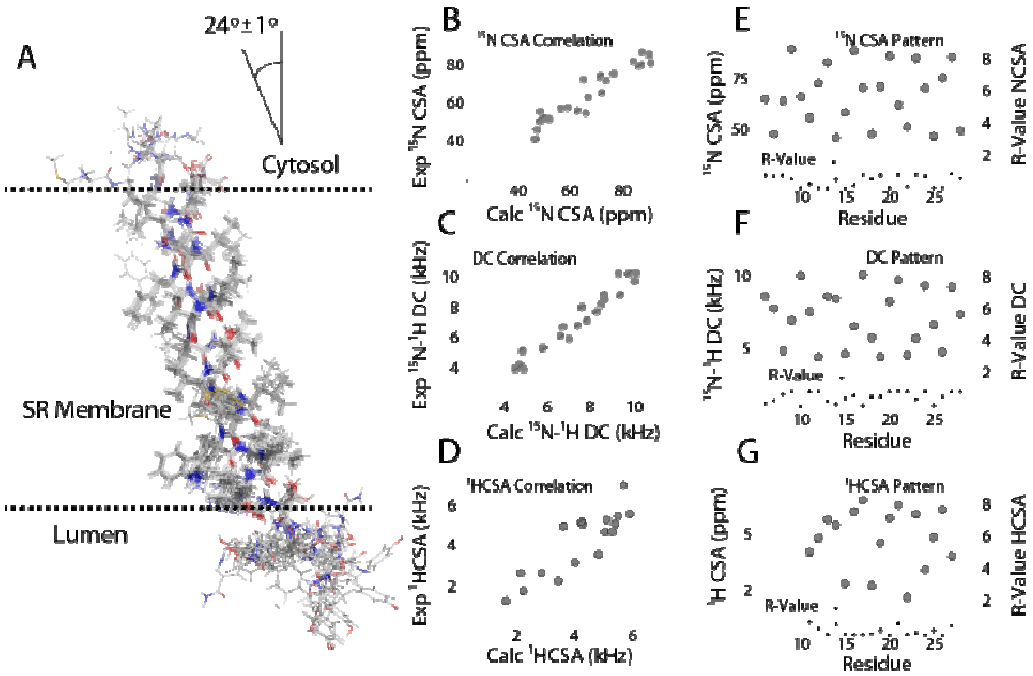

Figure 4.5: Structure ensemble obtained for SLN

(A) Structure ensemble obtained for SLN from the hybrid MAS/O-ssNMR structure calculations (10 lowest energy structures) (B-D) Correlation of experimental O-ssNMR restraints with the back-calculated restraints (E-F) Oscillation patterns for all orientation restraints and the R-values of back-calculated restraints

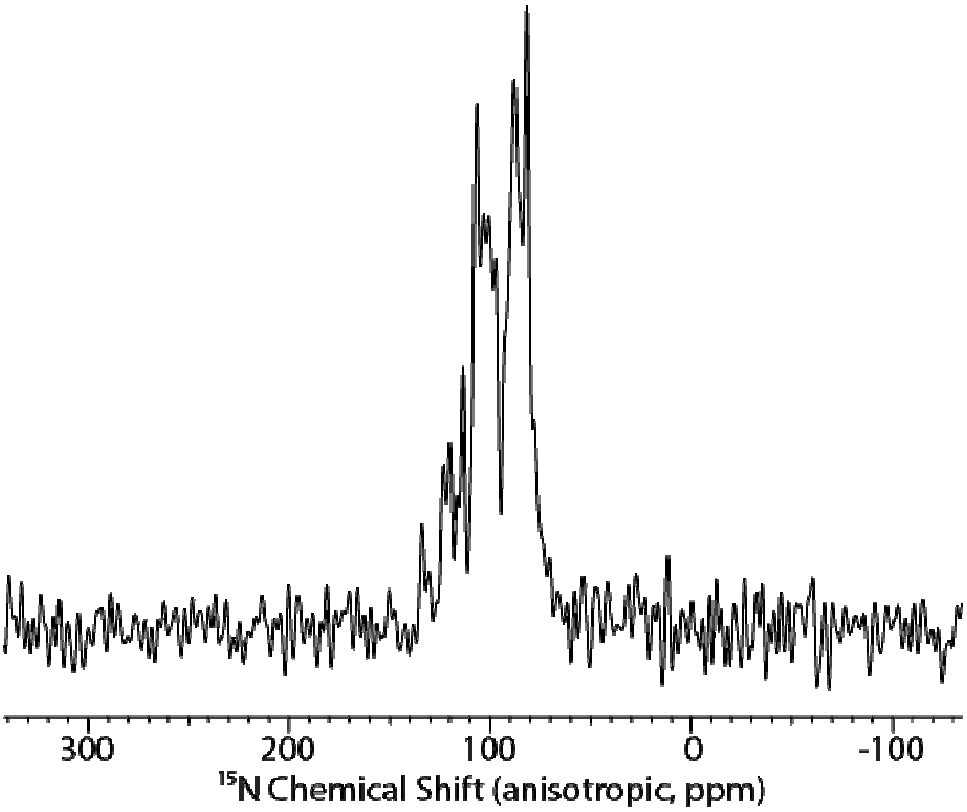

Figure S4.1: 1D-cross polarization ^{15}N spectrum of U^{15}N-SLN

1D-cross polarization ^{15}N spectrum of U^{15}N-SLN in oriented DMPC/POPC/D6PC bicelles (184 transients, Fourier transformed without window function)

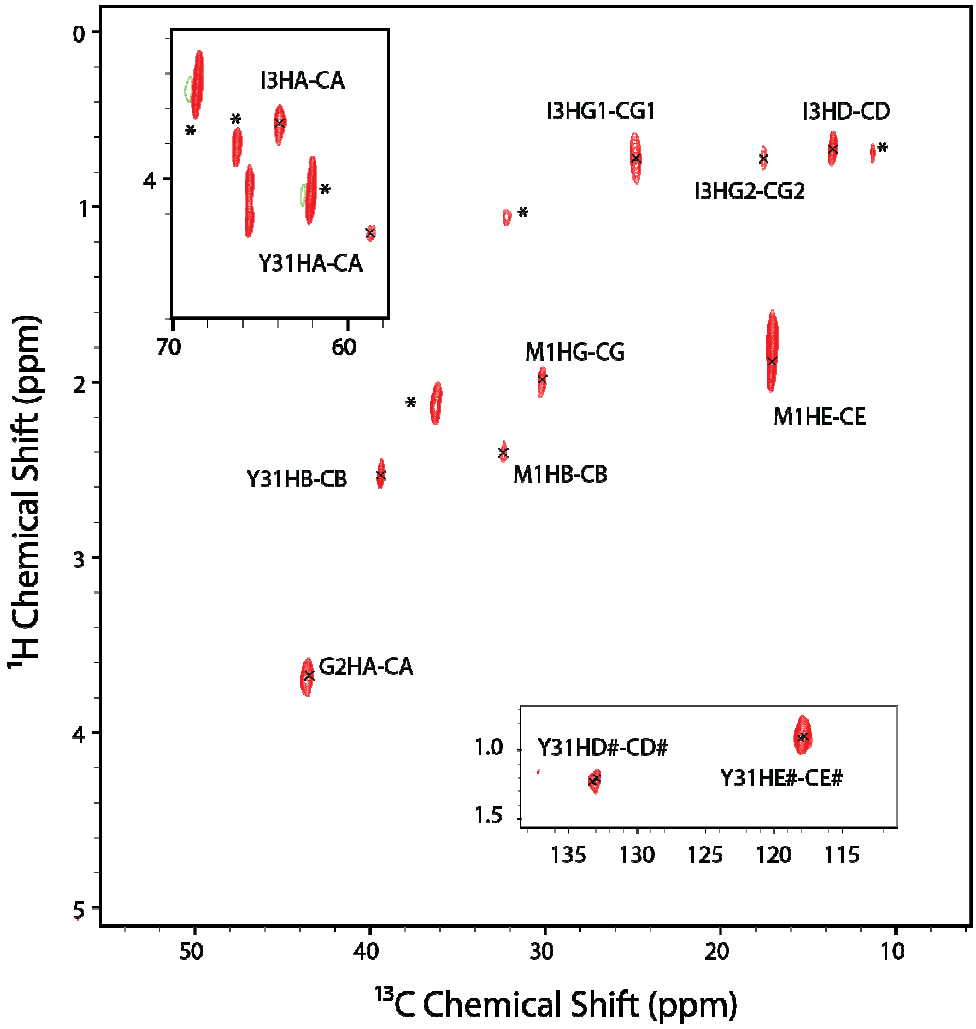

Figure S4.2: Refocused-INEPT spectrum of SLN

Spectrum is acquired at 298.15K. Residues 1-3 and 31 are assigned using this spectrum. Lipid peaks are marked by an asterix.

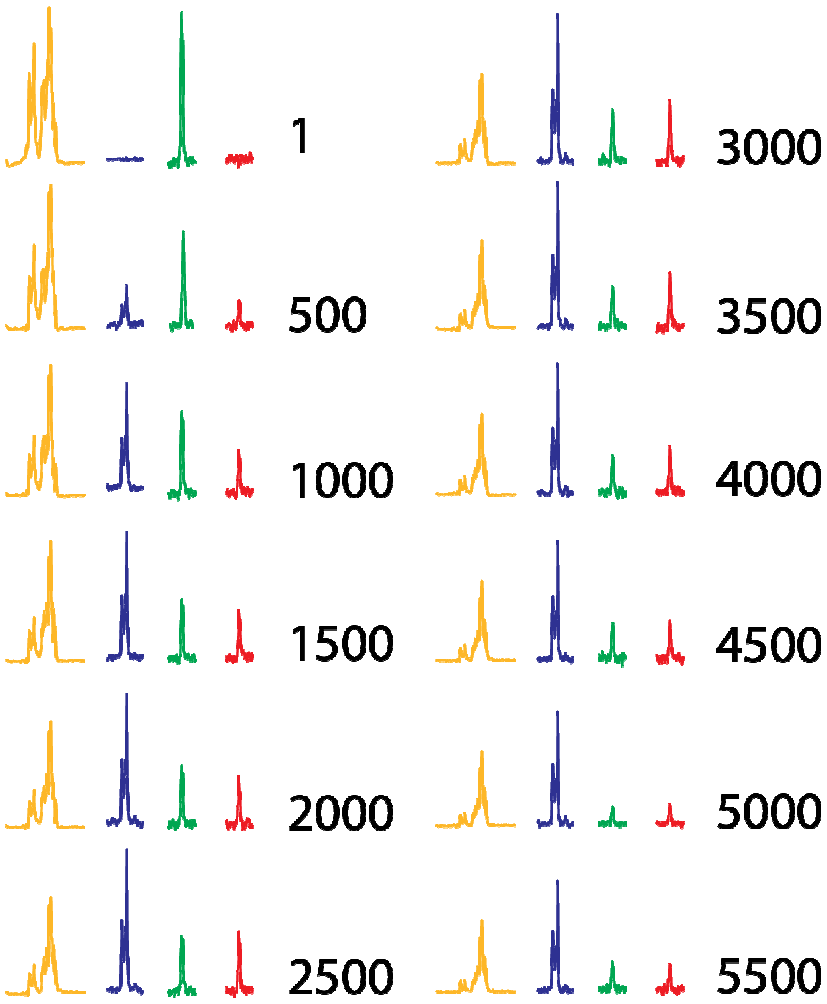

Figure S4.3: Polarization availability for the 4 pathways during MEIOSIS

In orange (lane 1), residual ^{13}C polarization after NCα transfer (used for ^{13}C-^{13}C DARR experiment) in blue (lane 2) ^{15}N polarization after the NCα transfer (used for the N(CA)CX experiment); in green (lane 3), residual ^{15}N polarization after the NCα transfer (used for the NCO experiment) and in red (lane 4), ^{13}C polarization coming via ^{15}N (used in the CA(N)CO experiment).

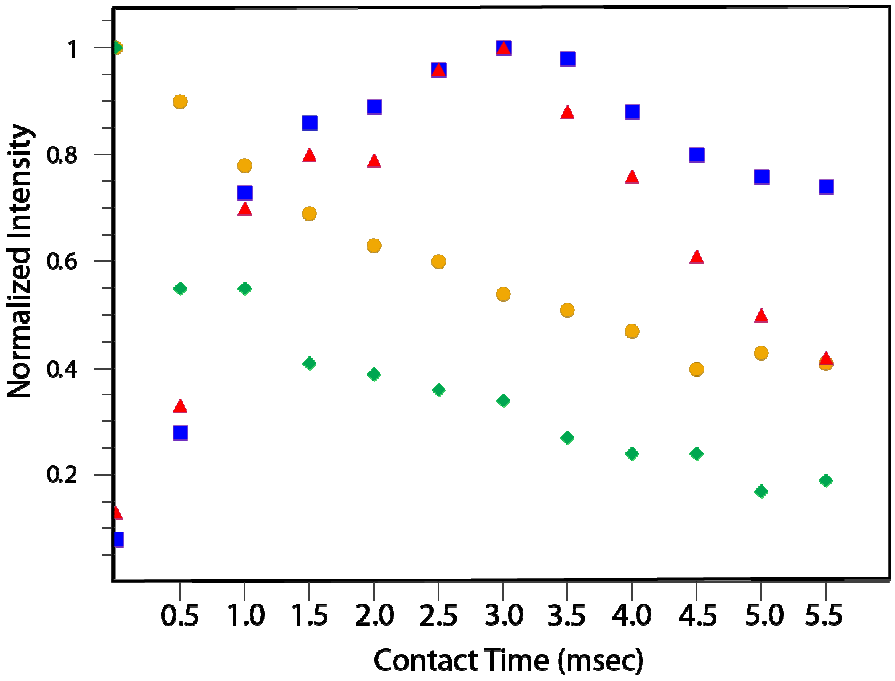

Figure S4.4: Integrated intensities of the spectra for the four pathways in MEIOSIS

This figure is color coded as shown in Figure S4.3. The maximum for ^{15}N-^{13}C and ^{13}C-^{15}N polarization transfer occurs at the contact time of 3.0msec and the relative intensity at this point for residual ^{13}C polarization is 54% and residual ^{15}N polarization is 34%.

Setting up 2D-DUMAS and 2D MEIOSIS Experiments

On the indirect evolution in ^{15}N and ^{13}C dimensions

The evolution time for ^{15}N and ^{13}C are independent for 2D-DUMAS and 2D MEIOSIS and this gives the flexibility to choose any spectral width and any evolution time. For 2D-MEIOSIS, the DARR mixing time for ^{13}C-^{13}C DARR and N(CA)CX time is the same. The t1 evolution time for N(CA)CX and NCO will be the same and ^{13}C-^{13}C DARR and CA(N)CO will be the same.

Keep in mind that spectral width for most uniformly labeled proteins will be 20-25ppm for ^{15}N and 180-200ppm for ^{13}C. Such a difference between spectral widths is, however, not a requirement for any of the POE experiments in MAS-ssNMR. For example, these experiments will work just as well in the case of partially/specifically labeled samples, where the ^{13}C spectral widths will be much smaller than 180-200ppm).

Of consideration here is the choice of setup depending on sample conditions. We discuss the cases below:

1. **High sensitivity for ^{15}N-edited but poor sensitivity for ^{13}C-edited experiment** (typically this would be in situations where DARR mixing > 150ms, partial ^{13}C labeling or ^{13}C-single quantum-double quantum correlation experiment):

In this case one would ideally like to acquire a ^{13}C-edited experiment (eg. DARR) with a large number of scans and a^{15}N-edited experiment (eg. NCA) with shorter number of scans. Let's say, DARR is being acquired with 'x' scans and 'y' indirect increments. While you can run this DARR experiment, you can acquire during the second acquisition:

a. Two independent ^{15}N-edited experiments with y/2 increments each. (eg. NCA with x scans and y/2 increments and NCO with x scans and y/2 increments)
b. NCACX (or NCOCX) with 2 different mixing times, each with x scans and y/2 increments

c. ^{15}N and ^{13}C T_2 relaxation can be quite different in the same protein and this must be accounted for wile setting up t_1 evolution times. As the dwell time for ^{15}N evolution (τ_N) is independent of the dwell time during ^{13}C evolution (τ_C), you can shorten your dwell time ($\tau_N \leq 10\tau_C$ for most proteins), and acquire:
   i. y/6 increments for NCA and then repeat this experiment 6 times (6x scans with t_1 evolution of $y*\tau_N/6$)
   ii. y/4 increments and repeat 4 times (4x scans, $y*\tau_N/4$ t_1 evolution)
   iii. y/3 increments and repeat 3 times (3x scans, $y*\tau_N/3$ t_1 evolution)

d. You are not restricted to the same experiment for the different options in (d). You can acquire NCA, NCACX with different mixing times, NCO or NCOCX with different mixing times all in the same experiment.

2. **High sensitivity for ^{13}C-edited but poor sensitivity for ^{15}N-edited experiment** (typically this would be in situations SPECIFIC-CP transfers are inefficient – membrane proteins, disordered aggregates, etc.):
   a. All of the points in (1) above still apply.
   b. Let's say, the t1 evolution parameters are the same as before. You can reduce the number of transients and do the entire experiment (DARR with x/2 scans and y increments, NCA with x/2 scans and y increments). Then repeat the experiment after changing the ^{13}C-edited block (to a different mixing time, or a different experiment altogether) and keeping the ^{15}N-edited block the same. The multiple ^{15}N-edited experiments thus acquired can be added up later to augment the SNR.
   c. Point (c) from Case 1 will help augment SNR in this case for the ^{15}N edited experiment

The 2D-MEIOSIS experiment will also be beneficial for membrane proteins and fibrils where the NCA transfers are inefficient and N(CA)CX experiment requires a lengthy acquisition. Note that:

a. DARR spectrum is from residual ^{13}C polarization, which is 54%. Hence, if you need to acquire a traditional DARR with the same SNR as that of MEIOSIS-DARR, you would need ~0.25x the experimental time. Also, only the cross-peaks corresponding the transfer of magnetization from side chains to Cα will be observed as the Cα to N transfer occurs before the DARR mixing element.
b. NCO is from residual ^{15}N-magnetization, which is 30% of what one would get if you wanted to obtain an NCO spectrum. So, one would need ~0.09x the experimental time for a conventional NCO with same SNR as that of MEIOSIS-NCO
c. NCA and CA(N)CO are from direct ^{15}N and ^{13}C polarization respectively. The total experimental times need to acquire these spectra independently with the same SNR as that in a MEIOSIS experiment are thus, 0.9x and 1.0x, respectively.
d. Trasseth and co-workers (*25*) described how residual polarization can be used for resonance assignment in combination with selective labeling schemes. In addition to the residual-NCO pathway suggested in this experiment, MEIOSIS provides the CA(N)CO pathway that can be used to supplement such a strategy.

This experiment is ideal if one wants to set up 3D experiments as it will allow a quick determination of relative dispersion in each dimension, choosing the appropriate mixing times as well as help choosing an appropriate 3D experiment that gives the best chance of assigning a majority of the residues. That is why we chose to implement this experiment on SLN before setting up the 3D experiments.

Comparison of DUMAS-DARR-NCA and Conventional DARR and NCA experiments

In the comparison given in Table S4.1 and Fig S4.5, the DUMAS-DARR–NCA is acquired in the following manner:

1. 32 transients co-added for each t1 increment.
2. 128 total increments for ^{13}C giving a total evolution time of 4.1ms
3. 8 experiments of NCA repeated with 16 increments each giving total evolution time of 4.8ms for ^{15}N

Table S4.1: Time savings for DUMAS experiments

Conventional 2D			**2D DUMAS**		
Expt.	Time	Relative SNR	Expt.	Time	Relative SNR
DARR	4.1 hrs	1	DARR	4.1 hrs	1
NCA	4.1 hrs	1	NCA		0.8
	Total Time = 8 hrs			**Total Time = 4.1 hrs**	

Conventional 3D			**3D DUMAS**		
Expt.	Time	Relative SNR	Expt.	Time	Relative SNR
CANCO	12 days*	1	CANCO	12 days	1
NCACX	11 days*	1	NCACX		1
	Total Time = 23 days (*24*)			**Total Time = 11 days**	

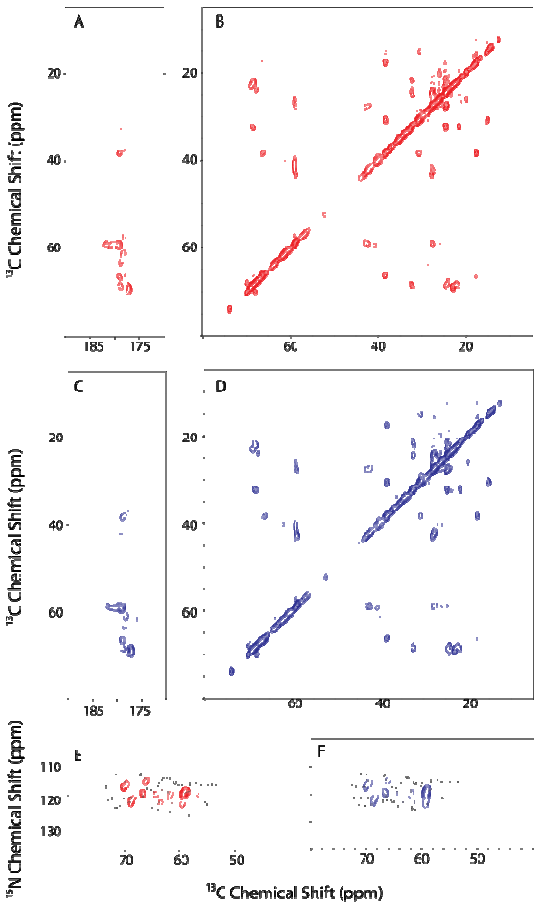

Figure S4.5: Comparison of DUMAS and COnventional 2D experiments

Comparison of spectra acquired using:

(A) DUMAS-DARR (C' region)

(B) DUMAS-DARR (Cα-Cβ region)

(C) Conventional-DARR (C' region)

(D) Conventional DARR (Cα–Cβ region)

(E) DUMAS-NCA

(F) Conventional NCA

Comparison of MEIOSIS-(DARR-NCACX-CANCO-NCO) with conventional experiments

In the comparison given in Figure S4.6 and Table S4.2, the experimental setup was as follows:

1. 64 transients for each t1 increment (due to an 8 step-phase cycle, this corresponds to 128 transients when compared to conventional experiment which is generally obtained with only a 4-step phase cycle)
2. 128 t1 increments, giving ^{13}C evolution time of 4.1ms
4. 8 experiments of NCA repeated with 16 increments each giving total evolution time of 4.8ms for ^{15}N

Table S4.2: Time Savings for 2D-MEIOSIS experiments

Conventional			**MEIOSOS**		
EXPT	Time (h)	Relative SNR	EXPT	Time (h)	Relative SNR
DARR	2	1	DARR	9.15	1
NCACX	9.15	1	NCACX		0.8
CANCO	1.2	1	CANCO		1
NCO	9.15	1	NCO		0.8
	Total Time 21.2 h			**Total Time 9.15 h**	

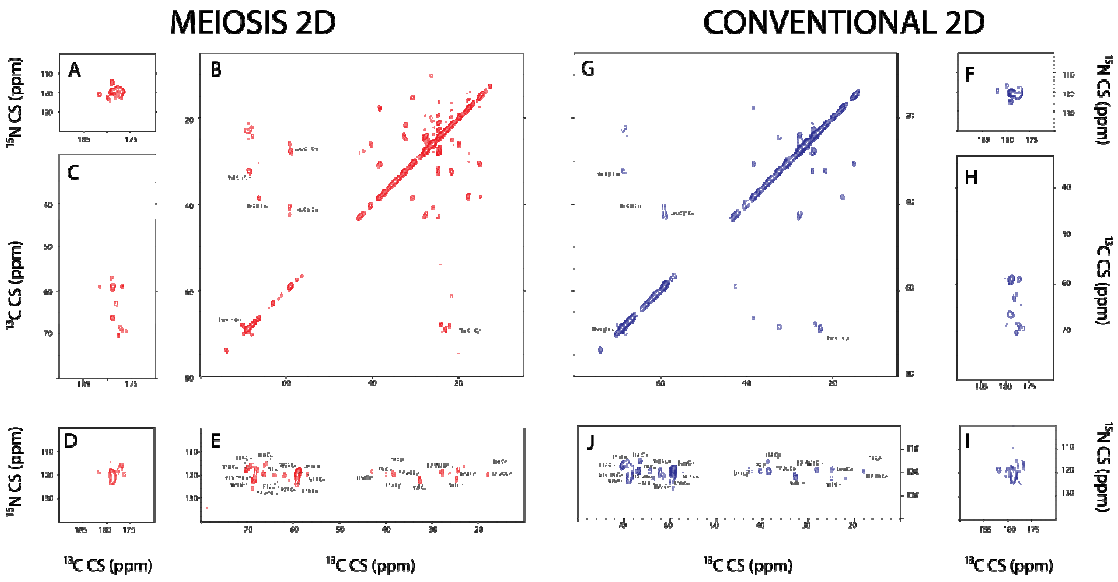

Figure S4.6: Comparison of MEIOSIS and Conventional experiments

Comparison of spectra acquired using:

(A) MEIOISIS-NCO (residual ^{15}N pathway)

(B) MEIOSIS-DARR (residual ^{13}C pathway)

(C) MEIOSIS-CANCO

(D) MEIOSIS-NCACX (C' region)

(E) MEIOSIS-NCACX (Cα-Cβ region)

(F) Conventional-NCO

(G) Conventional -DARR

(H) Conventional -CANCO

(I) Conventional -NCACX (C' region)

(J) Conventional -NCACX (Cα-Cβ region)

A-E are acquired simultaneously using 2D-MEIOSIS (Fig 4.1B in the main text)

Table S4.3: Isotropic Chemical Shift Assignments in Lipid Bilayers

NA=Not Assigned.

Res No	**RES TYPE**	**Cα (ppm)**	**N (ppm)**	**Cβ (ppm)**	**Cγ1 (ppm)**	**C' (ppm)**	**Cγ2 (ppm)**	**Cδ/Cε (ppm)**
1	M	NA	NA	34.4	32.2	NA	NA	19.1
2	G	45.5	NA	NA	NA	NA	NA	
3	I	65.9	NA	NA	26.84	NA	19.6	15.6
4	N	52.7	NA	40.6	NA	NA		
5	T	NA	NA	NA	NA	NA		
6	R	NA	NA	NA	NA	NA		
7	E	61.9	119.1	28.6	38.4	177.5		179
8	L	57.8	118.4	39.5	24.8	177.7		26.9
9	F	63.3	118.6	37.3	NA	178.9		
10	L	58.2	122.3	40	24.8	178.7		26.9
11	N	55.1	118.4	41.5	NA	177.1		
12	F	63.4	118.5	36.4	NA	176.3		
13	T	68.8	115.4	68.8	22.2	177.6		
14	I	65.5	114.4	37.6	NA	176.4	16.6	
15	V	67.9	121.1	31.7	30	177.6	20.8	
16	L	58.1	119.2	39.5	NA	178.3		26.9
17	I	66.1	118.4	37.4	NA	176.2	16.9	14.1
18	T	69.4	116.1	67.1	21.3	176.1		
19	V	67.3	120.2	31.3	30	177.6	20.8	
20	I	65.7	118.3	37.3	NA	177.8		
21	L	58	118.4	39.1	24.8	179.9		26.9
22	M	60.4	120.3	33.4	34	181.1		
23	W	61.6	121	28	NA	178.1		
24	L	57.8	118.3	42.3	24.8	181		26.9
25	L	57.7	118.3	39.6	24.8	179.1		26.9
26	V	68.1	123	31	23.8	176.1		
27	R	60.2	120.2	30.4	NA	175.3		
28	S	61.8	113.2	64.0	NA	NA		
29	Y	60.8	118.3	39.5	NA	NA		
30	Q	59.3	118.6	29.7	NA	NA		
31	Y	60.7	NA	41.4	NA	NA		

Table S4.4: Assignments for Chemical Shift Anisotropy and Dipolar Couplings in Lipid Bicelles. NA= Not Assigned, DO=Shifts scaled by conformational dynamics.

Res No	RES TYPE	NCSA (ppm)	NHDC (kHz)	HCSA (ppm)
1	M	NA	NA	NA
2	G	NA	NA	NA
3	I	NA	NA	NA
4	N	NA	NA	NA
5	T	NA	NA	NA
6	R	56.1	8.6	NA
7	E	57	7.2	NA
8	L	73.8	4	NA
9	F	82.5	6	NA
10	L	64.5	9.8	NA
11	N	58.6	8.1	5
12	F	73.2	4	5.2
13	T	83.4	8.9	4.7
14	I	42.6	8.3	3.6
15	V	59.1	4.3	1.8
16	L	87	6.2	5.1
17	I	75.9	10.3	5.6
18	T	51.8	5.4	2.7
19	V	67	4.1	3.2
20	I	88.2	7.8	5.3
21	L	57.5	10.3	7
22	M	53.1	4.1	1.3
23	W	81	5.4	4.7
24	L	75.3	8.9	2.7
25	L	47.4	6.8	5.1
26	V	76.9	5.2	5.5
27	R	81.6	10.3	2.3
28	S	53.5	6.9	NA
29	Y	DO	DO	NA
30	Q	DO	DO	NA
31	Y	DO	DO	NA

5. Topological allostery architects sarcolipin's regulation of the SR-Ca^{2+}-ATPase

Kaustubh R. Mote, Vitaly V. Vostrikov, Sanjaya K. Sahoo, Alysha Dicke, Allesandro Cembran, Martin Gustavsson, Tata Gopinath, Muthu Periasamy and Gianluigi Veglia

Manuscript in preparation

The coupling of active Ca^{2+} transport into the lumen with ATP hydrolysis in the sarcoplasmic reticulum of muscle cells achieved by the sarco(endo)plasmic reticulum Ca^{2+}-ATPase (SERCA) is disrupted by its interaction with sarcolipin. Futile ATP hydrolysis caused by this disruption is primarily responsible for skeletal muscle based non-shivering thermogenesis. The molecular basis for this is achieved by sarcolipin is however, not understood. Using solid state NMR spectroscopy under fully functional conditions, we show that the topological coupling between transmembrane domains of SERCA and SLN plays a central role in this regulation. We find that the transmembrane topology of sarcolipin is sensitive to the conformational state of SERCA. The transition of SERCA to the catalytically competent Ca^{2+} and nucleotide bound state is accompanied by a large change in the tilt of SLN transmembrane domain. As a penalty for this topological change the transition of SERCA is blunted, thereby reducing Ca^{2+} affinity. Orthogonal cross-linking experiments show how these conformational changes are propagated throughout the catalytic cycle. This mechanism, which we dub *topological allostery*, paves a way to understand this evolutionarily conserved regulatory mechanism, as well as sheds light on the mechanics of the role of this complex in heat generation via non-shivering thermogenesis.

Introduction

SR-membrane calcium ATPases are regulated by peptides encoded by small open reading frames (smORFs) that show evolutionary conservation amongst diverse species ranging from anthropods to mammals (*52*). Mutations and abnormal expression of these peptides is implicated in pathological conditions in humans (*53, 74*). Sarcolipin (SLN) is one such regulator known to interact with and regulate the SERCA1a isoform in skeletal muscle and the SERCA-2a isoform in cardiac atria (*67, 164, 211*). It decreases the rate of Ca^{2+}-dependent ATP hydrolysis and Ca^{2+}-dependent Ca^{2+} transport in vivo and in reconstituted systems (*55, 59, 67*). Consequently, cardiac relaxation is impaired by SLN overexpression in atria and improved in SLN-knockout mice (*68–70*). Another important

aspect of SLN's interaction with SERCA is the increase in heat production (*79*). This was shown to profound effect on heat generation via non-shivering thermogenesis in skeletal muscle (*59, 76*). SLN-knockout mice are unable to maintain core body temperatures and become susceptible to cold-induced hypothermia, irrespective of the presence or absence of the brown adipose tissue (*76*).

The mechanistic details of SERCA function are understood in terms of a catalytic cycle with sequential, reversible steps resulting in exchange of Ca^{2+} from the cytosol with H^{+} from the lumen, against a steep concentration gradient, facilitated by ATP hydrolysis (Fig. 5.1) (*4, 212–216*). The structural changes in SERCA implied by these inter-converting forms are visualized through X-ray crystal structures of the skeletal muscle isoform SERCA1a trapped at several different stages of the transport cycle (*217–221*). Auto-phosphorylation of residue Asp-351 in the cytosolic portions by ATP which triggers large conformational changes in the actuator-domain (A-domain) which is propagated to the transmembrane domain harboring the Ca^{2+} binding sites. This entails a large conformational transition between two major states of SERCA – a high Ca^{2+}-affinity E1-state with the Ca^{2+}-pore open towards the cytosol and a low Ca^{2+}-affinity (and high H^{+}-affinity) E2 form, with the pore open towards the lumen (*221*). The coupled movements of the M1-M2 helices collapse the grove formed by M2,M4,M6 and M9 helices bringing about an opening of the cytosolic Ca^{2+} pathway leading up to the intra-membrane binding sites. This is followed by an upward movement of the M1-M2 helix in response of ATP binding (*219*), closing up of the cytosolic Ca^{2+} entry pathway and opening up of the lumenal pore for Ca^{2+}-occlusion coupled to the dephosphorylation of Asp-351 (*218, 219, 221*). The topology of the transmembrane helices forming this groove is one of the most defining characteristics of the conformational state of SERCA. An open groove is an indicator of the E2 conformation, while a collapsed groove is an indicator of the E1 conformation (*4*). The binding of nucleotide and phosphoryl transfer are tightly coupled to this conformational change, which brings about a coupling between ATP hydrolysis and Ca^{2+} occlusion (*219*).

In agreement with previous mutational (*55*, *67*, *76*) and cross-linking studies (*76*), the crystal structures of SLN bound to SERCA under saturating Mg^{2+} concentrations show that it binds in this very groove (which will henceforth be referred to as the *regulatory groove*) (*56*, *57*). Interestingly, the SERCA's TM domains show only minor rearrangements so as not to fit SLN deep in the regulatory groove. Instead, the structure seems to be a perfect candidate for an intermediate along the E2 to E1 transition. SLN is seen as forming a distorted α-helix, with an average tilt angle of ~40º with respect to the lipid bilayer. A similar conformation of SERCA was also reported in its complex with a super-inhibitory mutant of phospholamban, a homologue of SLN in cardiac muscle (*58*). We confirmed that SERCA accesses similar conformations in presence and absence of SLN using partial labeling of free cysteine sulfhydryl groups in SERCA by ^{13}C-labeled ethyl-methyl thiosulphonate. Cysteine accessibility is sensitive to the conformational state of SERCA, and we were able to define a fingerprint for the E1ATP and E2ATP states of lipid reconstituted SERCA using the DARR experiment in magic angle spinning NMR. Although the presence of SLN bound to shows minor perturbations of the chemical shift for resonances of both these spectra, the overall pattern is consistent with the same conformation of SERCA being accessed in the E1ATP and E2ATP states in the presence of SLN.

Experimental Methods

All lipids used were purchased from Avanti Polar Lipids (Alabaster, AL). Uniformly ^{15}N and uniformly ^{13}C, ^{15}N labeled sarcolipin was purified from *E. coli* using the methods described earlier. Non-labeled SLN was produced using Fmoc-based solid phase peptide synthesis. SERCA1a from rabbit hind-legs was purified into $C_{12}E_8$ detergent using reactive red affinity chromatography.

SERCA was labeled with ^{13}C-EMTS by incubating the enzyme (90nmol at a concentration of 9μM in 0.5% $C_{12}E_8$) with 5-fold excess of the reagent for 2hrs at room temperature. The sample was immediately reconstituted in d_{38}-DMPC by adding the

solubilized lipids to the reaction mixture and incubating with Biobeads-SM2 for 3hrs. The buffer was 20mM HEPES, 50mM KCl, 2mM $MgCl_2$. The pH of the buffer was adjusted to 7.5 and 6.5 for E1 and E2 states respectively. SLN was added to a final molar ration of 1:1.7 with SERCA for the experiments in presence of SLN

For MAS-ssNMR experiments, SERCA (7.5mg, ~70nmol) and U-$^{13}C^{15}N$-SLN (0.34mg, ~70nmol) were co-reconstituted in a 1:1 ratio in 10mg d_{38}-DMPC solubilized in a buffered solution containing in ~30mg C12E8, 20mM HEPES, 50mM KCl, 2mM $MgCl_2$ 0.25mM DDT and 0.5% glycerol and 2mM EGTA at pH 7.0. This was followed by incubation with Biobeads SM2 (30:1 ratio with detergent) for 3 h at room temperature. The protein-vesicle complex was collected after centrifugation at 70,000xg at 4˚C and suspended in 2mL of the same sample buffer with addition of AMPPCP (100μM). It was then further centrifuged at 200,000 x g at 4˚C for 1hr and finally packed into a 3.2mm bioMAS rotor without further treatment. This gave SERCA-SLN complex in the E2ATP state. For experiments in the E1ATP state, Ca^{2+} was added to the same sample to give a 2:1 ratio with SERCA and repacked into the rotor.

For O-ssNMR studies, SERCA (7.5 mg, 70nmol) was reconstituted in 38.6mg DMPC/POPC/DMPE-PEG2000 (4:1:0.01 molar ratio) by first adding the protein to the $C_{12}E_8$ solubilized lipids in a buffered solution containing 20mM HEPES, 50mM KCl, 2mM $MgCl_2$, 0.25mM DDT and 0.5% glycerol at pH 7.0 and subsequently removing the detergent by incubation with Biobeads SM2 (30:1 ratio with detergent) for 3 h at room temperature. The resulting SERCA-lipid vesicle complex was centrifuged at 4˚C at 60,000xg. 0.25mg SLN (70nmol) reconstituted in a buffered solution containing 5.8mg D6PC was added to the SERCA-lipid vesicle pellet and thoroughly mixed by vortexing. Bicelles were formed after several temperature cycles between 0˚C and 25˚C. The final concentration of the SERCA-SLN complex (1:1) was ~450μM with a SERCA to lipid ratio of 1:800. AMPPCP (2mM) and $CaCl_2$ or EGTA (2mM) was added this stage to trap the complex in E1ATP or E2ATP state, respectively. The bicelle solution was then concentrated to 150μL using a 0.5mL spin concentrator with M.W. cutoff of ~10,000 Da and transferred to a cylindrical sample holder for NMR experiments. Based on a

conservative estimate of K_d of 40μM in micelles, more than 80% of sarcolipin is present as bound to the pump under these conditions and thus mainly contribute to the NMR signal. Note than in membranes, this K_d is expected to be higher, giving greater than 95% complex formation. For MAS experiments, the lower lipid to protein ratio essentially give greater than 95% complex formation. Due to high affinity of Mg^{2+} to nucleotide and nucleotide analogs (K_d ~ 50μM), the free Mg^{2+} concentrations in these preparations are expected to be 5-10μM, shifting the equilibrium towards truly Ca^{2+}/Mg^{2+}-free-E2-ATP-SLN and Ca^{2+}-bound-E1-ATP-SLN states.

NMR experiments

MAS-ssNMR experiments were carried out at 298K or 279K on a 16.85T or 14.09T Agilent VNMRS spectrometer with a 3.2mm Bio-MAS^{TM} probe (Agilent Technologies) at a rotor spinning speed of 10000Hz. ^{13}C-^{13}C DARR correlation spectra were acquired with 880 transients for each of the 50 t1 increments (1.54ms evolution) with 50ms mixing time during the DARR element.

O-ssNMR experiments were carried out on with a low-E bicelle probes built by the RF Program at NHMFL, Tallahassee, FL and Revolution NMR. Temperature was maintained constant at 25˚C and bicelle alignment was confirmed by ^{31}P spectra (Fig S1). Typically, SE-PISEMA spectra were acquired with 2000-5000 transients for each of the 16 t1 increments corresponding to the final evolution time of 1.28 ms. Cross polarization time of 1000 μs was used in all experiments. 50 kHz ^{1}H RF was used during FSLG decoupling during t1evolution and 50 kHz SPINAL-64 decoupling was used on ^{1}H during acquisition. A recycle delay of 3 s was used in all the experiments. Total experimental time for each spectrum was ~2-5 days. Spectra were processed in NMRPipe and analyzed using SPARKY.

Results and discussion

The high resolution structure of SLN calculated in the lipid bilayers using oriented ssNMR reveals a tilt angle of 24˚±1˚ with respect to the membrane normal (*29, 39*). This

topology is conserved under different concentrations of Ca^{2+}, nucleotide and even different lipids. This is probably due to stringent restrictions placed on the tilt and rotation angle by the interfacial residues W23, R27, F9 and R6 which anchor the TM domain to lipid head groups. In contrast, SLN bound to SERCA shows remarkably different topology depending on the step of the cycle the pump is trapped in. As in the X-ray structure, SLN showed a large tilt angle of ~40º in the $2Ca^{2+}$-E1-ATP state (Fig 5.1C). The close agreement of topology of SLN by ssNMR measurements performed under dilute, fully functional conditions suggest with the topology observed in the X-ray structure is close to the native state of SLN in the $2Ca^{2+}$-E1-ATP state. In the calcium-free E2-ATP state however, SLN retains a tilt angle of ~24º (Fig. 5.1A). Structure modeling and molecular dynamic simulations in explicit bilayer environment show that SLN does make more intimate contacts with open groove of the pump while conserving its preferred topology in this state. We conclude that the large movement of M1-M2 helix upon transition from E2-like to E1-like state forces SLN to adopt a less preferred, highly tilted topology. Remarkably, the presence of Ca^{2+} alone causes only a minor change in the tilt angle of SLN to ~28º, contrary to the expectation of a collapsed groove and therefore, a large tilt angle, from the X-ray structures in $2Ca^{2+}$E1 state (Fig 5.1B). It is apparent that the transition to an E1-like conformation is delayed in the presence of SLN and is not completed unless nucleotide induced conformational changes force SLN to adopt a more tilted topology. In other words, SLN forms a wedge that interferes with the transition of SERCA from E2-like to E1-like conformation. This manifests as a decreased calcium affinity and K_M for ATP hydrolysis in presence of SLN. In order to get a complete picture of how the topology of SLN is affected by the conformational state of SERCA, we determined the topology of SLN bound to SERCA in the E2P, E2P-ATP as well as the Ca^{2+}E1-ADP-AlF_4 states. As for the E2ATP state, a low tilt angle was observed for both the phosphorylated states, indicating that SLN changes its topology to the preffered orientation of 24º upon phosphorylation (Fig. 5.1 D-E). The Ca^{2+}E1~P:ADP state mimicked by the ADP:AlF_4 crystallizes in a conformational state indistinguishable from the Ca^{2+}E1ATP state. However, proteinase K and cysteine accessibility assays have

shown that the state is more E2-like in solution (*219*). It is proposed that in lipid bilayers, a significant population of the E2-like state is accessed by SERCA as the phosphoryl group is transferred from ATP to Asp351. This is in part, responsible for the coupling between ATP hydrolysis and Ca^{2+}-transport. We see that SLN when bound in to the Ca^{2+}-E1~P:ADP form, is present with a topology similar to the E2-like states. Thus, we show that the topology of SLN is a remarkably sensitive indicator of the topology of the TM helices of SERCA and thus directly reports on the conformational changes occurring from E1 to E2-like states.

The mechanism we propose is inconsistent with the proposed detachment of SLN from the calcium pump at elevated Ca^{2+} concentrations which is posited as a mechanism of loss inhibition at elevated Ca^{2+} concentrations. Evidence for this comes from decreasing crosslinking efficiency between SLN and SERCA at high Ca^{2+} concentrations, which is often explained by detachment of SLN. In order to reconcile our results with these crosslinking studies, we monitored cross-linking between two alternate sites: L8C-SLN to W932C-SERCA and S936C-SERCA. As expected from our model for the Ca^{2+}-E1ATP-SLN state, the cross-linking efficiency was not only immune to high Ca^{2+} concentrations, but shows a small increase (Fig 5.3). A conformation change for SLN resulting in the tilting of the TM helix by ~20º towards the M4 helix is consistent with this result.

How does SLN mediate the increase in heat production by SERCA? In contrast to previously reported measurements (*79*), we show that the heat released per ATP hydrolyzed by SERCA remains constant (8.5 ± 0.5 kcal/mol). The assay technique employed here involved a single injection of ATP up to a final concentration of 300μM and then measuring the total heat released due to complete hydrolysis of the ATP over several hours at the free Ca^{2+} concentration of 4μM. This avoids comparison from different assay techniques that may otherwise bias datasets. We find that irrespective of the conditions explored – presence and absence of SLN, Ca^{2+} ionophore and H^{+} ionophore, the heat released per ATP does not change. What changes is the rate at which

ATP is hydrolyzed. In order to ascertain the effect of SLN on the rate of ATP hydrolysis, we followed ATP hydrolysis by SERCA by ITC as a function of Ca^{2+} concentration (Fig. 5.4). As observed for coupled enzyme assays, we found that SLN decreases both Ca^{2+} affinity and the maximal rate of ATP hydrolysis in presence of Ca^{2+} ionophore. In absence of Ca^{2+} ionophore, SLN still decreases Ca2+ affinity, but the maximal rate of ATP hydrolysis is 2.5 fold higher when compared to SERCA alone.

The surest sign of uncoupled ATP hydrolysis is the increase in heat released per ATP hydrolyzed, as no energy is spent to overcome the high energy barrier for the conformational change from Ca^{2+}E1~P:ADP to Ca^{2+}E2-P:ADP states. This is not the case with SLN. The most likely scenario is that SLN causes increase in uncoupled Ca^{2+} efflux, i.e. transport of Ca^{2+} from the lumen into the cytosol without ATP synthesis. As these observation are true for as small as 1.5 fold excess of SLN over SERCA, such a mechanism will require that SLN increase the slippage of Ca^{2+} *via* SERCA and not by itself.

Conclusion

In conclusion, we have shown the coupled movements of the topology of transmembrane domains of SERCA and SLN is responsible for the observed biological effects of the complex. This mechanism may be viewed as a particularly mild form of 'topological frustration' as described by von Heijne (*222*). The incompatible topologies of transmembrane domains of SERCA and SLN in the E1-like states force SLN to adopt a less preferred, highly tilted topology in order for the catalytic cycle to proceed (Fig 5.5). This hinders calcium binding and calcium occlusion, and manifests as a decrease in Ca^{2+}-affinity in ATP hydrolysis assays.

The heat released per ATP hydrolyzed by SERCA does not change when it is bound to sarcolipin. Instead, SLN seems to increase the rate of slippage via SERCA. *In vivo,* this will manifest as a decrease in the rate of relaxation in the muscle cell. As more ATP

needs to be consumed in order to efficiently remove Ca^{2+} from the cytosol, an increase in the energy expenditure is observed.

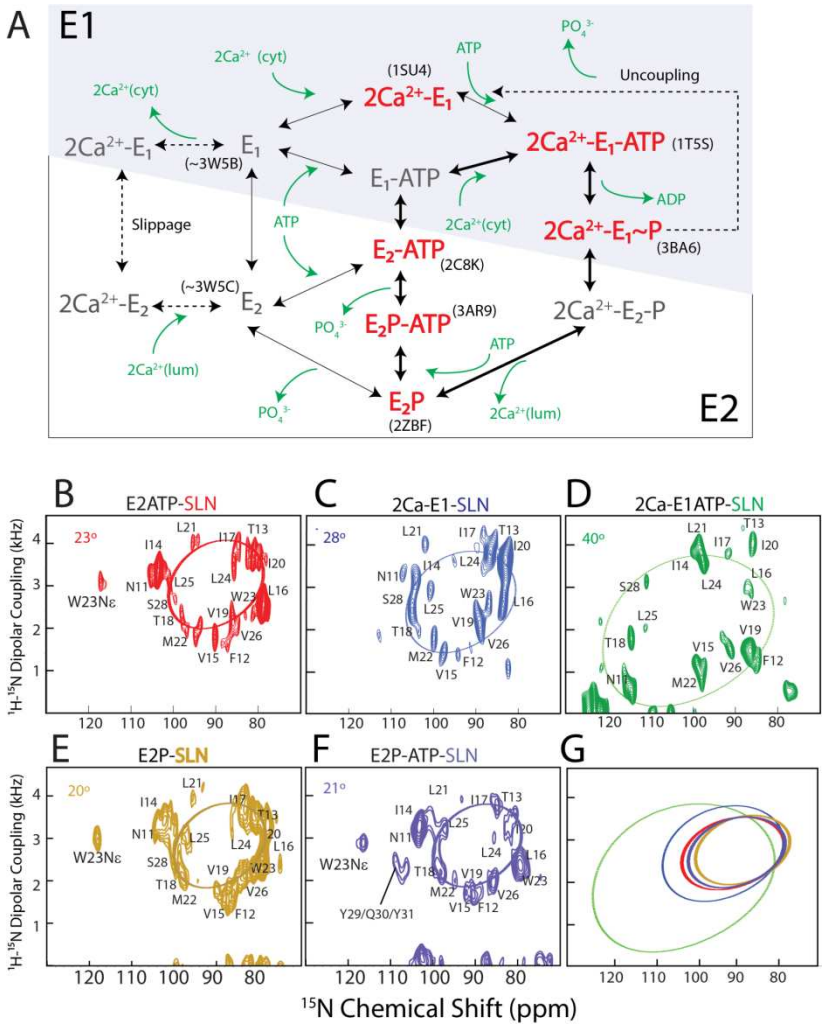

Figure 5.1: Topology of sarcolipin bound to SERCA

(A) Mechanism for the Catalytic Cycle of SERCA (B-F) SEPISEMA spectra of U15N-SLN bound to SERCA, with SERCA trapped in the conformation indicated on the top of each panel. (G) Overlay of best fit PISA wheel patterns for SE-PISEMAs in panels B-F

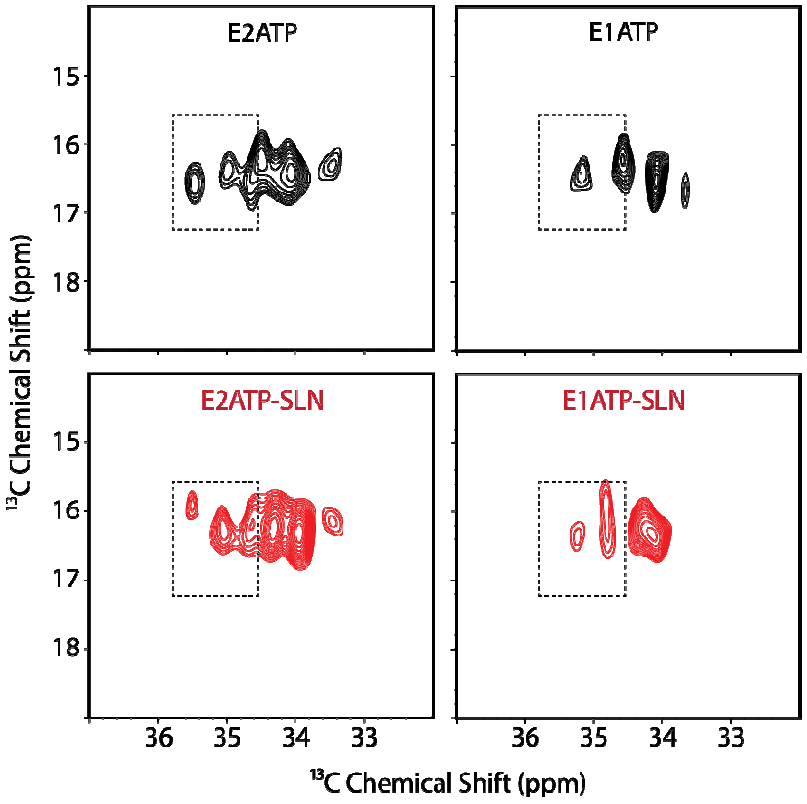

Figure 5.2: Conformational transitions mapped by MAS-ssNMR

Conformation of SERCA in the E1ATP and E2ATP states mapped in absence (black) and presence (red) of bound sarcolipin

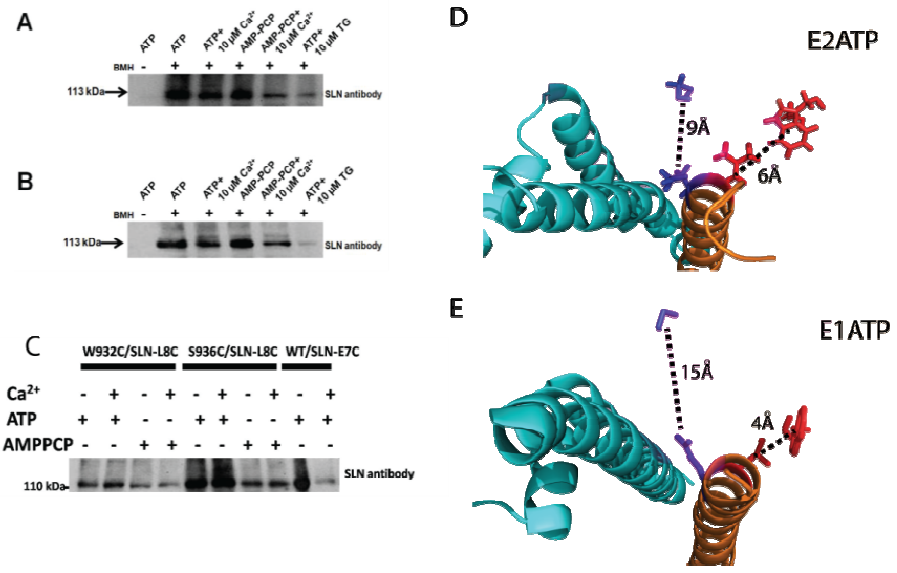

Figure 5.3: Crosslinking efficiency depends of SERCA conformation

(A) Cross-linking of E7C-SLN to 318-SERCA under in absence of Ca^{2+}. (B) Cross-linking of V26C-SLN to V89C-SERCA under different conditions. (C) Crosslinking of SLN-L8C to W932C SERCA and S936 SERCA in E2 and E1 states. (D) Structure of E2ATP form (NMR data) which shows that both E7C-SLN C-318 SERCA (blue) and L8C-SLN S936 SERCA can be cross-linked. (E) Only L8C-SLN can be cross-linked in the E1 state as the position of SLN has changed due to the large tilt angle and movement of M2 helix within the cavity.

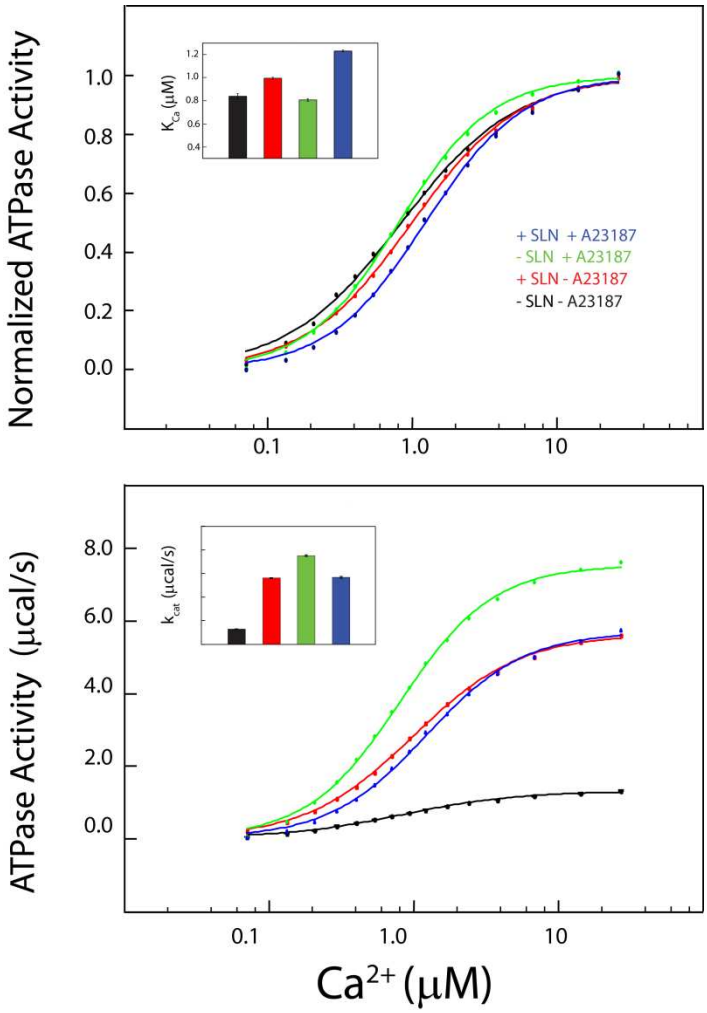

Figure 5.4: Regulation of SERCA Activity by Sarcolipin

Black: SERCA alone without Ca^{2+} ionophore, Red: SERCA in presence of SLN without Ca^{2+} ionophore, Green: SERCA alone with Ca^{2+} ionophore and Blue: SERCA in presence of SLN without Ca^{2+} ionophore

(A) Normalized ATPase activity, inset: K_{Ca} values for all samples

(B) ATPase activity (heat released due to ATPase activity in μcal/s); inset: k_{cat} for all samples

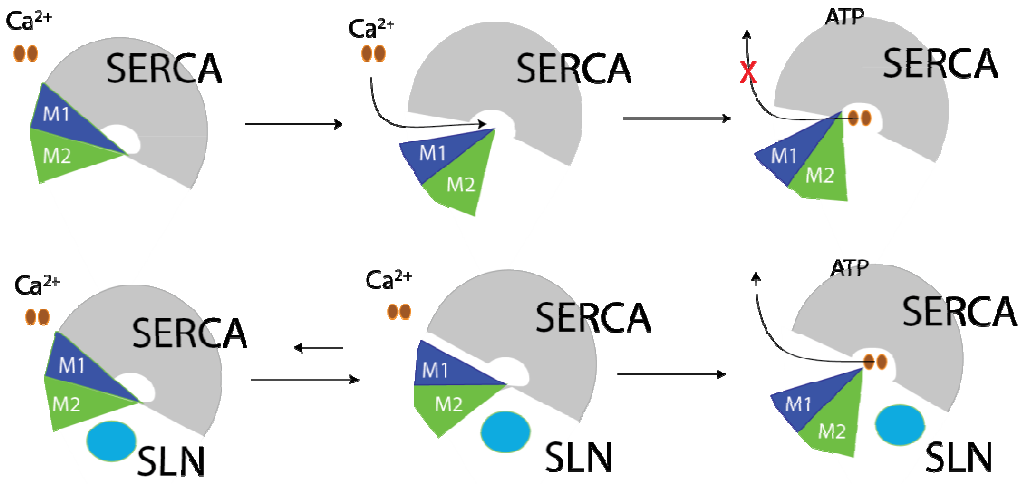

Figure 5.5: Mechanism of sarcolipin's inhibition of SERCA

Top: SERCA alone – The movement of M1-M2 helices closes up the regulatory groove and opens up cytosolic Ca^{2+} pathway. The binding of Ca^{2+} and ATP causes a conformational change that prevents backflow of Ca^{2+}. For SERCA bound to SLN (bottom), the regulatory groove cannot close due to the presence of SLN. Only at the final stage when ATP and Ca^{2+} are bound, the cytosolic pathway opens due after the change in the orientation of SLN

6. Structural dynamics and topology of phosphorylated phospholamban homopentamer reveal its role in the regulation of calcium transport.

Vitaly V. Vostrikov, Kaustubh R. Mote, Raffaello Verardi and Gianluigi Veglia

Reprinted with permission from **Structure (2013), 21, 12, 2119**

Phospholamban (PLN) inhibits the sarco(endo)plasmic reticulum Ca^{2+}-ATPase (SERCA), thereby regulating cardiac diastole. In membranes, PLN assembles into homopentamers that in both the phosphorylated and nonphosphorylated states have been proposed to form ion-selective channels. Here, we determined the structure of the phosphorylated pentamer using a combination of solution and solid-state nuclear magnetic resonance methods. We found that the pinwheel architecture of the homopentamer is preserved upon phosphorylation, with each monomer having an L-shaped conformation. The TM domains form a hydrophobic pore approximately 24 Å long and 2 Å in diameter, which is inconsistent with canonical Ca^{2+}-selective channels. Phosphorylation, however, enhances the conformational dynamics of the cytoplasmic region of PLN, causing partial unwinding of the amphipathic helix. We propose that PLN oligomers act as storage for active monomers, keeping SERCA function within a physiological window.

Introduction

Phospholamban (PLN), a 52-residue membrane protein, is involved in the Ca^{2+} regulation pathway in cardiac myocytes (*53*, *223*, *224*). To initiate muscle contraction, Ca^{2+} ions enter the sarcolemmal membrane and stimulate the release of Ca^{2+} from the sarcoplasmic reticulum (SR) by the ryanodine receptors (the calcium-induced-calcium-release mechanism). Ca^{2+} ions then bind the troponin complex, signaling muscle contraction. The relaxation phase takes place when Ca^{2+} is transferred back into the SR by the sarco(endo)plasmic reticulum Ca^{2+}-ATPase, SERCA2a. A small membrane protein, PLN, binds and downregulates SERCA function by reducing its apparent Ca^{2+} binding affinity. PLN's secondary structure comprises two helical segments joined by a short dynamic loop (*225*). The transmembrane (TM) helix, spanning residues 25–51, constitutes the inhibitory domain (*226*), and the cytoplasmic helix bearing the phosphorylation sites has a regulatory role, reversing PLN's inhibitory function upon phosphorylation at Ser16 (*227*). Both in vitro and in vivo studies have demonstrated that PLN forms a stable

homopentamer (*227*). However, the role of this homopentamer is at the center of an active debate.

One hypothesis is that PLN forms Ca^{2+} (*228*) or Cl^- (*229*) selective channels, based on initial patch-clamp measurements and electrochemical measurements with PLN reconstituted in artificial membranes, which indicated that several different ions were likely transported by PLN. In contrast, other groups hypothesize that the PLN homopentameric assembly may act as a buffer or as storage, regulating the concentration of active monomers available to bind SERCA and keeping its function (Ca^{2+} concentration) within a physiological window. The latter notion is supported by biochemical and molecular biology data showing that the presence of SERCA shifts the homopentamer/monomers equilibrium toward PLN monomers, forming 1:1 SERCA/PLN complexes (*230*). Additionally, it has been shown that mutants that promote PLN oligomerization upregulate SERCA, whereas mutants that enhance deoligomerization downregulate the ATPase, reducing Ca^{2+} flux and resulting in heart failure progression in mice models (*231*). The recently solved structure of the nonphosphorylated state of PLN in lipid membranes revealed a pinwheel topology of the homopentamer, with a long hydrophobic TM pore (∼24 Å) of relatively small diameter (∼2 Å) that cannot accommodate passive transport of hydrated Ca^{2+} or Cl− ions (*87*, *232*). However, recent physiological studies reinstated the Ca^{2+} channel hypothesis, proposing that phosphorylated PLN pentamer may form ion channels that increase Ca^{2+} leak (*233*).

In this work, we sought to clarify the role of phosphorylation in pentameric PLN. Using a combination of solution and solid-state nuclear magnetic resonance (ssNMR) spectroscopy, we determined the structure, topology, and conformational dynamics of the phosphorylated PLN pentamer. We found that upon phosphorylation, pentameric PLN retained its overall architecture within the lipid membranes, with an average structure resembling the pinwheel conformation found for the nonphosphorylated PLN. In combination with earlier electrochemical measurements (*234*), the structural topology of phosphorylated PLN is not consistent with the formation of an ion-selective channel, and

instead supports an active role of oligomerization in maintaining the population of active monomers within a physiological window of SERCA inhibition.

Results

Hybrid solution/ssNMR structure of phosphorylated PLN pentamer

On an SDS-PAGE gel, we observed the pentameric assembly of PLN at an apparent molecular weight of ~25 kDa, which is lower than its formula weight (~30 kDa) (Wegener and Jones, 1984). Despite this difference in mobility, we readily identified the phosphorylated species by the gel shift relative to the nonphosphorylated form of the protein (Figure S1 available online). The correct molecular weight was confirmed by electrospray ionization mass spectrometry (ESI-MS). Under ESI-MS conditions, deoligomerization of the pentamer occurred and the protomers were detectable in the 700–1,300 m/z window, corresponding to the PLN forms bearing five to nine charges. In all cases, PLN incubated with PKA-C exhibited a mass shift corresponding to one phosphate group per monomer.

The [^{1}H-^{15}N] heteronuclear single-quantum correlation spectroscopy ([^{1}H-^{15}N]-HSQC) spectra of the nonphosphorylated and phosphorylated forms of wild-type PLN (PLNWT) reconstituted in dodecylphosphocholine (DPC) micelles are very similar (Fig. S6.3). A single resonance is observed for each residue, indicative of the symmetric nature of the pentamer. The hydrophobic segments of the proteins (clusters of peaks centered at ~8.5 ppm in 1H dimension) are essentially superimposable. The residues that were most affected by phosphorylation are located close to Ser16, with other chemical shift perturbations detected for residues in the flexible loop and domain Ib. These structural features closely resemble those observed for the phosphorylated monomeric PLN, where the three cysteine residues in the TM domain are mutated into Ala and Phe to prevent pentamerization (*235*). The plots of the chemical shift perturbations of the phosphorylated proteins (monomer and pentamer) relative to the nonphosphorylated form are very similar, showing that phosphorylation perturbs both forms and these changes are

independent of the oligomeric state of PLN. The chemical shift data have been deposited in the Biological Magnetic Resonance Bank under accession code 18952.

The [^{1}H, ^{15}N] nuclear Overhauser effect spectroscopy (NOESY)-HSQC spectra of PLNWT phosphorylated at S16 (pS16-PLNWT) show the typical signature of regular α helices, including (α, α+3), (α, α+4), and (β, β+3) NOE connectivities. This pattern is present in the TM domain and the N-terminal segment of the cytoplasmic domain, but is interrupted for the residues spanning 16–26, indicating a disruption of the helical secondary structure.

To determine the architecture of the phosphorylated pentamer in lipid bilayers, we reconstituted pS16-PLNWT in mechanically aligned 1,2-dioleoyl-sn-glycero-3-phosphocholine (DOPC)/1,2-dioleoyl-sn-glycero-3-phosphoethanolamine (DOPE) lipid bilayers and carried out [1H,15N] polarization inversion spin exchange at the magic angle ([1H,15N]-PISEMA) experiments. The PISEMA spectrum displays three main features: a cluster of resonances corresponding to the TM segment, a region where the amide groups of the in-plane cytoplasmic helix resonate, and high-intensity signals centered around the isotropic chemical shift values that correspond to highly dynamic residues as well as the side-chain resonances. The TM region of PLN comprises 25 hydrophobic residues arranged in an α-helical conformation, giving rise to a complex spectrum with only a few resolved resonances (*179*). To assign the individual signals, we employed a combination of residue-type labeling schemes using recombinant proteins as well as synthetic samples (Figure 6.1). Synthetic samples with four sequentially labeled residues yielded well-resolved spectra in which we were able to identify the individual residues. The α helix geometry dictates the unique assignments of the labeled four amino acid stretches that constitute part of the hydrophobic zipper motif (*236*, *237*). The PISEMA spectral signature is similar to that observed for the nonphosphorylated form (*179*). This spectrum enabled us to define the assignment of all the resonances.

The spectrum of the ^{15}N-Leu-labeled sample confirmed the tilt and azimuthal rotation angle adopted by the TM domain. The dispersions of the chemical shifts and dipolar couplings, as well as the intensities of the resonances, are indicative of residues clustered primarily on one face of the helix (Figure 6.1C). The ^{15}N-Leu spectrum obtained using synthetic samples provided additional assignments for the remaining Leu residues; these were then used as restraints in the structure calculations and classified as ambiguous (*238*) (Figure 6.S4). The resonances at the C terminus show scaled dipolar and chemical shift values due to their dynamic nature; therefore, these values were not used as constraints for the structure calculation. To assess the orientation of the juxtamembrane domain Ib and the loop, we labeled PLN with ^{15}N-Gln and ^{15}N-Glu. Whereas the values of the dipolar couplings and chemical shifts of those residues located in the loop are scaled by conformational dynamics, residues in the juxtamembrane domain Ib are more rigid, giving valuable constraints to determine PLN topology and assisting in the determination of the orientation of the cytoplasmic domain Ia (Figure 6.1).

To compare the tilt angles between the nonphosphorylated and phosphorylated forms of PLNWT, we recorded PISEMA spectra of U-^{15}N-labeled proteins in dimyristoylphosphatidylcholine (DMPC) / 1-palmitoyl,2-oleoyl-sn-glycero-3-phosphocholine (POPC) / dihexanoylphosphatidylcholine (DHPC) bicelles. The samples were prepared in D_2O to eliminate those resonances that are in contact with the bulk solvent (Figures S6.5B and S6.5C). From the analysis of the two spectra, we concluded that the dipolar coupling and anisotropic chemical shift pattern for the TM domains overlaps with that of the nonphosphorylated form, indicating that the tilt and rotation angles of the pS16-PLNWT species are similar to those of the nonphosphorylated protein. Because the hydrophobic length of the DMPC/POPC is ∼4 Å shorter than the DOPC/DOPE membrane (*239*), the tilt angle of PLN is affected by the protein-lipid interactions. In fact, the size of the PISA wheel (dipolar coupling and anisotropic chemical shift pattern) (*144*, *150*, *240*) in bicelles is larger than that measured in mechanically aligned lipid bilayers. The dipolar couplings measured for the TM domain

in mechanically aligned samples range from 4 to 9 kHz; in contrast, those measured in bicelles range from 2 to 8 kHz. In principle, the data from both bicelles and mechanically aligned samples can be used to determine the topology of PLN; however, we used only those determined in the DOPC/DOPE mixture, which closely mimics SR membrane composition for structural refinement (*14*).

To determine intermonomer distances in the pentameric assembly in the lipid bilayer membrane, we reconstituted the pentameric phosphorylated PLN in lipid vesicles and performed magic angle spinning (MAS) experiments. We employed an asymmetric labeling scheme previously utilized for both solution NMR and ssNMR experiments, labeling ^{13}C Leu of one protomer and ^{13}C Ile of the other protomer (*35*). The isotopically labeled proteins were expressed individually and mixed together in a 1:1 molar ratio (*241*). Using this isotopic scheme in concert with dipolar-assisted rotational resonance (DARR) experiments (*209*), we were able to detect the dipolar contacts between adjacent protomers. The DARR spectrum of pS16-PLNWT reported in Figure 2 exhibits several cross-peaks between Leu and Ile of the adjacent protomers. Remarkably, the interactions are not limited to the methyl-methyl contacts alone; several interprotomer cross-peaks between Cβ and Cα resonances are also detected. The DARR cross-peaks show multiple dipolar interactions between one or more Leu (nine residues in the domain II) and one or more Ile (six residues), with the latter indicating the tight packing of the protomers' interface. Although this labeling scheme does not provide resonance-specific assignments, the dipolar contacts can be used in structure calculations as ambiguous long-range distances, and can easily be assigned when combined with the orientational restrains from SLF experiments (Figure 2C). The network of dipolar interactions coincides with that observed for PLNWT, indicating a similar arrangement of the TM domains. The rotation angles calculated from the SLF data restrict the interfacial orientations between the protomers, defining the Leu-Ile zipper motif between residues 33, 40, 47 (Ile) and 37, 44, 51 (Leu). Furthermore, the rotation angle of the TM helices positions the helices such that Ile residues of a given protomer interlock with Leu of an

adjacent protomer located clockwise, resulting in a left-handed coiled-coil arrangement (Figure 6.3) (*242*).

Summaries of the experimental restraints and the common metrics used to assess the structure quality are provided in Tables 1 and 2, respectively. Since the azimuthal orientation of the cytoplasmic domains relative to the TM domains is restrained only by steric interactions between them, the cytoplasmic helix for an individual protomer can cover an azimuthal range of approximately 180° (Figure 3), leading to a large root-mean-square deviation (rmsd) for the whole pentameric assembly in both the nonphosphorylated and phosphorylated forms. Nevertheless, if the structures are analyzed in terms of the individual domains, the rmsd values drop sharply to acceptable values. Orientation of the TM domain is still governed by the Leu-Ile side-chain packing, which tolerates little variation in topology of the TM helix (Table 3). The ordered segment of the cytoplasmic domain is not altered by phosphorylation either, as the negatively charged phosphate group does not shift the domain's amphiphilic character. The structural ensemble has been deposited in the Protein Data Bank (PDB) under accession code 2M3B.

As shown previously (*243*), the monomeric mutant of PLN is capable of inhibiting SERCA and the monomer is likely to be the biologically active species, although recent works have proposed the pentamer to be the inhibitory species (*244*). To assess the inhibitory activity of PLNWT in the nonphosphorylated and pS16 states, we performed coupled-enzyme assays to establish the shift of the calcium concentration required for SERCA in the presence of PLN to regain its initial activity (ΔpKCa). As shown in Figure 4, the addition of PLNWT shifts the activity curve toward the higher calcium concentrations, causing a pKCa shift of 0.3, which is nearly 50% of the monomeric PLNAFA ΔpK_{Ca} (*14*). For the phosphorylated species of PLNWT, we observe the complete relief of inhibition, in line with what was observed for pS16-PLNAFA. If the pentamer were indeed the inhibitory form of PLN, one would expect it to increase SERCA inhibition in comparison with the monomeric PLNAFA; however, we observe

the opposite trend. As noted earlier, pentameric PLNWT exists in equilibrium with the monomeric species, with the equilibrium being shifted toward the former. The decrease in the available monomeric units for PLNWT and the decrease in SERCA inhibition caused by PLNWT in comparison with PLNAFA are in line with the explanation that monomeric PLN is the active inhibitory form.

Conformational dynamics of pentameric phosphorylated PLN

To probe the motions of PLN, we measured the longitudinal (T1) and transverse (T2) nuclear relaxation times and converted them into longitudinal and transverse relaxation rates (R1 and R2, respectively). As a proxy for conformational dynamics, we also measured ^{1}H-^{15}N heteronuclear steady-state NOE (HX NOE; Figure S6.6). These relaxation parameters were measured at two magnetic field strengths. The relaxation parameters for the TM regions of both phosphorylated and nonphosphorylated forms of PLN were very similar. Domains Ia and II exhibited different spin-lattice relaxation rates, and the mean values of the cytoplasmic domain were approximately 20%–50% higher for the nonphosphorylated and pS16 forms (Figure S6.6). Both nonphosphorylated and phosphorylated PLNWT showed very similar R1 values, which were mostly sensitive to the global tumbling of the proteins. At higher fields, there was a uniform increase in the longitudinal relaxation rates, suggesting that the global correlation time is not influenced by phosphorylation.

The relaxation parameters for pentameric WT and monomeric (AFA) PLN are compared in Figures 6.5 and S6.6. To estimate the local correlation times, we plotted the R2/R1 ratios along the sequence of PLN (*245*). We note substantial differences between resonances located in the cytoplasmic domains and those belonging to the TM domains. However, the dimensionless values of the R2/R1 ratios of the pentamers are similar to those of the monomeric species, indicating that the dominant factor contributing to the rotational correlation times is the size of the DPC micelle coating the proteins (*15*, *246*). Similar to the case with monomeric PLNAFA (*235*, *247*), phosphorylation of PLNWT did not affect the motions of the TM helix. Nevertheless, the differences in the R2 values

for the nonphosphorylated and phosphorylated proteins led to a decreased R2/R1 ratio for pS16-PLN. These changes are apparent for PLNWT, as the R2/R1 ratios are relatively constant throughout the sequence, with the exception of residues located near Ser16.

The difference between the two major helical domains of PLN is also apparent in the R1 × R2 products (*248*) (Figure S6.6). Although the values for the TM helices are similar within experimental error, the values for the cytoplasmic domain of the pS16-PLN are consistently lower than those of the nonphosphorylated form. Moreover, the changes near Ser16 are more pronounced and also present in the flexible loop. Other variations are also observed in the N-terminal residues of domain Ib from residue 22 to approximately residue 25, a crucial region for SERCA regulation (*249*). Interestingly, this region shows opposite effects upon phosphorylation, exhibiting the highest R1 × R2 values throughout the entire sequence. These elevated R1 × R2 values are indicative of the presence of motion in the microseconds-to-milliseconds timescale. The pentameric and monomeric forms of pS16-PLN differ in the length of this region, i.e., whereas PLNWT has higher R1 × R2 values immediately after P21, the monomer PLN has a longer stretch of residues with higher values, extending to the loop.

Finally, we calculated R1 × (1 – NOE) values that are used to characterize fast (picoseconds-to-nanoseconds) timescale dynamics (*245*). Figure 6.5 shows that phosphorylation at S16 leads to an increase of the local motions manifested by the elevated R1 × (1 – NOE) values. Considerable differences are observed between the pS16 forms of WT and monomeric proteins. For pS16-PLNWT, the N-terminal residues are largely unaffected, whereas those located in the middle of the cytoplasmic domain up to the beginning of domain II display increased motions. Conversely, pS16-PLNAFA displays changes in the fast-motion regime throughout the entire cytoplasmic region, including domain Ia, loop, and domain Ib.

The increased conformational dynamics of the phosphorylated cytoplasmic helix were confirmed by solvent accessibility data. To determine the exposure of each residue to the

solvent, or its depth of insertion into the aliphatic core of the micelle, we performed [^{1}H, ^{15}N]-NOESY experiments on pS16-PLNWT in protonated DPC and quantified the NOE cross-peaks between the amide resonances and the water peak (for solvent-exposed residues), or between amides and the aliphatic resonances of the DPC molecules (for residues buried in the membrane; Figure S6.5) (*250*). Although the nonphosphorylated PLN exhibited an oscillatory NOE pattern demonstrating a strong association between the amphipathic domain Ia and the micelle (*87*), the majority of the pS16 cytoplasmic domain exhibited NOE cross-peaks between amide groups and the water resonance. The only exceptions were Y6 and L7, which showed cross-peaks with both the bulk solvent and the micelles, demonstrating that these residues populate two major states: one in contact with the micelle and one exposed to the solvent. Residues 26–27 in domain Ib located at the membrane interface show several NOE cross-peaks with the aliphatic chains of the DPC micelle. Nonetheless, these residues are still partially accessible to water, whereas the rest of the sequence makes contact only with the micelle. Together with the spin relaxation data, the NOE patterns indicate that phosphorylation increases the dynamics in this domain, and shifts the population of PLN from the micelle-absorbed T state toward the micelle-desorbed R state (*62*).

Discussion

The physiological response to PLN phosphorylation is a net increase of the ATPase's apparent affinity for Ca^{2+}, with a concomitant augmentation of muscle contractility. The molecular mechanisms for this process are unknown. One possibility is that PLN forms ion channels that increase Ca^{2+} flux into the SR membrane, thereby increasing diastole. Patch-clamp experiments, electrochemical measurements with synthetic membranes, and the PLN pentamer structure determined in detergent micelles support this hypothesis (*229*, *251*). However, the structural topology of the PLN pentamer in lipid bilayers does not reveal the canonical architecture of an ion channel (*87*, *164*, *179*). The pentameric assembly with a pinwheel topology displays a narrow and hydrophobic pore ~25 Å in

length and ~2 Å in diameter on average (*87*, *164*, *179*). Free-energy calculations show that the energy barrier for Ca^{2+} ion transport is ~40 kcal/mol, which is prohibitive in the absence of an energy source (*232*). A recent paper raised the possibility that phosphorylation at Ser16 might be responsible for ion transport or Ca^{2+} leakage (*252*), motivating our structural studies.

Several previous biophysical studies have examined pS16-PLN using methods such as circular dichroism (*253*), fluorescence (*227*), electron paramagnetic resonance (*254*), solution NMR in an organic/aqueous mixture (*255*), and site-specific ssNMR (*256*). These studies excluded major conformational changes in the TM domain of PLN, which would justify the formation of a channel. Cornea et al. (*254*) showed that upon phosphorylation, the thermostability of the pentamer increases and may affect the number of regulatory monomeric protomers, suggesting that electrostatic interactions due to phosphorylation at Ser16 cause a complete rearrangement of the cytoplasmic amphipathic helix. However, the structure and dynamics of the Ser16 phosphorylated monomeric PLN in DPC micelles revealed only a local unwinding of the cytoplasmic helix in the proximity of the phosphorylation site, without substantial long-range structural effects in the TM domain (*247*). The latter finding was supported by a study carried out by Abu-Baker and Lorigan (*257*), who used site-specific ssNMR measurements to demonstrate that the TM domains of PLN are essentially intact upon phosphorylation, with minor structural and dynamical effects localized to the cytoplasmic domain. On the other hand, fluorescence resonance energy transfer (FRET) experiments with probes engineered in both the cytoplasmic and TM domains of PLN suggested an increase in helical content (*258*). A comparison between PLNWT and its pseudophosphorylated analog, in which negatively charged glutamic acid is substituted for serine, did not reveal significant differences between the two states (*259*).

The present study, which was carried out with phosphorylated PLN in lipid bilayers and micelles, establishes that the overall architecture of the pS16-PLNWT is similar to that of the nonphosphorylated form, with a reduced helicity of the cytoplasmic domain in

proximity to the phosphorylation site. The calculated cavity and its maximum diameter as a function of the Z coordinate are represented in Figure 6.6. As with the nonphosphorylated pentamer, the pore of the phosphorylated pentameric assembly does not exceed 3 Å. The pore is coated exclusively by side chains; none of the polar backbone atoms are accessible from the inside. Three of the side chains located in the juxtamembrane region are moderately hydrophilic (Q23, Q26, and Q29), and form interprotomer (Q29) and possibly intraprotomer (Q23 to Q26 or Q26 to Q29) polar contacts. The rest of the residues in the pore are hydrophobic methyl groups of the zipper motif (Leu 37, 44, 51, and Ile 33, 40, 47). Although this organization is reminiscent of ion channel architecture (i.e., hydrophilic residues that provide selectivity and hydrophobic ones that strip the water shell), there is a restriction of the pore around residues 26, 29, 33, and 37, with the average diameter ranging from 1.4 to 1.8 Å, which would prevent Ca^{2+} ion transport (*260*). In a recently solved structure of the Orai Ca^{2+} channel, the average pore diameter is 3 Å and can reach 1.5 Å (*261*). In this case, however, the charges are present in the side chains coating the inner pore and their rearrangement would facilitate ion translocation.

For the pS16-PLNWT pentamer, the juxtamembrane region does not possess negatively charged residues that could constitute a selectivity filter, which in Orai closely matches the diameter of the ion. The pore constrictions at glutamines 26 and 29 are defined mainly by the amide group, a less efficient ligand for Ca^{2+}. Importantly, the hydrophobic residues span five helical turns, constituting a high-energy barrier to ion transport. Also, the preferred coordination geometry for Ca^{2+} ions is pentagonal bipyramid (akin to the EF-hand motif), which requires an additional ligand positioned deeper in the pore. The pore of PLN is devoid of such a ligand, and it is unlikely to be water (*232*). Recent electrochemical impedance spectroscopy measurements on pS16-PLNWT also revealed its inability to conduct ions at physiologically relevant TM potentials (*234*).

The most significant changes that occur upon phosphorylation are located in the cytoplasmic domains. The amphipathic cytoplasmic domain Ia of PLN populates both

folded, membrane-associated (T-state) and unfolded, membrane-detached (R-state) conformations (*62*, *262*). This equilibrium, which is critical for SERCA regulation, is present for the phosphorylated protein, with the population of the unfolded state increasing upon phosphorylation (*62*, *263*). The phosphate group in position 16 increases conformational dynamics in the pico- to nanosecond timescale, encompassing residues in the loop up to the distal sites of the N terminus. These conformational dynamics facilitate the folded-to-unfolded (order-to-disorder) transition of the cytoplasmic domain, which can bind and regulate SERCA function (*46*).

Previously, we demonstrated that there is an inverse correlation between the enhanced conformational dynamics of domain Ia and PLN inhibitory potency (*49*, *63*). Site-specific mutations that increase PLN's internal dynamics, promoting detachment of domain Ia from the membrane and concomitant unfolding, also upregulate SERCA. Thus, the nonphosphorylated form of monomeric PLNAFA bearing the P21G mutation shows enhanced dynamics in this region and behaves functionally as the pseudophosphorylated S16E mutation, whereas two glycine mutations fully mimic the effects of phosphorylation (*49, 264*). Nonetheless, the coupling between the two domains remains essential, and it was shown that an overly flexible loop does not follow the linear trend (*63*). The phosphorylation event described here introduces disorder in the C-terminal portion of the cytoplasmic domain, leading to its partial unfolding and detachment from the membrane (with the conformation of the cytoplasmic domain being akin to the T′ state) (*62*) along the energy landscape of this polymorphic domain.

Although they dismiss the formation of a classical ion channel, our results for pentameric pS16-PLNWT support our regulatory model, in which oligomerization has buffer effects on SERCA regulation, fine-tuning the concentration of phosphorylated monomers that can bind and upregulate SERCA. Both phosphorylated and nonphosphorylated PLN keep SERCA function within a well-defined physiological window, and exceeding this window by either superinhibition or loss of function causes the progression of heart disease (*265*). Keeping PLN regulation of SERCA within this physiological window

requires maintenance of a correct equilibrium between its monomeric and oligomeric states (*72*, *231*), the ability of PLN to be effectively phosphorylated (*266*, *267*), a net charge of the regulatory domain (*268*, *269*), and structural communication between TM and regulatory domains for effective signal transduction (*63*).

Since SERCA and PLN are emerging as targets for gene therapy by adeno-associated gene transfer, knowledge about all the functional states of these proteins is central to the design of appropriate strategies for intervention (*270–273*).

Experimental methods

Protein preparation

PLNWT was cloned in a pMal expression vector (New England Biolabs) and expressed in Escherichia coli cells grown in M9 media, supplemented with $^{15}NH^{4}Cl$ as the sole source of ^{15}N (uniform labeling), or in combination with the nonlabeled amino acids (residue type reverse labeling) (*274*). Isotope-labeled compounds were purchased from Isotec or Cambridge Isotope Laboratories. Maltose binding protein-PLN fusion protein was purified on amylose resin, cleaved with tobacco etch virus protease, and purified by high-performance liquid chromatography (HPLC) utilizing a Vydac C8 column (Grace) with a linear water-isopropanol gradient at 1.5%/min at a 2 ml/min flow rate (*166*, *275*). The phosphorylation of S16 was accomplished by incubating PLNWT in β-D-octylglucoside (1/100 w/w) with the recombinant catalytic subunit of protein kinase A (PKA-C) at pH 7.0 and 30°C for 12–16 hr. Completion of the phosphorylation reaction and sample purity were assessed by gel-shift assays and ESI-MS (Figure S6.1).

Selectively labeled PLNWT was prepared using a Liberty microwave-assisted peptide synthesizer (CEM). The synthesis was performed on a 0.05 mmol scale using preloaded PEG-polystyrene resin. The activators used were HBTU (regular coupling, 10-fold amino acid excess) and PyClock (isotope coupling, 2-fold amino acid excess) (*276*). Each residue was double coupled. Methionine and cysteine residues were coupled in the

conventional (nonmicrowave) fashion to reduce the risk of racemization. Side-chain deprotection and cleavage were accomplished using modified Reagent K (room temperature, 3 hr), with 1,2-ethanedithiol substituted with 3,6-dioxa-1,8-octanedithiol (*277*, *278*). Synthetic PLNWT was purified using reverse-phase HPLC under the conditions described above for the recombinant protein.

Solution NMR

Solution NMR experiments were performed on a 600 MHz Varian and a 750 MHz Bruker Avance III DMX equipped with cryogenic probe. PLN was reconstituted in DPC-d38 micelles (1:70 w/w) by mixing the appropriate amounts of protein and detergent powder, and dissolving them in 50 mM phosphate buffer with 100 mM NaCl, pH 6.0. For PLN/detergent NOE, U-^{2}H, ^{15}N-PLNWT and fully protonated DPC were employed. Relaxation experiments were carried out at 37°C at the two magnetic field strengths, utilizing the pulse sequences described by Farrow et al. (1994). Experimental uncertainties were estimated from duplicate delays (R1 and R2) or duplicate experiments (^{1}H-^{15}N NOE). Errors in the products or ratios of R1 and R2 were calculated according to

Solid state NMR

Separated local field (SLF) (*143*) data were acquired on PLNWT incorporated in DOPC/DOPE (4/1 mol/mol; Avanti Polar Lipids). The total amount of lipid was 60 μmol with a pentamer/lipid ratio of 1/100 mol/mol (*86*, *87*). Protein in trifluoroethanol and lipids in chloroform were comixed, organic solvent was removed under a stream of nitrogen gas, and residual organic solvent was removed under high vacuum. The protein-lipid mixture was resuspended in water, deposited evenly between 36 glass slides (Marienfeld), partially dehydrated at 33% relative humidity (saturated solution of $MgCl_2$), and rehydrated by adding water up to 45% w/w (*279*, *280*). Lipid alignment was verified using ^{31}P (Figure S6.2). Typically, a 300–500 μs cross-polarization contact time was employed, the dipolar evolution was 400–600 μs, and 1,500–3,000 scans per increment were acquired. Data were acquired at 600 MHz (Bruker DRX) and 700 MHz (Varian) with a low-E ^{15}N-^{1}H probe (*22*). Bicelle samples were prepared using the long-

chain lipid DMPC/POPC (4/1 mol/mol) and the short-chain lipid DHPC. Importantly, the presence of POPC lipid reduces the optimal temperature necessary to form an aligned bicellar phase. To induce parallel orientation of lipid bilayers relative to B_0, $YbCl_3$ was added to the sample to a final concentration of 10 mM. The q value employed was 4.5, as a lower value (i.e., q = 3.2) resulted in incomplete alignment and smaller dipolar couplings (data not shown). The SLF spectra for bicelle preparations were acquired on a Varian spectrometer operating at 700 MHz.

DARR experiments (*209*) were performed on a phosphorylated PLN sample consisting of an asymmetric isotopic mixture of $^{15}N/^{13}C$-Leu PLNWT and $^{15}N/^{13}C$-Ile PLNWT reconstituted in DOPC/DOPE 4/1 (mol/mol) multilamellar vesicles (MLVs), 20 μmol total lipid. The MAS rate was 8 kHz and the DARR mixing time was 400 ms. Data were acquired at −15°C.

Structure calculations were performed with Xplor-NIH 2.33 (*204*). Structural restraints (Table 6.1) were obtained through HSQC-NOESY at 600 MHz field (Varian), utilizing a 200 ms mixing time, and binned as described previously (*87*). Chemical shift data were converted to dihedral restraints with Talos+ (*203*). SLF data were modeled using the Xplor-NIH routines (Straus et al., 2011) with ^{15}N chemical shift tensor components of σ11 = 64, σ22 = 77, σ33 = 216 ppm (*149*). The D_a component of the dipolar coupling alignment tensor was set to 9.5 kHz, corresponding to the value of the generalized order parameter of 0.93 (assuming a 1.06 Å NH bond length, with the maximum dipolar coupling therefore being 10.22 kHz) and the chemical shift alignment tensor was scaled accordingly. As noted previously, minor variations in the order parameter or chemical shift tensor components do not have a profound effect on the quality of the structure, but do lead to higher energies of the corresponding terms resulting from a poor data fit (*15*, *149*). The DARR data were modeled as ambiguous restraints between L37, L44, L51, and I33, I40, I47 based on the structure of the nonphosphorylated form as well as mutagenesis data, indicating that all of these residues are essential for the stability of the pentamer (*237*). The distance range for the observed DARR cross-peaks was set between 1.8 and

6.5 Å irrespective of the peak intensity. The Ez potential energy function (*149*, *206*) was employed at the monomer calculation step for the depth of insertion, and then switched to planar restraints during the pentamer refinement. In addition to the standard Xplor-NIH potentials (Table S1), knowledge-based hydrogen bonding, Ramachandran, and residue affinity potentials were employed. Structures were visualized with PyMOL.

ATPase activity assays

Consumption of ATP by SERCA was measured using an enzyme-coupled assay in DOPC/DOPE 4/1 MLVs as previously described (*49*, *281*). Temperature was maintained at 37°C and the PLN/SERCA/lipid ratio was 6:1:700. Enzyme activity was monitored at 340 nm continuously for 8 min with a 9 s dwell time and fitted to a linear curve. The curve slopes at different Ca^{2+} concentrations were fitted to the Hill equation, with the midpoint of the sigmoidal curve being the pK_{Ca} value.

Author contributions

V.V., K.R.M., R.V., and G.V. designed the experiments and participated in manuscript preparation. V.V., K.R.M., and R.V. performed the experiments and analyzed the data.

Accession numbers

The BMBB accession number for the chemical shifts reported in this paper is 18952. The PDB accession number for the pS16-PLNWT reported in this paper is 2M3B.

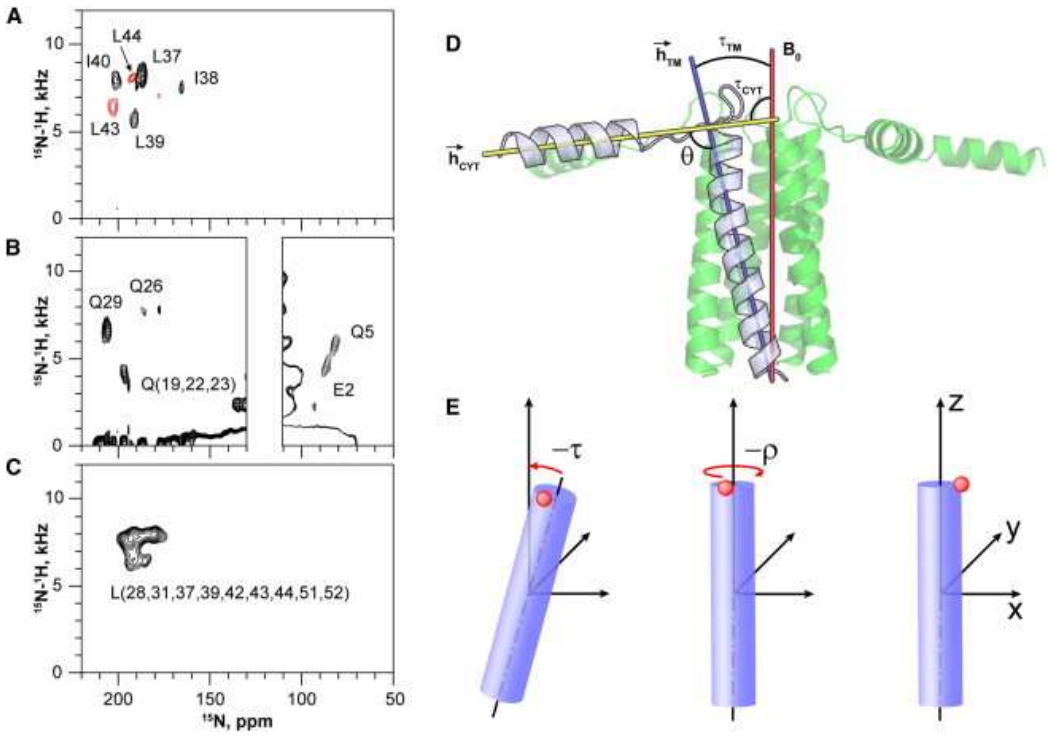

Figure 6.1: PISEMA spectra of selectively labeled pS16-PLNWT in mechanically aligned DOPC/DOPE lipid bilayers

(A–C) Samples were prepared with synthetic (A) or recombinant (B and C) proteins. Two spectra obtained from different synthetic samples are color-coded in (A). (D and E) Definitions of topological angles τ (tilt), ρ (rotation), θ (angle between helices) (D), and their calculation from the structural data (E). The structural model of pS16-PLNWT pentamer illustrates the tilt angles of the TM (τTM) and cytoplasmic (τCYT) helices, defined as the angles between the applied magnetic field (B0) and the corresponding α helix vectors View the MathML source. The interdomain angle θ is defined between the vectors View the MathML source and View the MathML source. Performing successive right-handed rotations of an α helix by negative τ and negative ρ aligns the reference atom (blue) with the x axis (see Table 1). Helical axes were calculated using the average direction of carbonyl bonds, employing script from the PyMOL repository.

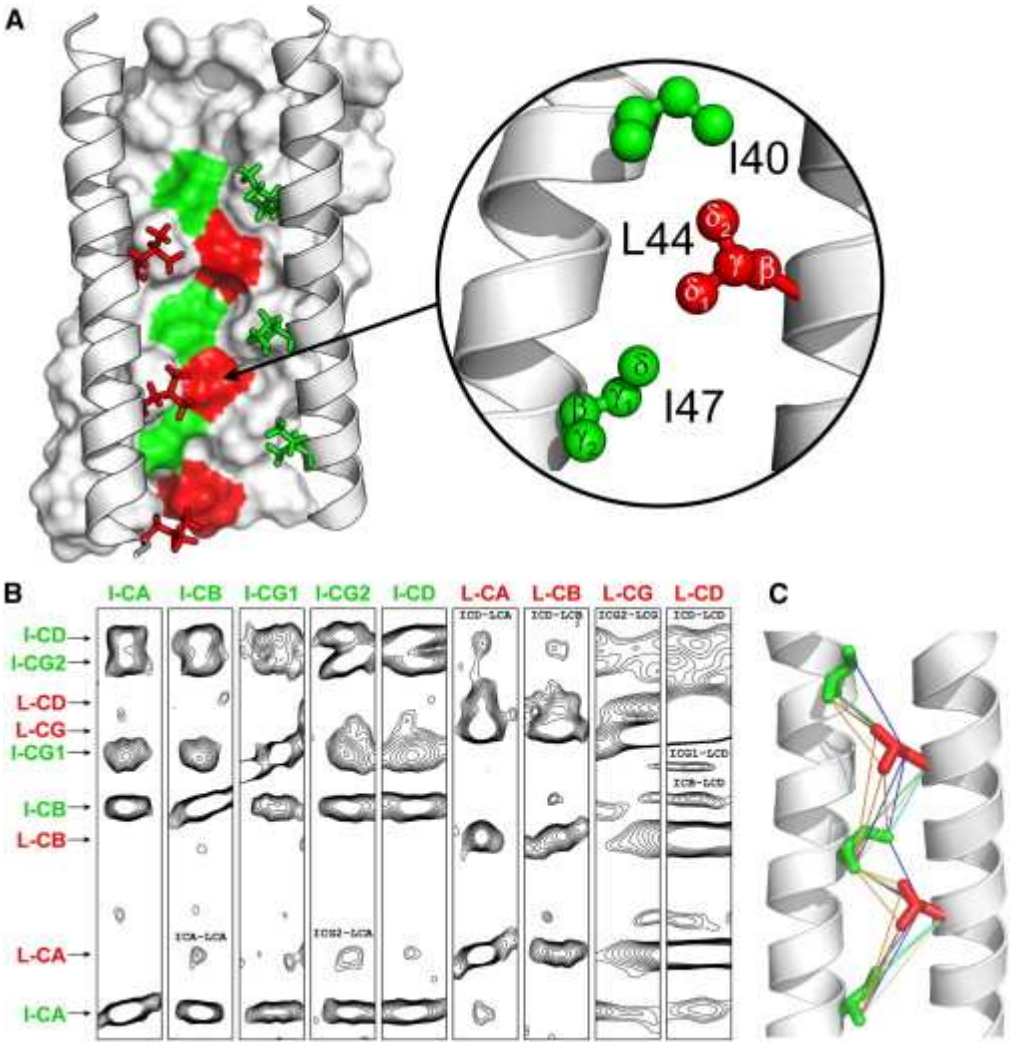

Figure 6.2: Leu-Ile zipper in pS16-PLNWT

(A) Arrangement of Leu (red) and Ile (green) side chains on the structure of pS16 form (one protomer is removed for clarity).

(B) Strips from DARR spectrum of the mixed Ile and Leu pS16-PLNWT (each protomer labeled with only one amino acid type).

(C) Ambiguous restraints modeled from the DARR data.

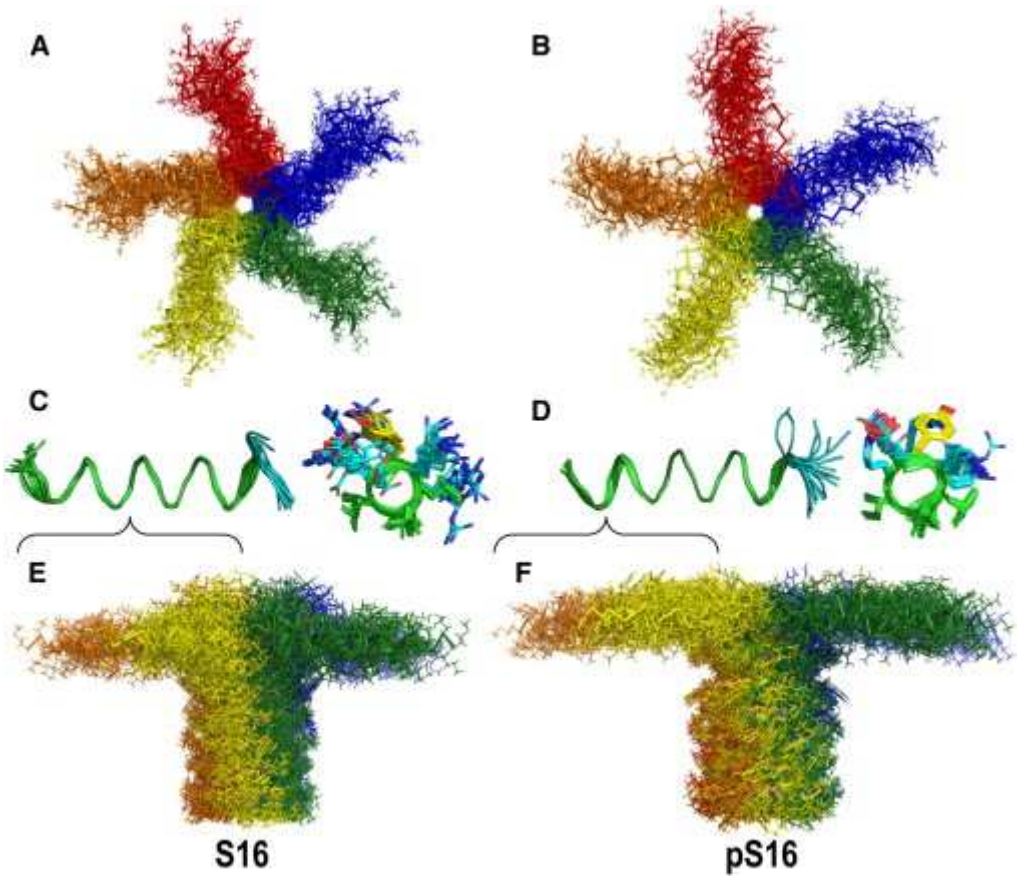

Figure 6.3: NMR ensembles of PLNWT in non-phosphorylated and phosphorylated Forms

Structural ensembles of PLNWT in the nonphosphorylated (left) and pS16 (right) forms as viewed along the membrane normal (A and B) or perpendicular to it (E and F). Structures are aligned on all backbone atoms. Residues 1–17 are shown in ribbon projection, illustrating disorder near the phosphorylation site when the alignment is performed on the heavy atoms of only these residues (C and D). Side chains of the cytoplasmic domain are shown as sticks. Carbon atoms of the side chains are colored green for hydrophobic residues and cyan for hydrophilic ones. Structural statistics are reported in Tables 1, 2, and S3 and Figures S7 and S8.

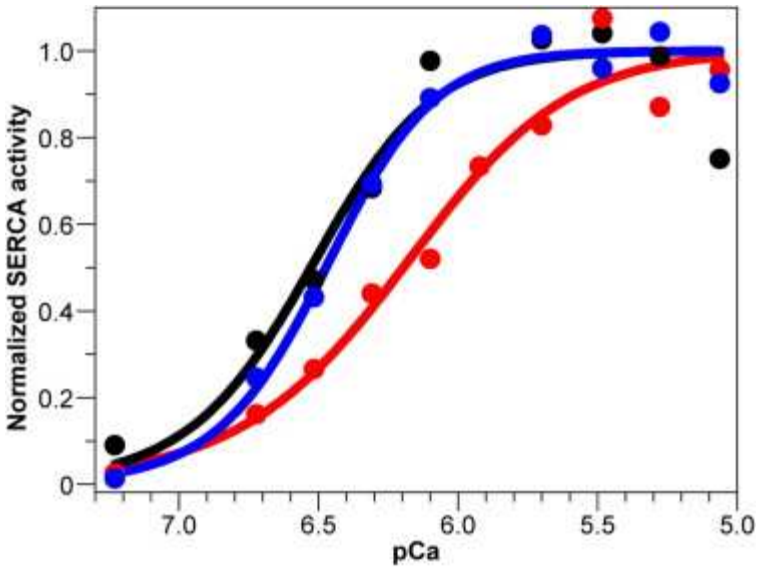

Figure 6.4: SERCA activity in the presence of pS16-PLNWT

Coupled-enzyme assays for SERCA alone (black), SERCA in the presence of PLNWT (red), or pS16-PLNWT (blue).

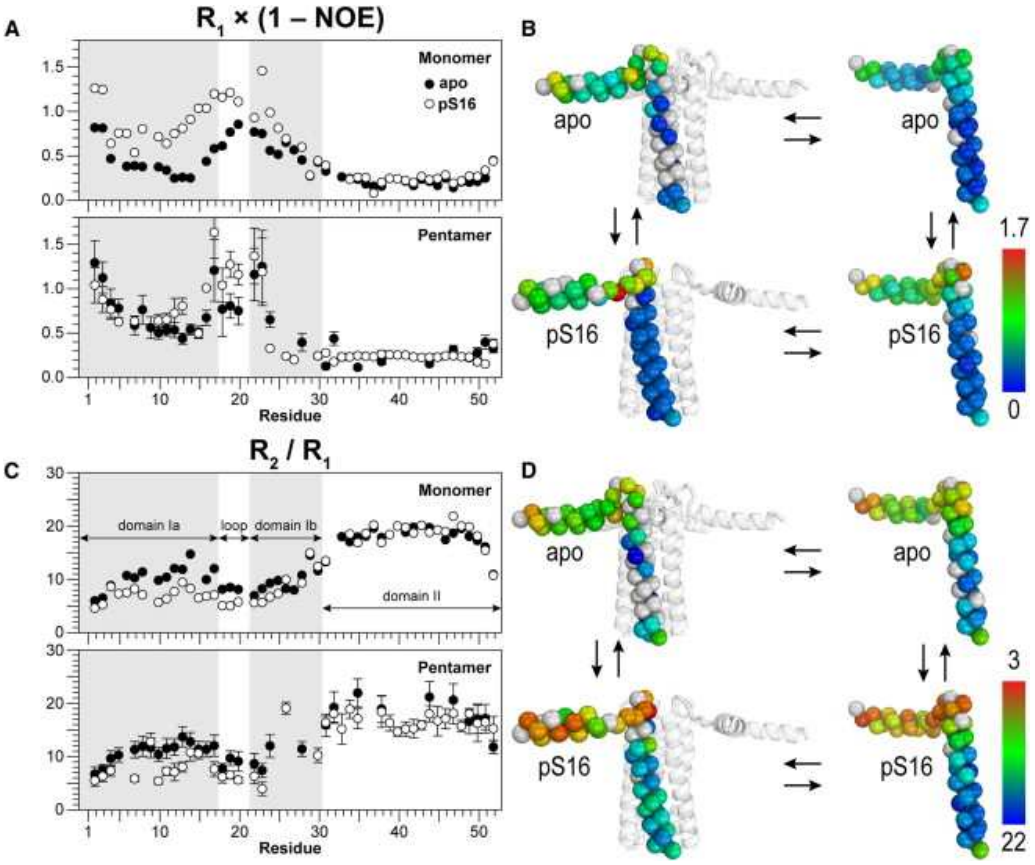

Figure 6.5:NMR dynamics of phospholamban species

(A and C) Model-independent relaxation parameters for nonphosphorylated and pS16 forms of pentameric PLNWT and monomeric PLNAFA at 600 MHz.

(B and D) Model-independent relaxation parameters derived from the 600 MHz data plotted as a color map on the structures of PLN in the nonphosphorylated and pS16 forms. Color scales for a given parameter are indicated and ramped in increments of one unit; white spheres indicate absent data.

See also Figure S6**.**

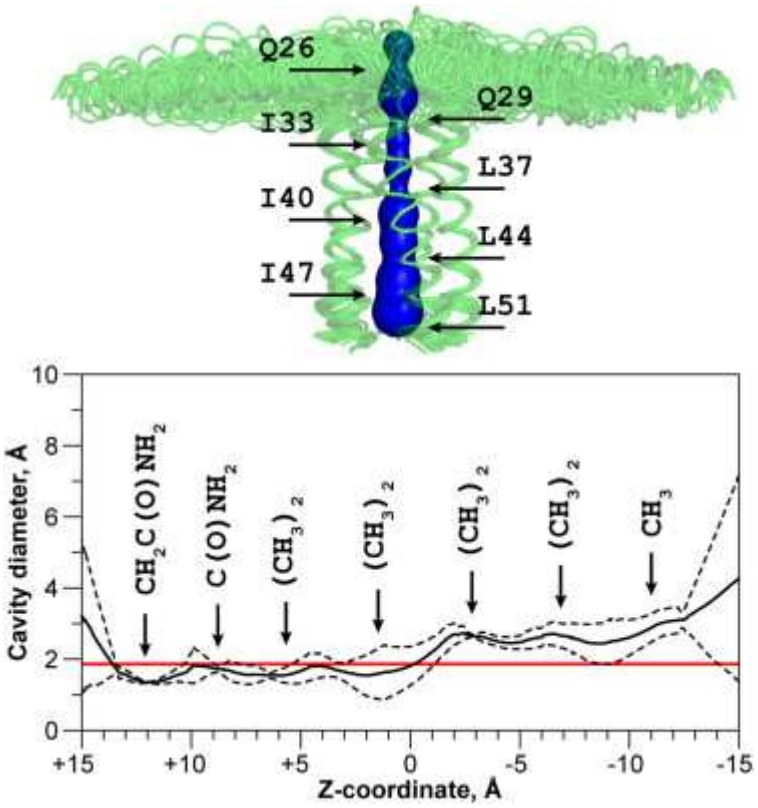

Figure 6.6: Inner pore of the pentameric assembly of pS16-PLNWT

Structural features were analyzed with the program MOLE (Petrek et al., 2007). The surface of the pore is shown in blue and is overlaid with the structural ensemble, aligned at the TM domains. The maximum pore diameter was calculated for the five lowest-energy structures and is presented as mean ± SD. The red line indicates the diameter of the nonhydrated Ca2+ ion (1.98 Å; Tsien et al., 1987).

Table 6.1: Experimental structural restraints employed during the structure calculation (per protomer).

NOE	
Strong	42
Medium	111
Weak	259
Dihedral restraints	
Phi	43
Psi	43
DARR restraints	9
Planar restraints	3
SLF restraints, unique / ambiguous	
Chemical shifts	10 / 4
Dipolar couplings	10 / 4

Table 6.2: Potential breakdown of the structural ensemble.

Geometry terms

Bonds	527 ± 15
Angles	1227 ± 47
Impropers	210 ± 30
Non-bonded	-1674 ± 40

Symmetry terms

Non-crystallographic symmetry	132 ± 39
Symmetry NOE	3 ± 2

Experimental terms

NOE	38 ± 12
Dihedrals	48 ± 25
DARR	0
Planarity	0
Anisotropic ^{15}N chemical shifts	0
Anisotropic ^{15}N-^{1}H dipolar couplings	3

Database terms

Ramachandran	-3388 ± 88
Hydrogen bonding	-492 ± 37
Residue affinity	-5 ± 1

Total energy: -3373 ± 166

Table S6.1: Structural statistics of apo (PDB entry 2KYV) and pS16 forms of WT PLN

Data was evaluated using Protein Structure Validation Suite (Bhattacharya *et al.*, 2007), Molprobity (Davis *et al.*, 2007), Pymol (DeLano, 2008) and in-house scripts. (ensemble of 20 structures).

Criterion	Apo	pS16
Ramachandran angles (Procheck), per cent		
Most favored	93.9	93.0
Additionally allowed	5.8	6.4
Generously allowed	0.3	0.3
Disallowed	0.0	0.3
Helical residues (DSSP)	3-17 and 25-51	2-14 and 24-51
Clashscore (Molprobity)	3.1 ± 1.6	6.0 ± 1.7
Molprobity score	1.8 ± 0.3	2.4 ± 0.2
RMSD of helical domains, Å		
Backbone (pentamer)	4.8 and 0.6[1]	5.6 and 1.6
Heavy atom (pentamer)	5.4 and 1.3	5.8 and 2.1
Backbone (protomer)	1.0 and 0.4	0.2 and 1.3
Heavy atom (protomer)	1.6 and 1.1	0.5 and 1.8

1. The first value is for the cytoplasmic helix, the second is for the transmembrane helix.

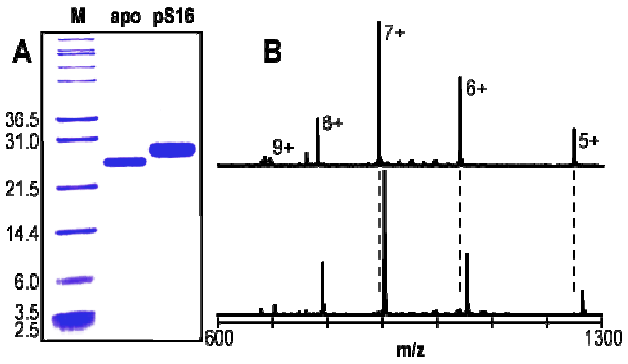

Figure S6.1: SDS-PAGE of apo and pS16 forms of PLN^{WT}

(A). Mass spectra of apo and pS16 PLN^{WT} forms (B).

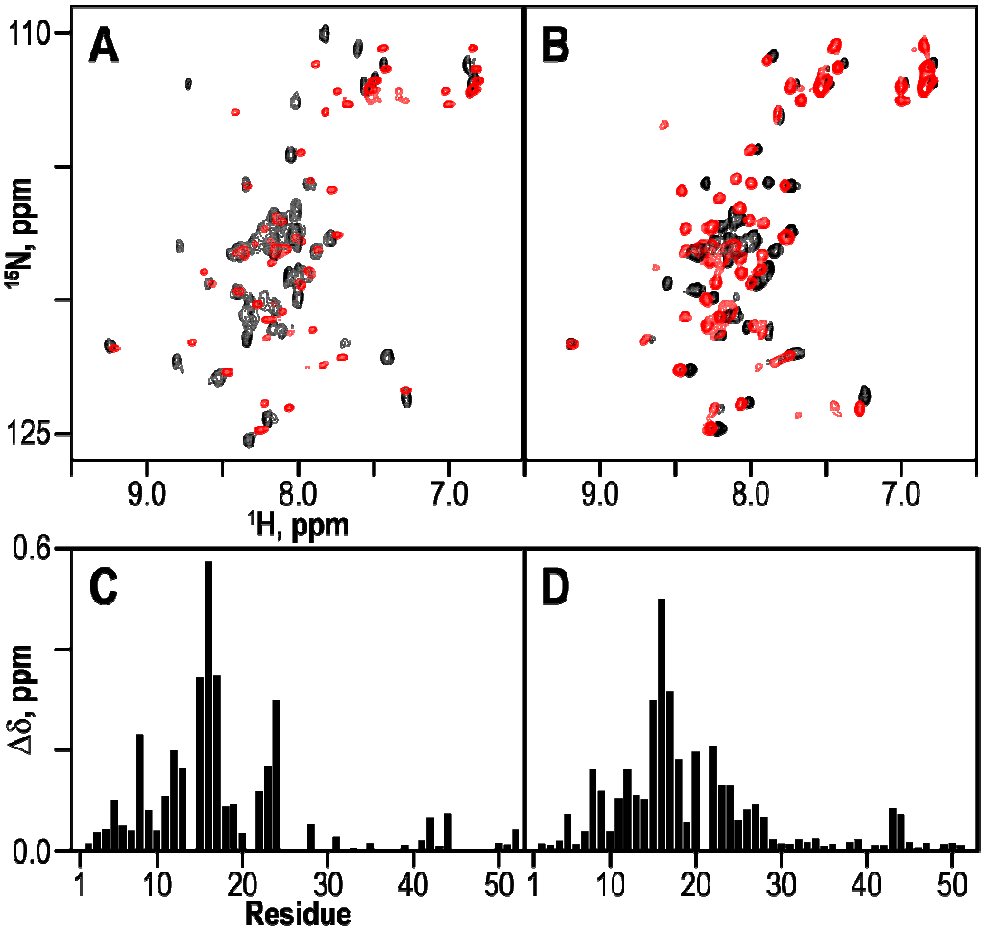

Figure S6.2: HSQC overlay of apo (black) and pS16 (red) forms of PLN and chemical shift perturbations.

A, C – PLN^{WT} (pentamer); B, D – PLN^{AFA} (monomer).

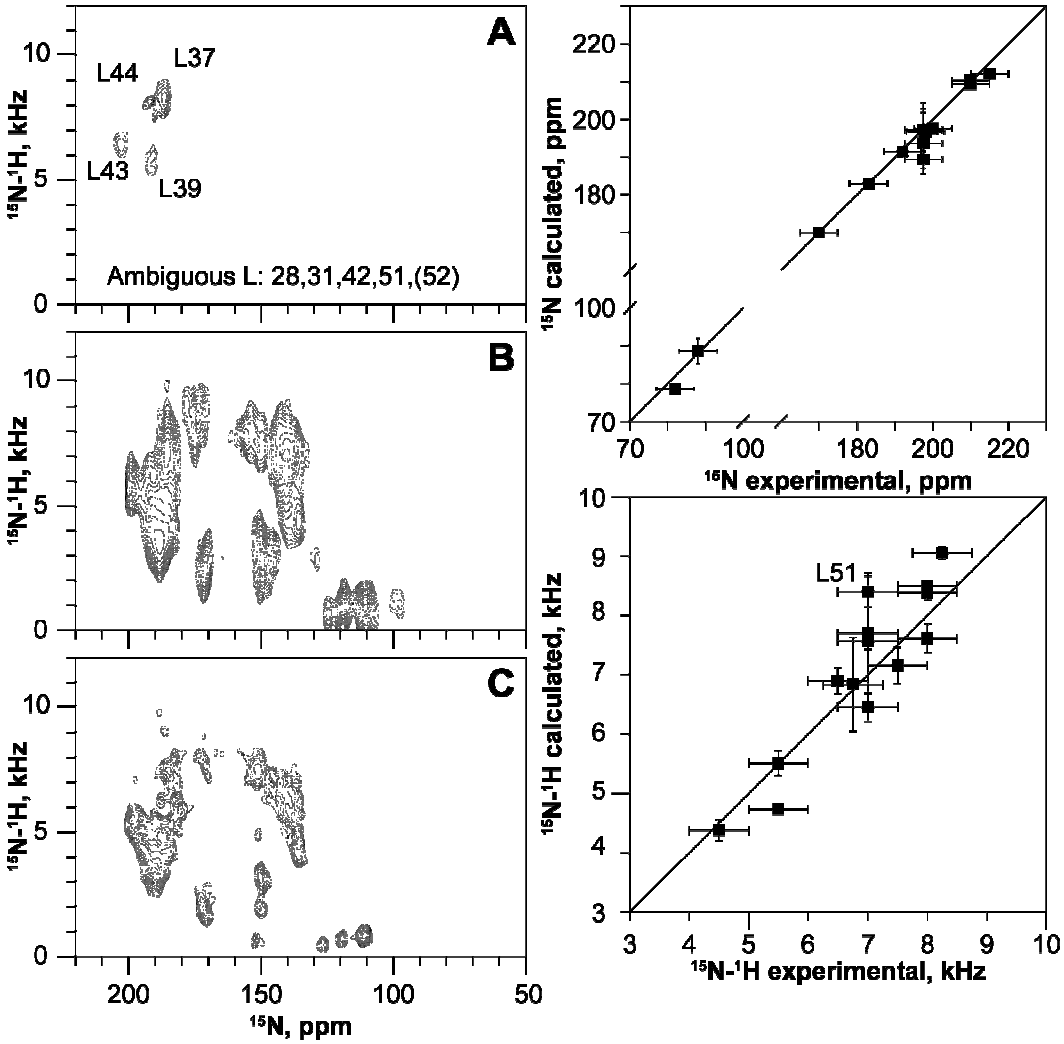

Figure S6.3: PISEMA spectra of the Leu resonances from the synthetic samples (**Figure 1, A**) overlaid with the ^{15}N-Leu sample (**Figure 1, C**), which allowed for establishing the ambiguous restraints for the remaining leucine residues (A). U-^{15}N transmembrane domain of apo (B) and pS16 (C) PLN^{WT} in magnetically aligned DMPC:POPC:DHPC bicelles.

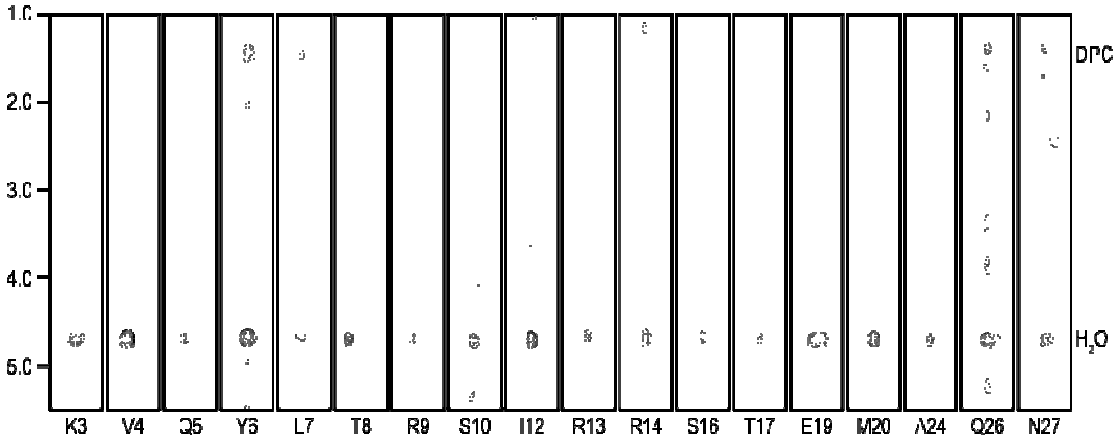

Figure S6.4: Strips from HSQC-NOE of the cytoplasmic domain of U-^{2}H,^{15}N-PLN^{WT} and fully protonated DPC.

These indicate the contacts between the back-exchanged amide sites and either DPC, or water.

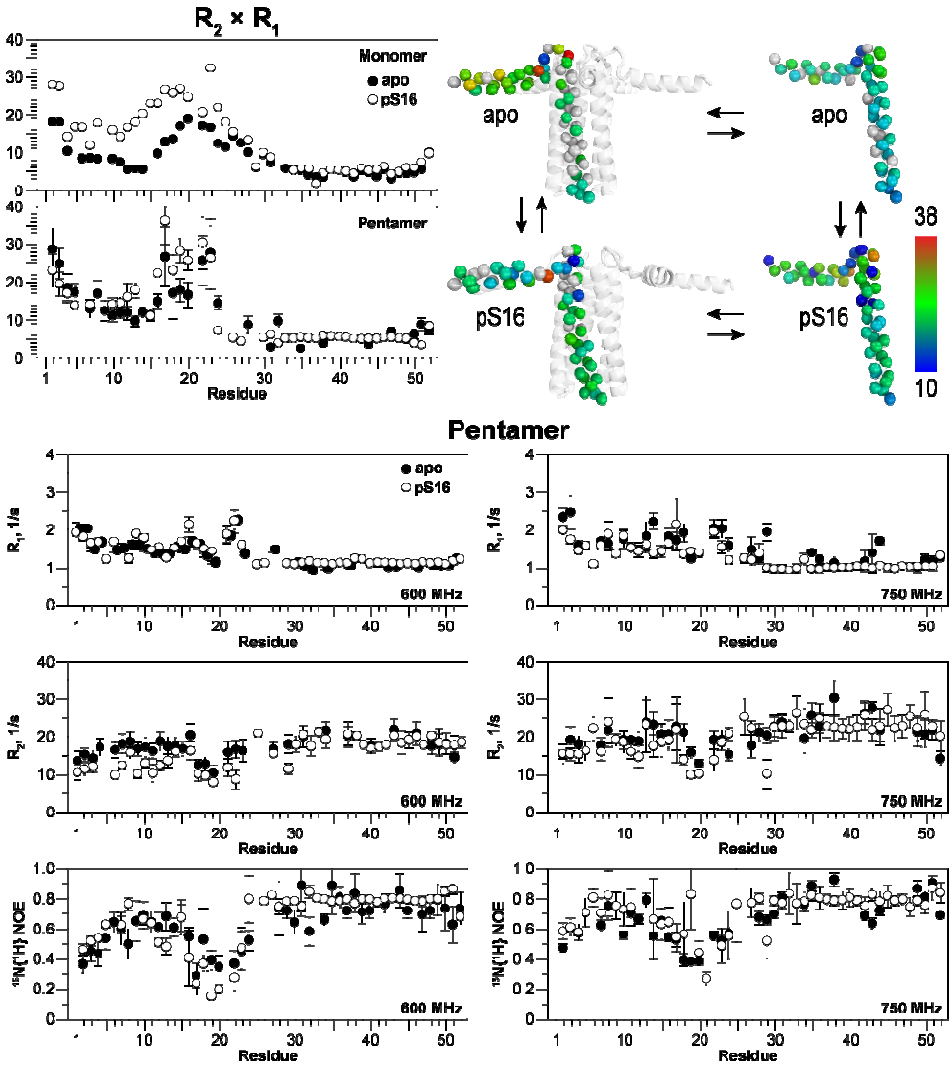

Figure S6.5: Longitudinal and transverse relaxation rates and ^{15}N-^{1}H NOE for apo and pS16 PLN^{WT}

Data is obtained ar 600 MHz and 700 MHz. Model-independent product of relaxation ratios at 600 MHz (see also Figure 4).

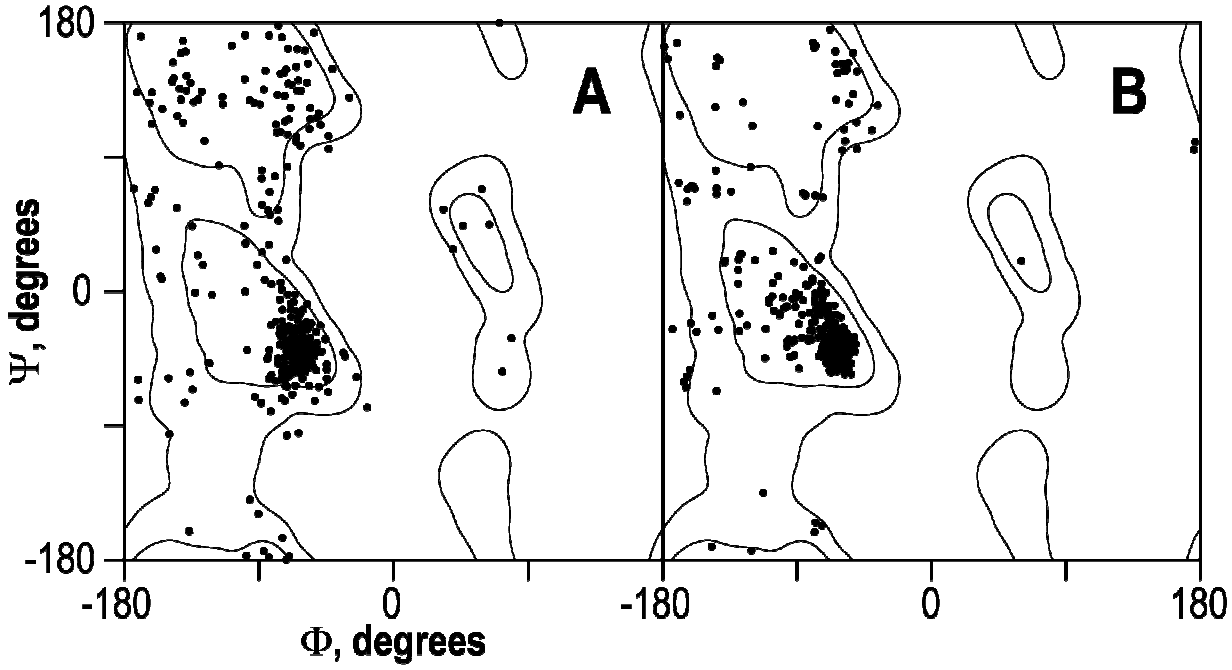

Figure S6.6: Ramachandran plots of the PLN monomer (in pentamer)

pS16-PLN^{WT} (A) and apo form (B).

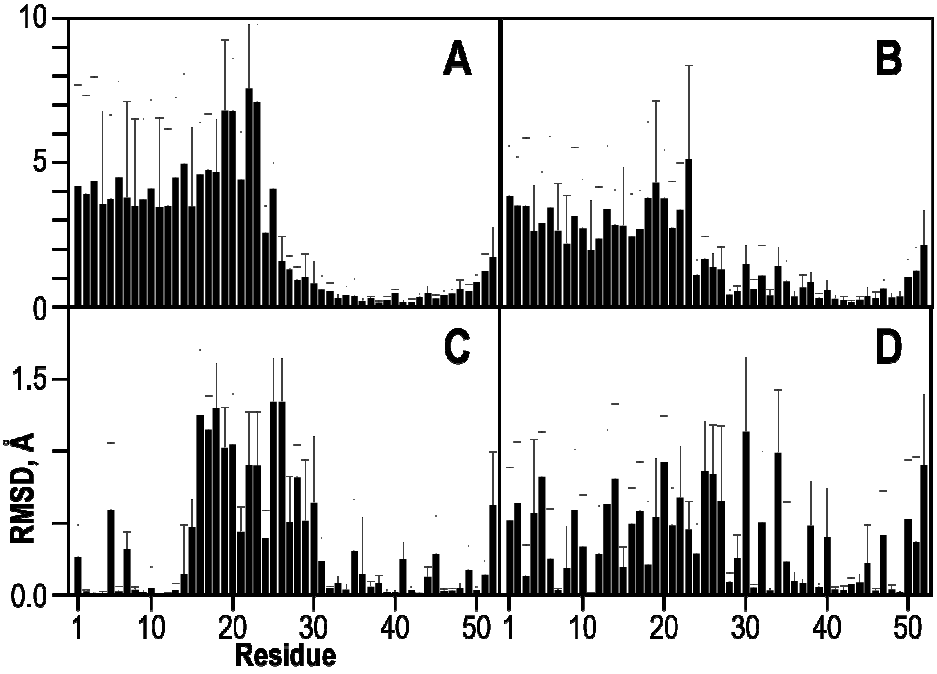

Figure S6.7: Heavy atom root mean square deviation for the structural ensemble

Value are relative to the lowest energy structure for pS16 WT PLN (A, C) and apo form (B, D). Plots are shown for the pentameric assembly (A, B) and individual protomer (C, D).

7. Allosteric regulation of SERCA by phosphorylation-mediated conformational shift of phospholamban

Martin Gustavsson, Raffaello Verardi, Daniel G. Mullen, Kaustubh R. Mote, Nathaniel J. Traaseth and Gianluigi Veglia

Reprinted with permission from **Proc. Nat. Acad Sci., USA (2013), 110, 43, 17338**

The membrane protein complex between the sarcoplasmic reticulum Ca^{2+}-ATPase (SERCA) and phospholamban (PLN) controls Ca^{2+} transport in cardiomyocytes, thereby modulating cardiac contractility. β-Adrenergic-stimulated phosphorylation of PLN at Ser-16 enhances SERCA activity via an unknown mechanism. Using solid-state nuclear magnetic resonance spectroscopy, we mapped the physical interactions between SERCA and both unphosphorylated and phosphorylated PLN in membrane bilayers. We found that the allosteric regulation of SERCA depends on the conformational equilibrium of PLN, whose cytoplasmic regulatory domain interconverts between three different states: a ground T state (helical and membrane associated), an excited R state (unfolded and membrane detached), and a B state (extended and enzyme-bound), which is noninhibitory. Phosphorylation at Ser-16 of PLN shifts the populations toward the B state, increasing SERCA activity. We conclude that PLN's conformational equilibrium is central to maintain SERCA's apparent Ca^{2+} affinity within a physiological window. This model represents a paradigm shift in our understanding of SERCA regulation by posttranslational phosphorylation and suggests strategies for designing innovative therapeutic approaches to enhance cardiac muscle contractility.

Introduction

The sarcoplasmic reticulum Ca^{2+}-ATPase (SERCA)/phospholamban (PLN) complex regulates Ca^{2+} translocation into the sarcoplasmic reticulum (SR) of cardiomyocytes and constitutes the main mechanism of cardiac relaxation (diastole) (*48*, *53*, *282*). SERCA is a P-type ATPase that translocates two Ca^{2+} ions per ATP molecule hydrolyzed in exchange for three H^+ (Fig. 7.1) (*4*, *217*). PLN binds and allosterically inhibits SERCA function, decreasing its apparent affinity for Ca^{2+} ions (*53, 283*). On β-adrenergic stimulation, cAMP-dependent protein kinase A phosphorylates PLN at Ser-16, reversing the inhibition and augmenting cardiac output (*53*). Disruptions in this regulatory mechanism degenerate into Ca^{2+} mishandling and heart failure (*53*).

Several X-ray structures of SERCA have been determined along its enzymatic coordinates, providing atomic details on the structural transitions in the absence of PLN (*4*, *217*). The first image of the SERCA/PLN complex resulted from cryo-EM studies (*284*), but the low-resolution data prevent an atomic view of PLN structure and architecture within the complex. In addition, mutagenesis and cross-linking data were used to model the complex, suggesting that the inhibitory transmembrane (TM) region of PLN is positioned into a binding groove far from the putative Ca^{2+} entry, as well as the ATP binding site, and located between TM helices M2, M4, M6, and M9 of SERCA. The location of PLN's TM domain agrees with a recent crystal structure of the SERCA/PLN complex (*58*) and is remarkably similar to the one recently identified for a PLN homolog, sarcolipin, in complex with SERCA (*56*, *57*) (Fig. 7.1).

In the SERCA/PLN model, which was further refined using NMR constraints (*285*), the loop bridging the TM and cytoplasmic domain of PLN adopts an unfolded configuration, stretching toward the N domain of the enzyme (*286*, *287*). Also, PLN's cytoplasmic domain binds SERCA's N domain in an α-helical conformation, suggesting that the inhibitory effect may be elicited via an induced fit mechanism.

Interestingly, PLN's cytoplasmic domain in the recent X-ray structure of the complex is completely unresolved (*58*), leaving many questions regarding its regulatory function unanswered. Moreover, there have been few structural data on the complex between SERCA and phosphorylated PLN. On the basis of cross-linking and sparse spectroscopic data, two different mechanistic models have been proposed: a dissociative model, in which phosphorylation causes PLN detachment from SERCA, reestablishing Ca^{2+} flux (*288*), and the subunit model, in which phosphorylation induces conformational rearrangements of PLN's cytoplasmic domain without dissociation (*289–291*). Nevertheless, the two models fall short in the interpretation of the recent structure–function correlations (*13*, *49*, *62*, *289*).

In lipid bilayers, PLN adopts a helix-turn-helix structure arranged in an L-shaped configuration (Fig. 7.1) (*86*), with the helical membrane-spanning region (inhibitory) divided into hydrophilic domain Ib and hydrophobic domain II and an amphipathic region (regulatory) domain Ia, which harbors the recognition sequence for cAMP-dependent protein kinase A. A prominent feature of PLN is its conformational dynamics. Although domain II is relatively rigid and membrane-embedded, the cytoplasmic domain Ia, domain Ib, and the intervening loop are more dynamic. Importantly, domain Ia is metamorphic, adopting a helical structure when in contact with membrane (T or ground state) and becoming unfolded when detached (R or high energy, conformationally excited state) (*62, 263, 285, 289*). On average, the L-shaped T state is the most populated in either monomeric or pentameric PLN (Fig. 1) (*86, 87*), with the R state accounting for 16–20% of the conformational ensemble (*292*). Remarkably, PLN's conformational equilibrium has been detected in both synthetic and natural SR lipid membranes (*263*) and persists in the presence of SERCA (*289, 293*). Phosphorylation of PLN at Ser-16 shifts the equilibrium, inducing an order-to-disorder transition and increasing the R state population (*62, 247, 257, 289*). To date, however, PLN's conformational equilibrium and its different structural states have never been correlated to SERCA's regulation.

Here, we used magic angle spinning (MAS) solid-state NMR spectroscopy in combination with different isotopic and spin-labeling schemes to elucidate the role of PLN's conformational equilibrium and phosphorylation in the context of the allosteric regulation of SERCA. We found that in the presence of SERCA, the TM domain of PLN remains anchored to the ATPase, whereas the cytoplasmic domain Ia populates three conformational states: T, R, and SERCA-bound (B). The inhibitory T state is in equilibrium with both the excited R state and a sparsely populated B state, which is noninhibitory and maintains the Ca^{2+} flux within a physiological window. Phosphorylation at Ser-16 shifts the equilibrium toward the B state, reversing PLN inhibitory action. We propose that enhancement of SERCA activity on PLN phosphorylation is achieved through a shift of PLN's conformational equilibrium toward

the B state, with the phosphorylated domain Ia binding a site located between the N and P domains of SERCA.

Experimental methods

All lipids were purchased from Avanti Polar Lipids. Spin-labeled sl-PE lipid was synthesized by attaching a TEMPO spin label to the head groups of PE lipids (SI Appendix, Supplementary Methods). Recombinant PLNAFA was expressed and purified according to Buck et al. (*166*) with either uniform ^{13}C,^{15}N labeling or specific amino acid labeling. PLNAFA and Graphic were synthesized using a microwave synthesizer (CEM Corporation). PLNAFA-sl was obtained according to Shi et al. (*178*), and PLNAFA was phosphorylated according to previously published methods (*62*). All PLN preparations were tested for activity on SERCA using ATPase assays (*49*). MAS samples were prepared by reconstituting SERCA and PLNAFA in lipid vesicles (SI Appendix, Supplementary Methods). The final samples contained >60% bulk water with a lipid:SERCA:PLN molar ratio of 150:1:1. MAS NMR experiments were performed on Varian (VNMRS) spectrometers operating at 600 and 700 MHz and equipped with $^{1}H/^{13}C$ 3.2-mm BioMAS probes. A summary of samples and experiments is shown in SI Appendix, Table S1.

Results and discussion

SERCA Selects the R-State Conformation of PLN's Domain Ia. MAS NMR experiments carried out in synthetic and SR lipid membranes reveal that PLN's cytoplasmic domain Ia populates two major states (T and R) in slow exchange (*263*). To detect both states simultaneously, it is necessary to perform NMR experiments in a temperature range between 277 and 293 K. In fact, at lower temperatures (235–270 K), the R state is virtually invisible to NMR (*285*) and can only be detected by electron paramagnetic resonance (EPR) (*292*). In the 277–293 K temperature range, the dynamic R state can be detected by refocused insensitive nuclei enhanced by polarization transfer (rINEPT) and

dipolar assisted rotational resonance (DARR) experiments. The rINEPT experiment filters out the resonances associated with the T-state of domain Ia, as well as those of domains Ib and II, but detects only the mobile resonances of the R state in domain Ia (SI Appendix, Fig. S7.1) (*263*, *294*). In contrast, the DARR experiment detects both T and R states simultaneously but requires selective ^{13}C labeling to eliminate the intense signals arising from residues of domains Ib and II (SI Appendix, Fig. S1) (*263*).

To map the conformational equilibrium in lipid membranes, we coreconstituted SERCA with ^{13}C labeled PLN. To eliminate the pentamer/monomer equilibrium, we used a functional monomeric variant of PLN, PLNAFA, carrying C36A, C41F, and C46A mutations (*295*). The SERCA/PLNAFA complex was then co-reconstituted in phosphatidylcholine / phosphatidylethanolamine / phosphatidic acid (PC/PE/PA) lipid vesicles (8:1:1 molar ratio) at a 150:1:1 lipid:SERCA:PLNAFA molar ratio to mimic the SR membrane composition (*296*). Under these experimental conditions, SERCA and PLNAFA form a fully functional complex (Fig. 7.1 C and D), with their cytoplasmic domains facing mostly the outside of the lipid vesicles (*297*, *298*). On binding SERCA, the Cα chemical shifts of the residues of PLNAFA domains II and Ib are virtually superimposable on those of the free state, with a chemical shift index (CSI) indicative of a helical conformation of the membrane-spanning helix on binding (Fig. 2 A and B and SI Appendix, Fig. S7.2 and S7.3). The only exceptions are the Cα resonances of Asn-30 and Asn-34, which display chemical shift changes of ∼1 ppm. In contrast, the methyl resonances of the TM domain show significant chemical shift perturbations (e.g., Ile-38 and Leu-42 in Fig. 7.2D). These residues were predicted to be cofacial to the TM residues of the ATPase (*286*) (Fig. 7.2E). Importantly, several residues of domain Ia display two distinct chemical shifts, corresponding to helical and unfolded conformations (Fig. 7.2C). The relative intensity (population) of these resonances changes as a function of the temperature, demonstrating the presence of a slow conformational exchange in the NMR time scale (SI Appendix, Fig. S7.4). In the absence of SERCA, the two conformations correspond to T and R states. On SERCA binding, the majority of the resonances in the T

state show only slight chemical shift changes, whereas marked perturbations are observed for residues in the R state, which shift from the R to a B state (Fig. 7.2C and SI Appendix, Fig. S7.3). Remarkably, the chemical shifts of the B state correspond to an extended conformation, demonstrating that the interaction with SERCA does not promote a helix in domain Ia, as previously proposed (*285*, *286*). Altogether, the chemical shift mapping demonstrates that SERCA binds PLN with the inhibitory domains Ib and II in helical conformations, with a well-defined face of PLN binding to SERCA. These data are in remarkable agreement with mutagenesis, X-ray crystallography, and cross-linking data (*58*, *286*, *299*). Importantly, the T state of the cytoplasmic domain does not interact with the enzyme, whereas the R state shifts to an extended B state.

Mapping of SERCA/PLN interactions by paramagnetic relaxation enhancements

Mapping the physical interactions between membrane protein complexes such as the SERCA/PLN complex (~116 kDa) is very challenging. Therefore, we designed a comprehensive strategy combining several isotopic and spin-labeling schemes that involve both proteins and lipid membranes (SI Appendix, Fig. S7.5). To detect protein–protein and protein–lipid interactions, we used paramagnetic relaxation enhancements (PREs), as measured by MAS NMR spectroscopy (*300*). First, we engineered a (2,2,6,6-tetramethylpiperidin-1-yl) oxidanyl (TEMPO) spin label at Cys-674 of SERCA (SERCAC674-sl; SI Appendix, Fig. S7.6). This residue, situated in the P domain of the enzyme, is an ideal reporter for interactions between SERCA and the cytoplasmic domains of PLN. Next, we reconstituted SERCAC674-sl with uniformly or selectively ^{13}C-labeled PLNAFA and mapped the PRE effects, monitoring intensities of the 13C resonances, using ^{13}C-^{13}C DARR experiments. Although the spin label at Cys-674 did not affect the residues in domains Ib and II of PLNAFA (SI Appendix, Fig. S7.7), several resonances of domain Ia in the B state were quenched (Fig. 7.3). The most affected residues are located in the middle of domain Ia, with Tyr-6 and Leu-7 almost completely broadened out (Fig. 7.4 and SI Appendix, Fig. S7.8). The latter demonstrates that these

residues must be within a sphere with radius ~15 Å defined by the centroid of the spin label attached to C674 in the P domain of SERCA. The intensities of residues located at both the N-terminal end of domain Ia and in the loop (Ala-0, Met-1, Met-20, and Pro-21) remain largely unperturbed (Fig. 7.4 B and C). Remarkably, the resonances of domain Ia corresponding to the T state remain essentially unquenched relative to the B state (Fig. 7.3C), suggesting that this state remains associated with the lipid membrane. Taken together, the PRE patterns show that the central region of domain Ia binds SERCA at a site located near Cys-674 in the P domain of the enzyme.

To better define the location of the B state of PLN domain Ia, we inverted the spin-labeling scheme, engineering an (1-Oxyl-2,2,5,5-tetramethylpyrroline-3- methyl) methanethiosulfonate (MTSSL) spin label at residue 7 of PLNAFA (PLNAFA-sl) and labeling SERCA with ^{13}C- methyl methanethiosulfonate (*301*). The ^{13}C- methyl methanethiosulfonate reacts with SERCA's native cysteines, forming methyl thiocysteines (MTC). Under these experimental conditions, six cysteine residues of SERCA are methylated, as assessed by solution NMR spectroscopy, and the MTC-labeled SERCA (MTC-SERCA) retains its ATPase activity (Fig. 7.4D and SI Appendix, Fig. S7.9). To map SERCA/PLN interactions, we coreconstituted MTC-SERCA with PLNAFA-sl in 1,2-dimyristoyl-sn-glycero-3-phosphatidylcholine lipid vesicles. The methyl group signals from MTC-SERCA were detected using conventional and water-edited cross-polarization (CP) experiments (*302*) in the presence of reduced and oxidized PLNAFA-sl. A single unresolved peak for all six labeled sites is observed at ~25 ppm (Fig. 7.4E and SI Appendix, Fig. S7.9). The water-edited CP eliminated most of the lipid background and enhanced the peak envelope corresponding to the MTC groups. PLNAFA-sl binding to the enzyme quenched the intensity of MTC-SERCA methyl peaks significantly (Fig. 7.4E and SI Appendix, Fig. S7.9), suggesting domain Ia binds a site located between the N and P domains of SERCA. Although at this stage we cannot assign the methyl resonances of MTC-SERCA individually, these data complement the PRE quenching data obtained with SERCAC674-sl on the PLN backbone.

To confirm that the T state of domain Ia remains associated with the lipid membrane, we monitored the PRE effects of PLNAFA-sl in complex with SERCA on the ^{13}C natural abundance resonances of the lipid bilayer. The ^{13}C lipid resonances display a bimodal distribution of their intensities (Fig. 7.5A). Although a significant decrease in intensity was observed for the peaks corresponding to the lipid chain and head groups, the glycerol moiety was virtually unaffected. Therefore, we deduced that the nitroxide spin label at position 7 of the T state must be deeply embedded in the membrane, as it quenches the intensities of the resonances corresponding to the alkyl groups in the core of the lipid bilayer. In contrast, the reduction of the peak intensities corresponding to the head groups can be explained by transient interactions of the spin label in the mobile R state with the surface of the lipid bilayer. To further validate these results, we engineered a nitroxide spin label on a PE head group of the lipid (PEsl, 1,2-dioleoyl-sn-glycero-3-phosphoethanolamine-N-amido-TEMPO; SI Appendix, Fig. S7.10) and measured PRE from PEsl to selectively 13C-labeled PLNAFA in complex with SERCA (Fig. 5B). The nitroxide spin label of PEsl positioned in the glycerol region of the lipid bilayer (SI Appendix, Fig. S7.11) selectively quenches the T-state resonances of domain Ia (Fig. 7.5B), supporting the conclusion that domain Ia in the T state is absorbed on the surface of the lipid membrane.

PLN Phosphorylation and SERCA Regulation. To determine the effects of phosphorylation on the SERCA/PLN complex, we repeated the MAS NMR analysis on PLNAFA phosphorylated at Ser-16 (PLNpS16AFA). We found that the chemical shifts in domain II are similar for SERCA/PLNAFA and SERCA/ PLNpS16AFA (SI Appendix, Fig. S7.12). Specifically, the significant change in Cα shift with respect to free PLNAFA is a strong indicator of SERCA binding and confirms that the TM domain remains bound to SERCA on phosphorylation, as recently demonstrated by EPR spectroscopy (17).

When monitored by rINEPT experiments, the intensities of the 13C resonances of PLNpS16AFA domain Ia in the free form are much higher than those of the

unphosphorylated PLNAFA, a finding indicative of an order-to-disorder transition on phosphorylation (SI Appendix, Fig. S7.12). In contrast, on binding SERCA, the intensities of the resonances for domain Ia of PLNpS16AFA decrease dramatically compared with the unphosphorylated form. At the same time, we detect an increase of the B-state peaks in the DARR experiments. For instance, the intensities of the Ala-0, Ala-11, and Ala-15 peaks of PLNpS16AFA in the rINEPT spectrum decrease by more than 30%, with respect to the free state (SI Appendix, Fig. S7.12) but increase substantially in the DARR spectrum (Fig. 7.6A). These data suggest that the cytoplasmic domain of phosphorylated PLN undergoes a disorder-to-order transition on binding SERCA (i.e., the equilibrium is shifted from the R to a more rigid B state). We also acquired PRE experiments for the SERCA/ PLNpS16AFA complex, detecting a pattern similar to that found for the SERCA/PLNAFA complex (Fig. 7.6B). Importantly, the 13C resonances of residues Lys-3, Val-4, Tyr-6, Leu-7, Ala-11, and Ala-15 are almost completely quenched by SERCAC674-sl, providing solid evidence that domain Ia of phosphorylated PLN binds SERCA's cytoplasmic domain (Fig. 7.6B). Therefore, phosphorylation does not cause dissociation of domain Ia from the ATPase; rather, it acts on the conformational equilibrium of PLN's regulatory domain, shifting its populations toward the B state. The small differences in the quenching profiles between PLNAFA and PLNpS16AFA indicate a slight rearrangement of the B state on phosphorylation, suggesting that the phosphorylated cytoplasmic region of PLN relieves inhibition of SERCA by interacting with an allosteric site located between the N and P domains. For example, this could be achieved by electrostatic interactions between the phosphate group of PLNpS16 and an acidic patch in the ATPase.

The Conformational Equilibrium of PLN Regulates SERCA Activity. On the basis of our findings, we propose that SERCA function is controlled by PLN's conformational equilibrium and that phosphorylation promotes the B state via a conformational shift mechanism (*303*). In the presence of SERCA, PLN exists in equilibrium between three conformational states: T, R, and a sparsely populated B state (noninhibitory). In the

inhibitory T state, PLN interacts with SERCA only via the TM domain, with domain Ia lying on the surface of the lipid bilayer. In the R state, the TM domain of PLN is still helical and bound to SERCA, whereas domain Ia is unfolded and in equilibrium with the B state. In the absence of phosphorylation, the population of the B state is low, but phosphorylation of PLN at Ser-16 increases its population, activating SERCA (Fig. 6A).

To validate our mechanistic model, we synthesized a truncated version of PLNAFA, corresponding to domains Ib and II (Graphic), and coreconstituted it with SERCA. If our hypothesized mechanism (Fig. 7.7) were correct, we would expect an increase of inhibitory potency of PLN on removal of the sparsely populated cytoplasmic B state. In fact, the deletion of the regulatory domain Ia resulted in an ∼25% increase in inhibitory potency with respect to full-length PLNAFA (SI Appendix, Fig. S7.13), confirming the role of a sparsely populated B state in maintaining SERCA activity within a physiological range.

From our model, the idea emerges that PLN does not function as a simple on/off switch for Ca^{2+} translocation; rather, its conformational equilibrium exerts a gradual control ("physiological rheostat") on SERCA activity that determines SERCA's physiological window of function (*304*). PLN phosphorylation at Ser-16 skews the conformational ensemble toward the B state (i.e., the non-inhibitory complex), increasing SERCA's apparent Ca^{2+} affinity and augmenting contractility within the physiological window. Aberrant or abolished PLN phosphorylation would cause SERCA's activity to be outside the physiological window, resulting in Ca^{2+} handling degeneration and cardiomyopathies (*305*). Finally, the current model explains why dominant-negative mutants of PLN can be obtained by biasing PLN conformational equilibrium toward the excited, more dynamic R state (*49*, *62*, *63*).

In conclusion, we mapped the interactions between the two membrane proteins SERCA and PLN. We found that an equilibrium among different conformations (ground, excited, and bound states), rather than one unique state of PLN, contributes to SERCA regulation.

This conformational equilibrium explains the reversibility of the inhibitory action to enable cyclic translocation of Ca^{2+} ions, contributing to the coupled cardiac contraction and relaxation processes. According to our model, inhibition reversal depends on the population of the noninhibitory B state that probably undergoes a slight structural rearrangement on binding. The latter represents a paradigm shift with respect to the dissociative model proposed for SERCA regulation and explains why promoting the R state via point mutations generates dominant-negative mutants of PLN (*49*, *62*, *63*). These mutants or, alternatively, small molecules mimicking the effect of PLN phosphorylation could be potential candidates for protein therapy aimed at reversing heart failure by fine-tuning Ca^{2+} transport (*306*, *307*).

Supplementary methods

Sample preparation

SERCA Ia was purified from hind-leg rabbit skeletal muscle as previously described, eluting the protein either in C12E8 (1) or DPC (2). Labeling of SERCA with 4-(2-Iodoacetamido)-TEMPO (Sigma) on Cys 674 of SERCA was achieved by incubation of rabbit skeletal muscle SR with a two-fold molar excess of spin label for 1h in 30 mM MOPS buffer containing 300 mM sucrose prior to purification of the protein. Labeling was quantified using electron paramagnetic resonance (EPR) and determined to be 1:1 label:SERCA (molar ratio). Methylthiocysteine (MTC)-labeling of SERCA was achieved by incubating $C_{12}E_8$-solubilized sarcoplasmic reticulum (1% (w/v) $C_{12}E_8$) for 16h with a 10-fold molar excess of ^{13}C-MMTS prior to purification of SERCA.

Solution NMR samples were prepared by concentrating DPC-solubilized MTC-SERCA to 10 mg/mL. The final sample contained 250 mM DPC, 1 mM $MgCl_2$, 20 mM MOPS, 1 mM $CaCl_2$, 2.5% (v/v) glycerol, 5% D_2O, and 4 mM Adenosine diphosphate (ADP). For magic angle spinning (MAS) NMR samples 9 mg of either d_{54}-DMPC (MTC-SERCA samples) or 9 mg of an 8:1:1 (w/w/w) mixture of egg PC/PE/PA lipids (all other samples) in chloroform were dried down under N_2(g), lyophilized, and resuspended in 500 □L of buffer (20 mM HEPES, 1 mM $MgCl_2$, 100 mM KCl, pH 7.0). 25 mg of $C_{12}E_8$ (detergent/lipid ratio of 4:1 w/w) was added to form a clear solution of mixed micelles. For samples with spin labeled bilayers, 2 % (mole/mole) of the lipids were substituted by sl-PE. 0.5 mg of PLN (PLN^{AFA}, $PLN^{pS16AFA}$ or sl-PLN^{AFA}) was solubilized in 1% (w/v) $C_{12}E_8$ and added to the mixed micelles. 9 mg of SERCA was added from an 8 mg/mL solution containing 1% $C_{12}E_8$ (w/v), 1 mM $MgCl_2$, 20 mM MOPS, 1 mM $CaCl_2$ and 20% (v/v) glycerol. The sample volume was adjusted to 10 mL and the sample was incubated 3h with Biobeads at a 30:1 Biobeads:$C_{12}E_8$ ratio (w/w). After removal of the Biobeads, the sample was diluted to 50 mL with buffer (20 mM HEPES, 1 mM $MgCl_2$, 100 mM KCl, 2.5% glycerol, 1 mM EGTA, pH 7.0) and centrifuged at 200,000×g at 4°C for 30

min. The hydrated pellet from the centrifugation was transferred directly to a 3.2 mm MAS rotor for NMR measurements. The final sample contained >60% bulk water with a lipid:SERCA:PLN molar ratio of 150:1:1.

NMR experiments

Solution NMR experiments were carried out at 25°C on Varian (VNMRS) spectrometers operating at proton frequencies of 600 and 700 MHz equipped with triple resonance HCN probes. [^{13}C,^{1}H]-HSQC experiments were acquired with 512 scans in the direct ^{1}H dimension and 100 increments and a spectral width of 3000 Hz in the indirect ^{13}C dimension. MAS NMR experiments were performed on Varian (VNMRS) spectrometers equipped with ^{1}H/^{13}C 3.2 mm BioMAS Varian probes, operating at proton frequencies of 600 and 700 MHz. SQ-DQ experiments were acquired at a spinning rate of 8 kHz, a cross-polarization (CP) time of 1 ms and spectral widths of 100 and 16 kHz in the single and double quantum dimensions, respectively. A 500 μs SPC5 element (3) was used for double quantum excitation and reconversion. Dipolar assisted rotational resonance (DARR) (4), and refocused Insensitive Nuclei Enhanced by Polarization Transfer (rINEPT) (5) experiments were acquired at 20°C using a spinning rate of 8 kHz. Pulse widths were 2.5 μs for ^{1}H and 5.5 μs for ^{13}C and proton TPPM decoupling was applied at 71.4-100 kHz. DARR experiments were acquired using a 1 ms CP time and a 200 ms DARR mixing time. 4000 points with a spectral width of 100 kHz were acquired in the direct ^{13}C dimension, and 24-48 increments with spectral widths of 16 or 32 kHz were acquired in the indirect ^{13}C dimension. rINEPT experiments were acquired with a spectral width of 100 kHz in the direct ^{13}C dimension and a spectral width of 4 kHz in the indirect ^{1}H dimension. In water-edited CP experiments, the ^{1}H polarization of water is transferred via spin diffusion to ^{1}Hs of protein, followed by cross polarization to ^{13}C. This experiment utilized a 3 ms Gaussian pulse was used for selective excitation of water resonance, a T_2 filter of 2 ms, and a spin diffusion time of 200 ms. Chemical shifts of PLN^{AFA} were assigned from DARR experiments of synthetically and recombinantly ^{13}C,^{15}N labeled samples. Experiments were acquired at -20°C and 20°C to assign the T

and R state peaks, respectively. For PRE measurements, spectra were acquired before and after quenching of the spin label by addition of 10 mM DTT (for spin labeled SERCA) or 10 mM ascorbate (for $PLN^{AFA\text{-}sl}$) and the PRE was quantified as

$$PRE = I/I_0$$

where I and I_0 are the peak intensities before and after quenching of the spin label, respectively. Errors were estimated from

$$\sigma_{PRE}/PRE = \sqrt{((\sigma_I/I_I)^2 + (\sigma_{I0}/I_{I0})^2)}$$

where σ_I and σ_{I0} is the baseline noise in the respective spectra and σ_{PRE} is the estimated error for the PRE value. Data were processed by NMRPipe(6) and viewed and analyzed using Sparky. Chemical shifts were referenced to the CH_2 signal of adamantane (40.48 ppm) for MAS samples and to 2,2-dimethyl-2-silapentane-5-sulfonate for solution NMR samples.

ATPase activity assays

SERCA and PLN were co-reconstituted in an 8:1:1 mixture of egg PC/PE/PA lipids as described elsewhere (*49*). The final samples contained a lipid:PLN:SERCA molar ratio of 700:5:1. A coupled enzyme assay was used to monitor SERCA activity at 25 ºC as a function of calcium concentration as previously described (*14*, *49*). Data were fit using the Hill equation:

$$V = V_{max}\frac{1}{1 + 10^{-n(pKCa-pCa)}}$$

to determine the calcium concentration needed to achieve half maximal activity (pK_{Ca}).

Synthesis of spin-labeled lipid (PE^{sl})

1,2-dioleoyl-sn-glycero-3-phosphoethanolamine (DOPE) (8.2 mL, of a 2 % w/v solution in $CHCl_3$) (0.22 mmol, 164 mg) was placed in a 25 mL round bottom flask and the $CHCl_3$ was removed under a stream of N_2. Dichloromethane (10 mL) was added and removed *in vacuo* to remove possible traces of ethanol. A solution of EDC (0.22 mmol, 38.4 mg) with 4-carboxy-TEMPO (0.22 mmol, 40.0 mg) in dichloromethane (1.0 mL) was added to DOPE lipids dissolved in dichloromethane (9 mL). DIEA (0.22 mmol, 39.0 uL) was added to the mixture and the reaction was stirred for ~48 h. The dichloromethane was removed *in vacuo* and the residue was taken up in ethyl acetate (25 mL) and transferred to a separatory funnel. The solution was washed with 1N HCl (3 x 15 mL). An emulsion formed that was partially broken by addition of small amounts of MeOH and saturated NaCl solution. The emulsion was mainly found in the aqueous phase and could be extracted without loss of product. The organic phase was dried over $MgSO_4$ and concentrated using a vacuum pump. The crude product was analyzed by TLC (R_f = 0.71, $CHCl_3$/MeOH/H_2O, 65:31:4). The final yield was 118 mg, 58 %. Deconvoluted ESI-MS, calc.: 925.7, found: 925.7.

FRET experiments

SERCA was incubated for 30 min by a 20-fold excess of 5-((((1-iodoacetyl)amino)ethyl)amino)naphthalene-1-sulfonic acid (IAEDANS) (Invitrogen) to attach the fluorescent AEDANS group to Cys 674. The label-ing extent was determined by absorbance at 334 nm (εAEDANS= 6100 M-1 cm-1). To introduce an acceptor for energy transfer, PLN^{AFA} was incubated in 1% SDS, 100 mM $NaHCO_3$ at pH 9 for 16 h with a 20-fold excess of 4-((4-(dimethylamino)phenyl)azo)benzoic acid, succinimidyl ester (dabcyl-SE), and free label was removed using reverse-phase HPLC. Labeling efficiency was determined by electrospray ionization mass spectrometry (ESI-MS). $SERCA^{AEDANS}$ was co-reconstituted with PLN^{Dab} at molar ratios of 1:0, 1:1 and 1:2 at a 700:1 lipid:$SERCA^{AEDANS}$ ratio. Steady-state fluorescence was measured with a Varian

Eclipse Fluorimeter, using an excitation wavelength of 351 nm (20 nm bandwidth) and emission wavelengths between 400 and 600 nm.

Mass spectrometry

$SERCA^{C674SL}$ solubilized in $C_{12}E_8$ was subjected to sodium dodecyl sulfate polyacrylamide gel electrophoresis (SDS-PAGE). The gel band corresponding to SERCA was cut out of the gel and trypsin digested. The resulting peptides were separated using a nano-HPLC system in-line with a LTQ Orbitrap Velos (Thermo scientific) mass spectrometer. Spin labeled peptides were identified by dual mass spectrometry (MS/MS).

Table S7.1: Solid State NMR samples

Labeling (PLN^{AFA})	Labeling (SERCA/ lipid)	Experiment	Temp (°C)	Time (h)
Assignment				
u 13C,15N		DARR (6ms)	20	41
		DARR (25ms)	20	50
		DARR (200ms)	20	60
		SQ-DQ	20	73
		SQ-DQ	-20	46
		rINEPT	20	45
13C QEN		DARR (200ms)	20	53
		SQ-DQ	20	77
		rINEPT	20	32
13C QENPYR		DARR (200ms)	4	143
13C QENSKT 13C A		DARR (25ms)	4	100
		DARR (200ms)	20	70
		rINEPT	20	35
13C V4,L7,A11,I12,A15,I18		DARR (200ms)	20	135
		DARR (200ms)	-20	135
		SQ-DQ	-20	91
		rINEPT	20	64
13C N30,L31,F32,I33		SQ-DQ	20	105
		DARR (15ms)	20	68
13C N34,F35,A36,L37,I38		SQ-DQ	20	97
		DARR (15ms)	20	91
		DARR (200ms)	20	56
13C L39,I40,F41,L42		SQ-DQ	20	96

		DARR (200ms)	20	59
13C L44,I45,A46,I47		SQ-DQ	20	114
13C A24,I48,V49,L51		SQ-DQ	20	114
pS16 u13C		DARR (6ms)	20	16
		DARR (200ms)	20	80
		rINEPT	20	55
pS16 13C QEN 13C A		DARR (25ms)	20	57
		DARR (200ms)	20	57

PRE

13C V4,L7,A11,I12,A15,I18	C674SL	DARR (200ms)	4	68*2
		rINEPT	20	46*2
u 13C	C674SL	DARR (200ms)	20	60*2
		rINEPT	20	36*2
pS16 u13C	C674SL	DARR (200ms)	20	45*2
		rINEPT	20	43*2
13C V4,L7,A11,I12,A15,I18	sl-PE	DARR	4	112*2
L7-SL	MTC	CP	20	2.2*2
		Water-CP	20	17*2

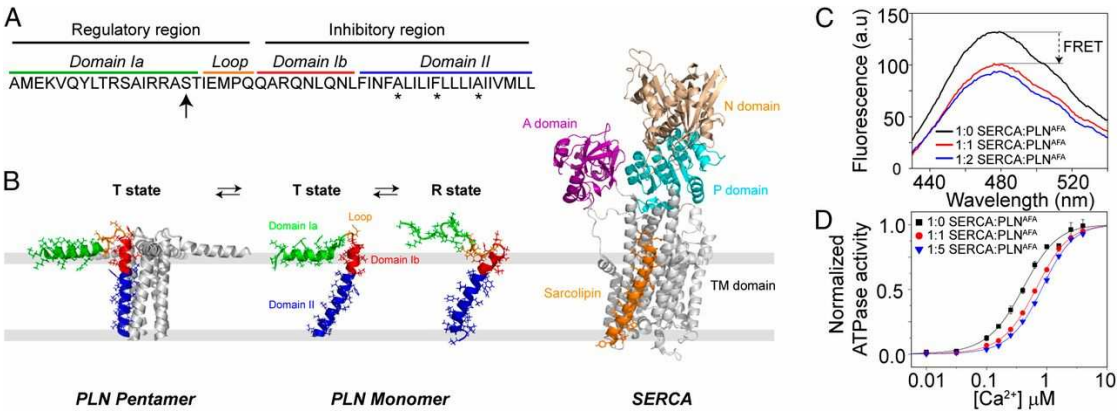

Figure 7.1: Structures of PLN and SERCA.

(A) Primary sequence and domains of PLNAFA. The S16 phosphorylation site is marked with an arrow, and mutation sites (C36A, C41F, C46A) are indicated with asterisks. (B) 3D structures of PLN pentamer [Protein Data Bank (PDB) ID code 2KYV], PLNAFA monomer in the T (PDB ID code 2KB7) and R states (PDB ID code 2LPF), and SERCA in complex with sarcolipin (PDB ID code 3W5A). SERCA includes 10 TM helices and three cytoplasmic domains: nucleotide binding (N domain), actuator (A domain), and phosphorylation (P domain). (C) Fluorescence energy transfer (FRET) between SERCAAEDANS (donor) and PLNDab-AFA (acceptor), showing the formation of the complex. (D) Ca^{2+}-dependent ATPase activity of the SERCA/PLN complex in PC/PE/PA lipid vesicles at lipid:PLN:SERCA molar ratios of 700:1:1 and 700:5:1.

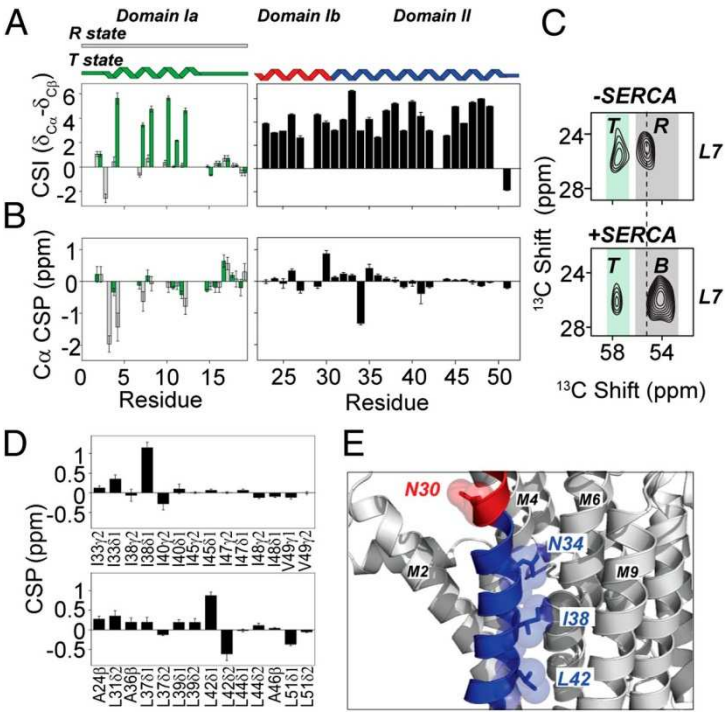

Figure 7.2: NMR mapping of PLNAFA changes on SERCA binding.

(A) CSI (δCα-δCβ) of PLNAFA in complex with SERCA obtained from [13C,13C]-DARR and single quantum-double quantum (SQ-DQ) correlation experiments at −20 °C, 4 °C, and 20 °C in 8:1:1 PC/PE/PA bilayers . The CSI was calculated as δ13Cα−δ13Cβ−(δ13Cα,RC−δ13Cβ,RC), where RC stands for the random coil chemical shifts. (B) Cα chemical shift changes on SERCA binding. Chemical shift perturbations (CSPs) are calculated as the difference in the chemical shifts with and without SERCA (δT,+SERCA - δT-SERCA for the T state; δB,+SERCA - δR,-SERCA for the B state). The peaks corresponding to E2, S16, T17, I18, and E19 were not resolved. (C) Portion of the [13C,13C]-DARR spectrum showing Cα-Cδ correlations of Leu-7 in the absence (Upper) and presence (Lower) of SERCA. In the absence of SERCA, the T state is in slow exchange with the R state. SERCA binding shifts the populations toward the B state. Shaded areas indicate α-helical (green) and coil (gray) chemical shift ranges. (D) CSP of the TM methyl groups. (E) TM region of the molecular model by Toyoshima et al. (9), with PLN residues with large CSP highlighted.

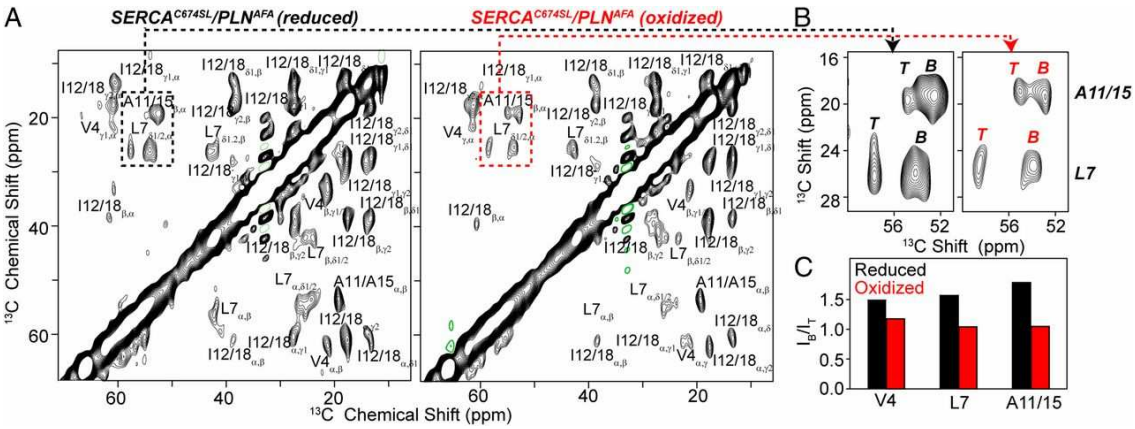

Figure 7.3: Mapping protein–protein interactions using PREs effects from SERCAC674-sl to PLNAFA.

(A) Selected region of the [13C,13C]-DARR spectra (4 °C) of 13C,15N-labeled PLNAFA at Val-4, Leu-7, Ala-11, Ile-12, Ala-15, and Ile-18 (PLNAFA6cyt) in complex with SERCAC674-sl before and after addition of DTT. (B) Portion of the [13C,13C]-DARR spectra showing Cα-Cβ and Cα-Cδ correlations for Ala-11 and Leu-7 corresponding to the T and B states. (C) Relative peak intensities (IB/IT) for T- and B-state resonances for V4, L7, and A11/A15 peaks in the presence of reduced (black bars) and oxidized (red bars) SERCAC674-sl, respectively.

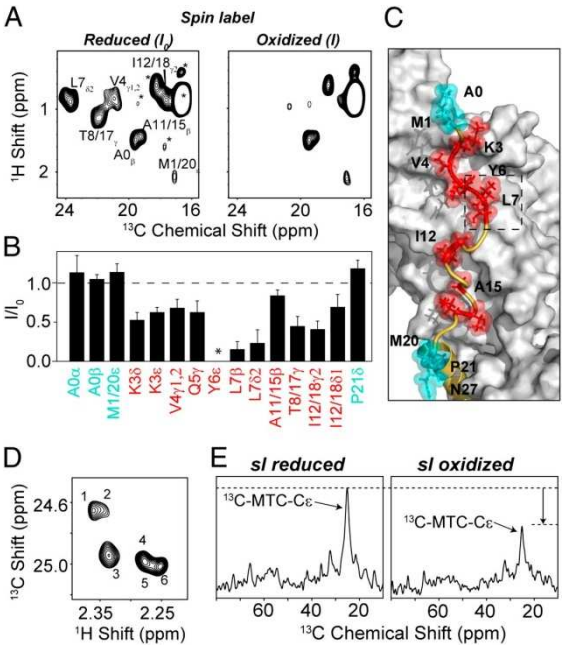

Figure 7.4: Mapping the interactions between domain Ia of PLN and SERCA.

(A) Methyl region of rINEPT spectra in the presence and absence of SERCAC674-sl. Lipid peaks are marked with asterisks. (B) Intensity retention plot for residues in domain Ia, as probed by rINEPT experiments. I and Io are the peak intensities before and after addition of DTT. Error bars reflect the signal-to-noise ratio in the spectra. Resonances broadened beyond detection are marked with asterisks. (C) PRE effects mapped onto PLN structure: affected residues are in red, and unaffected are in cyan. Dashed box highlights resonances broadened beyond detection. The model was obtained by manual unfolding of domain Ia from the Toyoshima complex (9). (D) [1H,13C] heteronuclear single quantum correlation (HSQC) spectrum of 13C-MTC-SERCA in dodecylphosphocholine (DPC) micelles. (E) Water-edited CP spectra of 13C-MTC-SERCA in the presence of PLNAFA-sl before and after addition of ascorbate to reduce the spin label. The additional peaks correspond to the natural abundance 13C resonances of lipids and proteins.

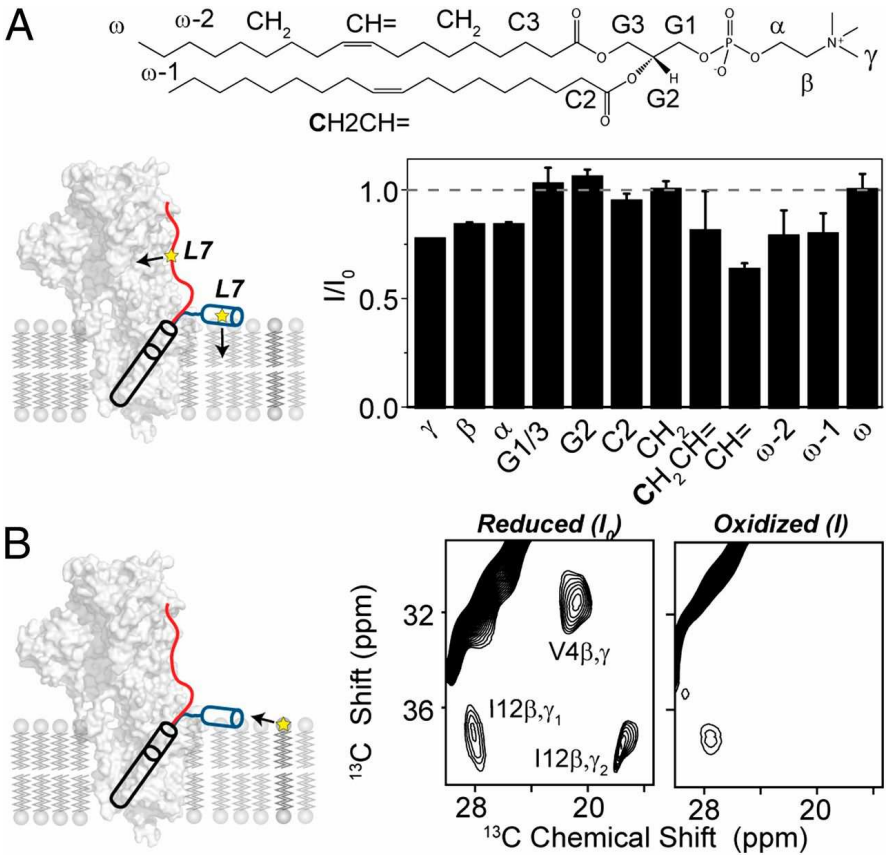

Figure 7.5: Lipid association for the T state of domain Ia mapped by PREs.

(A, Upper) Chemical structure and nomenclature of 1,2-dioleoyl-sn-glycero-3-phosphocholine (DOPC); (Lower) PRE effects of SERCA/PLNAFA-sl complex on the PC/PE/PA lipid resonances. I and I0 correspond to the peak intensities before and after addition of 10 mM ascorbate, respectively. (B) Representative regions of [13C,13C]-DARR spectra of V4, L7, and I12 of PLNAFA in complex with SERCA in the presence of PEsl lipids before and after addition of 10 mM DTT, showing that the T state of domain Ia is quenched by the spin label on the membrane surface. Experiments were acquired at 4 °C.

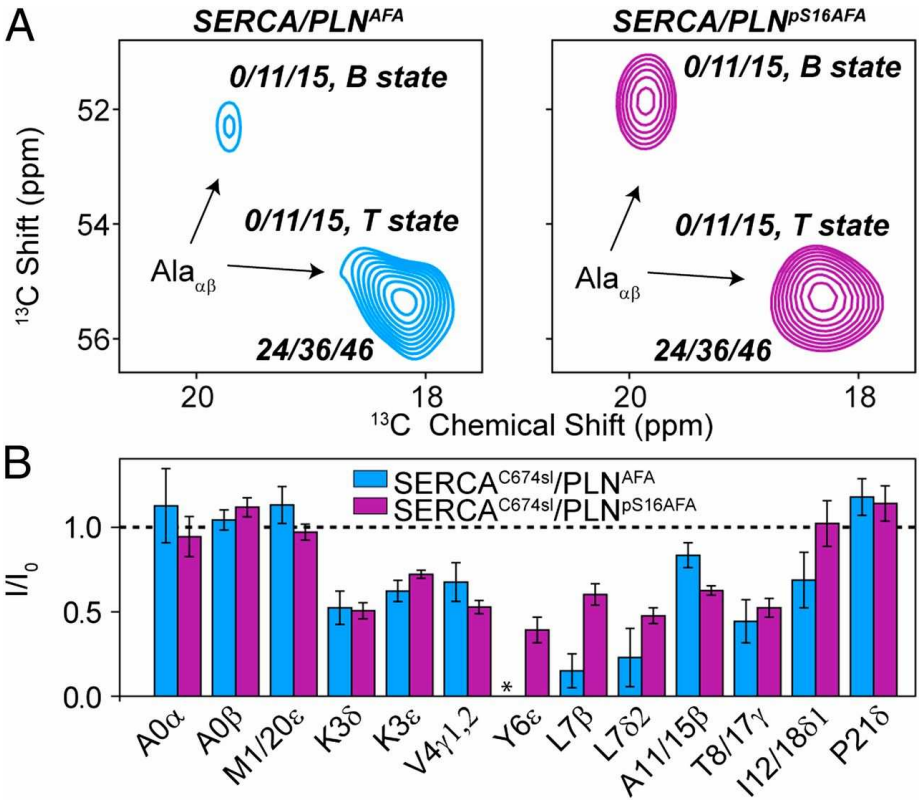

Figure 7.6: Effects of Ser-16 phosphorylation of PLN on the conformational equilibrium.

(A) Representative region of [13C,13C]-DARR spectra showing Ala resonances of PLNAFA and PLNpS16AFA in complex with SERCA. The DARR spectra were acquired at 20 °C with 200 ms mixing time. (B) Intensity retention of phosphorylated and unphosphorylated PLN in the presence of SERCAC674-sl. Undetectable peaks in the presence of spin label are marked with asterisks.

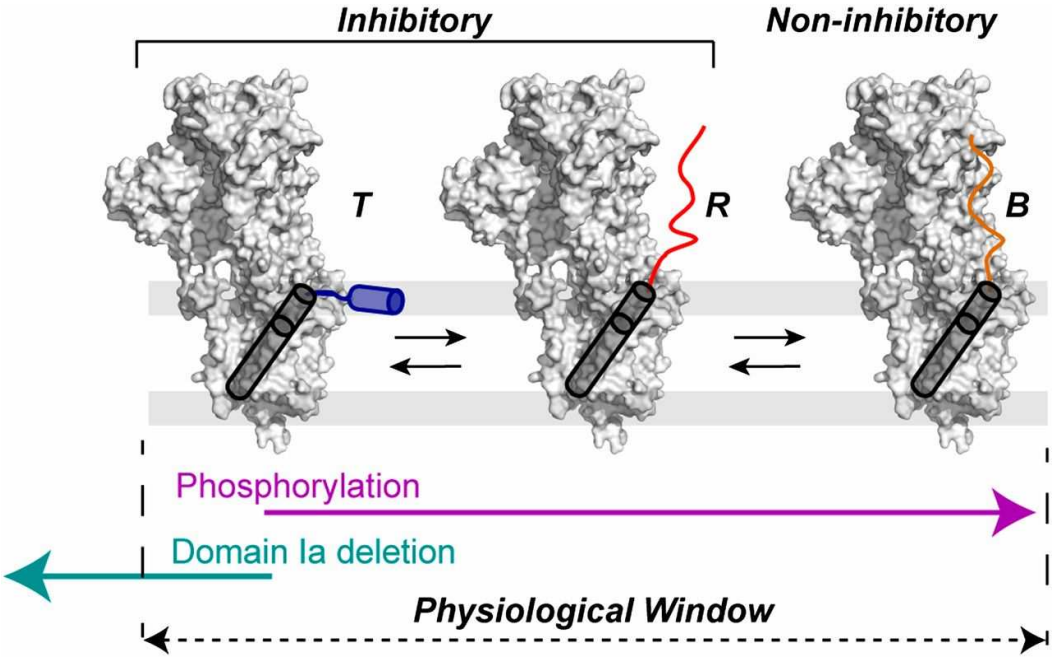

Figure 7.7: Allosteric regulatory model of SERCA by PLN.

Conformational equilibrium of PLN bound to SERCA with inhibitory T and R states and noninhibitory B state. Phosphorylation shifts the equilibrium toward the noninhibitory B state, whereas deletion of cytoplasmic domain Ia results in an inhibitory effect greater than full-length PLN, which is outside the physiological window of inhibition.

Supplementary results

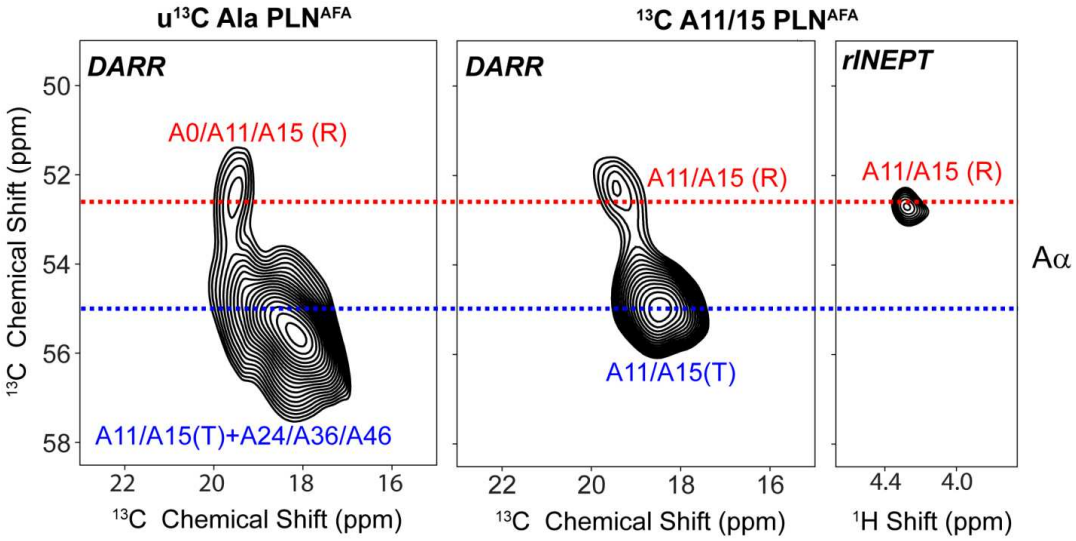

Figure S7.1: Detection of the conformational equilibrium of free PLN^{AFA}.

Left: [^{13}C,^{13}C] DARR spectrum of uniformly labeled AFA, displaying the resonances of A11 and A15 from cytoplasmic residues and A24, A36, A46 from the TM domain. Center: [^{13}C,^{13}C] DARR spectum A11/15 labeled PLN^{AFA}, revealing both the T and R states of domain Ia. Right: rINEPT experiment showing only the mobile R state resonances for A11 and A15. All spectra were acquired at 20°C

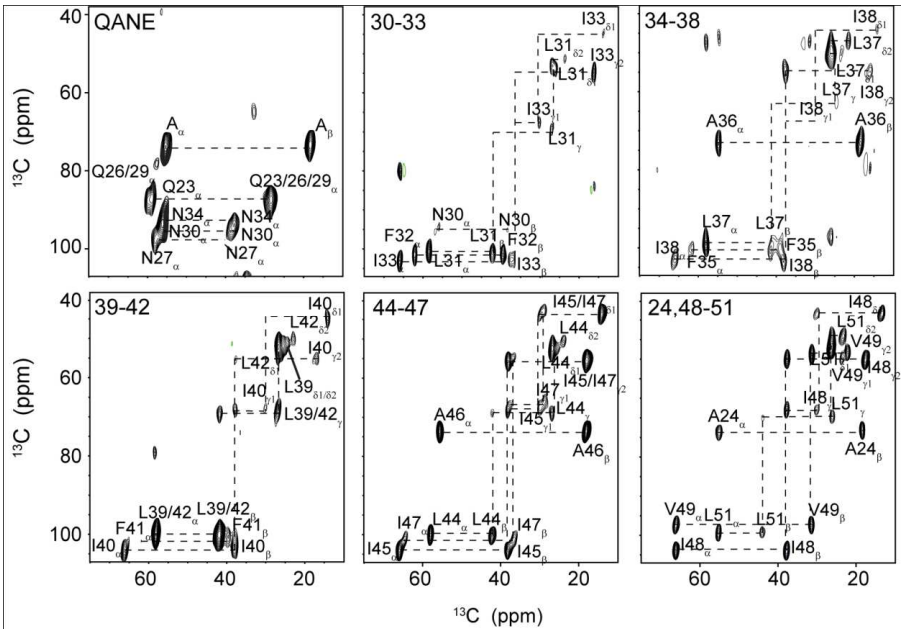

Figure S7.2: Representative SQ-DQ [^{13}C,^{13}C] spectra used for assignment of PLN^{AFA} in complex with SERCA

Spectra are from synthetic and recombinant ^{13}C-labeled PLN^{AFA} samples. The residue numbers of ^{13}C-labeled residues are indicated in top left corner of the spectra. All of the experiments were acquired at 20°C.

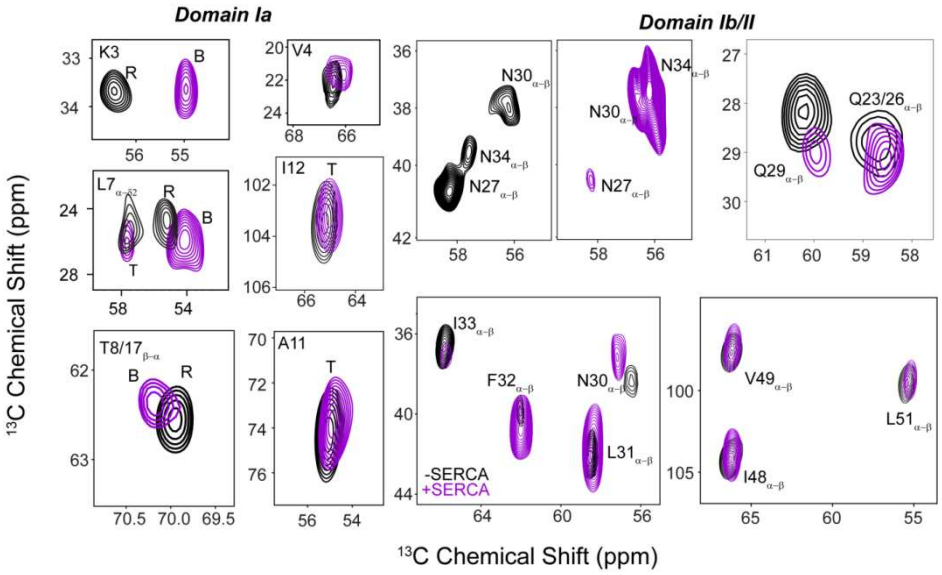

Figure S7.3: Chemical shift changes of PLN^{AFA} upon binding SERCA.

Selected regions of the [^{13}C,13C]-DARR and SQ-DQ spectra of synthetic and recombinant ^{13}C-labeled PLN^{AFA} samples acquired in the presence (purple) and absence (black) of SERCA.

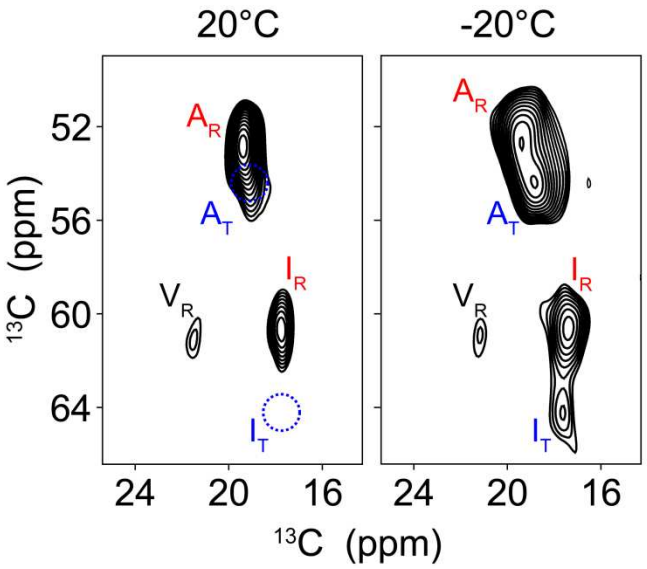

Figure S7.4: Selected regions of the [^{13}C,^{13}C]-DARR spectra of the SERCA/PLN^{AFA} complex

Spectra are at 20 and -20 °C. PLN^{AFA} was synthesized with ^{13}C-labeled V4,L7,A11,I12,A15, and I18. Dotted circles highlight the positions of Ile and Ala T state peaks that are not detectable or significantly attenuated at 20°C.

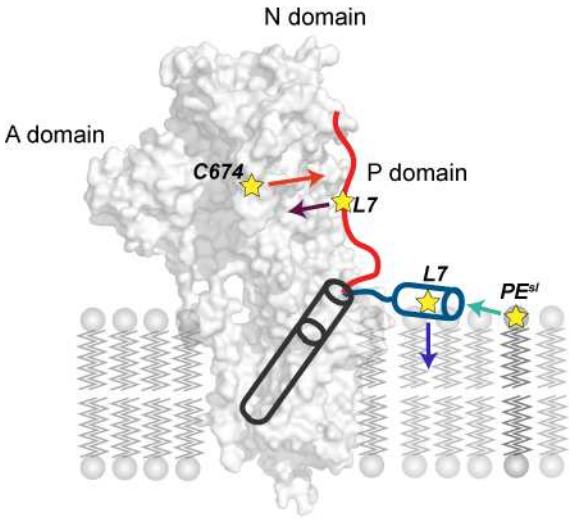

Figure S7.5: Strategy utilized to map the conformational equilibrium of PLN bound to SERCA.

PREs were measured using spin-labeled SERCA at Cys 674(SERCA$^{C674\text{-}sl}$) on the resonances of ^{13}C-labeled PLN^{AFA} (orange arrows). Also, complementary PREs were measured using spin-labeled PLN^{AFA} with MTSSL at position 7 (PLN$^{AFA\text{-}sl}$) on the methyl resonances of ^{13}C MTC-SERCA (purple arrow). Membrane association of domain Ia was obtained monitoring the PREs from PLN$^{AFA\text{-}sl}$ to ^{13}C natural abundance signals of the aliphatic resonances of the lipid (blue arrow), and from spin labeled PE lipids (PE^{sl}) on the resonances of ^{15}N,^{13}C-labeled PLN^{AFA} (cyan arrow).

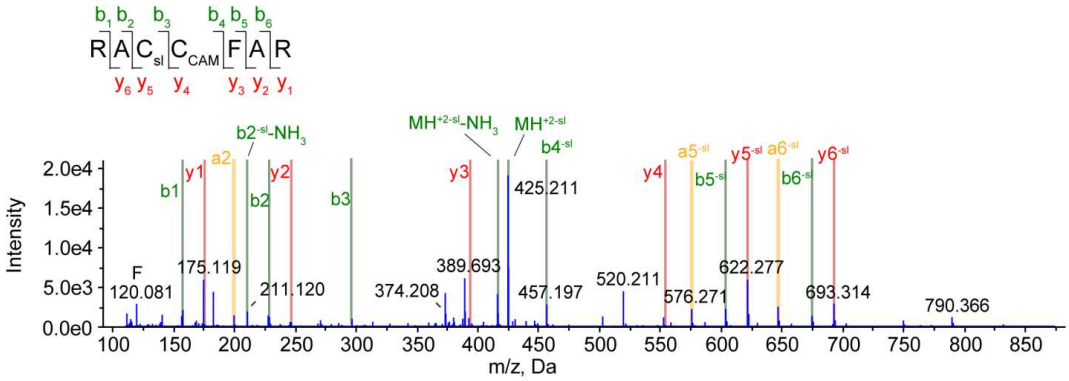

Figure S7.6: Identification of spin label site on SERCA using ESI-MS/MS.

The detected peptide corresponds to $RAC_{IASL}CFAR$ (residues 672-678) with a measured MW of 1094.5433 (theoretical MW: 1094.5477). Peaks labeled with –sl are due to fragmentation of the spin labeled side chain to dehydroalanine (mass loss of 246.14135 Da). CAM indicates caramidomethylation of C675 due to incubation of the tryspinized peptides with iodoacetamide to block disulfide formation during sample preparation.

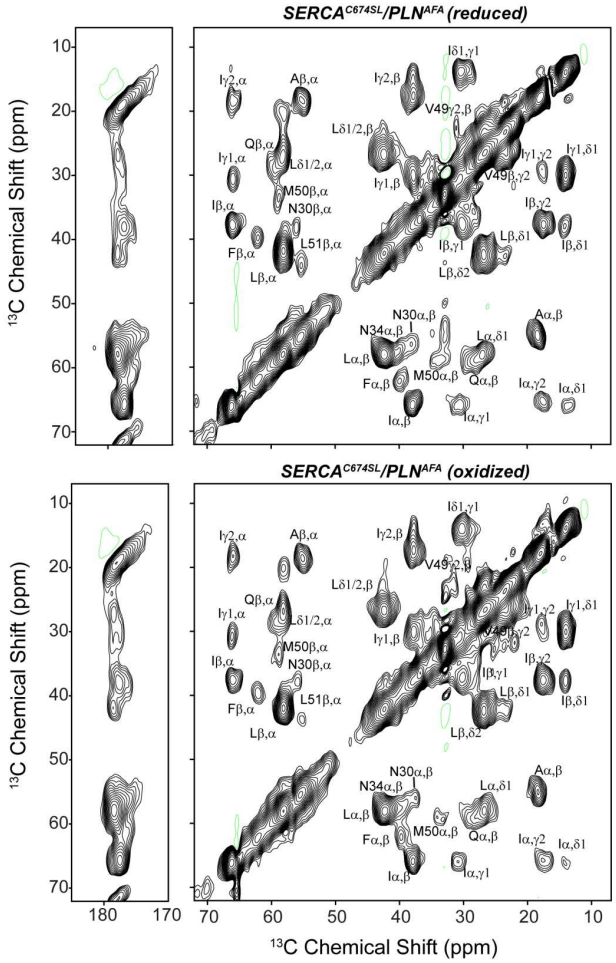

Figure S7.7: [^{13}C,^{13}C]-DARR spectra of uniformly labeled ^{13}C-PLN^{AFA} in complex with SERCA$^{C674\text{-}sl}$

Spectra are before (top) and after (bottom) addition of 10 mM DTT. Experiments were acquired with a 6 ms DARR mixing time at 20°C.

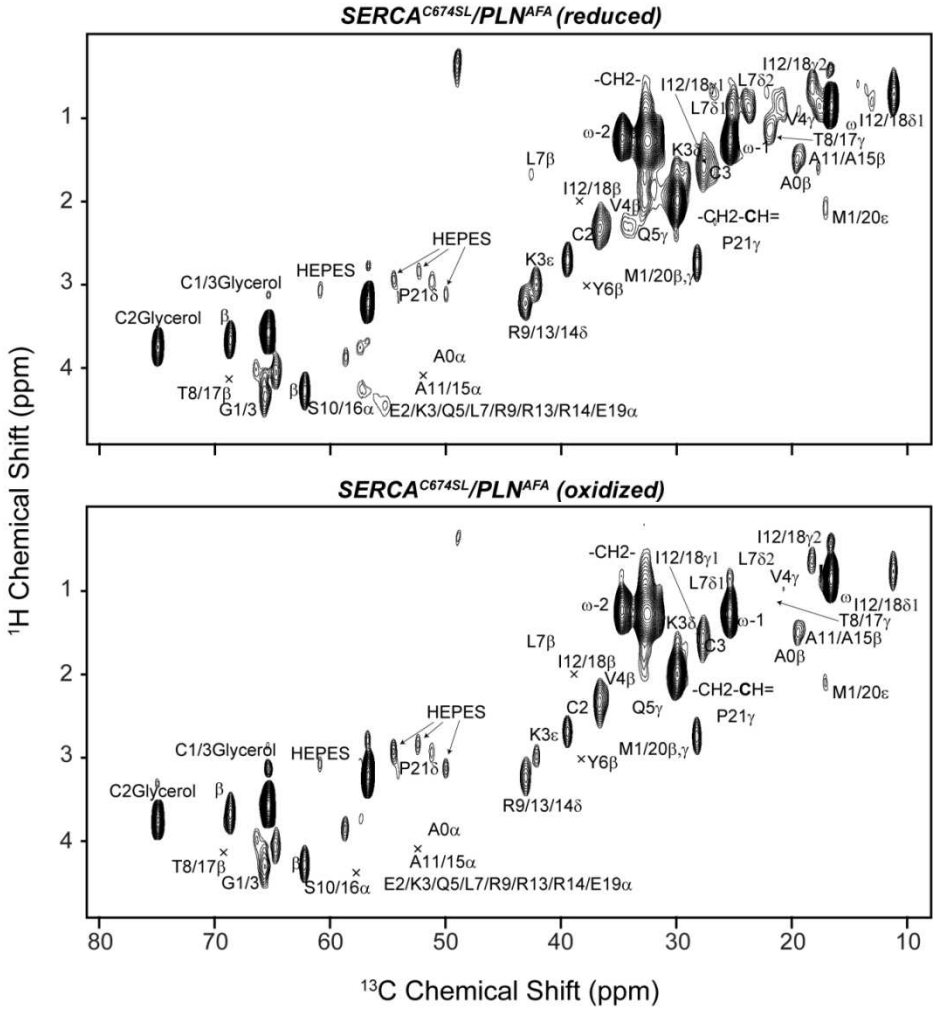

Figure S7.8: [^{1}H,^{13}C]-rINEPT spectra of PLN^{AFA} in complex with SERCA$^{C674\text{-}sl}$

Spectra are before (bottom) and after (top) addition of 10 mM DTT to reduce the spin label. Spectra were acquired at 20°C

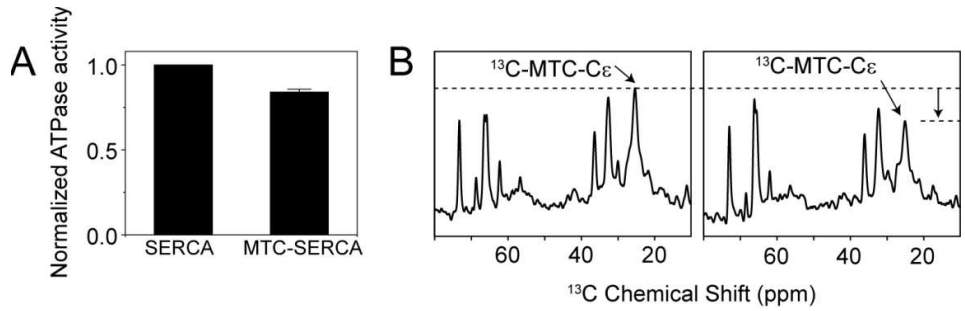

Figure S7.9: A) Comparison of SERCA activity before and after methylation at the cysteine residues.

The activity was normalized to an unlabeled control. Error bars represent the standard deviation of three independent measurements. B) CP spectra of ^{13}C-MTC-SERCA in the presence of PLN$^{AFA\text{-}sl}$ acquired before and after addition of ascorbate. The additional peaks in the spectra correspond to the natural abundance ^{13}C resonances of lipids and proteins.

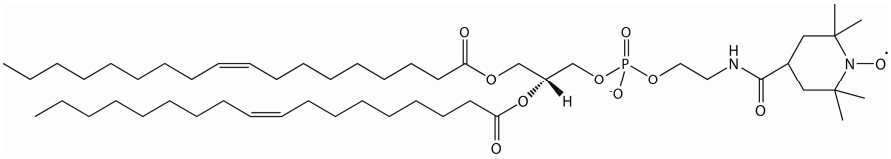

Figure S7.10: Chemical structure of the synthesized spin labeled PE lipid (PE^{-sl}).

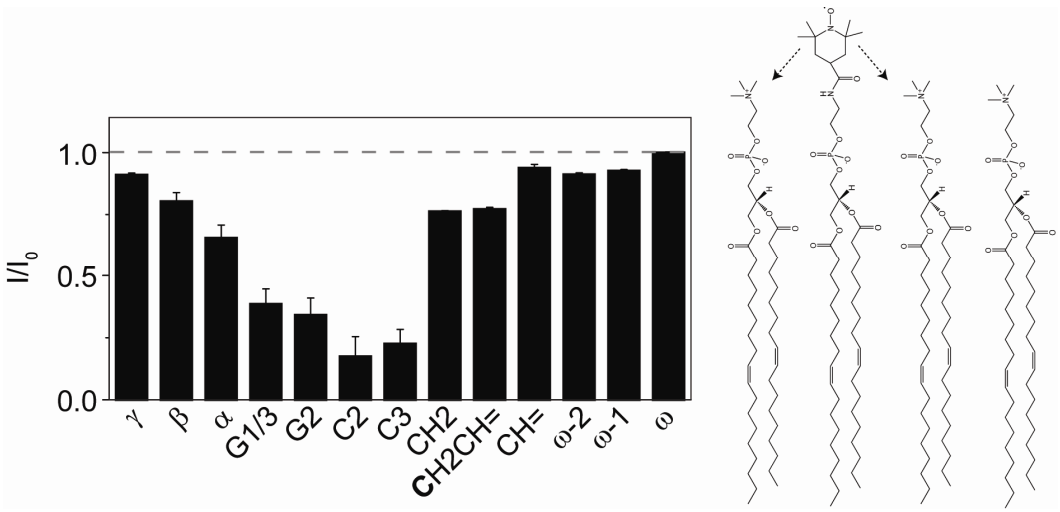

Figure S7.11: Intensity retention of the ^{13}C resonances of PC/PE/PA lipid bilayers

The bilayers (8:1:1 molar ratio) were doped with PE^{sl} (2% w/w) obtained from the [^{13}C,^{13}C]-rINEPT experiments at 20°C before (I) and after (I_0) addition of 10 mM DTT.

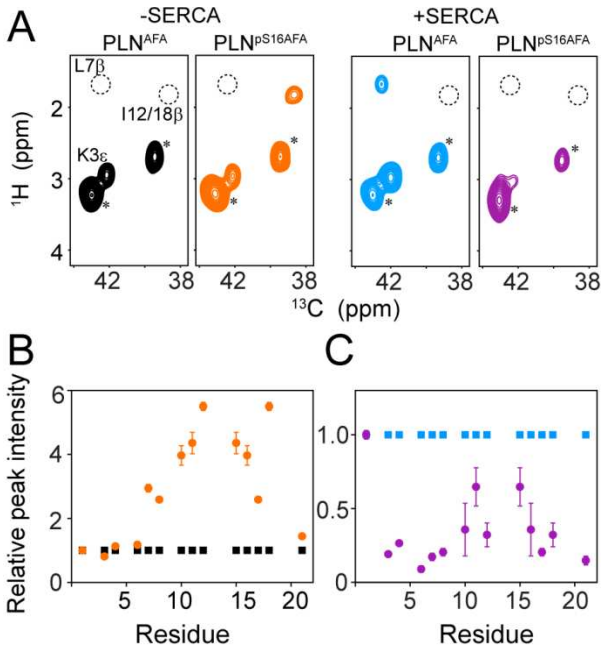

Figure S7.12: r-INEPT spectra in presence and absence of SERCA

(A) Representative regions of the rINEPT spectra of PLN^{AFA} and $PLN^{pS16AFA}$ in the absence and presence of SERCA. Lipid peaks are indicated by asterisks. B) Comparison between the intensities of the resonances of $PLN^{pS16AFA}$ and PLN^{AFA} obtained from the rINEPT spectra. Signal intensities were normalized to the peak corresponding to the methyl group of Met-1 (M1δ). Error bars reflect the signal-to-noise in the spectrum. C) Comparison between the intensities of the resonances of $PLN^{pS16AFA}$ and PLN^{AFA} obtained from the rINEPT spectra in the presence of SERCA.

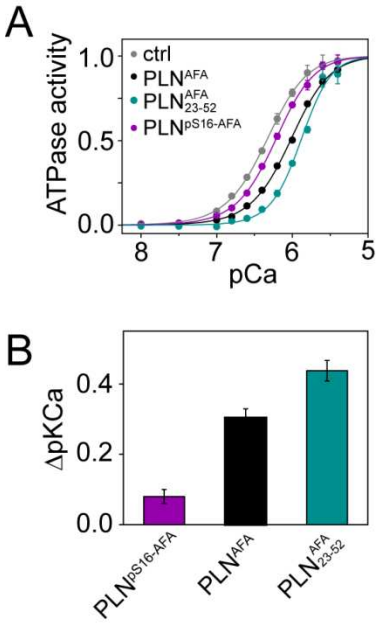

Figure S7.13: ATPase activity

A) ATPase activity in the absence of PLN (ctrl) and in the presence of a 5-fold molar excess of PLN^{AFA}, $PLN^{pS16AFA}$, and the PLN^{AFA}_{23-52} peptide. B) Differences in the apparent Ca^{2+} affinity (ΔpK_{Ca}) of SERCA in the presence of the PLN variants. ΔpK_{Ca} was calculated as $pK_{Ca,SERCA}$- $pK_{Ca,PLN}$, error bars represent the standard errors of four independent reconstitutions.

Bibliography

1. D. T. Murray, N. Das, T. A. Cross, Solid State NMR Strategy for Characterizing Native Membrane Protein Structures., *Acc. Chem. Res.* (2013), doi:10.1021/ar3003442.

2. S. H. White, The progress of membrane protein structure determination., *Protein Sci.* **13**, 1948–1949 (2004).

3. M. Sharma *et al.*, Insight into the mechanism of the influenza A proton channel from a structure in a lipid bilayer., *Science* **330**, 509–12 (2010).

4. J. V Moller, C. Olesen, A.-M. M. L. M. L. Winther, P. Nissen, J. V Møller, The sarcoplasmic Ca2+-ATPase: design of a perfect chemi-osmotic pump., *Q. Rev. Biophys.* **43**, 501–566 (2010).

5. S. Villinger *et al.*, Functional dynamics in the voltage-dependent anion channel., *Proc. Natl. Acad. Sci. U. S. A.* **107**, 22546–22551 (2010).

6. S. Herzig *et al.*, Identification and functional expression of the mitochondrial pyruvate carrier., *Science.* **337**, 93–6 (2012).

7. A. I. Sobolevsky, M. P. Rosconi, E. Gouaux, X-ray structure, symmetry and mechanism of an AMPA-subtype glutamate receptor., *Nature* **462**, 745–56 (2009).

8. M. P. Bokoch *et al.*, Ligand-specific regulation of the extracellular surface of a G-protein-coupled receptor., *Nature* **463**, 108–12 (2010).

9. D. M. Rosenbaum, S. G. F. Rasmussen, B. K. Kobilka, The structure and function of G-protein-coupled receptors., *Nature* **459**, 356–63 (2009).

10. L. K. Tamm, *Protein Lipid Interactions: From Membrane Domains to Cellular Networks* (Wiley-VCH Verlag GmbH & Co. KGaA, Weinheim, Germany, 2005).

11. S. J. Singer, G. L. Nicolson, The fluid mosaic model of the structure of cell membranes., *Science* **175**, 720–31 (1972).

12. D. M. Engelman, Membranes are more mosaic than fluid., *Nature* **438**, 578–80 (2005).

13. J. Li, Z. M. James, X. Dong, C. B. Karim, D. D. Thomas, Structural and functional dynamics of an integral membrane protein complex modulated by lipid headgroup charge., *J. Mol. Biol.* **418**, 379–389 (2012).

14. M. Gustavsson, N. J. Traaseth, G. Veglia, Activating and deactivating roles of lipid bilayers on the Ca(2+)-ATPase/phospholamban complex., *Biochemistry* **50**, 10367–74 (2011).

15. V. V Vostrikov *et al.*, Gramicidin A backbone and side chain dynamics evaluated by molecular dynamics simulations and nuclear magnetic resonance experiments. II: nuclear magnetic resonance experiments., *J. Phys. Chem. B* **115**, 7427–7432 (2011).

16. J. P. Overington, B. Al-Lazikani, A. L. Hopkins, How many drug targets are there?, *Nat. Rev. Drug Discov.* **5**, 993–6 (2006).

17. S. Wakatsuki, E. P. Carpenter, K. Beis, A. D. Cameron, S. Iwata, Overcoming the challenges of membrane protein crystallography., *Curr. Opin. Struct. Biol.* **18**, 581–586 (2008).

18. C. Toyoshima, R. Kanai, F. Cornelius, First crystal structures of Na+,K+-ATPase: new light on the oldest ion pump., *Structure* **19**, 1732–8 (2011).

19. C. Toyoshima, F. Cornelius, New crystal structures of PII-type ATPases: excitement continues., *Curr. Opin. Struct. Biol.* **23**, 507–14 (2013).

20. T. A. Cross, V. Ekanayake, J. Paulino, A. Wright, Solid state NMR: The essential technology for helical membrane protein structural characterization., *J. Magn. Reson.* (2013), doi:10.1016/j.jmr.2013.12.006.

21. H. Yao, M. Hong, Conformation and lipid interaction of the fusion peptide of the paramyxovirus PIV5 in anionic and negative-curvature membranes from solid-state NMR., *J. Am. Chem. Soc.* (2014), doi:10.1021/ja4121956.

22. P. L. Gor'kov *et al.*, Using low-E resonators to reduce RF heating in biological samples for static solid-state NMR up to 900 MHz., *J. Magn. Reson.* **185**, 77–93 (2007).

23. D. H. Zhou *et al.*, Solid-state NMR analysis of membrane proteins and protein aggregates by proton detected spectroscopy., *J. Biomol. NMR* **54**, 291–305 (2012).

24. T. Gopinath, G. Veglia, 3D DUMAS: simultaneous acquisition of three-dimensional magic angle spinning solid-state NMR experiments of proteins., *J. Magn. Reson.* **220**, 79–84 (2012).

25. J. R. Banigan, A. Gayen, N. J. Traaseth, Combination of ^{15}N reverse labeling and afterglow spectroscopy for assigning membrane protein spectra by magic-angle-spinning solid-state NMR: application to the multidrug resistance protein EmrE., *J. Biomol. NMR* **55**, 391–9 (2013).

26. M. Hong, T. V Mishanina, S. D. Cady, Accurate measurement of methyl 13C chemical shifts by solid-state NMR for the determination of protein side chain conformation: the influenza a M2 transmembrane peptide as an example., *J. Am. Chem. Soc.* **131**, 7806–7816 (2009).

27. S. H. Park *et al.*, Structure of the chemokine receptor CXCR1 in phospholipid bilayers., *Nature* **491**, 779–783 (2012).

28. C. M. Rienstra *et al.*, Determination of multiple torsion-angle constraints in U-(13)C,(15)N-labeled peptides: 3D (1)H-(15)N-(13)C-(1)H dipolar chemical shift NMR spectroscopy in rotating solids., *J. Am. Chem. Soc.* **124**, 11908–11922 (2002).

29. K. R. Mote, T. Gopinath, G. Veglia, Determination of structural topology of a membrane protein in lipid bilayers using polarization optimized experiments (POE) for static and MAS solid state NMR spectroscopy., *J. Biomol. NMR* **57**, 91–102 (2013).

30. A. Loquet *et al.*, Atomic model of the type III secretion system needle., *Nature* **486**, 276–279 (2012).

31. F. Castellani *et al.*, Structure of a protein determined by solid-state magic-angle-spinning NMR spectroscopy., *Nature* **420**, 98–102 (2002).

32. S. Wang *et al.*, Solid-state NMR spectroscopy structure determination of a lipid-embedded heptahelical membrane protein., *Nat. Methods* (2013), doi:10.1038/nmeth.2635.

33. T. Gopinath, G. Veglia, Dual acquisition magic-angle spinning solid-state NMR-spectroscopy: simultaneous acquisition of multidimensional spectra of biomacromolecules., *Angew. Chemie, Int. Ed.* **51**, 2731–2735 (2012).

34. J. R. Banigan, N. J. Traaseth, Utilizing afterglow magnetization from cross-polarization magic-angle-spinning solid-state NMR spectroscopy to obtain simultaneous heteronuclear multidimensional spectra., *J. Phys. Chem. B* **116**, 7138–44 (2012).

35. R. Verardi, N. J. Traaseth, L. R. Masterson, V. V Vostrikov, G. Veglia, Isotope labeling for solution and solid-state NMR spectroscopy of membrane proteins., *Adv. Exp. Med. Biol.* **992**, 35–62 (2012).

36. A. Loquet, G. Lv, K. Giller, S. Becker, A. Lange, 13C spin dilution for simplified and complete solid-state NMR resonance assignment of insoluble biological assemblies., *J. Am. Chem. Soc.* **133**, 4722–4725 (2011).

37. B. B. Das *et al.*, Structure determination of a membrane protein in proteoliposomes., *J. Am. Chem. Soc.* **134**, 2047–2056 (2012).

38. B. J. Wylie *et al.*, Ultrahigh resolution protein structures using NMR chemical shift tensors., *Proc. Natl. Acad. Sci. U. S. A.* **108**, 16974–16979 (2011).

39. K. R. Mote *et al.*, Multidimensional oriented solid-state NMR experiments enable the sequential assignment of uniformly 15N labeled integral membrane proteins in magnetically aligned lipid bilayers., *J. Biomol. NMR* **51**, 339–46 (2011).

40. T. V Can *et al.*, Magic angle spinning and oriented sample solid-state NMR structural restraints combine for influenza a M2 protein functional insights., *J. Am. Chem. Soc.* **134**, 9022–9025 (2012).

41. T. Gopinath, N. J. Traaseth, K. Mote, G. Veglia, Sensitivity enhanced heteronuclear correlation spectroscopy in multidimensional solid-state NMR of oriented systems via chemical shift coherences., *J. Am. Chem. Soc.* **132**, 5357–63 (2010).

42. T. Gopinath, K. R. Mote, G. Veglia, Proton evolved local field solid-state nuclear magnetic resonance using Hadamard encoding: theory and application to membrane proteins., *J. Chem. Phys.* **135**, 074503 (2011).

43. T. Gopinath, G. Veglia, Sensitivity enhancement in static solid-state NMR experiments via single- and multiple-quantum dipolar coherences., *J. Am. Chem. Soc.* **131**, 5754–5756 (2009).

44. T. Gopinath, K. R. Mote, G. Veglia, Sensitivity and resolution enhancement of oriented solid-state NMR: application to membrane proteins., *Prog. Nucl. Magn. Reson. Spectrosc.* **75**, 50–68 (2013).

45. V. V Vostrikov, K. R. Mote, R. Verardi, G. Veglia, Structural dynamics and topology of phosphorylated phospholamban homopentamer reveal its role in the regulation of calcium transport., *Structure* **21**, 2119–30 (2013).

46. M. Gustavsson *et al.*, Allosteric regulation of SERCA by phosphorylation-mediated conformational shift of phospholamban., *Proc. Natl. Acad. Sci. U. S. A.* **110**, 17338–43 (2013).

47. S. Lutsenko, J. H. Kaplan, Organization of P-type ATPases: significance of structural diversity., *Biochemistry* **34**, 15607–13 (1995).

48. D. M. Bers, Cardiac excitation-contraction coupling., *Nature* **415**, 198–205 (2002).

49. K. N. Ha *et al.*, Controlling the inhibition of the sarcoplasmic Ca2+-ATPase by tuning phospholamban structural dynamics., *J. Biol. Chem.* **282**, 37205–37214 (2007).

50. L. G. Reddy, J. M. Autry, L. R. Jones, D. D. Thomas, Co-reconstitution of phospholamban mutants with the Ca-ATPase reveals dependence of inhibitory function on phospholamban structure., *J. Biol. Chem.* **274**, 7649–7655 (1999).

51. M. Periasamy, A. Kalyanasundaram, SERCA pump isoforms: their role in calcium transport and disease., *Muscle Nerve* **35**, 430–442 (2007).

52. E. G. Magny *et al.*, Conserved Regulation of Cardiac Calcium Uptake by Peptides Encoded in Small Open Reading Frames, *Science* **1116** (2013), doi:10.1126/science.1238802.

53. D. H. MacLennan, E. G. Kranias, Phospholamban: A crucial regulator of cardiac contractility., *Nat. Rev. Mol. Cell Biol.* **4**, 566–577 (2003).

54. P. Bhupathy, G. J. Babu, M. Periasamy, Sarcolipin and phospholamban as regulators of cardiac sarcoplasmic reticulum Ca2+ ATPase., *J. Mol. Cell. Cardiol.* **42**, 903–911 (2007).

55. P. a Gorski, J. P. Glaves, P. Vangheluwe, H. S. Young, Sarco(endo)plasmic reticulum calcium ATPase (SERCA) inhibition by sarcolipin is encoded in its luminal tail., *J. Biol. Chem.* **288**, 8456–67 (2013).

56. C. Toyoshima *et al.*, Crystal structures of the calcium pump and sarcolipin in the Mg2+-bound E1 state., *Nature* **495**, 260–4 (2013).

57. A.-M. L. Winther *et al.*, The sarcolipin-bound calcium pump stabilizes calcium sites exposed to the cytoplasm., *Nature* **495**, 265–9 (2013).

58. B. L. Akin, T. D. Hurley, Z. Chen, L. R. Jones, The structural basis for phospholamban inhibition of the calcium pump in sarcoplasmic reticulum., *J. Biol. Chem.* **288**, 30181–30191 (2013).

59. S. K. Sahoo, S. a Shaikh, D. H. Sopariwala, N. C. Bal, M. Periasamy, Sarcolipin protein interaction with sarco(endo)plasmic reticulum Ca2+ATPase (SERCA) is distinct from phospholamban protein, and only sarcolipin can promote uncoupling of the SERCA pump., *J. Biol. Chem.* **288**, 6881–9 (2013).

60. B. Mueller, C. B. Karim, I. V Negrashov, H. Kutchai, D. D. Thomas, Direct detection of phospholamban and sarcoplasmic reticulum Ca-ATPase interaction in membranes using fluorescence resonance energy transfer., *Biochemistry* **43**, 8754–8765 (2004).

61. J. M. Autry *et al.*, Oligomeric interactions of sarcolipin and the Ca-ATPase., *J. Biol. Chem.* **286**, 31697–706 (2011).

62. M. Gustavsson *et al.*, Lipid-mediated folding/unfolding of phospholamban as a regulatory mechanism for the sarcoplasmic reticulum Ca2+-ATPase., *J. Mol. Biol.* **408**, 755–65 (2011).

63. K. N. Ha, M. Gustavsson, G. Veglia, Tuning the structural coupling between the transmembrane and cytoplasmic domains of phospholamban to control sarcoplasmic reticulum Ca2+-ATPase (SERCA) function., *J. Muscle Res. Cell Motil.* **33**, 485–492 (2012).

64. L. R. Masterson, A. Cembran, L. Shi, G. Veglia, Allostery and binding cooperativity of the catalytic subunit of protein kinase A by NMR spectroscopy and molecular dynamics simulations., *Adv. Protein Chem. Struct. Biol.* **87**, 363–389 (2012).

65. L. R. Masterson *et al.*, Dynamics connect substrate recognition to catalysis in protein kinase A., *Nat. Chem. Biol.* **6**, 821–8 (2010).

66. P. Bhupathy, G. J. Babu, M. Ito, M. Periasamy, Threonine-5 at the N-terminus can modulate sarcolipin function in cardiac myocytes., *J. Mol. Cell. Cardiol.* **47**, 723–9 (2009).

67. A. Odermatt *et al.*, Sarcolipin regulates the activity of SERCA1, the fast-twitch skeletal muscle sarcoplasmic reticulum Ca2+-ATPase., *J. Biol. Chem.* **273**, 12360–9 (1998).

68. G. J. Babu *et al.*, Ablation of sarcolipin enhances sarcoplasmic reticulum calcium transport and atrial contractility., *Proc. Natl. Acad. Sci. U. S. A.* **104**, 17867–17872 (2007).

69. M. Shanmugam *et al.*, Ablation of phospholamban and sarcolipin results in cardiac hypertrophy and decreased cardiac contractility., *Cardiovasc. Res.* **89**, 353–361 (2010).

70. G. J. Babu *et al.*, Targeted overexpression of sarcolipin in the mouse heart decreases sarcoplasmic reticulum calcium transport and cardiac contractility., *J. Biol. Chem.* **281**, 3972–3979 (2006).

71. A. R. Tupling, M. Asahi, D. H. MacLennan, Sarcolipin overexpression in rat slow twitch muscle inhibits sarcoplasmic reticulum Ca2+ uptake and impairs contractile function., *J. Biol. Chem.* **277**, 44740–44746 (2002).

72. K. N. Ha *et al.*, Lethal Arg9Cys phospholamban mutation hinders Ca2+-ATPase regulation and phosphorylation by protein kinase A., *Proc. Natl. Acad. Sci. U. S. A.* **108**, 2735–2740 (2011).

73. G. J. Babu, P. Bhupathy, C. A. Carnes, G. E. Billman, M. Periasamy, Differential expression of sarcolipin protein during muscle development and cardiac pathophysiology., *J. Mol. Cell. Cardiol.* **43**, 215–222 (2007).

74. H. M. Nef *et al.*, Abnormalities in intracellular Ca2+ regulation contribute to the pathomechanism of Tako-Tsubo cardiomyopathy., *Eur. Heart J.* **30**, 2155–2164 (2009).

75. J. S. Schneider *et al.*, Increased sarcolipin expression and decreased sarco(endo)plasmic reticulum Ca(2+) uptake in skeletal muscles of mouse models of Duchenne muscular dystrophy., *J. Muscle Res. Cell Motil.* (2013), doi:10.1007/s10974-013-9350-0.

76. N. C. Bal *et al.*, Sarcolipin is a newly identified regulator of muscle-based thermogenesis in mammals., *Nat. Med.* **18**, 1575–9 (2012).

77. M. J. Berardi, W. M. Shih, S. C. Harrison, J. J. Chou, Mitochondrial uncoupling protein 2 structure determined by NMR molecular fragment searching., *Nature* **476**, 109–13 (2011).

78. E. Bombardier *et al.*, Sarcolipin trumps β-adrenergic receptor signaling as the favored mechanism for muscle-based diet-induced thermogenesis., *FASEB J.* 1–8 (2013).

79. S. Mall *et al.*, The presence of sarcolipin results in increased heat production by Ca(2+)-ATPase., *J. Biol. Chem.* **281**, 36597–36602 (2006).

80. G. Meissner, Ryanodine receptor/Ca2+ release channels and their regulation by endogenous effectors., *Annu. Rev. Physiol.* **56**, 485–508 (1994).

81. S. Vittorini, S. Storti, M. S. Parri, A. G. Cerillo, A. Clerico, SERCA2a, phospholamban, sarcolipin, and ryanodine receptors gene expression in children with congenital heart defects., *Mol. Med.* **13**, 105–111 (2007).

82. M. V Westfall, J. M. Metzger, Troponin I isoforms and chimeras: tuning the molecular switch of cardiac contraction., *News Physiol. Sci.* **16**, 278–81 (2001).

83. T. A. Cross, M. Sharma, M. Yi, H.-X. Zhou, Influence of solubilizing environments on membrane protein structures., *Trends Biochem. Sci.* **36**, 117–25 (2011).

84. D. E. Warschawski *et al.*, Choosing membrane mimetics for NMR structural studies of transmembrane proteins., *Biochim. Biophys. Acta* **1808**, 1957–74 (2011).

85. R. R. Ketchem, W. Hu, T. A. Cross, High-resolution conformation of gramicidin A in a lipid bilayer by solid-state NMR., *Science* **261**, 1457–1460 (1993).

86. N. J. Traaseth *et al.*, Structure and topology of monomeric phospholamban in lipid membranes determined by a hybrid solution and solid-state NMR approach., *Proc. Natl. Acad. Sci. U. S. A.* **106**, 10165–10170 (2009).

87. R. Verardi, L. Shi, N. J. Traaseth, N. Walsh, G. Veglia, Structural topology of phospholamban pentamer in lipid bilayers by a hybrid solution and solid-state NMR method., *Proc. Natl. Acad. Sci. U. S. A.* **108**, 9101–9106 (2011).

88. K. G. Valentine *et al.*, Structure and topology of a peptide segment of the 6th transmembrane domain of the Saccharomyces cerevisae alpha-factor receptor in phospholipid bilayers., *Biopolymers* **59**, 243–256 (2001).

89. B. A. Buck-Koehntop, A. Mascioni, J. J. Buffy, G. Veglia, Structure, dynamics, and membrane topology of stannin: a mediator of neuronal cell apoptosis induced by trimethyltin chloride., *J. Mol. Biol.* **354**, 652–665 (2005).

90. J. J. Buffy *et al.*, Two-dimensional solid-state NMR reveals two topologies of sarcolipin in oriented lipid bilayers., *Biochemistry* **45**, 10939–10946 (2006).

91. V. V Vostrikov, C. V Grant, S. J. Opella, R. E. Koeppe II, R. E. Koeppe, On the combined analysis of ^{2}H and ^{15}N/^{1}H solid-state NMR data for determination of transmembrane peptide orientation and dynamics., *Biophys. J.* **101**, 2939–47 (2011).

92. V. V Vostrikov, A. E. Daily, D. V Greathouse, R. E. Koeppe, Charged or aromatic anchor residue dependence of transmembrane peptide tilt., *J. Biol. Chem.* **285**, 31723–30 (2010).

93. V. V Vostrikov, B. A. Hall, D. V Greathouse, R. E. Koeppe 2nd, M. S. Sansom, Changes in transmembrane helix alignment by arginine residues revealed by solid-state NMR experiments and coarse-grained MD simulations., *J. Am. Chem. Soc.* **132**, 5803–5811 (2010).

94. C. Aisenbrey, M. Michalek, E. S. Salnikov, B. Bechinger, Solid-state NMR approaches to study protein structure and protein-lipid interactions., *Methods Mol. Biol.* **974**, 357–87 (2013).

95. B. Bechinger, Membrane insertion and orientation of polyalanine peptides: a (15)N solid-state NMR spectroscopy investigation., *Biophys. J.* **81**, 2251–6 (2001).

96. C. Li *et al.*, Uniformly aligned full-length membrane proteins in liquid crystalline bilayers for structural characterization., *J. Am. Chem. Soc.* **129**, 5304–5305 (2007).

97. F. M. Marassi, A. Ramamoorthy, S. J. Opella, Complete resolution of the solid-state NMR spectrum of a uniformly 15N-labeled membrane protein in phospholipid bilayers., *Proc. Natl. Acad. Sci. U. S. A.* **94**, 8551–8556 (1997).

98. S. J. Opella, C. Ma, F. M. Marassi, Nuclear magnetic resonance of membrane-associated peptides and proteins., *Methods Enzymol.* **339**, 285–313 (2001).

99. A. Naito, Structure elucidation of membrane-associated peptides and proteins in oriented bilayers by solid-state NMR spectroscopy., *Solid State Nucl. Magn. Reson.* **36**, 67–76 (2009).

100. S. J. Opella, F. M. Marassi, Structure determination of membrane proteins by NMR spectroscopy., *Chem. Rev.* **104**, 3587–3606 (2004).

101. S. Ozdirekcan, C. Etchebest, J. A. Killian, P. F. J. Fuchs, On the orientation of a designed transmembrane peptide: toward the right tilt angle?, *J. Am. Chem. Soc.* **129**, 15174–81 (2007).

102. I. Marcotte, M. Auger, Bicelles as model membranes for solid- and solution-state NMR studies of membrane peptides and proteins., *Concepts Magn. Reson. Part A* **24A**, 17–37 (2005).

103. U. H. N. Dürr, M. Gildenberg, A. Ramamoorthy, The magic of bicelles lights up membrane protein structure., *Chem. Rev.* **112**, 6054–74 (2012).

104. A. A. De Angelis, S. J. Opella, Bicelle samples for solid-state NMR of membrane proteins., *Nat. Protoc.* **2**, 2332–2338 (2007).

105. A. A. Nevzorov, S. J. Opella, Selective averaging for high-resolution solid-state NMR spectroscopy of aligned samples., *J. Magn. Reson.* **185**, 59–70 (2007).

106. C. Aisenbrey, B. Bechinger, Investigations of polypeptide rotational diffusion in aligned membranes by 2H and 15N solid-state NMR spectroscopy., *J. Am. Chem. Soc.* **126**, 16676–16683 (2004).

107. S. H. Park *et al.*, Local and global dynamics of the G protein-coupled receptor CXCR1., *Biochemistry* **50**, 2371–2380 (2011).

108. S. H. Park, S. J. Opella, Triton x-100 as the “short-chain lipid” improves the magnetic alignment and stability of membrane proteins in phosphatidylcholine bilayers for oriented-sample solid-state NMR spectroscopy., *J. Am. Chem. Soc.* **132**, 12552–12553 (2010).

109. C. Aisenbrey, B. Bechinger, Tilt and rotational pitch angle of membrane-inserted polypeptides from combined 15N and 2H solid-state NMR spectroscopy., *Biochemistry* **43**, 10502–10512 (2004).

110. M. F. Mesleh, G. Veglia, T. M. DeSilva, F. M. Marassi, S. J. Opella, Dipolar waves as NMR maps of protein structure., *J. Am. Chem. Soc.* **124**, 4206–4207 (2002).

111. T. Gopinath, R. Verardi, N. J. Traaseth, G. Veglia, Sensitivity enhancement of separated local field experiments: application to membrane proteins., *J. Phys. Chem. B* **114**, 5089–5095 (2010).

112. T. Gopinath, G. Veglia, Improved Resolution in Dipolar NMR Spectra Using Constant Time Evolution PISEMA Experiment., *Chem. Phys. Lett.* **494**, 104–110 (2010).

113. T. Nakai, T. Terao, Measurements of heteronuclear dipolar powder patterns due only to directly bonded couplings., *Magn. Reson. Chem.* **30**, 42–44 (1992).

114. M. Hong, K. Schmidt-Rohr, D. Nanz, Study of phospholipid structure by H-1, C-13, P-31 dipolar couplings from two-dimensional NMR., *Biophys. J.* **69**, 1939–1950 (1995).

115. K. Schmidt-Rohr, D. Nanz, L. Emsley, A. Pines, NMR Measurement of resolved heteronuclear dipole couplings in liquid crystals and lipids., *J. Phys. Chem.* **98**, 6668–6670 (1994).

116. S. Dvinskikh, U. H. Durr, K. Yamamoto, A. Ramamoorthy, A high-resolution solid-state NMR approach for the structural studies of bicelles., *J. Am. Chem. Soc.* **128**, 6326–6327 (2006).

117. J. W. Emsley *et al.*, A comparison of proton-detected 13C local field experiments with deuterium NMR at natural abundance for studying liquid crystals., *Liq. Cryst.* **35**, 443–464 (2008).

118. S. Jayanthi, P. K. Madhu, N. D. Kurur, K. V Ramanathan, Heteronuclear polarization transfer in static oriented systems using a windowless multiple-pulse sequence., *Chem. Phys. Lett.* **439**, 407–411 (2007).

119. S. V Dvinskikh, K. Yamamoto, U. H. Durr, A. Ramamoorthy, Sensitivity and resolution enhancement in solid-state NMR spectroscopy of bicelles., *J. Magn. Reson.* **184**, 228–235 (2007).

120. R. Soong *et al.*, Proton-evolved local-field solid-state NMR studies of cytochrome b5 embedded in bicelles, revealing both structural and dynamical information., *J. Am. Chem. Soc.* **132**, 5779–5788 (2010).

121. J. S. Waugh, M. Huber, U. Haeberlen, Approach to high resolution NMR in solids., *Phys. Rev. Lett.* **20**, 180–183 (1968).

122. U. Haeberlen, J. S. Waugh, Coherent averaging effects in magnetic resonance., *Phys. Rev.* **175**, 453–467 (1968).

123. P. Mansfield, Symmetrized pulse sequences in high resolution NMR in solids., *J. Phys. C Solid State Phys.* **4**, 1444–1452 (1971).

124. W. K. Rhim, D. D. Elleman, R. W. Vaughan, Analysis of multiple pulse NMR in solids., *J. Chem. Phys.* **59**, 3740–3749 (1973).

125. D. P. Burum, W. K. Rhim, Analysis of multiple pulse NMR in solids., *J. Chem. Phys.* **71**, 944 (1979).

126. M. Lee, W. Goldburg, Nuclear magnetic resonance line narrowing by a rotating RF field., *Phys. Rev.* **140**, A1261–A1271 (1965).

127. E. Vinogradov, P. K. Madhu, S. Vega, Phase modulated Lee–Goldburg magic angle spinning proton nuclear magnetic resonance experiments in the solid state: A bimodal Floquet theoretical treatment., *J. Chem. Phys.* **115**, 8983 (2001).

128. D. P. Burum, M. Linder, R. R. Ernst, Low-power multipulse line narrowing in solid-state., *J. Magn. Reson.* **44**, 173–188 (1981).

129. M. Hohwy, N. C. Nielsen, Elimination of high order terms in multiple pulse nuclear magnetic resonance spectroscopy: Application to homonuclear decoupling in solids., *J. Chem. Phys.* **106**, 7571 (1997).

130. G. J. Lu, S. H. Park, S. J. Opella, Improved 1H amide resonance line narrowing in oriented sample solid-state NMR of membrane proteins in phospholipid bilayers., *J. Magn. Reson.* **220**, 54–61 (2012).

131. R. Fu, E. D. Gordon, D. J. Hibbard, M. Cotten, High resolution heteronuclear correlation NMR spectroscopy of an antimicrobial peptide in aligned lipid bilayers:

peptide-water interactions at the water-bilayer interface., *J. Am. Chem. Soc.* **131**, 10830–1 (2009).

132. A. A. Nevzorov, Orientational and motional narrowing of solid-state NMR lineshapes of uniaxially aligned membrane proteins., *J. Phys. Chem. B* **115**, 15406–15414 (2011).

133. A. A. Maudsley, R. R. Ernst, Indirect detection of magnetic resonance by heteronuclear two-dimensional spectroscopy., *Chem. Phys. Lett.* **50**, 368–372 (1977).

134. G. J. Lu, W. S. Son, S. J. Opella, A general assignment method for oriented sample (OS) solid-state NMR of proteins based on the correlation of resonances through heteronuclear dipolar couplings in samples aligned parallel and perpendicular to the magnetic field., *J. Magn. Reson.* **209**, 195–206 (2011).

135. D. J. States, R. A. Haberkorn, D. J. Ruben, A two-dimensional nuclear overhauser experiment with pure absorption phase in 4 quadrants., *J. Magn. Reson.* **48**, 286–292 (1982).

136. L. Kay, P. Keifer, T. Saarinen, Pure absorption gradient enhanced heteronuclear single quantum correlation spectroscopy with improved sensitivity., *J. Am. Chem. Soc.* **114**, 10663–10665 (1992).

137. J. Cavanagh, A. G. Palmer, P. E. Wright, M. Rance, Sensitivity improvement in proton-detected two-dimensional heteronuclear correlation NMR spectroscopy., *J. Magn. Reson.* **91**, 151–170 (1991).

138. S. H. White, Biophysical dissection of membrane proteins., *Nature* **459**, 344–346 (2009).

139. A. A. De Angelis, S. C. Howell, A. A. Nevzorov, S. J. Opella, Structure determination of a membrane protein with two trans-membrane helices in aligned phospholipid bicelles by solid-state NMR spectroscopy., *J. Am. Chem. Soc.* **128**, 12256–12267 (2006).

140. R. Mani *et al.*, Membrane-dependent oligomeric structure and pore formation of a beta-hairpin antimicrobial peptide in lipid bilayers from solid-state NMR., *Proc. Natl. Acad. Sci. U. S. A.* **103**, 16242–16247 (2006).

141. S. D. Cady *et al.*, Structure of the amantadine binding site of influenza M2 proton channels in lipid bilayers., *Nature* **463**, 689–692 (2010).

142. R. Hester, J. Ackerman, B. Neff, J. Waugh, Separated local field spectra in NMR: Determination of structure of solids., *Phys. Rev. Lett.* **36**, 1081–1083 (1976).

143. C. H. Wu, A. Ramamoorthy, S. J. Opella, High-resolution heteronuclear dipolar solid-state NMR spectroscopy., *J. Magn. Reson. Ser. A* **109**, 270–272 (1994).

144. J. Wang *et al.*, Imaging membrane protein helical wheels., *J. Magn. Reson.* **144**, 162–167 (2000).

145. D. K. Lee, T. Narasimhaswamy, A. Ramamoorthy, PITANSEMA, a low-power PISEMA solid-state NMR experiment., *Chem. Phys. Lett.* **399**, 359–362 (2004).

146. S. V Dvinskikh, D. Sandstrom, Frequency offset refocused PISEMA-type sequences., *J. Magn. Reson.* **175**, 163–169 (2005).

147. S. V Dvinskikh, K. Yamamoto, A. Ramamoorthy, Heteronuclear isotropic mixing separated local field NMR spectroscopy., *J. Chem. Phys.* **125**, 034507–034519 (2006).

148. R. Bertram, J. R. Quine, M. S. Chapman, T. A. Cross, Atomic refinement using orientational restraints from solid-state NMR., *J. Magn. Reson.* **147**, 9–16 (2000).

149. L. Shi *et al.*, A refinement protocol to determine structure, topology, and depth of insertion of membrane proteins using hybrid solution and solid-state NMR restraints., *J. Biomol. NMR* **44**, 195–205 (2009).

150. A. Mascioni, G. Veglia, Theorotical analysis of residual dipolar couplings in regular secondary structure of proteins., *J. Am. Chem. Soc.* **125**, 12520–6 (2003).

151. F. M. Marassi, S. J. Opella, Simultaneous assignment and structure determination of a membrane protein from NMR orientational restraints., *Protein Sci.* **12**, 403–11 (2003).

152. T. Asbury *et al.*, PIPATH: an optimized algorithm for generating alpha-helical structures from PISEMA data., *J. Magn. Reson.* **183**, 87–95 (2006).

153. N. M. Szeverenyi, M. J. Sullivan, G. E. Maciel, Observation of spin exchange by two-dimensional fourier transform 13C cross polarization-magic-angle spinning., *J. Magn. Reson.* **47**, 462–475 (1982).

154. D. Suter, R. Ernst, Spin diffusion in resolved solid-state NMR spectra., *Phys. Rev. B* **32**, 5608–5627 (1985).

155. T. A. Cross, M. H. Frey, S. J. Opella, Nitrogen-15 spin exchange in a protein., *J. Am. Chem. Soc.* **105**, 7471–7473 (1983).

156. F. M. Marassi *et al.*, Dilute spin-exchange assignment of solid-state NMR spectra of oriented proteins: acetylcholine M2 in bilayers., *J. Biomol. NMR* **14**, 141–148 (1999).

157. F. Aussenac, B. Lavigne, E. J. Dufourc, Toward bicelle stability with ether-linked phospholipids: Temperature, composition, and hydration diagrams by H-2 and P-31 solid-state NMR., *Langmuir* **21**, 7129–7135 (2005).

158. A. A. Nevzorov, Mismatched Hartmann-Hahn conditions cause proton-mediated intermolecular magnetization transfer between dilute low-spin nuclei in NMR of static solids., *J. Am. Chem. Soc.* **130**, 11282–11283 (2008).

159. R. W. Knox, G. J. Lu, S. J. Opella, A. A. Nevzorov, A resonance assignment method for oriented-sample solid-state NMR of proteins., *J. Am. Chem. Soc.* **132**, 8255–8257 (2010).

160. J. Xu, J. Struppe, A. Ramamoorthy, Two-dimensional homonuclear chemical shift correlation established by the cross-relaxation driven spin diffusion in solids., *J. Chem. Phys.* **128**, 52308 (2008).

161. J. Xu, P. E. Smith, R. Soong, A. Ramamoorthy, A proton spin diffusion based solid-state NMR approach for structural studies on aligned samples., *J. Phys. Chem. B* **115**, 4863–4871 (2011).

162. A. Mascioni, C. Karim, G. Barany, D. D. Thomas, G. Veglia, Structure and orientation of sarcolipin in lipid environments., *Biochemistry* **41**, 475–482 (2002).

163. J. J. Buffy *et al.*, Defining the intramembrane binding mechanism of sarcolipin to calcium ATPase using solution NMR spectroscopy., *J. Mol. Biol.* **358**, 420–429 (2006).

164. N. J. Traaseth *et al.*, Structural and dynamic basis of phospholamban and sarcolipin inhibition of Ca(2+)-ATPase., *Biochemistry* **47**, 3–13 (2008).

165. N. J. Traaseth, T. Gopinath, G. Veglia, On the performance of spin diffusion NMR techniques in oriented solids: prospects for resonance assignments and distance measurements from separated local field experiments., *J. Phys. Chem. B* **114**, 13872–13880 (2010).

166. B. Buck *et al.*, Overexpression, purification, and characterization of recombinant Ca-ATPase regulators for high-resolution solution and solid-state NMR studies., *Protein Expr. Purif.* **30**, 253–261 (2003).

167. G. Veglia, K. N. Ha, L. Shi, R. Verardi, N. J. Traaseth, What can we learn from a small regulatory membrane protein?, *Methods Mol. Biol.* **654**, 303–319 (2010).

168. B. M. Fung, A. K. Khitrin, K. Ermolaev, An improved broadband decoupling sequence for liquid crystals and solids., *J. Magn. Reson.* **142**, 97–101 (2000).

169. F. Delaglio *et al.*, NMRPipe: a multidimensional spectral processing system based on UNIX pipes., *J. Biomol. NMR* **6**, 277–293 (1995).

170. E. Vinogradov, P. K. P. K. Madhu, S. Vega, High-resolution proton solid-state NMR spectroscopy by phase-modulated Lee–Goldburg experiment., *Chem. Phys. Lett.* **314**, 443–450 (1999).

171. R. Fu, T. A. Cross, Solid-state nuclear magnetic resonance investigation of protein and polypeptide structure., *Annu. Rev. Biophys. Biomol. Struct.* **28**, 235–268 (1999).

172. L. Shi, A. Cembran, J. Gao, G. Veglia, Tilt and azimuthal angles of a transmembrane peptide: a comparison between molecular dynamics calculations and solid-state NMR data of sarcolipin in lipid membranes., *Biophys. J.* **96**, 3648–3662 (2009).

173. R. C. Page, T. A. Cross, Transmembrane helix uniformity examined by spectral mapping of torsion angles., *Structure* **16**, 787–797 (2008).

174. J. R. Quine *et al.*, Intensity and mosaic spread analysis from PISEMA tensors in solid-state NMR., *J. Magn. Reson.* **179**, 190–198 (2006).

175. G. Veglia *et al.*, in *Comprehensive Biophysics*, E. H. Egelman, Ed. (Elsevier, Amsterdam, 2012), pp. 182–198.

176. C. G. Canlas, D. Ma, P. Tang, Y. Xu, Residual dipolar coupling measurements of transmembrane proteins using aligned low-q bicelles and high-resolution magic angle spinning NMR spectroscopy., *J. Am. Chem. Soc.* **130**, 13294–13300 (2008).

177. F. Hu, W. Luo, M. Hong, Mechanisms of proton conduction and gating in influenza M2 proton channels from solid-state NMR., *Science* **330**, 505–508 (2010).

178. L. Shi *et al.*, Paramagnetic-based NMR restraints lift residual dipolar coupling degeneracy in multidomain detergent-solubilized membrane proteins., *J. Am. Chem. Soc.* **133**, 2232–2241 (2011).

179. N. J. Traaseth *et al.*, Spectroscopic validation of the pentameric structure of phospholamban., *Proc. Natl. Acad. Sci. U. S. A.* **104**, 14676–14681 (2007).

180. S. H. Park, F. M. Marassi, D. Black, S. J. Opella, Structure and dynamics of the membrane-bound form of Pf1 coat protein: implications of structural rearrangement for virus assembly., *Biophys. J.* **99**, 1465–1474 (2010).

181. S. D. Cady, T. V Mishanina, M. Hong, Structure of amantadine-bound M2 transmembrane peptide of influenza A in lipid bilayers from magic-angle-spinning solid-state NMR: the role of Ser31 in amantadine binding., *J. Mol. Biol.* **385**, 1127–1141 (2009).

182. A. A. Nevzorov, S. J. Opella, A "magic sandwich" pulse sequence with reduced offset dependence for high-resolution separated local field spectroscopy., *J. Magn. Reson.* **164**, 182–186 (2003).

183. M. J. Knight *et al.*, Structure and backbone dynamics of a microcrystalline metalloprotein by solid-state NMR., *Proc. Natl. Acad. Sci. U. S. A.* **109**, 11095–11100 (2012).

184. L. Shi, I. Kawamura, K.-H. Jung, L. S. Brown, V. Ladizhansky, Conformation of a seven-helical transmembrane photosensor in the lipid environment., *Angew. Chemie, Int. Ed.* **50**, 1302–1305 (2011).

185. M. Tang *et al.*, High-resolution membrane protein structure by joint calculations with solid-state NMR and X-ray experimental data., *J. Biomol. NMR* **51**, 227–233 (2011).

186. A. J. Nieuwkoop, C. M. Rienstra, Supramolecular protein structure determination by site-specific long-range intermolecular solid state NMR spectroscopy., *J. Am. Chem. Soc.* **132**, 7570–7571 (2010).

187. Y. Miao *et al.*, M2 proton channel structural validation from full-length protein samples in synthetic bilayers and *E. coli* membranes., *Angew. Chemie, Int. Ed.* **51**, 8383–8386 (2012).

188. M. Renault *et al.*, Cellular solid-state nuclear magnetic resonance spectroscopy., *Proc. Natl. Acad. Sci. U. S. A.* **109**, 4863–4868 (2012).

189. J. P. Demers, V. Chevelkov, A. Lange, Progress in correlation spectroscopy at ultra-fast magic-angle spinning: basic building blocks and complex experiments for the study of protein structure and dynamics., *Solid State Nucl. Magn. Reson.* **40**, 101–113 (2011).

190. B. Reif, Ultra-high resolution in MAS solid-state NMR of perdeuterated proteins: implications for structure and dynamics., *J. Magn. Reson.* **216**, 1–12 (2012).

191. S. Asami, K. Szekely, P. Schanda, B. H. Meier, B. Reif, Optimal degree of protonation for ^{1}H detection of aliphatic sites in randomly deuterated proteins as a function of the MAS frequency., *J. Biomol. NMR* **54**, 155–168 (2012).

192. A. Marchetti *et al.*, Backbone assignment of fully protonated solid proteins by (1)H detection and ultrafast magic-angle-spinning NMR spectroscopy., *Angew. Chemie, Int. Ed.* **51**, 10756–10759 (2012).

193. B. Reif, C. P. Jaroniec, C. M. Rienstra, M. Hohwy, R. G. Griffin, 1H-1H MAS correlation spectroscopy and distance measurements in a deuterated peptide., *J. Magn. Reson.* **151**, 320–327 (2001).

194. L. J. Sperling, D. A. Berthold, T. L. Sasser, V. Jeisy-Scott, C. M. Rienstra, Assignment strategies for large proteins by magic-angle spinning NMR: the 21-kDa disulfide-bond-forming enzyme DsbA., *J. Mol. Biol.* **399**, 268–282 (2010).

195. J. J. Lopez, C. Kaiser, S. Asami, C. Glaubitz, Higher sensitivity through selective (13)C excitation in solid-state NMR spectroscopy., *J. Am. Chem. Soc.* **131**, 15970–1 (2009).

196. D. A. Hall *et al.*, Polarization-enhanced NMR spectroscopy of biomolecules in frozen solution., *Science* **276**, 930–932 (1997).

197. M. Renault *et al.*, Solid-state NMR spectroscopy on cellular preparations enhanced by dynamic nuclear polarization., *Angew. Chemie, Int. Ed.* **51**, 2998–3001 (2012).

198. R. Linser, B. Bardiaux, V. Higman, U. Fink, B. Reif, Structure calculation from unambiguous long-range amide and methyl 1H-1H distance restraints for a microcrystalline protein with MAS solid-state NMR spectroscopy., *J. Am. Chem. Soc.* **133**, 5905–5912 (2011).

199. A. B. Nielsen *et al.*, Simultaneous acquisition of PAR and PAIN spectra., *J. Biomol. NMR* **52**, 283–8 (2012).

200. N. Giraud *et al.*, Quantitative analysis of backbone dynamics in a crystalline protein from nitrogen-15 spin-lattice relaxation., *J. Am. Chem. Soc.* **127**, 18190–201 (2005).

201. T. Gopinath, G. Veglia, Orphan spin operators enable the acquisition of multiple 2D and 3D magic angle spinning solid-state NMR spectra., *J. Chem. Phys.* **138**, 184201 (2013).

202. T. G. Goddard, D. G. Kneller, SPARKY 3.114 *Univ. California, San Fr.* (2008) (available at http://www.cgl.ucsf.edu/home/sparky/).

203. Y. Shen, F. Delaglio, G. Cornilescu, A. Bax, TALOS+: a hybrid method for predicting protein backbone torsion angles from NMR chemical shifts., *J. Biomol. NMR* **44**, 213–223 (2009).

204. C. D. Schwieters, J. J. Kuszewski, N. Tjandra, G. M. Clore, The Xplor-NIH NMR molecular structure determination package., *J. Magn. Reson.* **160**, 65–73 (2003).

205. L. Yao, A. Grishaev, G. Cornilescu, A. Bax, The impact of hydrogen bonding on amide 1H chemical shift anisotropy studied by cross-correlated relaxation and liquid crystal NMR spectroscopy., *J. Am. Chem. Soc.* **132**, 10866–10875 (2010).

206. A. Senes *et al.*, E(z), a depth-dependent potential for assessing the energies of insertion of amino acid side-chains into membranes: derivation and applications to determining the orientation of transmembrane and interfacial helices., *J. Mol. Biol.* **366**, 436–448 (2007).

207. R. A. Laskowski, J. A. Rullmannn, M. W. MacArthur, R. Kaptein, J. M. Thornton, AQUA and PROCHECK-NMR: programs for checking the quality of protein structures solved by NMR., *J. Biomol. NMR* **8**, 477–486 (1996).

208. I. W. Davis *et al.*, MolProbity: all-atom contacts and structure validation for proteins and nucleic acids., *Nucleic Acids Res.* **35**, W375–383 (2007).

209. K. Takegoshi, S. Nakamura, T. Terao, Dipolar-assisted rotational resonance in magic-angle spinning NMR., *Chem. Phys. Lett.* **344**, 631–637 (2001).

210. Y. Su, A. J. Waring, P. Ruchala, M. Hong, Structures of beta-hairpin antimicrobial protegrin peptides in lipopolysaccharide membranes: mechanism of gram selectivity obtained from solid-state nuclear magnetic resonance., *Biochemistry* **50**, 2072–2083 (2011).

211. M. Asahi *et al.*, Sarcolipin regulates sarco(endo)plasmic reticulum Ca2+-ATPase (SERCA) by binding to transmembrane helices alone or in association with phospholamban., *Proc. Natl. Acad. Sci. U. S. A.* **100**, 5040–5045 (2003).

212. C. Tanford, The sarcoplasmic reticulum calcium pump. Localization of free energy transfer to discrete steps of the reaction cycle., *FEBS Lett.* **166**, 1–7 (1984).

213. C. M. Pickart, W. P. Jencks, Energetics of the calcium-transporting ATPase., *J. Biol. Chem.* **259**, 1629–43 (1984).

214. X. Yu, G. Inesi, Variable stoichiometric efficiency of Ca2+ and Sr2+ transport by the sarcoplasmic reticulum ATPase., *J. Biol. Chem.* **270**, 4361–7 (1995).

215. G. Inesi, F. Tadini-Buoninsegni, Ca(2+)/H (+) exchange, lumenal Ca(2+) release and Ca (2+)/ATP coupling ratios in the sarcoplasmic reticulum ATPase., *J. Cell Commun. Signal.* (2013), doi:10.1007/s12079-013-0213-7.

216. L. de Meis, Uncoupled ATPase activity and heat production by the sarcoplasmic reticulum Ca2+-ATPase. Regulation by ADP., *J. Biol. Chem.* **276**, 25078–87 (2001).

217. C. Toyoshima, M. Nakasako, H. Nomura, H. Ogawa, Crystal structure of the calcium pump of sarcoplasmic reticulum at 2.6 Å resolution., *Nature* **405**, 647–655 (2000).

218. C. Toyoshima, H. Nomura, T. Tsuda, Lumenal gating mechanism revealed in calcium pump crystal structures with phosphate analogues., *Nature* **432**, 361–368 (2004).

219. T. L.-M. Sørensen, J. V. Møller, P. Nissen, T. L. Sorensen, J. V Moller, Phosphoryl transfer and calcium ion occlusion in the calcium pump., *Science* **304**, 1672–5 (2004).

220. C. Olesen, T. L.-M. Sørensen, R. C. Nielsen, J. V. Møller, P. Nissen, Dephosphorylation of the calcium pump coupled to counterion occlusion., *Science* **306**, 2251–5 (2004).

221. C. Olesen *et al.*, The structural basis of calcium transport by the calcium pump., *Nature* **450**, 1036–42 (2007).

222. G. Gafvelin, G. von Heijne, Topological “frustration” in multispanning E. coli inner membrane proteins., *Cell* **77**, 401–12 (1994).

223. H. K. Simmerman, D. E. Lovelace, L. R. Jones, Secondary structure of detergent-solubilized phospholamban, a phosphorylatable, oligomeric protein of cardiac sarcoplasmic reticulum., *Biochim. Biophys. Acta* **997**, 322–329 (1989).

224. M. Tada, M. A. Kirchberger, A. M. Katz, Phosphorylation of a 22,000-dalton component of cardiac sarcoplasmic-reticulum by adenosine 3’-5'-monophosphate-dependent protein kinase., *J. Biol. Chem.* **250**, 2640–2647 (1975).

225. J. Zamoon, A. Mascioni, D. D. Thomas, G. Veglia, NMR solution structure and topological orientation of monomeric phospholamban in dodecylphosphocholine micelles., *Biophys. J.* **85**, 2589–98 (2003).

226. Y. Kimura, K. Kurzydlowski, M. Tada, D. H. MacLennan, Phospholamban regulates the Ca2+-ATPase through intramembrane interactions., *J. Biol. Chem.* **271**, 21726–21731 (1996).

227. M. Li, R. L. Cornea, J. M. Autry, L. R. Jones, D. D. Thomas, Phosphorylation-induced structural change in phospholamban and its mutants, detected by intrinsic fluorescence., *Biochemistry* **37**, 7869–7877 (1998).

228. R. J. Kovacs, M. T. Nelson, H. K. Simmerman, L. R. Jones, Phospholamban forms Ca2+-selective channels in lipid bilayers., *J. Biol. Chem.* **263**, 18364–18368 (1988).

229. K. Oxenoid, J. J. Chou, The structure of phospholamban pentamer reveals a channel-like architecture in membranes., *Proc. Natl. Acad. Sci. U. S. A.* **102**, 10870–10875 (2005).

230. Y. Kimura, K. Kurzydlowski, M. Tada, D. H. MacLennan, Phospholamban inhibitory function is activated by depolymerization., *J. Biol. Chem.* **272**, 15061–15064 (1997).

231. G. X. Chu *et al.*, Monomeric phospholamban overexpression in transgenic mouse hearts., *Circ. Res.* **81**, 485–492 (1997).

232. L. Becucci *et al.*, On the function of pentameric phospholamban: ion channel or storage form?, *Biophys. J.* **96**, L60–2 (2009).

233. S. Smeazzetto, I. Schroeder, G. Thiel, M. R. Moncelli, Phospholamban generates cation selective ion channels., *Phys. Chem. Chem. Phys.* **13**, 12935–12939 (2011).

234. L. Becucci, M. L. Foresti, A. Schwan, R. Guidelli, Can proton pumping by SERCA enhance the regulatory role of phospholamban and sarcolipin?, *Biochim. Biophys. Acta-Biomembranes* **1828**, 2682–2690 (2013).

235. E. E. Metcalfe, J. Zamoon, D. D. Thomas, G. Veglia, (1)H/(15)N heteronuclear NMR spectroscopy shows four dynamic domains for phospholamban reconstituted in dodecylphosphocholine micelles., *Biophys. J.* **87**, 1205–1214 (2004).

236. W. H. Landschulz, P. F. Johnson, S. L. Mcknight, The leucine zipper - a hypothetical structure common to a new class of DNA-binding proteins, *Science* **240**, 1759–1764 (1988).

237. H. K. Simmerman, Y. M. Kobayashi, J. M. Autry, L. R. Jones, A leucine zipper stabilizes the pentameric membrane domain of phospholamban and forms a coiled-coil pore structure., *J. Biol. Chem.* **271**, 5941–5946 (1996).

238. M. Nilges, Ambiguous distance data in the calculation of NMR structures., *Fold. Des.* **2**, S53–S57 (1997).

239. M. R. R. de Planque, J. A. Killian, Protein-lipid interactions studied with designed transmembrane peptides: role of hydrophobic matching and interfacial anchoring., *Mol. Membr. Biol.* **20**, 271–284 (2003).

240. F. M. Marassi, S. J. Opella, A solid-state NMR index of helical membrane protein structure and topology., *J. Magn. Reson.* **144**, 150–155 (2000).

241. N. J. Traaseth, R. Verardi, G. Veglia, Asymmetric methyl group labeling as a probe of membrane protein homo-oligomers by NMR spectroscopy., *J. Am. Chem. Soc.* **130**, 2400–2401 (2008).

242. R. F. S. Walters, W. F. DeGrado, Helix-packing motifs in membrane proteins., *Proc. Natl. Acad. Sci. U. S. A.* **103**, 13658–13663 (2006).

243. R. L. Cornea, J. M. Autry, Z. Chen, L. R. Jones, Reexamination of the role of the leucine/isoleucine zipper residues of phospholamban in inhibition of the Ca2+ pump of cardiac sarcoplasmic reticulum., *J. Biol. Chem.* **275**, 41487–41494 (2000).

244. J. P. Glaves, C. A. Trieber, D. K. Ceholski, D. L. Stokes, H. S. Young, Phosphorylation and mutation of phospholamban alter physical interactions with the sarcoplasmic reticulum calcium pump., *J. Mol. Biol.* **405**, 707–723 (2011).

245. V. A. Jarymowycz, M. J. Stone, Fast time scale dynamics of protein backbones: NMR relaxation methods, applications, and functional consequences., *Chem. Rev.* **106**, 1624–1671 (2006).

246. L. N. de Medeiros *et al.*, Backbone dynamics of the antifungal Psd1 pea defensin and its correlation with membrane interaction by NMR spectroscopy., *Biochim. Biophys. Acta-Biomembranes* **1798**, 105–113 (2010).

247. E. E. Metcalfe, N. J. Traaseth, G. Veglia, Serine 16 phosphorylation induces an order-to-disorder transition in monomeric phospholamban., *Biochemistry* **44**, 4386–4396 (2005).

248. J. M. Kneller, M. Lu, C. Bracken, An effective method for the discrimination of motional anisotropy and chemical exchange., *J. Am. Chem. Soc.* **124**, 1852–1853 (2002).

249. Y. Kimura, M. Asahi, K. Kurzydlowski, M. Tada, D. H. MacLennan, Phospholamban domain Ib mutations influence functional interactions with the Ca2+-ATPase isoform of cardiac sarcoplasmic reticulum., *J. Biol. Chem.* **273**, 14238–14241 (1998).

250. C. Fernandez, C. Hilty, G. Wider, K. Wuthrich, Lipid-protein interactions in DHPC micelles containing the integral membrane protein OmpX investigated by NMR spectroscopy., *Proc. Natl. Acad. Sci. U. S. A.* **99**, 13533–13537 (2002).

251. S. Smeazzetto, A. Saponaro, H. S. Young, M. R. Moncelli, G. Thiel, Structure-function relation of phospholamban: Modulation of channel activity as a potential regulator of SERCA activity., *PLoS One* **8**, e52744–e52744 (2013).

252. R. Aschar-Sobbi, T. L. Emmett, G. J. Kargacin, M. E. Kargacin, Phospholamban phosphorylation increases the passive calcium leak from cardiac sarcoplasmic reticulum., *Pflugers Arch. J. Physiol.* **464**, 295–305 (2012).

253. E. Terzi, L. Poteur, E. Trifilieff, Evidence for a phosphorylation-induced conformational change in phospholamban cytoplasmic domain by CD analysis., *FEBS Lett.* **309**, 413–416 (1992).

254. R. L. Cornea, L. R. Jones, J. M. Autry, D. D. Thomas, Mutation and phosphorylation change the oligomeric structure of phospholamban in lipid bilayers., *Biochemistry* **36**, 2960–2967 (1997).

255. P. Pollesello, A. Annila, Structure of the 1-36 N-terminal fragment of human phospholamban phosphorylated at Ser-16 and Thr-17., *Biophys. J.* **83**, 484–490 (2002).

256. S. Chu, S. Abu-Baker, J. Lu, G. A. Lorigan, (15)N Solid-state NMR spectroscopic studies on phospholamban at its phosphorylated form at ser-16 in aligned phospholipid bilayers., *Biochim. Biophys. Acta* **1798**, 312–317 (2010).

257. S. Abu-Baker, G. A. Lorigan, Phospholamban and its phosphorylated form interact differently with lipid bilayers: a 31P, 2H, and 13C solid-state NMR spectroscopic study., *Biochemistry* **45**, 13312–13322 (2006).

258. J. H. Li, D. J. Bigelow, T. C. Squier, Phosphorylation by cAMP-dependent protein kinase modulates the structural coupling between the transmembrane and cytosolic domains of phospholamban., *Biochemistry* **42**, 10674–10682 (2003).

259. K. Oxenoid, A. J. Rice, J. J. Chou, Comparing the structure and dynamics of phospholamban pentamer in its unphosphorylated and pseudo-phosphorylated states., *Protein Sci.* **16**, 1977–1983 (2007).

260. R. W. Tsien, P. Hess, E. W. Mccleskey, R. L. Rosenberg, Calcium channels - mechanisms of selectivity, permeation, and block. *Annu. Rev. Biophys. Biophys. Chem.* **16**, 265–290 (1987).

261. X. Hou, L. Pedi, M. M. Diver, S. B. Long, Crystal structure of the calcium release-activated calcium channel ORAI., *Science.* **338**, 1308–1313 (2012).

262. C. B. Karim, T. L. Kirby, Z. W. Zhang, Y. Nesmelov, D. D. Thomas, Phospholamban structural dynamics in lipid bilayers probed by a spin label rigidly coupled to the peptide backbone., *Proc. Natl. Acad. Sci. U. S. A.* **101**, 14437–14442 (2004).

263. M. Gustavsson, N. J. Traaseth, G. Veglia, Probing ground and excited states of phospholamban in model and native lipid membranes by magic angle spinning NMR spectroscopy., *Biochim. Biophys. Acta* **1818**, 146–53 (2012).

264. K. R. Chien, Beyond small molecule drugs for heart failure: prospects for gene therapy., *Novartis Found. Symp.* **274**, 244–249,272–276 (2006).

265. E. G. Kranias, R. J. Hajjar, Modulation of cardiac contractility by the phopholamban/SERCA2a regulatome., *Circ. Res.* **110**, 1646–1660 (2012).

266. D. K. Ceholski, C. A. Trieber, C. F. B. Holmes, H. S. Young, Lethal, hereditary mutants of pPhospholamban elude phosphorylation by protein kinase A., *J. Biol. Chem.* **287**, 26596–26605 (2012).

267. M. Said *et al.*, Role of dual-site phospholamban phosphorylation in the stunned heart: insights from phospholamban site-specific mutants., *Am. J. Physiol. Circ. Physiol.* **285**, H1198–H1205 (2003).

268. Z. Hou, E. M. Kelly, S. L. Robia, Phosphomimetic mutations increase phospholamban oligomerization and alter the structure of its regulatory complex., *J. Biol. Chem.* **283**, 28996–29003 (2008).

269. A. Medeiros *et al.*, mutations in the human phospholamban gene in patients with heart failure., *Am. Heart J.* **162**, 1088–U184 (2011).

270. M. E. Anderson, J. H. Brown, D. M. Bers, CaMKII in myocardial hypertrophy and heart failure., *J. Mol. Cell. Cardiol.* **51**, 468–473 (2011).

271. L. Hadri *et al.*, SERCA2a gene transfer enhances eNOS expression and activity in endothelial cells., *Mol. Ther.* **18**, 1284–1292 (2010).

272. A. R. Marks, Calcium cycling proteins and heart failure: mechanisms and therapeutics., *J. Clin. Invest.* **123**, 46–52 (2013).

273. C. Naim, A. Yerevanian, R. J. Hajjar, Gene therapy for heart failure: where do we stand?, *Curr. Cardiol. Rep.* **15**, 333 (2013).

274. G. W. Vuister *et al.*, Solution structure of the DNA-binding domain of Drosophila heat shock transcription factor., *Nat. Struct. Biol.* **1**, 605–614 (1994).

275. G. Veglia, K. N. Ha, L. Shi, R. Verardi, N. J. Traaseth, Membrane protein structure determination., J.-J. Lacapère, Ed. (Humana Press, Totowa, NJ, 2010) pp. 303–319.

276. R. Subiros-Funosas *et al.*, PyClocK, the phosphonium salt derived from 6-Cl-HOBt., *Chim. Oggi-Chemistry Today* **26**, 10–12 (2008).

277. D. S. King, C. G. Fields, G. B. Fields, A Cleavage method which minimizes side reactions following fmoc solid-phase peptide-synthesis., *Int. J. Pept. Protein Res.* **36**, 255–266 (1990).

278. A. Teixeira, W. E. Benckhuijsen, P. E. de Koning, A. R. P. M. Valentijn, J. W. Drijfhout, The use of DODT as a non-malodorous scavenger in fmoc-based peptide synthesis., *Protein Pept. Lett.* **9**, 379–385 (2002).

279. B. A. Cornell, F. Separovic, A. J. Baldassi, R. Smith, Conformation and orientation of gramicidin-A in oriented phospholipid-bilayers measured by solid-state C-13 NMR., *Biophys. J.* **53**, 67–76 (1988).

280. P. C. van der Wel, E. Strandberg, J. A. Killian, R. E. Koeppe 2nd, Geometry and intrinsic tilt of a tryptophan-anchored transmembrane alpha-helix determined by (2)H NMR, *Biophys. J.* **83**, 1479–1488 (2002).

281. T. D. Madden, D. Chapman, P. J. Quinn, Cholesterol modulates activity of calcium-dependent ATPase of the sarcoplasmic-reticulum., *Nature* **279**, 538–541 (1979).

282. M. Brini, E. Carafoli, Calcium pumps in health and disease., *Physiol. Rev.* **89**, 1341–1378 (2009).

283. A. D. Wegener, H. K. Simmerman, J. P. Lindemann, L. R. Jones, Phospholamban phosphorylation in intact ventricles. Phosphorylation of serine 16 and threonine 17 in response to beta-adrenergic stimulation., *J. Biol. Chem.* **264**, 11468–11474 (1989).

284. H. S. Young, L. R. Jones, D. L. Stokes, Locating phospholamban in co-crystals with Ca(2+)-ATPase by cryoelectron microscopy., *Biophys. J.* **81**, 884–894 (2001).

285. K. Seidel *et al.*, Structural characterization of Ca(2+)-ATPase-bound phospholamban in lipid bilayers by solid-state nuclear magnetic resonance (NMR) spectroscopy., *Biochemistry* **47**, 4369–76 (2008).

286. C. Toyoshima *et al.*, Modeling of the inhibitory interaction of phospholamban with the Ca2+ ATPase., *Proc. Natl. Acad. Sci. U. S. A.* **100**, 467–472 (2003).

287. P. James, M. Inui, M. Tada, M. Chiesi, E. Carafoli, Nature and Site of Phospholamban Regulation of the Ca-2+ Pump of Sarcoplasmic-Reticulum., *Nature* **342**, 90–92 (1989).

288. Z. Chen, B. L. Akin, L. R. Jones, Mechanism of reversal of phospholamban inhibition of the cardiac Ca2+-ATPase by protein kinase A and by anti-phospholamban monoclonal antibody 2D12., *J. Biol. Chem.* **282**, 20968–20976 (2007).

289. C. B. Karim, Z. Zhang, E. C. Howard, K. D. Torgersen, D. D. Thomas, Phosphorylation-dependent conformational switch in spin-labeled phospholamban bound to SERCA., *J. Mol. Biol.* **358**, 1032–1040 (2006).

290. M. Asahi, E. McKenna, K. Kurzydlowski, M. Tada, D. H. MacLennan, Physical interactions between phospholamban and sarco(endo)plasmic reticulum Ca2+-ATPases are dissociated by elevated Ca2+, but not by phospholamban phosphorylation, vanadate, or thapsigargin, and are enhanced by ATP., *J. Biol. Chem.* **275**, 15034–15038 (2000).

291. Z. M. James, J. E. McCaffrey, K. D. Torgersen, C. B. Karim, D. D. Thomas, Protein-protein interactions in calcium transport regulation probed by saturation transfer electron paramagnetic resonance., *Biophys. J.* **103**, 1370–1378 (2012).

292. Y. E. Nesmelov, C. B. Karim, L. Song, P. G. Fajer, D. D. Thomas, Rotational dynamics of phospholamban determined by multifrequency electron paramagnetic resonance., *Biophys. J.* **93**, 2805–2812 (2007).

293. J. Zamoon, F. Nitu, C. Karim, D. D. Thomas, G. Veglia, Mapping the interaction surface of a membrane protein: unveiling the conformational switch of phospholamban in calcium pump regulation., *Proc. Natl. Acad. Sci. U. S. A.* **102**, 4747–4752 (2005).

294. O. C. Andronesi *et al.*, Determination of membrane protein structure and dynamics by magic-angle-spinning solid-state NMR spectroscopy., *J. Am. Chem. Soc.* **127**, 12965–12974 (2005).

295. C. B. Karim, C. G. Marquardt, J. D. Stamm, G. Barany, D. D. Thomas, Synthetic null-cysteine phospholamban analogue and the corresponding transmembrane domain inhibit the Ca-ATPase., *Biochemistry* **39**, 10892–10897 (2000).

296. R. J. Bick, L. M. Buja, W. B. Van Winkle, G. E. Taffet, Membrane asymmetry in isolated canine cardiac sarcoplasmic reticulum: Comparison with skeletal muscle sarcoplasmic reticulum., *J. Membr. Biol.* **164**, 169–175 (1998).

297. C. A. Trieber, M. Afara, H. S. Young, Effects of phospholamban transmembrane mutants on the calcium affinity, maximal activity, and cooperativity of the sarcoplasmic reticulum calcium pump., *Biochemistry* **48**, 9287–9296 (2009).

298. H. S. Young, J. L. Rigaud, J. J. Lacapere, L. G. Reddy, D. L. Stokes, How to make tubular crystals by reconstitution of detergent-solubilized Ca2+-ATPase., *Biophys. J.* **72**, 2545–2558 (1997).

299. D. H. MacLennan, Y. Kimura, T. Toyofuku, R. G. K. Johnson EG, Ed. Sites of regulatory interaction between calcium ATPases and phospholamban., *Ann. N. Y. Acad. Sci.* **853**, 31–42 (1998).

300. I. Sengupta, P. S. Nadaud, J. J. Helmus, C. D. Schwieters, C. P. Jaroniec, Protein fold determined by paramagnetic magic-angle spinning solid-state NMR spectroscopy., *Nat. Chem.* **4**, 410–417 (2012).

301. T. L. Religa, A. M. Ruschak, R. Rosenzweig, L. E. Kay, Site-directed methyl group labeling as an NMR probe of structure and dynamics in supramolecular protein systems: applications to the proteasome and to the CIpP protease., *J. Am. Chem. Soc.* **133**, 9063–9068 (2011).

302. C. Ader *et al.*, Structural rearrangements of membrane proteins probed by water-edited solid-state NMR spectroscopy., *J. Am. Chem. Soc.* **131**, 170–176 (2009).

303. D. D. Boehr, R. Nussinov, P. E. Wright, The role of dynamic conformational ensembles in biomolecular recognition., *Nat. Chem. Biol.* **5**, 789–796 (2009).

304. P. Vangheluwe, K. R. Sipido, L. Raeymaekers, F. Wuytack, New perspectives on the role of SERCA2's Ca2+ affinity in cardiac function., *Biochim. Biophys. Acta* **1763**, 1216–1228 (2006).

305. K. Haghighi *et al.*, Superinhibition of sarcoplasmic reticulum function by phospholamban induces cardiac contractile failure., *J. Biol. Chem.* **276**, 24145–24152 (2001).

306. M. Hoshijima *et al.*, Chronic suppression of heart-failure progression by a pseudophosphorylated mutant of phospholamban via in vivo cardiac rAAV gene delivery., *Nat. Med.* **8**, 864–871 (2002).

307. C. Kho, A. Lee, R. J. Hajjar, Altered sarcoplasmic reticulum calcium cycling-targets for heart failure therapy., *Nat. Rev. Cardiol.* **9**, 717–733 (2012).

308. A. Abragam, *The Principles of Nuclear Magnetism.* (Oxford University Press, 1961;

309. H. Saitô, I. Ando, A. Ramamoorthy, H. Saito, Chemical shift tensor - the heart of NMR: Insights into biological aspects of proteins., *Prog. Nucl. Magn. Reson. Spectrosc.* **57**, 181–228 (2010).

310. A. Poon, J. Birn, A. Ramamoorthy, How does an amide-N chemical shift tensor vary in peptides?, *J. Phys. Chem. B* **108**, 16577–16585 (2004).

311. Y. Wei, D. K. Lee, A. Ramamoorthy, Solid-state (13)C NMR chemical shift anisotropy tensors of polypeptides., *J. Am. Chem. Soc.* **123**, 6118–6126 (2001).

312. J. R. Brender, D. M. Taylor, A. Ramamoorthy, Orientation of amide-nitrogen-15 chemical shift tensors in peptides: A quantum chemical study., *J. Am. Chem. Soc.* **123**, 914–922 (2001).

313. A. Ramamoorthy, C. H. Wu, S. J. Opella, Magnitudes and orientations of the principal elements of the 1H chemical shift, 1H− 15N dipolar coupling, and 15N chemical shift interaction tensors in 15Nε1-tryptophan and 15Nπ -histidine side chains determined by three-dimensional solid-state NMR spect., *J. Am. Chem. Soc.* **119**, 10479–10486 (1997).

314. R. R. Ketchem, W. Hu, F. Tian, T. A. Cross, Structure and dynamics from solid state NMR spectroscopy., *Structure* **2**, 699–701 (1994).

315. A. Mascioni, B. L. Eggimann, G. Veglia, Determination of helical membrane protein topology using residual dipolar couplings and exhaustive search algorithm: application to phospholamban., *Chem. Phys. Lipids* **132**, 133–44 (2004).

316. S. J. Opella, A. C. Zeri, S. H. Park, Structure, dynamics, and assembly of filamentous bacteriophages by nuclear magnetic resonance spectroscopy., *Annu. Rev. Phys. Chem.* **59**, 635–657 (2008).

317. K. Yamamoto, D. K. Lee, A. Ramamoorthy, Broadband-PISEMA solid-state NMR spectroscopy., *Chem. Phys. Lett.* **407**, 289–293 (2005).

318. G. A. Mueller *et al.*, Global folds of proteins with low densities of NOEs using residual dipolar couplings: Application to the 370-residue maltodextrin-binding protein., *J. Mol. Biol.* **300**, 197–212 (2000).

319. B. OuYang *et al.*, Unusual architecture of the p7 channel from hepatitis C virus., *Nature* **498**, 521–5 (2013).

320. N. Das, D. T. Murray, T. a Cross, Lipid bilayer preparations of membrane proteins for oriented and magic-angle spinning solid-state NMR samples., *Nat. Protoc.* **8**, 2256–70 (2013).

321. A. Diller *et al.*, Bicelles: A natural "molecular goniometer" for structural, dynamical and topological studies of molecules in membranes., *Biochimie* **91**, 744–751 (2009).

322. R. S. Prosser, J. S. Hwang, R. R. Vold, Magnetically aligned phospholipid bilayers with positive ordering: A new model membrane system., *Biophys. J.* **74**, 2405–2418 (1998).

323. W. S. Son *et al.*, "q-Titration" of long-chain and short-chain lipids differentiates between structured and mobile residues of membrane proteins studied in bicelles by solution NMR spectroscopy., *J. Magn. Reson.* **214**, 111–118 (2012).

324. S. Kim, T. A. Cross, Uniformity, ideality, and hydrogen bonds in transmembrane alpha-helices., *Biophys. J.* **83**, 2084–2095 (2002).

325. N. Sinha, C. V Grant, S. H. Park, J. M. Brown, S. J. Opella, Triple resonance experiments for aligned sample solid-state NMR of (13)C and (15)N labeled proteins., *J. Magn. Reson.* **186**, 51–64 (2007).

326. N. Sinha *et al.*, Peptides and the development of double- and triple-resonance solid-state NMR of aligned samples., *J. Pept. Res.* **65**, 605–620 (2005).

327. T. Vosegaard, N. C. Nielsen, Towards high-resolution solid-state NMR on large uniformly 15N- and [13C,15N]-labeled membrane proteins in oriented lipid bilayers., *J. Biomol. NMR* **22**, 225–47 (2002).

Appendix I: NMR Theory

NMR Interactions and Observables

Most NMR experiments can be described in terms of the interactions of *spins* (i.e. "nuclei with a non-zero spin-angular momentum") with the external (static) magnetic field, the radio-frequency applied, other spins, and in certain cases, the electronic spins. Nuclear spin physics lends itself naturally to a quantum mechanical treatment, and the time dependent Schrodinger equation offers a complete picture for all interactions involved. The Born-Oppenheimer approximation allows the spin part of the Hamiltonian to be separated from the parts containing the nuclear-electronic interactions and thus the equation for the spin part can be written as:

$$\frac{d}{dt}\,\psi_{spin}(t) = -i \cdot \hat{H}_{spin} \cdot \psi_{spin}(t) \quad (1)$$

The Spin Hamiltonian has the following terms:

$$\hat{H}_{spin} = \hat{H}_{Zeeman} + \hat{H}_{Chemical\ Shift} + \hat{H}_{Dipole-Dipole} + \hat{H}_{Quadropole} + \hat{H}_{Scalar\ Coupling} + \hat{H}_{RF} \quad (2)$$

By far the dominant term (under high magnetic fields used for NMR studies) is the Hamiltonian for the Zeeman interaction, which arises due to the degeneracy of the spin angular momentum in a magnetic field. The Zeeman 'splitting' of the energy levels in a static magnetic field provides a population difference, generating a static magnetic moment. The interaction of this magnetic moment with its environment forms the basis for all NMR experiments. The following two sections describe the chemical shift and dipole – dipole interactions, which are the most relevant to this thesis. Subsequent sections describe how these interactions are utilized in oriented and magic angle spinning ssNMR spectroscopies to provide a complete topology of a membrane protein in lipid bilayers.

Chemical Shift Interactions

In addition to the static magnetic field that causes the Zeeman splitting, nuclei experiences an induced magnetic field (B_{ind}) due to its surrounding electronic environment. The perturbation to the Zeeman splitting due to this induced magnetic field is proportional to the external static magnetic field, and is given by:

$$B_{ind} = \delta \cdot B_o \quad (3)$$

Where δ is the chemical shift tensor; and the Hamiltonian for the chemical shift is in turn given by:

$$\hat{H}_{chemical-shift} = -\gamma \cdot \boldsymbol{I} \cdot B_{ind} = -\gamma \cdot \boldsymbol{I} \cdot \delta \cdot B_0 \quad (4)$$

Where γ is the gyromagnetic ratio of the spin under study (***I***).

In general, γ for each spin can be represented by a unique 3rd rank tensor. It can be shown that this tensor is diagonalizable; and the orthogonal basis set in which it is diagonal is called the Principal Axis Frame (PAF). The 'observed' chemical shift (δ_{obs}) can then be described in PAF as follows:

$$\delta_{obs} = \begin{bmatrix} \delta_{11}^{Lab} & \delta_{12}^{Lab} & \delta_{13}^{Lab} \\ \delta_{21}^{Lab} & \delta_{22}^{Lab} & \delta_{23}^{Lab} \\ \delta_{31}^{Lab} & \delta_{23}^{Lab} & \delta_{33}^{Lab} \end{bmatrix} \begin{bmatrix} 0 \\ 0 \\ B_0 \end{bmatrix} = \begin{bmatrix} \delta_{11}^{PAF} & 0 & 0 \\ 0 & \delta_{22}^{PAF} & 0 \\ 0 & 0 & \delta_{33}^{PAF} \end{bmatrix} \begin{bmatrix} B_{0,x} \\ B_{0,y} \\ B_{0,z} \end{bmatrix} \quad (5)$$

The PAF for each nucleus contains the complete information on the chemical shift due to the induced magnetic field (The superscript 'PAF' is dropped henceforth while describing the tensor). In case of isotropic motion the tensor averages to its trace, and the detected chemical shift, called the *isotropic chemical shift* (δ_{iso}), is given by the following equation:

$$\delta_{iso} = \frac{1}{3}(\delta_{11} + \delta_{22} + \delta_{33}); with\ \delta_{33} > \delta_{22} > \delta_{11} \text{ (IUPAC convention)} \quad (6)$$

This is one of the most important NMR observables and is frequency of the resonance observed in solution NMR studies, where the nuclei under consideration undergo fast rotational diffusion. For static NMR studies, a powder pattern, which is the sum of individual resonance spread out over the tensor due to differing orientations, is observed. Fast mechanical rotation of the sample is used to average out the chemical shift tensor to its isotropic value in magic angle spinning NMR experiments, which gives resonance frequency as in solution NMR. Alternately, in oriented ssNMR, each atom has a specific orientation with respect to the magnetic field and hence a single resonance is observed.

Magnetic Dipole-Dipole Interactions

The dipolar interaction between two spins $\boldsymbol{I_1}$ and $\boldsymbol{I_2}$ is described by the 'classical' interaction energy equation:

$$H_{DD} = -\frac{\mu_0}{4\pi}\gamma_1\gamma_2\hbar^2\left(\frac{3(I_1\cdot r)(I_2\cdot r)}{r^5} - \frac{I_1\cdot I_2}{r^3}\right) \quad (7)$$

Here, γ is the gyromagnetic ratio of the nuclei under consideration and r is the vector connecting the two nuclei. This equation can be rewritten conveniently in terms of spherical coordinates (r, θ, □) and *raising* and *lowering* operators as a linear combination of 6 terms (*1*). In the homonuclear case (the two spins being of same nuclei), then the first two terms commute with the Zeeman Hamiltonian and thus, directly affect the position of a resonance in an NMR spectra, while for a heteronuclear pair, only the first term commutes. The angular dependency of these two terms (A and B) is most instructive, and is shown below:

$$H_{DD,term\,A} = \frac{\gamma_1\gamma_2\hbar^2}{r^3}(I_{1Z}I_{2Z})(1 - 3\,cos^2\,\theta) \quad (8)$$

$$H_{DD,term\,B} = -\frac{1}{4}\frac{\gamma_1\gamma_2\hbar^2}{r^3}(I_1^+I_2^- + I_1^-I_2^+)(1 - 3\,cos^2\,\theta) \quad (9)$$

As the remaining four terms do not commute with the Zeeman Hamiltonian, their effects are seen only indirectly (i.e. through their effect on nuclear spin relaxation). For a situation in which tumbling of a molecule averages 'θ' over an entire sphere (isotropic tumbling), both the terms described above are averaged to zero as $(1 - 3\cos^2\theta)$ goes to zero.

Oriented Solid State NMR spectroscopy

Static 'powder' samples can be thought to be made of small crystallites, each with an arbitrary orientation with respect to the external magnetic field B_0. A one dimensional NMR spectrum of such a sample gives rise to so-called 'powder-patterns'. Although this pattern contains a lot of information on the environment of a nucleus, multiple labels generate overlapping patterns that cannot be easily de-convoluted. However, for a static sample that has only one crystallite (i.e. a single crystal), only a few orientations with respect to B_0 are possible. This gives rise to distinct resonance, the position of which depends on the chemical shift tensor and the orientation of the tensor with respect to B_0. With the fore-knowledge of the chemical shift tensor, one can easily calculate the orientation of this particular tensor with respect to B_0 from its resonance frequency. Given the fixed relationship between the tensor and the chemical environment of the residue, this entails the determination of the orientation of a single chemical moiety with respect to B_0. Similarly, the knowledge of dipolar coupling between and two atoms allow the calculation of the orientation of the bond vector with respect to B_0. For proteins, the chemical shift tensor for amide ^{15}N atoms and its orientation with respect to the peptide plane is very well studied (*2–6*). The calculation of ^{15}N chemical shift and the ^{15}N-^{1}H dipolar coupling in a suitably oriented sample forms the basis for determining the topology of a protein (*7–9*). Note that these 'restraints' are, by themselves, degenerate (*10*, *11*). However, restraints on multiple residues combined with Monte-Carlo sampling of possible solutions can give rise to very precise solutions for a secondary structure (*12–16*).

NMR experiments to determine anisotropic parameters

The simplest experiment that allows the determination of the chemical shift and dipolar coupling in these samples is the *Polarity Index Spin Exchange at Magic Angle* (PISEMA) experiment (*17*). It belongs to a class of experiments known as the Separated Local Field (SLF) experiments and in ^{15}N-labeled membrane proteins, allows the correlation of the ^{15}N chemical shift (which in this case, is the anisotropic chemical shift) to the ^{15}N-^{1}H dipolar coupling. The experiment starts with generating a transverse magnetization on ^{1}H and then transferring it to ^{15}N using cross-polarization (Figure 2). The ^{15}N-magnetization is then allowed to oscillate (in the indirect dimension) at the ^{15}N-^{1}H dipolar coupling by spin locking ^{1}H and ^{15}N at the Hartmann-Hahn condition and removing with ^{1}H-^{1}H

dipolar coupling using a Phase-Modulated or a Frequency-Switched Lee-Goldberg (PMLG or FSLG) sequence. Finally, the ^{15}N-chemical shift is detected in the direct dimension after strong heteronuclear decoupling sequence is applied on ^{1}H. A number of variants of PISEMA have been proposed, all of them differing in the pulse scheme used for dipolar evolution (*18–20*). All these experiments are capable of giving a complete description of the topological parameters from a single experiment.

Aligned samples for soluble and membrane proteins

Although this is in theory applicable to all proteins, membrane and soluble, the preparation of a suitable oriented sample is a significant bottleneck. For soluble proteins, a partial alignment in anisotropic media, such as polyacrylamide gels, phage, bicelles and DNA-nanotubes induces partial alignment of a protein and allows the determination of *residual dipolar couplings* (RDC) and *residual chemical shift anisotropies* (RCSA) (*21*). In this case, the alignment tensor is dictated by the anisotropic media used and thus defines an external frame of reference for a protein. These values of can be RDCs and RCSAs can be used to align multiple domains in a single protein in conjugation with a distance restraints from the more traditional solution NMR experiments. Indeed, this approach has been used to determine the structures of a number of large proteins, including multi-domain membrane proteins in detergent micelles by solution NMR techniques (*22*, *23*).

Lipid-bilayers are capable of spontaneously spread and align when deposited on a flat surface, and any membrane protein that is embedded in such a bilayer will also be aligned. This is the traditional way in which membrane protein samples were made for oriented NMR studies (*24*). Membrane protein reconstituted in lipid vesicles are spread out on multiple glass plates, which are then stacked and placed in the NMR spectrometer at an orientation that would uniformly align the bilayer with its director (a vector perpendicular to the bilayer) parallel to B_0. Alternatively, lipid bicelles (i.e. lipid mixtures made up of short chain and long chain lipids) that are capable of spontaneously aligning in a magnetic field due to the highly anisotropic nature of their magnetic susceptibility can be used (*25–27*). Though restricted to only a subset of lipids, these bicelles offer a significant advantage over mechanically aligned samples because of better control over hydration , pH and also generate better alignment (*28*, *29*).

Topology from a SLF spectrum

The inherent helicity of a transmembrane α-helix gives rise to sinusoidal pattern for both anisotropic chemical shift and dipolar coupling (when plotted with respect to residue number) (*7*). As these two patterns are independent, they give rise to a circular pattern when correlated in two dimensions (*11*, *30*, *31*). Thus, the PISEMA spectrum for a well-defined transmembrane helix is typically a circular pattern of individual resonances and is called the *Polar Index Slant Angle* (PISA) wheel pattern. This is a direct image of transmembrane helicity (*30*). The size and position of the PISA wheel changes depending on the tilt angle of the helix with respect to B_0 (and indirectly, with respect to the lipid bilayer) (Figure 3). Comparing a PISEMA spectrum to a simulated PISA wheel of an

ideal helix directly gives the tilt angle of the transmembrane segment with respect to the lipid bilayer. Alternatively, the chemical shift and dipolar couplings can be incorporated as restraints in a simulated annealing protocol and the transmembrane topology of the protein determined without assuming an ideal helix (*8*, *32*). In addition to PISEMA, we can correlate the ^{1}H chemical shift with ^{15}N chemical shift in a HETCOR experiment. A 3D-experiment (PISEMAI-HETCOR) will correlate the ^{15}N chemical shift, ^{1}H chemical shift and the ^{15}N-^{1}H dipolar coupling, giving information to determine the complete topology of each peptide plane (*33*, *34*). An important point to note here is that these restraints, unlike distance restraints in solution NMR, are absolute, i.e. error in any one of them does not add to the error of another restraint (*35*). Obtaining these restraints for the purposes of determining a high-resolution structure is thus highly desirable, and imperative if transmembrane topology is to be experimentally determined.

Magic angle spinning ssNMR

Although a powerful technique, O-ssNMR has been so far limited to the backbone ^{15}N and ^{1}H atoms. In order to obtain a complete picture of a protein, probing the carbon atoms of both the backbone and side chains in a protein is desirable. Oriented ^{13}C NMR on proteins is still in infancy, as a limited number of experiments have been designed owing to the dense ^{13}C-^{13}C dipolar couplings in static sample that complicate spectroscopy (*36–38*). Magic angle spinning (MAS) ssNMR offers an alternative, as *isotropic* chemical shifts for all atoms in a protein can be detected using this technique (*39*). Although the pulse sequences and technical requirements for MAS-ssNMR are more demanding than for solution NMR, the interpretation of the spectra is analogous, and thus a description of protein in terms of well-established parameters such as chemical shift perturbation and secondary structure propensity is rendered possible.

To acquire a MAS-ssNMR spectrum, a sample (in our case, membrane proteins reconstituted in lipid vesicles) is spun at high speed at a fixed angle of 54.7º with respect to B_0. If the spinning speed in greater than the dipolar coupling, the average dipolar coupling averages to zero according to equations 8 and 9. Similarly, if the spinning speed is greater than the chemical shift tensor, the isotropic chemical shift is observed. Moderate spinning speeds (8 to 5kHz) are sufficient to remove most of the dipolar couplings (except the ^{1}H-^{1}H dipolar couplings) and average out most of the chemical shift tensors to the isotropic value. With perdeuteration and spinning speeds greater than 80 kHz, it is possible to perform the experiments used for solution state in the solid state (*40*).

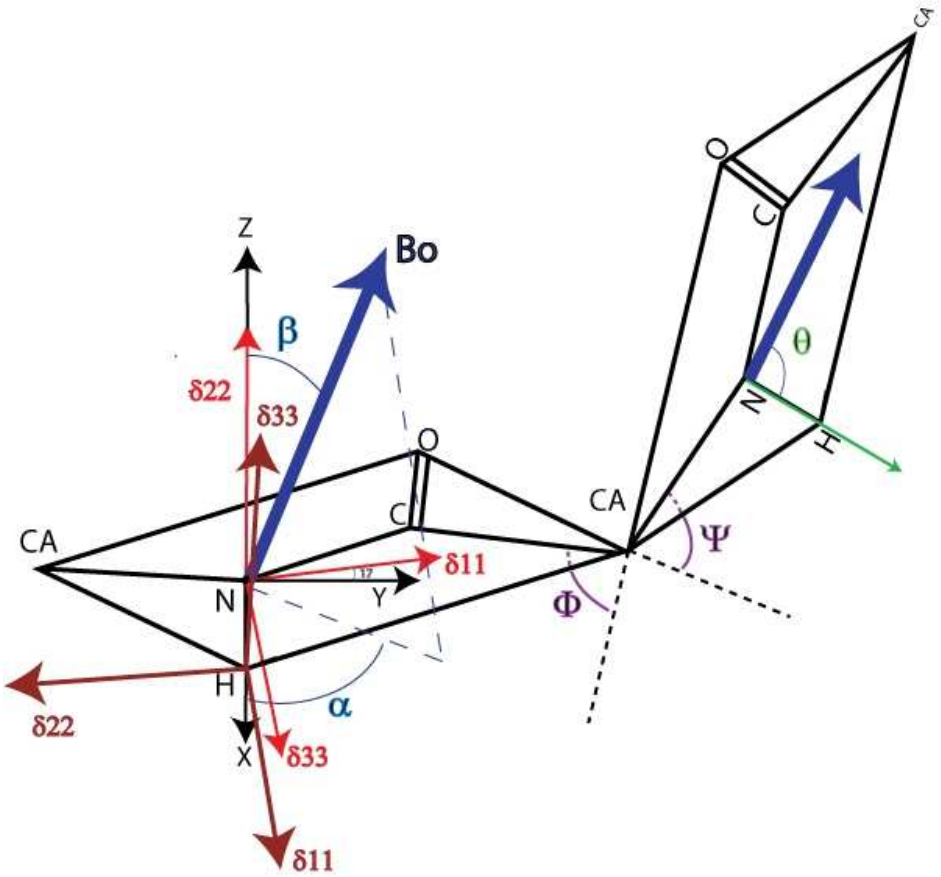

Figure A1: Chemical shift tensors for the peptide plane.

Orientation of chemical shift anisotropy tensors for amide ^{15}N and ^{1}H atoms with respect to the peptide plane for an arbitrary amide residue with an arbitrary orientation with respect to the external magnetic field B_0 are shown.

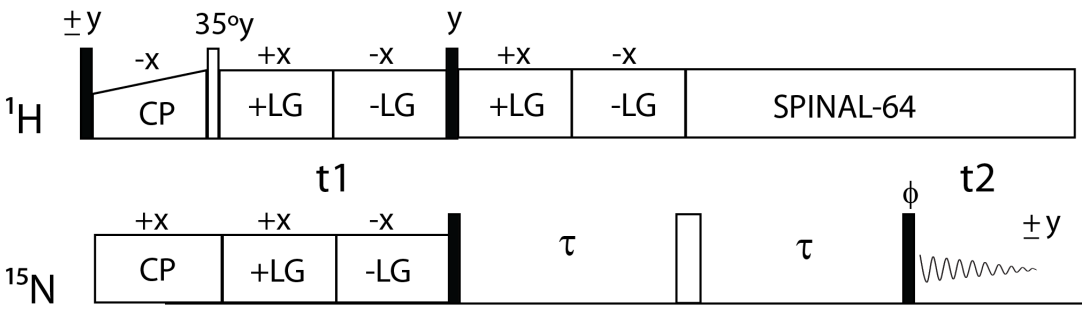

Figure A2: Pulse sequence for the SE-PISEMA Experiment

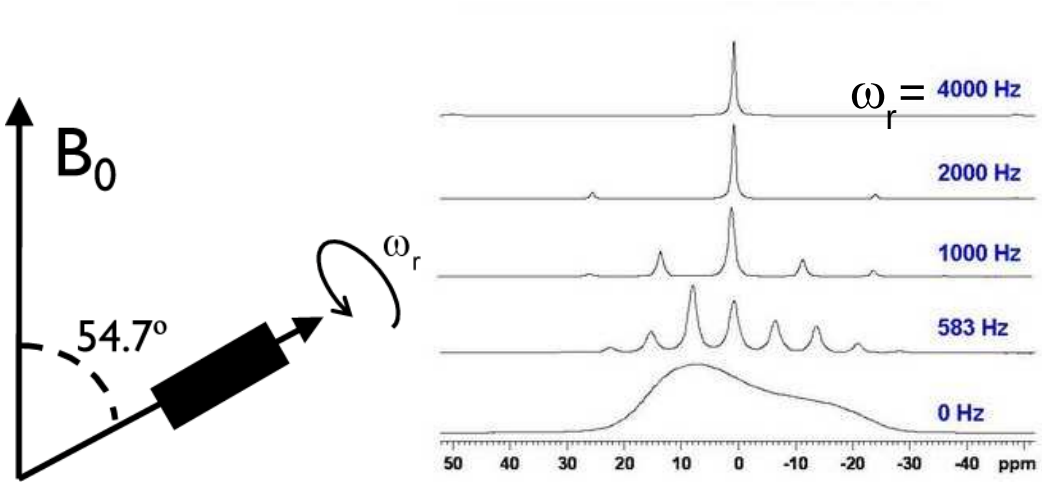

Figure A3: Magic Angle Spinning NMR.

For samples that do not possess fast rotational diffusion, mechanical rotation around an axis kept at an angle of 54.7º with respect to the external magnetic field. This allows the averaging out of CSA and DC interactions. At slow spinning speeds (i.e. rotation speed less than the CSA), spinning sidebands are seen, spaced at intervals equal to the spinning frequency and centered at the isotropic frequency. At faster spinning speed, only the isotropic chemical shift is observed.

References for the Appendix

1. A. Abragam, *The Principles of Nuclear Magnetism.* Oxford University Press, 1961.

2. H. Saitô, I. Ando, A. Ramamoorthy, H. Saito, Chemical shift tensor - the heart of NMR: Insights into biological aspects of proteins., *Prog. Nucl. Magn. Reson. Spectrosc.* **57**, 181–228 (2010).

3. A. Poon, J. Birn, A. Ramamoorthy, How does an amide-N chemical shift tensor vary in peptides?, *J. Phys. Chem. B* **108**, 16577–16585 (2004).

4. Y. Wei, D. K. Lee, A. Ramamoorthy, Solid-state (13)C NMR chemical shift anisotropy tensors of polypeptides., *J. Am. Chem. Soc.* **123**, 6118–6126 (2001).

5. J. R. Brender, D. M. Taylor, A. Ramamoorthy, Orientation of amide-nitrogen-15 chemical shift tensors in peptides: A quantum chemical study., *J. Am. Chem. Soc.* **123**, 914–922 (2001).

6. A. Ramamoorthy, C. H. Wu, S. J. Opella, Magnitudes and orientations of the principal elements of the 1H chemical shift, 1H− 15N dipolar coupling, and 15N chemical shift interaction tensors in 15Nε1-tryptophan and 15Nπ -histidine side chains determined by three-dimensional solid-state NMR spectroscopy., *J. Am. Chem. Soc.* **119**, 10479–10486 (1997).

7. M. F. Mesleh, G. Veglia, T. M. DeSilva, F. M. Marassi, S. J. Opella, Dipolar waves as NMR maps of protein structure., *J. Am. Chem. Soc.* **124**, 4206–4207 (2002).

8. R. Bertram, J. R. Quine, M. S. Chapman, T. A. Cross, Atomic refinement using orientational restraints from solid-state NMR., *J. Magn. Reson.* **147**, 9–16 (2000).

9. R. R. Ketchem, W. Hu, F. Tian, T. A. Cross, Structure and dynamics from solid state NMR spectroscopy., *Structure* **2**, 699–701 (1994).

10. L. Shi *et al.*, Paramagnetic-based NMR restraints lift residual dipolar coupling degeneracy in multidomain detergent-solubilized membrane proteins., *J. Am. Chem. Soc.* **133**, 2232–2241 (2011).

11. A. Mascioni, B. L. Eggimann, G. Veglia, Determination of helical membrane protein topology using residual dipolar couplings and exhaustive search algorithm: application to phospholamban., *Chem. Phys. Lipids* **132**, 133–44 (2004).

12. M. Sharma *et al.*, Insight into the mechanism of the influenza A proton channel from a structure in a lipid bilayer., *Science* **330**, 509–12 (2010).

13. S. J. Opella, A. C. Zeri, S. H. Park, Structure, dynamics, and assembly of filamentous bacteriophages by nuclear magnetic resonance spectroscopy., *Annu. Rev. Phys. Chem.* **59**, 635–657 (2008).

14. N. J. Traaseth *et al.*, Structure and topology of monomeric phospholamban in lipid membranes determined by a hybrid solution and solid-state NMR approach., *Proc. Natl. Acad. Sci. U. S. A.* **106**, 10165–10170 (2009).

15. R. Verardi, L. Shi, N. J. Traaseth, N. Walsh, G. Veglia, Structural topology of phospholamban pentamer in lipid bilayers by a hybrid solution and solid-state NMR method., *Proc. Natl. Acad. Sci. U. S. A.* **108**, 9101–9106 (2011).

16. K. R. Mote, T. Gopinath, G. Veglia, Determination of structural topology of a membrane protein in lipid bilayers using polarization optimized experiments (POE) for static and MAS solid state NMR spectroscopy., *J. Biomol. NMR* **57**, 91–102 (2013).

17. C. H. Wu, A. Ramamoorthy, S. J. Opella, High-resolution heteronuclear dipolar solid-state NMR spectroscopy., *J. Magn. Reson. Ser. A* **109**, 270–272 (1994).

18. A. A. Nevzorov, S. J. Opella, Selective averaging for high-resolution solid-state NMR spectroscopy of aligned samples., *J. Magn. Reson.* **185**, 59–70 (2007).

19. S. V Dvinskikh, K. Yamamoto, A. Ramamoorthy, Heteronuclear isotropic mixing separated local field NMR spectroscopy., *J. Chem. Phys.* **125**, 034507–034519 (2006).

20. K. Yamamoto, D. K. Lee, A. Ramamoorthy, Broadband-PISEMA solid-state NMR spectroscopy., *Chem. Phys. Lett.* **407**, 289–293 (2005).

21. G. A. Mueller *et al.*, Global folds of proteins with low densities of NOEs using residual dipolar couplings: application to the 370-residue maltodextrin-binding protein., *J. Mol. Biol.* **300**, 197–212 (2000).

22. M. J. Berardi, W. M. Shih, S. C. Harrison, J. J. Chou, Mitochondrial uncoupling protein 2 structure determined by NMR molecular fragment searching., *Nature* **476**, 109–13 (2011).

23. B. OuYang *et al.*, Unusual architecture of the p7 channel from hepatitis C virus., *Nature* **498**, 521–5 (2013).

24. N. Das, D. T. Murray, T. a Cross, Lipid bilayer preparations of membrane proteins for oriented and magic-angle spinning solid-state NMR samples., *Nat. Protoc.* **8**, 2256–70 (2013).

25. U. H. N. Dürr, M. Gildenberg, A. Ramamoorthy, The magic of bicelles lights up membrane protein structure., *Chem. Rev.* **112**, 6054–74 (2012).

26. A. Diller *et al.*, Bicelles: A natural "molecular goniometer" for structural, dynamical and topological studies of molecules in membranes., *Biochimie* **91**, 744–751 (2009).

27. R. S. Prosser, J. S. Hwang, R. R. Vold, Magnetically aligned phospholipid bilayers with positive ordering: a new model membrane system., *Biophys. J.* **74**, 2405–2418 (1998).

28. W. S. Son *et al.*, "q-Titration" of long-chain and short-chain lipids differentiates between structured and mobile residues of membrane proteins studied in bicelles by solution NMR spectroscopy., *J. Magn. Reson.* **214**, 111–118 (2012).

29. S. H. Park, S. J. Opella, Triton x-100 as the "short-chain lipid" improves the magnetic alignment and stability of membrane proteins in phosphatidylcholine bilayers for oriented-sample solid-state NMR spectroscopy., *J. Am. Chem. Soc.* **132**, 12552–12553 (2010).

30. R. C. Page, T. A. Cross, Transmembrane helix uniformity examined by spectral mapping of torsion angles., *Structure* **16**, 787–797 (2008).

31. S. Kim, T. A. Cross, Uniformity, ideality, and hydrogen bonds in transmembrane alpha-helices., *Biophys. J.* **83**, 2084–2095 (2002).

32. L. Shi *et al.*, A refinement protocol to determine structure, topology, and depth of insertion of membrane proteins using hybrid solution and solid-state NMR restraints., *J. Biomol. NMR* **44**, 195–205 (2009).

33. T. Gopinath, N. J. Traaseth, K. Mote, G. Veglia, Sensitivity enhanced heteronuclear correlation spectroscopy in multidimensional solid-state NMR of oriented systems via chemical shift coherences., *J. Am. Chem. Soc.* **132**, 5357–63 (2010).

34. G. J. Lu, S. H. Park, S. J. Opella, Improved 1H amide resonance line narrowing in oriented sample solid-state NMR of membrane proteins in phospholipid bilayers., *J. Magn. Reson.* **220**, 54–61 (2012).

35. D. T. Murray, N. Das, T. A. Cross, Solid State NMR Strategy for Characterizing Native Membrane Protein Structures., *Acc. Chem. Res.* (2013), doi:10.1021/ar3003442.

36. N. Sinha, C. V Grant, S. H. Park, J. M. Brown, S. J. Opella, Triple resonance experiments for aligned sample solid-state NMR of (13)C and (15)N labeled proteins., *J. Magn. Reson.* **186**, 51–64 (2007).

37. N. Sinha *et al.*, Peptides and the development of double- and triple-resonance solid-state NMR of aligned samples., *J. Pept. Res.* **65**, 605–620 (2005).

38. T. Vosegaard, N. C. Nielsen, Towards high-resolution solid-state NMR on large uniformly 15N- and [13C,15N]-labeled membrane proteins in oriented lipid bilayers., *J. Biomol. NMR* **22**, 225–47 (2002).

39. D. H. Zhou *et al.*, Solid-state NMR analysis of membrane proteins and protein aggregates by proton detected spectroscopy., *J. Biomol. NMR* **54**, 291–305 (2012).

40. J. P. Demers, V. Chevelkov, A. Lange, Progress in correlation spectroscopy at ultra-fast magic-angle spinning: basic building blocks and complex experiments for the study of protein structure and dynamics., *Solid State Nucl. Magn. Reson.* **40**, 101–113 (2011).